DISSERTATION

QUANTIFICATION OF THE DIRECTIONAL DETECTION CAPABILITY OF THE DRIFT-IIE DARK MATTER SEARCH DETECTOR VIA THE RANGE OF NUCLEAR RECOIL TRACKS IN TWO DIMENSIONS

Submitted by

Frederick G. Schuckman II

Department of Physics

In partial fulfillment of the requirements

For the Degree of Doctor of Philosophy

Colorado State University

Fort Collins, Colorado

Spring 2021

Doctoral Committee:

Advisor: John Harton

Walter Toki
Michael Mooney
Mario Marconi

ABSTRACT

QUANTIFICATION OF THE DIRECTIONAL DETECTION CAPABILITY OF THE DRIFT-IIE DARK MATTER SEARCH DETECTOR VIA THE RANGE OF NUCLEAR RECOIL TRACKS IN TWO DIMENSIONS

Evidence suggests that 83% of the matter content of the universe is dark matter. Despite its ubiquity, the identity of this matter is unknown. It is thought that a halo of dark matter surrounds and is distributed throughout our galaxy. The Weakly Interacting Massive Particle (WIMP) has been a popular dark matter candidate. As we move through this halo it should appear as a wind of WIMPs incident upon us. A properly-placed detector could have this wind blow through its top face at one time in the day, and through a side face 12 sidereal hours later. DRIFT-IIe is a low-pressure gas negative-ion time projection chamber designed for direct and directional detection of WIMPs elastically scattering from gas nuclei. Partial directional information of a WIMP recoil could be extracted by measuring the range of the track of ionization that it produces in two dimensions. To study this signature, the detector was exposed to a source of neutrons in a series of runs. In one run the source was placed above the detector and in a second run the source was placed to the side of the detector. Neutron recoils mimic those expected from WIMPs, and the source placement mimics a specific WIMP wind direction. For the two runs, the range information was compared with a Monte Carlo resampling test. It was found on average 302 +/- 4 neutron recoils, sampled with WIMP-like energy spectra, are required along each of these axes to discern the two populations with a significance of 3σ.

ACKNOWLEDGEMENTS

Mom and Dad, thank you for all that you have done and continue to do. I am truly grateful to have such loving and caring parents. Mom you are the kindest person. I aspire to be like you in that way. There is no greater expression of pure love than the embraces that I receive from you. Dad, you have always encouraged me and you have helped to shape the way that I look at the world. I see you in some of the quirks that I have and in the way I go about doing things. Lindsay, you are an amazing sister, and you have always been there for me. It brings me great happiness that you and Dustin have cultivated a family with three beautiful kids. Nolan, you are my brother. I love you all.

It was a pleasure to have John Harton as my advisor. Keeping the big picture in mind, being reasonable, being kind, while simultaneously-and-rigorously working on research or teaching describes the state in which I have seen John do things. I have gained insight from this. Thank you John.

With gratitude, I acknowledge the funding that I have received as a graduate student. Over the years, I have received teaching assistantships through the Colorado State University Department of Physics. I also received support in the form of research assistantships. This work was partially supported by the US National Science Foundation Division of Physics, Particle Astrophysics - Experiment. This material is based upon work supported by the National Science Foundation under Grant No. 1506116. For the summer of 2019, my work was supported by a High Energy Physics and Particle Astrophysics Programs of Research and Scholarly Excellence Fellowship Award.

This document was generated using the Texmaker LaTeX editor. The Colorado State University LaTeX Thesis Template created by Elliott Forney (2017) was utilized.

DEDICATION

To Maria and our two pups Toby and Aspen. I love you Belle.

TABLE OF CONTENTS

LIST OF TABLES

LIST OF FIGURES

Chapter 1

Introduction

1.1 Evidence in Support of Dark Matter

An early indication for the existence of Dark Matter (DM), came in the 1930s from Zwicky [1] [2]. Zwicky studied speeds of galaxies within the Coma cluster of galaxies. The Doppler shift of known elemental frequency spectra was used to extract the radial velocities of galaxies within the cluster for an Earth-based observer. The variance in these galactic speeds then provides a measurement of the speed of the galaxies relative to the cluster. Measurement of the radial velocity is only one component of the total velocity in three dimensions. With the assumption that the movement of galaxies with the cluster is isotropic, the total speed of a galaxy is the square root of three times the radial component squared. The virial theorem, which gives a relationship between the average kinetic energy and average gravitational potential energy, was used to extract the mass of the cluster. In the latter of the two referenced papers, Zwicky concluded that the average galaxy mass within the cluster was 4.5×10^{10} solar masses based on this method. The average galaxy luminosity was measured to be 8.5×10^{7} suns, the ratio these two values yield a mass-to-light ratio of $\frac{M}{L} \sim 530$ relative to that of the sun. He compared this value to the mass-to-light ratio of a system of stars within the solar neighborhood of our galaxy for which $\frac{M}{L} \sim 3$. With the large discrepancy, one possible conclusion is that far more mass is present in the cluster, and invisible or dark, than can be accounted for by visible mass alone.

The previous calculation relies on the Hubble constant which describes the expansion of the universe, it is a linear relationship between distance to an astronomical object and its speed away from Earth. Improved measurements of this constant require Zwicky's mass-to-light ratio to be reduced by a factor of 8.3 [3], upon scaling by this factor, the mass-to-light ratio is still indicative of more matter being present than what is visible. A review on mass-to-light ratios for various types of objects [4] indicates that $\frac{M}{L}$ in the solar neighborhood is less than $\frac{M}{L}$ for galaxies which is less

than $\frac{M}{L}$ for clusters of galaxies. One interpretation of this trend is that as the celestial length scale of a system of luminous-and-gravitationally-bound objects increases the fraction of DM within the system increases.

The study of rotation curves of galaxies offer a second piece of evidence. Using Doppler shifts in visible or radio frequencies of spectroscopic fingerprints allows one to map out the rotational velocity of objects, such as stars, about the galactic center. The velocity of an object in orbit is dependent on the distribution of mass interior to its orbit. So, the velocity is dependent on the distribution of matter, or density, within the galaxy. The density and therefore velocity can be decomposed into several components [5] [6], contributions coming from the galactic disk, the galactic bulge, if present, gas which may extend out of the plane of the galaxy, and the DM halo.

For an object in circular orbit about mass which can be reduced to a point mass residing at the galactic center, the velocity can be modeled with Newtonian mechanics. Where m is the object mass and $M(r)$ the mass contained within radius r.

$$\frac{GmM(r)}{r^2} = \frac{mv^2}{r} \quad \rightarrow \quad v^2 = \frac{GM(r)}{r}$$

If the density ρ is decomposed into components i, $M(r)$ is found by the sum of integrals over the volume V which extends to radius r.

$$M(r) = \sum_i \iiint_V dV \rho_i(r')$$

From the equations above, the velocity squared can be written as a sum of components.

$$v^2 = \sum_i \frac{G}{r} \iiint_V dV \rho_i(r') \equiv \sum_i v_i^2$$

In Figure 1.1, the rotation curve is plotted for spriral galaxy NGC 3198 [7]. A fit for the total velocity as a function of distance is found by assuming the total density was two-component. The mass of the galactic disk was accounted for by an exponential disk [8], $\rho_{disk} \propto e^{-r/a_{disk}}$, where the scale length $a_{disk} = 2.68$ kpc was determined from an exponential fit to the radial

luminosity profile of the galaxy. For the DM halo mass $\rho_{halo} \propto (1 + (\frac{r}{a_{halo}})^{\gamma})^{-1}$, where $\gamma = 2.1$ and $a_{halo} = 8.5$ kpc were free parameters found from fitting. The overall fit to the data, which includes both contributions, is found by $v_{fit} = \sqrt{v_{disk}^2 + v_{halo}^2}$. In this formula v_{disk} gives the expected orbital velocity of an object as a function of radius when only considering the mass profile of the luminous disk of the galaxy. Likewise, v_{halo} gives the orbital velocity as a function of radius due to the mass profile of the dark matter halo alone. In the figure, the data indicates that the velocity flattens out for large radii and does not match the expected velocity profile due to the galactic disk alone, indicating the need for more mass interior of the orbits of objects at these radii. Addition of the halo component is able to reproduce the flattening at large radii. Only one example of this phenomenon has been shown here, however, it has been observed for many galaxies. In reference [9] the rotation curves of 21 spiral galaxies are shown for which the profile either flattens out or slightly increases as radial distance increases. In reference [10], the rotation curves of 1100 spiral galaxies were studied to understand the universal nature of this phenomenon.

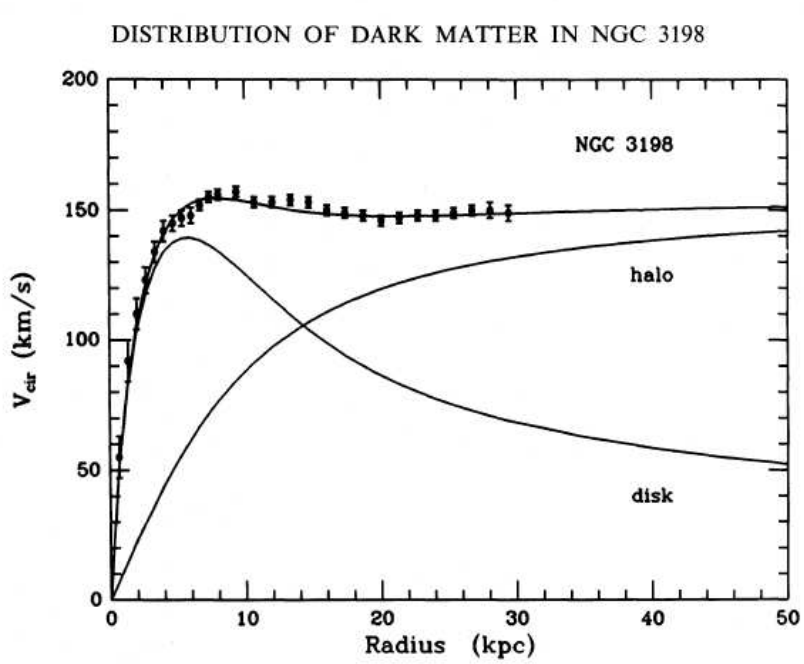

Figure 1.1: Points with error bars represent the measured rotation curve for spiral galaxy NGC 3198. The fit curve to the data is found by $\sqrt{v_{disk}^2 + v_{halo}^2}$. The contribution from disk alone does not match the measured velocity profile. This figured has been reproduced from [7].

Alternative to DM, missing mass, in galaxies and clusters described above, theories of Modified Newtonian Dynamics (MOND) have been proposed [11]. In these theories the gravitational interaction between objects, which is traditionally modeled with Newtonian mechanics, is reformulated to explain the observed phenomenon. This can be done with success for the types of systems described above. However, MOND theories struggle to reconcile some observations of gravitational lensing. For a review on MOND, see [12].

Light from a source passing by a massive object can be bent, or lensed, by that object on the way to an observer. This was predicted by Einstein with the general theory of relativity, and subsequently, has been verified by numerous observations [13]. The lensing, as seen by the observer, is dependent on the relative positioning of source, lens, and observer, as well as the mass of the gravitational lens. If all three are directly in alignment it is possible to observe a ring of lensed light. If they are not in alignment the observer may see a partial ring or distortion. From this information, as well as the relative positioning, the distribution of mass for the lens can be reconstructed.

A third piece of empirical evidence for the existence of DM comes from gravitational lensing studies of the Bullet cluster [14]. It is the merger of two galaxy clusters which collided $\sim$100 million years ago. In this case, the Bullet cluster plays the part of the lens. Using distortions of images of galaxies, which act as sources for this case, the mass distribution of the cluster was reconstructed. This is shown in Figure 1.2.

The interpretation of the figure requires further information on the composition of galaxy clusters. Most of the luminous mass of galaxy clusters is contained within the hot gas between galaxies and can be observed via x-ray emission [15]. In comparison, galaxies, which contain stars that emit visible light, are distributed much more sparsely throughout the cluster.

When the two clusters merged, the probability of the stellar components of the clusters colliding was small due to the sparse distribution. The intracluster gas, which pervades each, interacted, and further heated due to the friction-like forces of the collision. This caused the stellar components of each to move on relatively unaffected while the gas from each was slowed in the collision and decoupled from the stellar mass. In Figure 1.2, the left panel shows the visible or stellar distribution

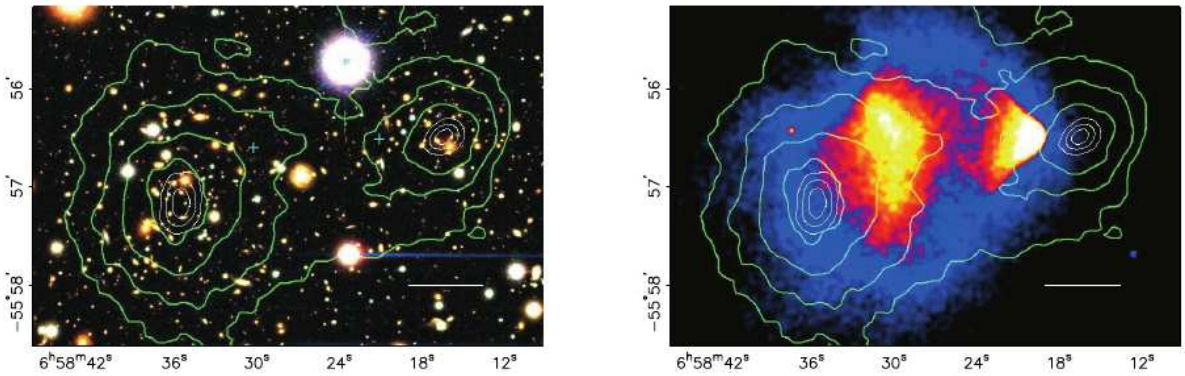

Figure 1.2: Two images of the Bullet cluster merger. Left panel: A visible light image of the stellar component of each cluster. Right panel: An x-ray image which shows that the intracluster gas of each cluster has been separated from the stellar component of each. For each panel the green lines are mass density contours, density increases as one steps inward line-to-line towards the two peaks. This figure has been reproduced from [14].

of mass, two clumps of galaxies can be seen within the green contour lines which are those for the two clusters of the merger. The right panel shows an x-ray image of the merger indicating that the intracluster gas has been separated from the stellar mass. Finally, the green contours on each are mass density reconstructed from gravitational lensing. The concentric contours describe increasing mass density going inward to a peak. The majority of the mass has moved on with the stars even though it is known that intracluster gas should be more massive than the stellar component. The interpretation is that the stellar components of each cluster are surrounded by DM which also were unaffected by the collision and continued to be coupled with the stellar component during the collision. Further investigation in reference [14] indicated that MOND theories were not able to adequately describe this observation. This specific piece of evidence has been considered strong evidence for DM since it empirically necessitates its existence, providing a case inconsistent with the alternative explanation. A second instance of a cluster merger exhibiting behavior similar to the Bullet cluster is reported in [16].

Above, only a few examples have been shown, however, they are sufficient to motivate a deeper investigation into the nature of DM. For a more complete history on the subject see [3]. Other strong pieces of evidence come from cosmology and the use of supercomputers, the latter of these

has demonstrated the need for DM as seed material in the early universe to obtain the structure visible today. These pieces of evidence will be discussed briefly in the following sections.

1.2 Non-Baryonic Cold Dark Matter

From the evidence in Section 1.1, DM interacts gravitationally, and a candidate DM particle must also be electrically neutral to be consistent with the lack of any detectable light. The DM particles must also be stable over large time scales. Stability is evident for the systems described above, which can be modeled as systems in steady states.

ΛCDM cosmology [15] is used to describe the evolution of the universe. The fundamental principle of this model is that on sufficiently large scales the univserse is homogeneous, that is it looks the same at each point, and isotropic, meaning the same in all directions [17]. It starts with the Big Bang and includes pieces of physics that go beyond the Standard Model of particle physics, which are necessary to describe the observed universe. In this theory, Λ indicates the need for dark energy, motivated by the accelerating rate of expansion of the universe and is related to Hubble's constant, mentioned in the previous section. CDM indicates the need for Cold Dark Matter, meaning the dark matter cannot be moving relativistically, which rules out Standard Model neutrinos as DM candidates. To replicate the observed large-scale filament structure in our universe CDM is required. This has been determined by N-body simulations that use ΛCDM cosmology as input. The Millennium-II simulation [18] tracked the evolution of more than 10 billion particles and large-scale filament structure was produced. Hot DM, which is relativistic, does not allow for the gravitational collapse of matter into clumps and into the filament structure of the universe observed today. Big Bang Nucleosynthesis (BBN) and measurements of the Cosmic Microwave Background (CMB), both of which are modeled using this cosmology, have been used to constrain the different components that comprise the universe, two being the densities of DM and dark energy. Each study implies the need for non-baryonic DM, baryons being the familiar three-quark particles, proton and neutrons, which make up most of the visible universe around us.

Based on the principles of isotropy and homogeneity, the geometry of three-dimensional space can take on three different forms [15]. The type of geometry is typically denoted by k. The case of $k = 0$ implies a Euclidean or flat geometry, which is the familiar geometry where the angles of a triangle sum to 180°, the circumference of a circle is the radius multiplied by 2π, and two lines drawn initially parallel to one another never meet upon extension. If $k > 0$, the geometry of the universe is analogous to being on the surface of sphere; isotropy and homogeneity can still be satisfied, but the universe is required to be finite or closed. If $k < 0$, the geometry of the universe is analogous to being on a hyperbolic surface and the universe can be infinite or open.

The total energy density in the universe can be decomposed into constituents and it is denoted by the dimensionless cosmological density parameter Ω. It contains contributions Ω_i, due to Standard Model particles and dark matter. The contribution from dark energy is Ω_Λ.

$$\Omega = \sum_i \Omega_i + \Omega_\Lambda - 1 \propto k$$

The Hubble constant, mentioned previously, as well as energy density in the universe are not actually constant but vary over time. At any point in time, a critical density ρ_c can be evaluated such that the conditions for a flat universe, or $k = 0$, are satisfied. Each Ω_i can be expressed as $\frac{\rho_i}{\rho_c}$, the ratio making the density parameter unitless. As of the 2018 Review of Particle Physics, Section 24.4 [19], $\Omega = 1.0002 \pm 0.0026$, providing evidence for flatness. With the assumption of flatness and letting $k = 0$, each constituent density parameter then gives its percent contribution to the total since they sum to unity. For the terms in the sum indexed by i, the dominate contributions are due to baryonic matter Ω_b and CDM Ω_c. Relativistic particles, photons and neutrinos, do not contribute significantly to the density at present. Using the assumptions above, $\Omega = \Omega_b + \Omega_c + \Omega_\Lambda = 1$. The approximate values are $\Omega_b \approx 0.05$, $\Omega_c \approx 0.25$, and $\Omega_\Lambda \approx 0.70$. These values have been determined by measurements of the CMB. A second measurement of the baryon density comes from BBN. Both measurements will be discussed briefly below. The values lead to the conclusion that the composition of the vast majority of the universe cannot be explained by contemporary physics since only $\sim$5% is encompassed in the Standard Model of particle physics. Of the total matter

density $\Omega_m \equiv \Omega_b + \Omega_c$, $\frac{\Omega_b}{\Omega_m} \approx 0.17$, and $\frac{\Omega_c}{\Omega_m} \approx 0.83$, resulting in 83% of the matter content of the universe being DM and $\sim$17% being ordinary matter.

The evolution in time of the universe can be equivalently cast as the evolution of the temperature of the universe, as described by statistical thermodynamics. The universe started in a hot and dense state, continuing to cool over time as it expands. BBN, also known primordial nucleosynthesis, occurred within the first few minutes of the universe when the temperature dropped below the binding energy for these nuclei. Light elements such as deuterium, helium, and lithium, were formed. Using nuclear physics to calculate reaction rates, light elemental abundances that exist directly after BBN can be calculated; a reivew on BBN is presented in reference [20]. The baryon density, that is the densities of proton and neutrons, during the period of nucleosynthesis sets the abundance of light elements observed today. The abundance of each light element relative to that of hydrogen can be measured by examining distant areas of the universe which appear to contain low levels of elements heavier than those which should be produced in BBN, which indicates the elemental content of these regions has not evolved substantially from this time period [21][1].

Using BBN theory, the relative abundances can be calculated and plotted versus the baryon density of the of the universe, see Figure 1.3. Shown is a comparison between theory and measurement for BBN as presented by the Planck collaboration [22]. The vertical axis gives primordial elemental abundance, that is the amount of a particular element present in the early universe. The horizontal axis is the baryonic density parameter scaled by the reduced Hubble constant squared, $\Omega_b h^2$. The top panel is for helium and the bottom for deuterium. The two vertical axes differ, for helium the abundance relative to the total baryonic (proton and neutron) density and then scaled by a factor of four is shown. For deuterium the relative abundance of deuterium to hydrogen multiplied by 10^5 is shown. Actual measurement is provided by the horizontal band in each panel. Two predictions from BBN theory are shown by the green bands and black dashed lines. For deuterium the green band represents the use of theoretical nuclear reaction rates while the blue band represents the use of experimentally measured reaction rates. The deuterium to hydrogen abundance

[1]The referenced article provides a concise introduction to the topic of dark matter.

in particular (bottom panel) constrains the primordial baryonic density. Finally, the primordial baryonic density from Planck CMB measurements is shown in the vertical red band. The intersection of the three curves for deuterium serves as validation for BBN theory. The region in which BBN theory overlaps the measured primordial abundance for deuterium gives one measurement of the primordial baryonic density, which is also overlapped by the independent measurement of this density from CMB measurements. This agreement provides validation for ΛCDM cosmology. All bands are 68% confidence levels. The agreement between BBN theory, BBN measurement, and CMB measurement in the figure indicate that only a small fraction, ∼5%, of the universe is composed of ordinary-baryonic matter.

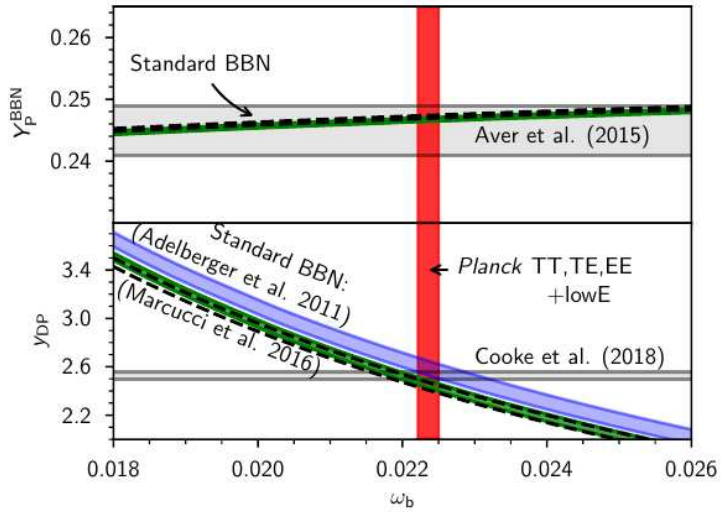

Figure 1.3: Plotted are measured primordial elemental abundances for helium (top panel) and deuterium (bottom panel) along with theoretical abundances according to BBN theory. The measurements correspond to the horizontal band in each panel and theory corresponds to the curved bands. The primordial baryonic density from Planck CMB measurements is shown by the vertical red band. See the body of the text for details. This figure has been reproduced from [22].

Moving further into the temperature history of the universe, up until ∼400,000 years after the Big Bang, the universe was dense and too hot for electrons to stay bound to nuclei in the formation of atoms, which created a condition in which the universe was opaque to photons. At this time, the universe had expanded and cooled to a point where neutral hydrogen began to form and photons

were able to escape. This is referred to as the surface of last scattering. This is the earliest time period observable by astronomy, since no light information was allowed to freely stream through the universe prior to this time. These photons are observable today as an uniform background emission across the sky, known as the CMB. Due to the expansion of the universe, these photons have been redshifted to microwave wavelengths. The frequency spectrum today is well-described by a blackbody radiation curve with a characteristic temperature of 2.72548 ± 0.00057 K [23]. Temperature fluctuations from the average are small, being of $\mathcal{O}\ 10^{-5}$. Temperature fluctuations, mapped out across the two-dimensional space of a sphere, the sky, can be represented by a sum of spherical harmonics. The size of fluctuations is then plotted against the multipole moment ℓ. Small ℓ corresponds to large angular scale. Measurements of these flucuations have been made by experiments such as the Wilkinson Microwave Anisotropy Probe (WMAP) [24] and the Planck satellite [22]; the Planck results, being the most recent and precise, are shown in Figure 1.4. Modeling the structure requires six free parameters, two of which are the baryonic and CDM density parameters. Assuming a flat universe, the dark energy density parameter can also be extracted. The results[2] are $\Omega_b h^2 = 0.02237 \pm 0.00015 \rightarrow \Omega_b \approx 0.049$ and $\Omega_c h^2 = 0.1200 \pm 0.0012 \rightarrow \Omega_c \approx 0.265$. The dark energy density parameter was reported as $\Omega_\Lambda = 0.6847 \pm 0.0073$.

In Summary, DM is required to be non-relativistic (cold) to reproduce the observable structure of the universe and two different methods have been used to constrain the baryonic density of the universe. This evidence suggests that non-baryonic DM is prevalent in the universe.

1.3 Weakly Interacting Massive Particles

A specific DM candidate, the Weakly Interacting Massive Particle (WIMP), is considered in this dissertation. Other DM candidates exist, for information on what properties constitute a good DM candidate see [25], and for reviews on candidates see [26] [19] [27]. In Section 1.2 it was reported that $\sim$83% of the matter content of the universe is thought to be non-baryonic DM. Even

[2]The density parameters were reported in the format $\Omega_i h^2$ where h is the reduced Hubble constant. In the referenced paper the Hubble constant H_0 was measured to be $H_0 = 67.36 \pm 0.54\ \mathrm{km{\cdot}s^{-1}{\cdot}Mpc^{-1}}$. The reduced Hubble constant is defined by $H_0 = 100h\ \mathrm{km{\cdot}s^{-1}{\cdot}Mpc^{-1}}$. Using this relation, the density parameters were estimated here.

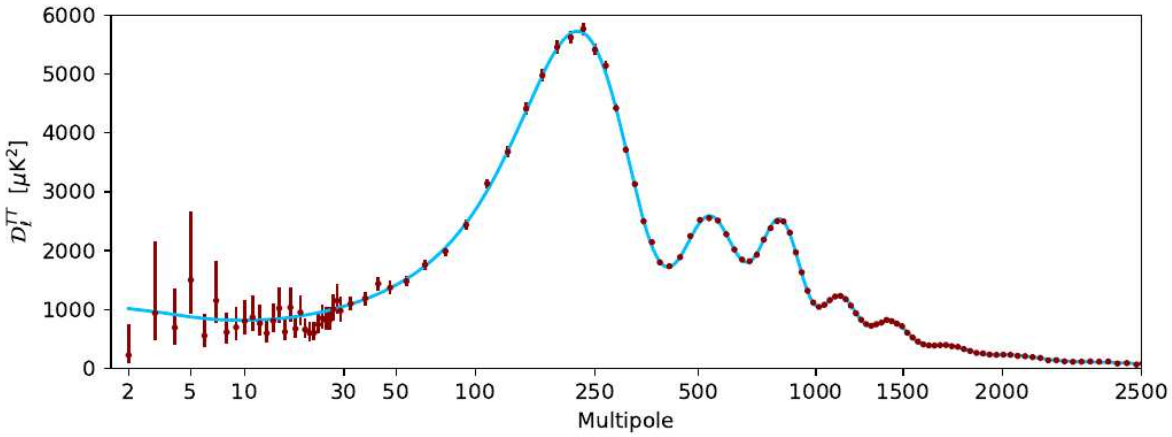

Figure 1.4: The anisotropy power spectrum for the CMB is shown here. The size of temperature fluctuations is plotted versus the size of the angular patch of sky being observed. Small values of ℓ correspond to a larger angular size. Data points with error bars as measured by the Planck satellite are plotted. The fit line involves six free parameters, two of which are the baryonic and CDM density parameters, allowing these to be constrained from this measurement. The ability to reproduce the observed structure from ΛCDM cosmology provides validation for the theory. This figure has been reproduced from [22].

though only a specific candidate is considered here, one should keep in mind that this large portion of the matter content may be composed of multiple components. If WIMP DM exists, it may only provide a partial understanding of the total DM density.

In the early-hot-dense universe, crossing symmetry in particle interactions as well as the abundance of available kinetic energy allowed massive particles to appear and disappear at equal rates, meaning that these particles were in thermal equilibrium. As the universe expanded, the thermal age of the universe advanced to cooler temperatures. Depending on particle mass, eventually the temperature of the universe was not sufficient to drive the production of the massive particles. At this point, the number density for these particles is set by their annihilation rate. The total annihilation rate includes contributions from all processes in which a particle is in the initial but not the final state of the interaction. Once the universe has expanded sufficiently, the chance of these particles encountering each other to annihilate approaches zero and the number density approaches a constant, this process in known as freeze-out. The particle density at freeze-out is known as the relic density.

The time evolution of the number density of a massive particle in the universe can be derived based on statistical thermodynamics and is known as the Boltzmann equation [28] [29], which is typically solved numerically. From this, one can calculate the relic density parameter of a specific particle type observed today which scales inversely with its thermally averaged annihilation cross section $\langle \sigma_{ann} v \rangle$, a large annihilation cross section corresponds to low relic density. In general the speed of massive particles are not fixed but follow a distribution, this implies that two particles involved in a particular annihilation channel have a relative probability distribution of speeds. Thermal averaging refers to integrating the cross section multiplied by velocity over all speeds with each being weighted by the probability distribution. Again, one must consider all channels that result in the disintegration of the particle in question [30] [31].

The inverse relationship between relic density and cross section $\langle \sigma_{ann} v \rangle$ is intuitive and comes from the typical formulation of interaction rate $\Gamma_f = \eta_f \langle \sigma_{ann} v \rangle$. The subscript f indicates the values for the temperature at which freeze-out occurs. Once the universe has expanded to a size such that the annihilation rate Γ_f becomes small, this causes the number density[3] η_f to freeze-out. It stays approximately constant moving forward in time. As shown in Section 1.2, the density parameter for a constituent of the total is typically expressed as $\Omega_i = \frac{\rho_i}{\rho_c}$, which is the ratio of the mass density per unit volume for constituent i relative to the critical density required to produce a flat universe. For a particle of mass m_i, the density parameter is then equivalent to $\Omega_i = \frac{m_i \eta_i}{\rho_c}$. It is seen that $\Omega_i \propto \eta_i$ and $\eta_i \propto \frac{1}{\langle \sigma_{ann} v \rangle_i}$.

The approximate relationship is

$$\Omega_c h^2 \approx \frac{3 \times 10^{-27} \text{ cm}^3 \cdot \text{s}^{-1}}{\langle \sigma_{ann} v \rangle_c}$$

[32] where the subscript, c, indicates that the particles of interest are those that compose CDM. In Section 1.2, we saw that a value of $\Omega_c h^2 = 0.1200$ has been measured, this results in $\langle \sigma_{ann} v \rangle \approx 3 \times 10^{-26}$ cm$^3 \cdot$s^{-1}. Using independent calculations from particle physics, if one considers particles

[3]This density is known as the comoving number density. Comoving coordinates are a set of coordinates that are allowed to expand with the universe. In this set of coordinates the number density is constant.

of weak-scale mass and a weak-scale coupling strength a similar value is found for the thermally averaged annihilation cross-section [33]. The fact that a known force, the weak force, can provide interactions with the amplitudes sufficient to produce the observed DM relic density is known as the WIMP miracle and provides the etymology for the word "Weak" appearing in Weakly Interacting Massive Particle. This remarkable coincidence has provided a motivation to search for these particles.

WIMP relic density expressed as a function of the temperature history of the universe, when considering the relevant thermally averaged annihilation cross sections, can be evaluated numerically. WIMP density is plotted as a function of the temperature history of the universe in Figure 1.5.

The vertical axis is proportional to the density Ω_c and the horizontal axis is the ratio x of WIMP mass to the temperature of the universe as it expands and cools. For a given WIMP mass as temperature decreases x increases, which corresponds to time increasing from left to right on the horizontal axis. The solid line represents the number density if a WIMP of specific mass is allowed to stay in thermal equilibrium, that is, sufficient kinetic energy is available to drive the production rate of the massive particles, which is in equilibrium with the annihilation rate. For a given WIMP mass, as the thermally averaged annihilation cross section increases, the WIMPs are able to stay in thermal equilibrium farther into the temperature history of the universe, resulting in a smaller relic density. The larger the annihilation rate, the further the universe must expand to sufficiently separate the particles to achieve freeze-out. The dashed lines represent the relic densities resulting from freeze-out for annihilation cross sections of differing size. One can see that these curves diverge from the equilibrium density and flatten out as the universe cools and expands at a rate consistent with the annihilation rate.

Calculation of the relic density is model dependent, and the range of possible WIMP masses[4] is typically quoted as $\sim$10 GeV to 1 TeV, for instance [26]. While the WIMP miracle provides

[4]Following a common particle physics convention, WIMP masses will typically be quoted in GeV opposed to GeV/c^2.

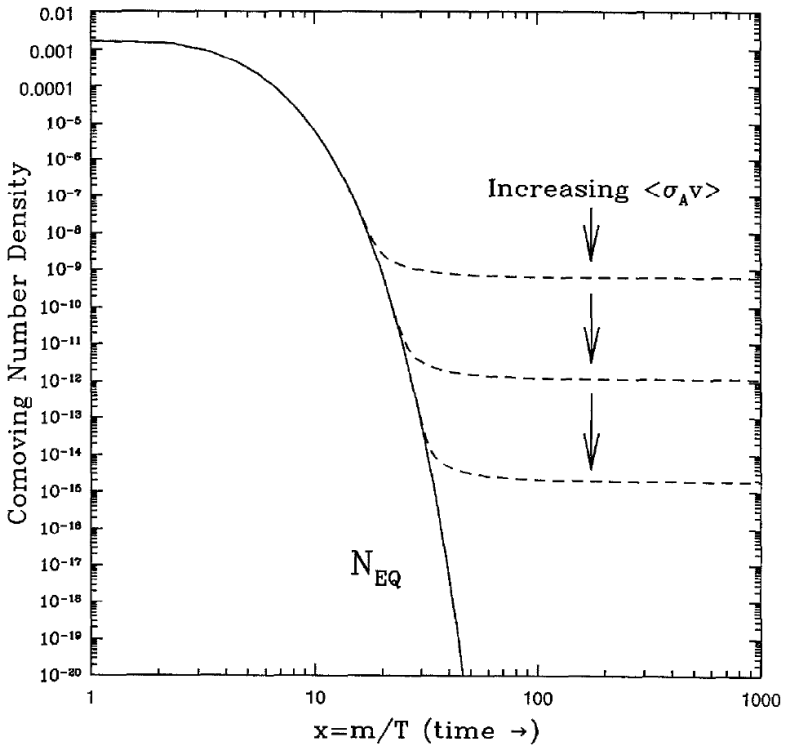

Figure 1.5: This plot describes the process of freeze-out which results in a relic density of dark matter. This comoving number density becomes constant (dashed lines) once the annihilation rate becomes small due to the expansion of the universe. This plot is described in detail in the text. This figure has been reproduced from [32] and the curves represent numerical solutions to the Boltzmann equation.

interaction amplitudes sufficient to account for the observed relic DM density, the weak-scale connection is not necessary to account for the observed relic density, other propositions have been made [34].

Modeling these interactions requires extension to the Standard Model of particle physics. One popular proposed extension are theories that contain supersymmetry, in which every Standard Model fermion(boson) has a superpartner which is a boson(fermion). Due to the requirements for DM, the candidate particle must be neutral and due to the requirement for stability over large time scales, the lightest supersymmetric particle for a theory provides a possible DM candidate [32]. Evidence for supersymmetry has not been observed in experiments such as the LHC which constrains supersymmetric DM theories [35].

1.4 The Standard Halo Model

With a candidate particle at hand, namely the WIMP, one can describe a model for the local distribution of these particles. That is, a model for a distribution for the halo of DM in our Milky Way galaxy and more particularly the properties of DM in the region of our solar system. Collectively, these properties constitute the Standard Halo Model. A model is required to be able to predict detection rates, for reviews see [36] [37], in addition, the model is also required to set constraints on WIMP interactions with ordinary matter in the absence of detection. In order to compare the results from different experiments, it is necessary to have a consistent model.

It is assumed that the halo can be described by an isotropic and isothermal sphere, where isothermal implies thermal equilibrium has been reached. In Section 1.1 it was shown that the velocity curves of spiral galaxies tend to flatten out at large radii r. Assuming the circular orbit speed of an object can be determined by $v = (GM)^{1/2}r^{-1/2}$ implies that $M \propto r$ at large radii in order for the speed to be constant. Assumption of a spherical distribution of mass for which density scales as r^{-2} is sufficient to describe the flattening of speeds at large radii.

Let us suppose there is a physical system, in this case a WIMP, that is in thermal equilibrium with a thermal reservoir. The canonical probability of finding a system, again the WIMP, in a particular state is proportional to the Boltzmann factor $e^{\frac{-E}{k_b T}}$ [38]. The energy associated with a particular state is represented by E, which in this case is the kinetic energy of the WIMP, and T is the characteristic temperature of the system. The state of each WIMP is described by its velocity vector $\vec{v} = v_x\hat{i} + v_y\hat{j} + v_z\hat{k}$. This is the velocity of the WIMP in a frame of reference stationary with the galaxy. This implies that the probability of having a WIMP of particular velocity is

$$P_{\vec{v}} \propto e^{\frac{-m|\vec{v}|^2}{2k_B T}} = e^{\frac{-|\vec{v}|^2}{v_0^2}}$$

with $k_B T \equiv \frac{1}{2}mv_0^2$.

It is convenient to consider that all WIMP velocity vectors compose a three-dimensional velocity space in spherical coordinates such that all WIMP velocity vectors of the same magnitude

constitute a spherical shell of radius $|\vec{v}|$. The volume element is this space is $dV = v^2 sin\theta d\theta d\phi dv$ with θ the polar angle and ϕ the azimuthal angle. In this space, the probability of randomly sampling a WIMP that has a velocity vector belonging to infinitesimal volume dV is given by:

$$P_{\vec{v}} = f_{\vec{v}} dV = Ze^{\frac{-|\vec{v}|^2}{v_0^2}} dV$$

for which Z is a normalization constant found by integrating over all available velocity space and forcing the sum of all probabilities to be unity. The distribution is typically truncated to account for the fact that WIMPs with speeds that are too large will not be able to stay gravitationally bound to a galaxy, this escape speed will be denoted v_{esc}.

$$1 = Z \int_0^{2\pi} d\phi \int_0^{\pi} d\theta sin\theta \int_0^{v_{esc}} dv v^2 e^{\frac{-|\vec{v}|^2}{v_0^2}} = 4\pi Z \int_0^{v_{esc}} dv v^2 e^{\frac{-|\vec{v}|^2}{v_0^2}}$$

For now, let the escape speed be ignored and let speeds go to infinity. Evaluating the integral results in $Z = (\pi v_0^2)^{-3/2}$, yielding an expression for the probability density.

$$f_{\vec{v}} = \frac{1}{(\pi v_0^2)^{3/2}} e^{\frac{-|\vec{v}|^2}{v_0^2}} = \frac{1}{(\pi v_0^2)^{3/2}} e^{\frac{-(v_x^2+v_y^2+v_z^2)}{v_0^2}} = (\frac{1}{(\pi v_0^2)^{1/2}} e^{\frac{-v_x^2}{v_0^2}})(\frac{1}{(\pi v_0^2)^{1/2}} e^{\frac{-v_y^2}{v_0^2}})(\frac{1}{(\pi v_0^2)^{1/2}} e^{\frac{-v_z^2}{v_0^2}})$$

The last expression provides a pragmatic way to implement sampling WIMP velocities into a simulation. The probability density is the multiplication of three normal distributions for which the width is characterized by $2\sigma^2 = v_0^2$. In practice, a WIMP velocity can be sampled by randomly drawing each of the three velocity components from a normal distribution where the width is characterized by v_0. If the magnitude of the velocity is larger than v_{esc} one can simply cull that specific draw and resample until the desired number of WIMPs have been simulated. This process is equivalent to sampling from the truncated distribution for which the normalization constant is found by integrating the probability density only to a finite v_{esc}.

Along with the Maxwell-Boltzmann WIMP velocity distribution described above, the values used for simulations that contributed to this dissertation are $v_0 = 230$ km/s, $v_{esc} = 600$ km/s, and $\rho_0 = 0.3$ GeV·c^{-2}·cm^{-3} as suggested by Lewin and Smith [36]. The latter value is the local, that is in the region of our solar system, DM density. The parameter v_0 is also the circular orbital speed of the sun about the galactic center. The relationship between the velocity dispersion σ and v_0 is motivated by the study of other spiral galaxies from which the properties of our own can be inferred, see [39]. Reference [37] provides a recent discussion on these parameters. In reference [40] 18 astrophysical masers were studied and the determination of the v_0 was found to depend on how the galactic rotation curve was modeled, resulting in values that span 200 ± 20 km/s to 279 ± 33 km/s. A study of ∼23,000 red giant stars in the galaxy has resulted in a recent, 2019, determination of 229.0 ± 0.2 km/s with systematic uncertainties of ∼5% [41]; additional recent discussions can be found in [42] [43].

The local escape speed can be determined, for instance, by the study of high-velocity stars within the galaxy. A work from 1990 [44] suggests an escape speed of 450 to 650 km/s at 90% confidence while also providing a more conservative constraint, stating that it must be greater than 430 km/s. Two more recent works, report 533^{+54}_{-41} km/s at 90% confidence [45] and 528^{+24}_{-25} km/s [46]. All three values are consistent with each other, but may indicate a choice of 600 km/s may be slightly elevated.

Determination of the local dark matter density ρ_0 is subject to model-dependence, in this case the model of the halo itself. In [37], it is reported that values in the range of (0.2 to 0.6) GeV·c^{-2}·cm^{-3} can be found in the literature. A review on the determination of this density along with a chronology of measurements is given in reference [47]. The same study [41] that used ∼23,000 red giant stars to determine v_0, also resulted in a determination of a local dark matter density of 0.30 ± 0.03 GeV·c^{-2}·cm^{-3}.

It is pertinent to mention the Gaia spacecraft, which is currently in operation with the goal of providing a three-dimensional mapping of our galaxy. The Gaia collaboration recently released data [48] for which some motion information is available for 1.3 billion sources of which 7.2

million sources have radial velocity measurements. This wealth of data may lead to better understanding of the model parameters used above.

Again, it should be emphasized that the Standard Halo Model is an approximation based on some reasonable assumptions and measured parameters, but the details of the actual halo profile are not contained in it. Above, it has been stated that a halo density that goes as r^{-2} is able to describe the flattening of galactic rotation curves. Using N-body simulations to study halo structure, it has been found that the halo density profile does follow the above density profile over a range of radii but is shallower than r^{-2} near the central region and steeper towards the edge, resulting in a profile known as the Navarro-Frenk-White profile [49]. Some further information regarding the description of mass density for DM halos can be found in reference [50].

1.5 Experimental Search Methods and Theoretical Dark Matter Signatures

Macroscopic, namely gravitational, evidence for the existence of DM was provided in Section 1.1. A few different methods exist to search for DM and probe its particle-like nature. Indirect searches aim to detect the decay or annihilation of DM particles into Standard Model particles [51]. This can be done, for instance, by looking for excess[5] gamma-ray emission from a variety of different objects such as dwarf spheroidal galaxies, the sun, and the galactic center. One experiment that pursues these types of gamma-ray signatures is the High Altitude Water Cherenkov (HAWC) observatory [52], which is sensitive to gamma-rays above energies of $\sim$100 GeV. For this experiment, limits have been set on some annihilation channels using data collected from dwarf spheroidal galaxies [53].

Complementary to indirect searches, one can collide Standard Model particles into each other at high energy and look for the production of DM. For an observed event, one would look for an

[5]By excess it is meant that more gamma-rays are being emitted from these sources than can be accounted for by current theoretical models that include Standard Model physics only. An excess could indicate an unaccounted for source of gamma-rays, such as due to DM annihilation resulting in the production of detectable Standard Model particles.

imbalance in momentum or missing energy, which may indicate that a DM particle was produced in the event, was not seen by the detector due to its small interaction cross section, and carried momentum and energy away as it exited the detector. This type of signature is sought in accelerator experiments such as the Large Hadron Collider (LHC) [54] [55]. Production of DM at an accelerator has not yet been observed. If DM were observed by this method, this type of DM could be different from or only provide a partial understanding for DM that is galactic in origin.

A third method, and the focus of this dissertation, is direct detection. In this scenario, a DM particle interacts with a Standard Model particle and the result of the interaction on the Standard Model particle is observed in a detector. Depending on the detector technology being used, examples of an observable signal can be one, or a combination of, ionization, light, or vibration. For reviews on DM and direct detection see [19] [56]. By nature of what is known about DM, observation of its existence by gravitational effects only, DM is thought not to couple with ordinary matter electromagnetically. With DM of larger masses not yet being observed, despite many experimental efforts, there has been a push in recent years to search for sub-GeV DM [57], for instance via electron scattering [58]. The interaction of interest for this work, is an elastic collision between a WIMP and an atomic nucleus. Theoretically, there is more than one way this type of interaction may manifest within the detector. Spin-independent and spin-dependent interactions are posited to exist, with the cross section being modified due to the target nucleus having net spin, for the latter case. Both types of interactions have been searched for by numerous experiments. A given experiment may be able to place constraints on both of these types of interactions dependent on target material. Inelastic interactions with individual nucleons are unfavored based on energy/momentum considerations for typical[6] WIMP DM [59], the size of the wavelength for these particles make it more probable for interaction with the target nucleus in whole. Inelastic interactions are a possibility, even if unfavored, and have been searched for with other experiments, for instance XENON100 [60].

[6]Here one assumes WIMP DM that has energies resulting from speeds based on the Standard Halo Model and expected masses motivated by the WIMP miracle.

For the Directional Recoil Identification From Tracks (DRIFT) experiment, a low-pressure gas is contained within a volume. If a WIMP enters the volume it may scatter off one of the atomic nuclei of the gas resulting in a nuclear recoil. The recoil will result in a track of ionization in the detector, and owing to the low gas pressure, have an observable extent of order a few millimeters. If a population of such recoils is observed, one may also be able to infer the direction from which the WIMP particles are originating.

DRIFT belongs to a class of experiments that is not only a direct search but also a directional search, and reference [37] provides a review of directional detection. One is able to both count the number of tracks observed as well as extract some information in regards to the orientation of the tracks. The strength of the DRIFT detectors is directional capability. Since a low-pressure gas is used to achieve this, the overall target mass is relatively small. This implies that non-directional large-mass, and for example liquid-noble, experiments are able to achieve larger exposures and set the most competitive constraints on DM interactions with ordinary matter. It is important to keep pursuing directional technologies. In the event that excesses are observed by large-target-mass experiments, one will then want a way to pursue testing excess events of this type against against a smoking-gun signature, to be discussed below, that would strengthen the argument that these events are indeed consistent with expectations for DM. The CYGNUS collaboration [61] is championing the use of directional detectors in the search for DM. The vision of this collaboration is a "multi-site galactic recoil observatory with directional sensitivity to WIMPs and neutrinos".

The intent of the above is not meant to be comprehensive, the three different search methods with some examples have been given in brief. Other interesting techniques exist, such as one in which a direct detection experiment runs parasitic to an accelerator experiment, such as BDX [62] [63]. The idea of placing a DRIFT detector behind an accelarator beam dump, namely DRIFT-BDX [64], has also been pursued.

A variety of measurable quantities exist for direct searches and a given experiment may be sensitive to one or more of them. In general, the more information one is able to glean from each DM candidate event, the fewer events are required to claim a significant detection [65] [66] [67].

Counting alone, energy deposition, track length in one, two, or three dimensions, and vector directionality that is also known as head-tail asymmetry [68], are all potentially measurable, depending on detector type. Measurement of energy via ionization, light, or vibration is advantageous to pure counting since models exist to understand what an expected WIMP energy distribution may look like for a given detector. Liquid-noble [69], such as xenon, detectors [70] are of this type, some of which measure energy in more than one form allowing for background discrimination. In searching for DM candidate events, one can reject events that appear in regions of this two-dimensional energy space known to be populated by backgrounds. Experiments of this type, owing to the large target mass, are able to set the leading limits on the cross section for interactions of DM with ordinary matter. In the case that an excess above expected backgrounds is observed, these experiments do not have directional capabilities to further test aspects of DM halo models. As the limit on cross section for interaction with ordinary matter is pushed to smaller values, a region of cross section versus WIMP mass space will eventually be reached in which one can expect to start observing coherent neutrino scatters on target material, this region of parameter space is termed the neutrino floor, see Figure 1.6. Neutrinos originate from the Sun, diffuse supernova background, and due to cosmic ray interactions in the atmosphere. From the perspective of a directionally sensitive detector on Earth, solar neutrinos should point back toward the Sun. Neutrinos from the other two backgrounds would appear nearly isotropic but could still be discerned from WIMPs on a statistical basis since the WIMP wind is expected to be directed, blowing from the direction of the Cygnus constellation. It is in this way that directional detectors have an advantage over those that measure energy only. It is possible that energy-only detectors may also be able to differentiate a WIMP signal from neutrinos on a high-statistics basis, since the expected energy distributions of WIMPs in comparison to neutrinos have theoretical differences [37].

In [66] it was determined that for a directional detector with three-dimensional vector readout, assuming zero background, $\mathcal{O}10$ events would need to be detected to reject the null hypothesis of an isotropic signal at a confidence level of 90%. Background-free operation is not unrealistic, for example, DRIFT-IId [77], achieved a 46.3 day exposure of 33.2 g of fluorine for a spin-dependent

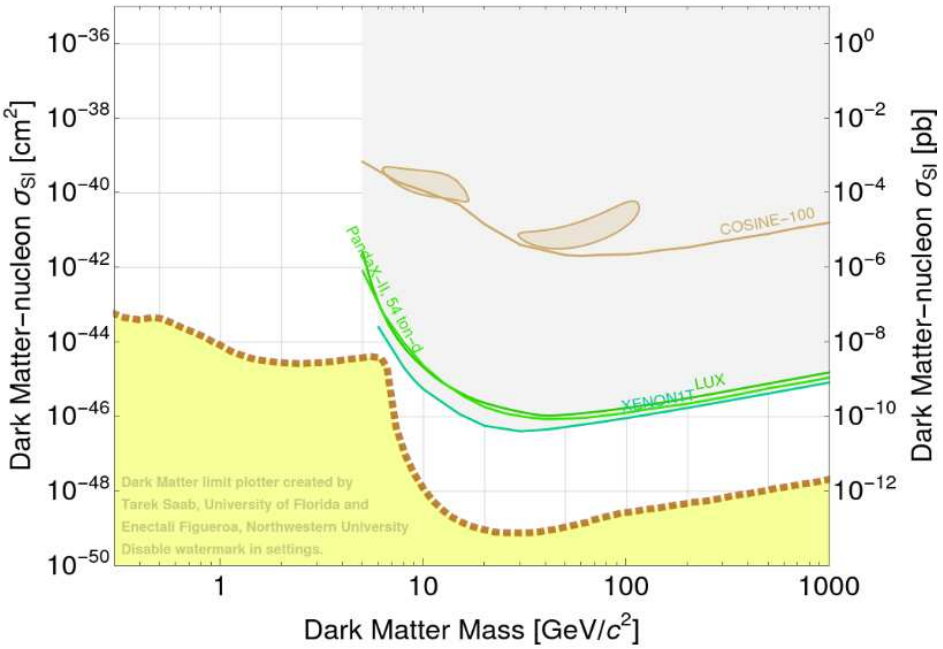

Figure 1.6: The plot shows limits on the WIMP-nucleon cross section vs WIMP mass for a few experiments. Each solid-open curve represents an experiment, the parameter space above that curve has been ruled out for that experiment at 90% confidence. DAMA/LIBRA has claimed a detection of the DM annual modulation signature. The two bubbles are regions of parameter space constrained to 3σ using the DAMA/LIBRA results. There are two bubbles since there are two elements sodium (right bubble) and iodine (left bubble) which compose their target material. The open-dashed line near the bottom corresponds to the neutrino floor for a xenon target. Reporting the WIMP-nucleon cross section may seem at odds with the discussion above where it has been stated that the interaction of interest is that of a WIMP interacting with the nucleus as a whole. However, theoretically, the WIMP interaction cross section with a given target material can be expressed in terms of the WIMP-nucleon cross section. Here it is the assumption that the coupling strengths for a WIMP to a proton or neutron are the same. Cross sections are typically reported in this way such that experiments of differing target material can be compared. Only the results of a few experiments are shown here. XENON1T, LUX, and PandaX-II all have xenon target material and have set leading limits. COSINE-100 results are also shown since it utilizes the same target material as DAMA/LIBRA. (Citations: XENON1T [71], LUX [72], PandaX-II [73], COSINE-100 [74], DAMA/LIBRA allowed regions [75], neutrino floor [76]) (Plot generated 6 July 2020 using the Dark Matter Limit Plotter v5.14, see watermark.)

DM search with no backgrounds observed. The data set was further extended to 54.7 days, with an improved low-threshold analysis, with no backgrounds observed [78]. If the directional capability is reduced to a two-dimensional vector readout the number of events needed increases by a factor of $\sim$2. For a two-dimensional axial readout, that is the vector sense cannot be distinguished, $\mathcal{O}100$ to 1000 events may be needed. The cases of two-dimensional vector or axial readout are most comparable to DRIFT-IIe, in principle DRIFT-IIe should be capable of at least axial readout in two

dimensions plus vector sense along one dimension. As will be elucidated in sections to follow, DRIFT-IIe is able to make measurements of lengths of recoils along the drift axis of the detector as well as perpendicular to the wires of the detector. It is also expected that one should be able to determine the vector sense of a recoil along the drift direction. Due to the combined effects of expected track lengths and the wire pitch, one does not expect to be able to get the vector sense of a recoil along the direction perpendicular to the wires on an event-by-event basis.

Above, an overview has been given as to the measurable quantities one can record in search of DM. A standard search method is to thoroughly study and model all backgrounds for a detector, push to reduce these backgrounds, and then run a DM search over a period time. A typical null hypothesis being that the number of observed counts is consistent with the number expected from backgrounds. An excess would indicate evidence against this hypothesis with a possible explanation being that these extra events result from DM. Based on the number of excess counts, target material of the detector, the exposure (run time multiplied by target mass), input from a WIMP halo model, and a using a particular interaction model, one could then constrain a region of cross-section WIMP-mass parameter space. Some current limits on the cross section for spin-independent interactions of DM with ordinary matter are shown in Figure 1.6. In addition to this method, two other theoretical WIMP wind signatures may be observed with direct detectors and are outlined below. For all detectors, it is the assumption that the detector is sufficiently shielded from backgrounds due to cosmic rays, such as deep underground.

Annual Modulation: For counting experiments[7], an annual modulation [39] [79] is expected in count rate due to the orbit of the Earth about the Sun. In the galactic frame of reference shown in Figure 1.7(a), as the Sun orbits the galactic center, it passes through the DM halo with a speed of $\sim 220\ \mathrm{km/s}$. In the frame of reference of the Sun, this would appear as a wind of WIMPs that are impinging upon the Sun (solar system) with this speed on average. Projected onto the celestial sphere[8] this wind would appear to be blowing on average from the constellation Cygnus. As a

[7] An experiment which measures any of the observables as discussed previously is also a counting experiment.

[8] The celestial sphere is a stationary spherical shell, arbitrarily far from and concentric to Earth, onto which all distant sky objects can be projected and assigned fixed coordinates. The coordinates on the celestial sphere can be

reminder, see Section 1.4, the particles of the DM halo are assumed to have a Maxwell-Boltzmann (randomized) velocity distribution in the galactic reference frame, and the solar system is moving through this distribution. In a solar reference frame, this velocity distribution is boosted opposite the direction of travel of the Sun.

Relative to the galactic plane, the plane of orbit of the Earth about the Sun is inclined at an angle of $\sim 60^{\circ}$. In June, the orbital velocity of the Earth about the Sun is most antiparallel to the WIMP wind which should result in observing a maximum count rate. In December, when the orbital velocity of the Earth about the Sun is most parallel to the WIMP wind, one would expect to see a minimum in count rate. The average relative Earth-WIMP speed in June was calculated to be $257.4\ \mathrm{km/s}$ and $229.5\ \mathrm{km/s}$ in December, resulting in a seasonal modulation amplitude in rate of $\sim$5% [36]. The size of the observed modulation is dependent on the recoil energy threshold of the detector. This modulation amplitude assumes sensitivity to the full WIMP-speed distribution. A similar expected modulation amplitude is reported in [80]. Interpolating, a sinusoidal modulation signature is expected in count rate over the course of a year.

The DAMA/LIBRA collaboration has observed an annual modulation which they claim to be consistent with a DM signal [82]. The DAMA/LIBRA detector is composed of scintillating thallium-doped sodium iodide crystals and is located in the Gran Sasso National Laboratory, in Italy. This signal is in tension with a myriad of other searches. Some leading limits on spin-independent interactions of WIMPs with normal matter are shown in Figure 1.6, some of which exclude the parameter space allowed by the DAMA/LIBRA experiments by orders of magnitude. The overall leading limit, XENON1T [71] is also located at the Gran Sasso National Laboratory but is dissimilar to DAMA/LIBRA in target material and detection technique. Due to this disparity, the DAMA/LIBRA observation has not been widely accepted in the field. One possible explanation is that a seasonal modulation in background rate is being observed. There are at least three experiments which are seeking a definitive conclusion to this discrepancy, namely COSINE-

---

defined such that the equator of the celestial sphere and that of Earth are coplanar. These coordinates are termed right ascension/declination and are analogous to longitude/latitude on Earth.

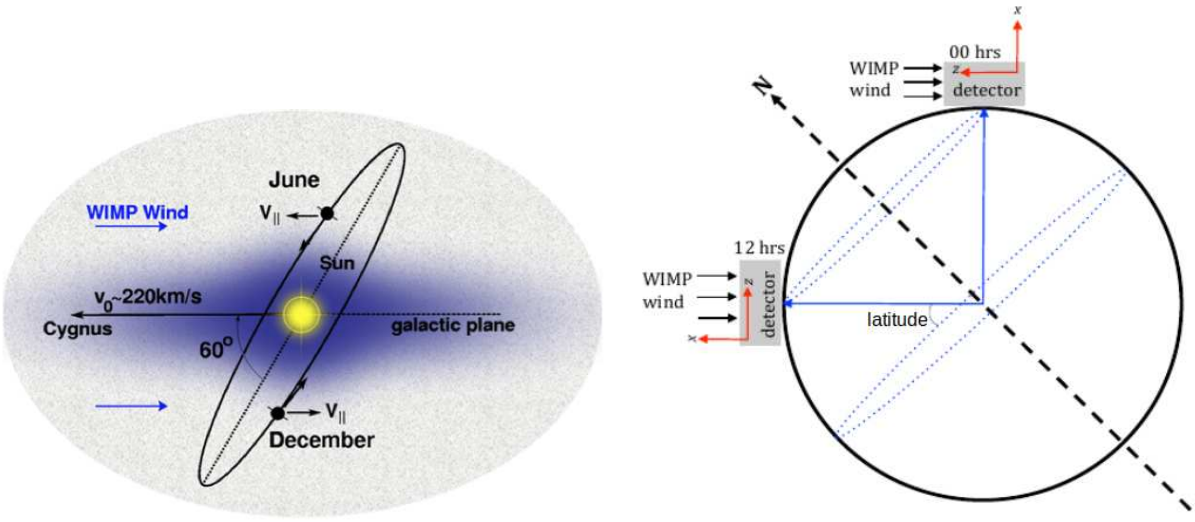

(a) Annual Modulation **(b)** Sidereal Modulation

Figure 1.7: (a) The solar system is in its orbit about the galactic center, which appears directly behind the sun, through the DM halo. In the frame of reference of the solar system, it appears that a wind of WIMPs is incident upon it. Since the Earth also orbits the Sun, in the Earth frame of reference, an annual modulation in WIMP event rate is expected. This figure has been copied from http://www.hep.shef.ac.uk/research/dm/drift.php. (b) The Earth rotates about its own axis, for a detector placed at the optimal latitude, $\sim 45^{\circ}$, a modulation in the WIMP wind direction with respect to the axes of the detector is expected over the course of a sidereal day. This figure originally appears in [81] and has been modified for use here.

100 [74], ANAIS-112 [83], and SABRE [84] [85]. All three employ the same detector material as DAMA/LIBRA. COSINE-100 and ANAIS-112 are both sited in the northern hemisphere. SABRE is in development and intends to have a detector located at Gran Sasso National Laboratory as well as a complementary detector in the southern hemisphere. Seasonal modulations in background rate, such as due to cosmic rays muons, will be opposite of one another at these two sites allowing modulations of this type to be identified. Both COSINE-100 [86] and ANAIS-112 [83] have collected initial data and are consistent with the hypotheses of no modulation or background only. These initial results are in tension with DAMA/LIBRA, but each experiment needs to gain more exposure to challenge DAMA/LIBRA with larger significance.

Sidereal Modulation: For experiments with directional sensitivity, a second signature due to the daily rotation of the Earth is possible [80] and is depicted in Figure 1.7(b). Suppose a detector is placed at a certain latitude and longitude on Earth. Now, imagine that at some given instant in

time, an object in the sky, as projected onto the celestial sphere, is directly to the zenith of the detector. A sidereal day is the amount of time that passes until that object is again at the zenith of the detector. This amount of time is about four minutes shorter than our familiar 24 hour solar day[9]. Let us now suppose that this object is the constellation Cygnus, from which the WIMP wind appears to be emanating. For this to be the case, requires the detector to be located at a latitude of $\sim 45^{\circ}$. When the WIMP wind is aligned antiparallel to the zenith of the detector, WIMP speeds are oriented generally downward, along the x axis of the detector in the figure. Half a sidereal day later, if the detector has been aligned properly in the lab, WIMPs are blowing generally south through the detector, along the z axis of the detector in the figure. This modulation in WIMP wind direction over the course of a sidereal day should lead to a modulation in recoil direction over the course of a sidereal day. For this simple discussion, effects due to precession of the Earth have been ignored. The period for precession is about $\sim$26,000 years and effects are negligible over small time periods, such as the life time of a detector.

Searching for a sidereal modulation is advantageous compared to searching for annual modulation in that one is immune to a possible false-positive observation due to backgrounds that modulate seasonally. Further, any observed background modulation that has a period of a solar day will be out of phase with a sidereally modulated signal. In galactic coordinates, the direction of the WIMP wind is fixed, coming from Cygnus. Backgrounds which are isotropic will not mimic this signal in the lab. In addition, it would take a sophisticated conspiracy of point sources in the lab to mimic a signal that in one part of the day should be directed along one axis of the detector and then 12 sidereal hours later directed along an axis perpendicular to the first. Observing a sidereal modulation of this type could provide a smoking-gun signature.

[9] A solar day is one sidereal day plus the amount of time it takes for the Earth to rotate an additional $\sim 1^{\circ}$ about its axis. This extra degree is needed to account for the amount of angular displacement incurred in a sidereal day as Earth orbits the Sun.

1.6 Sidereal Modulation

The sidereal modulation signature, discussed in Section 1.5 will be investigated in more detail in this section, specifically for a DRIFT-like detector sited at the Boulby Underground Science Facility [87]. Boulby has been the home to previous iterations of the DRIFT experiment, and would be that for DRIFT-IIe as well. Optimally, for the sidereal modulation signature discussed in the above section, the detector should be located at $\sim 45^{\circ}$ latitude. The Boulby lab is at a depth of 1.1 km, to shield from cosmics, and is at a (latitude,longitude) of (54.550450°, -0.821137°)[10].

The DRIFT-IIe detector is described in Section 2.1. For the current discussion, one can suffice with knowing that this detector is essentially a rectangular volume, filled with a particular gas mixture, and is designed to be sensitive to the range of nuclear recoil ionization tracks in two dimensions. These two dimensions are x and z, see Figure 1.7(b). The detector needs to be oriented in the lab such that the normal of the top and bottom of the detector is on axis with the zenith direction, which is defined to be the x axis of the detector. The normals of two of the sides need to be on axis with north/south, which is defined to be the z axis of the detector. The x and z axes are those for which range information of a nuclear recoil can be extracted. The normal of the remaining two sides are on axis with east/west. At a specific time in a sidereal day, the WIMP wind will be blowing downward through the detector. Twelve sidereal hours later, the wind will be blowing south through the detector. The two previous statements are only approximate for a detector at Boulby since the detector latitude differs from the optimal latitude of $\sim 45^{\circ}$.

A simulation[11] of the WIMP wind was developed and utilized, Appendix B, along with simulation of the resulting nuclear recoils for a DRIFT-IIe detector sited at Boulby. The gas within the detector, for the real data analyzed later in this work, is composed of C, S, and O. Only S recoils are considered in the simulation at present due to the combination of facts that O comprises only

[10]These coordinates have been obtained from Google Maps on 23 June 2020. The coordinates are listed in Decimal Degree notation, meaning that latitude is bounded within the range [-90,90] degrees from the equator and longitude is bounded within the [-180,180] degrees from the Prime Meridian.

[11]The WIMP wind simulation was originally started by Matt Williams, a previous graduate student at Colorado State University. I took over this simulation and built upon it to investigate the resulting nuclear recoils for the detector.

1.6% of the target by mass, and the observation of C recoils has been determined to be suppressed by a factor of $\sim$100 relative to S recoils with a previous DRIFT detector [88]. If WIMP DM exists, it is not known if all such particles will be of the same mass. For this particular run of the simulation, for simplicity, a single DM mass of 1000 GeV was chosen. Motivation for the choice of the mass will become evident in Section 3.2.3; the detector at hand is theoretically most sensitive to the recoil energy spectra produced by WIMPs at or above this mass.

Also specific to this run of the simulation, 10^5 WIMP-sulfur recoils were simulated, the time at which each interaction occurred was assigned a Greenwich Mean Time (GMT)[12], each sampled pseudorandomly from a uniform distribution of times over a one-year period. Each was converted to Local Sidereal Time (LST). To understand LST, one can imagine they have a clock for which one rotation of Earth about its axis corresponds to 24 sidereal hours on the clock. One then sets this clock to zero when the meridian (analogous to longitude and is a line running from the north to south poles of a sphere) at which they are standing on Earth is lined up with the meridian defined as zero right ascension on the celestial sphere. Two components of the recoil velocity, axial with north and axial with up (zenith), were extracted. Recoils were grouped by LST interaction time into 144 bins that were 10 sidereal minutes in length. For each bin the average of each recoil velocity component was calculated and this is plotted in Figure 1.8. The vertical error bars on each data point are the corresponding standard deviation about the average divided by the square root of the number of events that happened to fall in that 10-minute bin.

To be clear, the velocities plotted in Figure 1.8, are the averages for each of the two components. The error bars represent an assumed-Gaussian uncertainty on the mean values. A more informative description of the spread in recoil velocities per sidereal time is shown in Figure 1.9. Bands have been drawn which indicate 68.27% and 95.45% containment of the recoil velocity component distributions per sidereal time in the Standard Halo Model. Due to escape speed, WIMP velocities in a galactic frame of reference are assumed to compose a truncated Maxwell-Boltzmann distribution in velocity three-space. In the frame of reference of the Sun, these velocities are boosted along the

[12]GMT and Coordinated Universal Time (UTC) may be used interchangeably here.

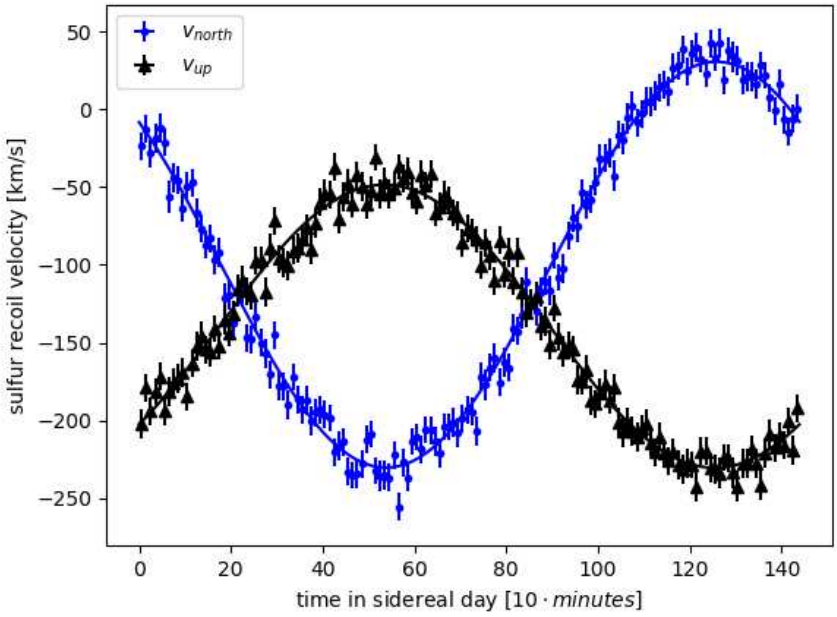

Figure 1.8: Two components of the WIMP recoil velocity are plotted as a function of time in a sidereal day. These components oscillate due to the direction of the WIMP wind changing with respect to the detector over the course of a day.

line of travel of the Sun about the center of galaxy. Further transformation is required to account for the motion of Earth about the Sun and the rotation of the Earth about its axis. Due to the factors above, the WIMP wind appears on average to be blowing from the constellation Cygnus, but this should not be interpreted as all WIMPs are coming from this direction.

The two recoil velocity components have been fit[13] with a function of the form

$$v = a{\cdot}cos(\omega t + \phi) + v_0$$

where a is the amplitude of oscillation, ω the angular frequency, ϕ the phase, and v_0 the vertical offset[14]. All parameters were allowed to float during the fit except for the angular frequency which is fixed, $\omega = \frac{2\pi}{144\ [10{\cdot}\text{minute}]}$. The fit values are reported in Table 1.1.

[13]Fits were performed with Python, using the curve_fit() routine of the scipy.optimize package [89].

[14]The symbol v_0 here is a fit parameter. It is not the same as v_0 that appears in Section 1.4 and is the circular orbital speed of the sun about the galactic center.

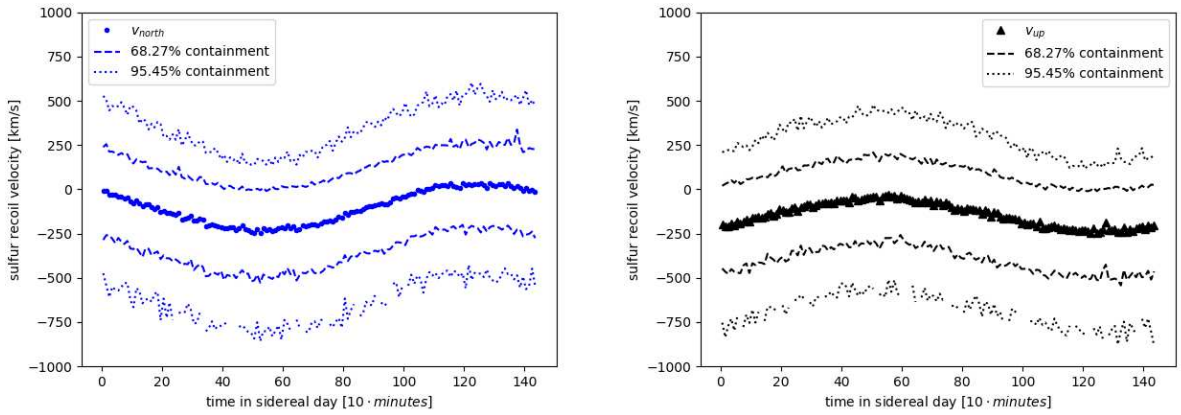

(a) v_{north} spread **(b)** v_{up} spread

Figure 1.9: The spread in the WIMP recoil velocity components is plotted per LST. The averages, as in Figure 1.8, have been plotted here. Dashed(dotted) lines enclose 68.27%(95.45%) of the velocity distribution about each average. These lines are not exactly representative of standard deviation. They were obtained by normalizing the area of each velocity distribution, for each sidereal time, to unity and then iterating across the distribution to each side about the average until the desired percent containment was found. Each distribution contained 100 bins, choice of the full range was automated.

Table 1.1: Listed are the fit parameters for the north and up components of the recoil velocity. The uncertainty on the fit parameters were found by taking the square root of the diagonal elements of the covariance matrix output from the fit routine.

	$a\ [\frac{\text{km}}{\text{s}}]$	ϕ [radians]	$v_0\ [\frac{\text{km}}{\text{s}}]$
v_{north}	130.5 $\pm$ 1.1	-24.34 $\pm$ 0.01	-99.92 $\pm$ 0.80
v_{up}	-91.02 $\pm$ 1.1	19.66 $\pm$0.01	-139.5 $\pm$ 0.8

The LSTs that correspond to each velocity component being at absolute-value-maximum amplitude occur at the minima of the two curves. To find the times for these minima, one can solve for the time at which each velocity component has a value of $-(|a| + |v_0|)$. Since the time of interest are those for which the first minima occur, the modulo operation has been utilized to reduce each reported phase shift to its smallest equivalent phase.

$$t_i \equiv \frac{cos^{-1}(\frac{-(|a_i|+|v_{0i}|)-v_{0i}}{a_i}) - (\phi_i \; modulo \; 2\pi)}{\omega} \qquad i = north, up$$

From the above, it is found that these times are approximately $t_{north} = 53.82$ 10·minutes and $t_{up} = -18.52$ 10·minutes. For a DRIFT detector, sited at Boulby and positioned as described

above, one expects the recoils from the WIMP wind to be oriented most along the north/south axis of the detector ~ 538.2 minutes into the local sidereal day, and generally oriented along the south direction of this axis. One expects the recoils to be oriented most along the up/down axis of the detector $1440 - (\sim 185.2) = \sim 1255$ minutes into the local sidereal day, and generally be oriented along the down direction of this axis.

Later in this dissertation, experimental runs with the DRIFT-IIe detector will be described, where it has been exposed to a neutron source that has been placed at various locations around the detector. Neutrons, within a range of kinetic energies, provide a proxy for what one may observe with the detector from WIMPs. Knowing the LSTs when the wind is blowing most south or most down will prove useful in comparing these neutron runs in the lab to what one may expect to observe due to WIMPs.

Chapter 2

The DRIFT-IIe Dark Matter Search Experiment

2.1 Detector Description

The DRIFT-IIe detector was a R&D project in preparation of building a larger DRIFT-III detector. DRIFT-IIe is the successor of DRIFT-IId. Some of the main differences between the two iterations are the construction of the Multi Wire Proportional Counters (MWPCs) as well as the readout schemes for the wires of the MWPCs. A description of earlier iterations of the DRIFT experiments is provided in [90], and a nice brief description of DRIFT-IId in particular is provided in [78]. The DRIFT-IId detector MWPCs each are composed of three planes of wires, the wires of the central plane are orthogonal to and sandwiched between the two other planes. This MWPC configuration allows for the two-dimensional length measurement for a track of ionization deposited in the detector volume, and the length in time of a signal combined with the known drift speed of the ionization allows reconstruction of the third dimension of the track. Each MWPC of the DRIFT-IIe detector is one plane of parallel wires, resulting in the loss of ability to reconstruct one of the spatial dimensions of the track. A single plane of wires is advantageous in that it takes less materials to construct, hence it is more cost effective, and it is easier to manufacture. The two previous qualities are especially desirable if one has the intent to scale up the size of the detector. If considering only the ability to reconstruct the length of a track in three or two dimensions, the loss of the one dimension may result in the need to observe up to an order of magnitude more events to claim a significant detection [66].

The actual DRIFT-IIe detector was under construction at the Boulby laboratory when funding to continue the project was depleted. A second full-scale replica of the detector is housed in a lab space at Occidental College[15]. This replica detector is not sited deep underground to shield from

[15] Daniel Snowden-Ifft, a primary investigator for the collaboration, and Jean-Luc Gauvreau, a collaborator heavily involved with the research and development of the DRIFT experiments, are based at Occidental College. They contributed both resources and time that were necessary to collect the neutron exposure data used in this dissertation.

cosmics. A full-scale replica allows one to perform tests and debug any issues before implementing them on the WIMP search detector, for which any operations must be planned out more carefully due to the complexities of working underground. In this dissertation, all of the experimental work and data collection occurred at Occidental College using the replica DRIFT-IIe detector.

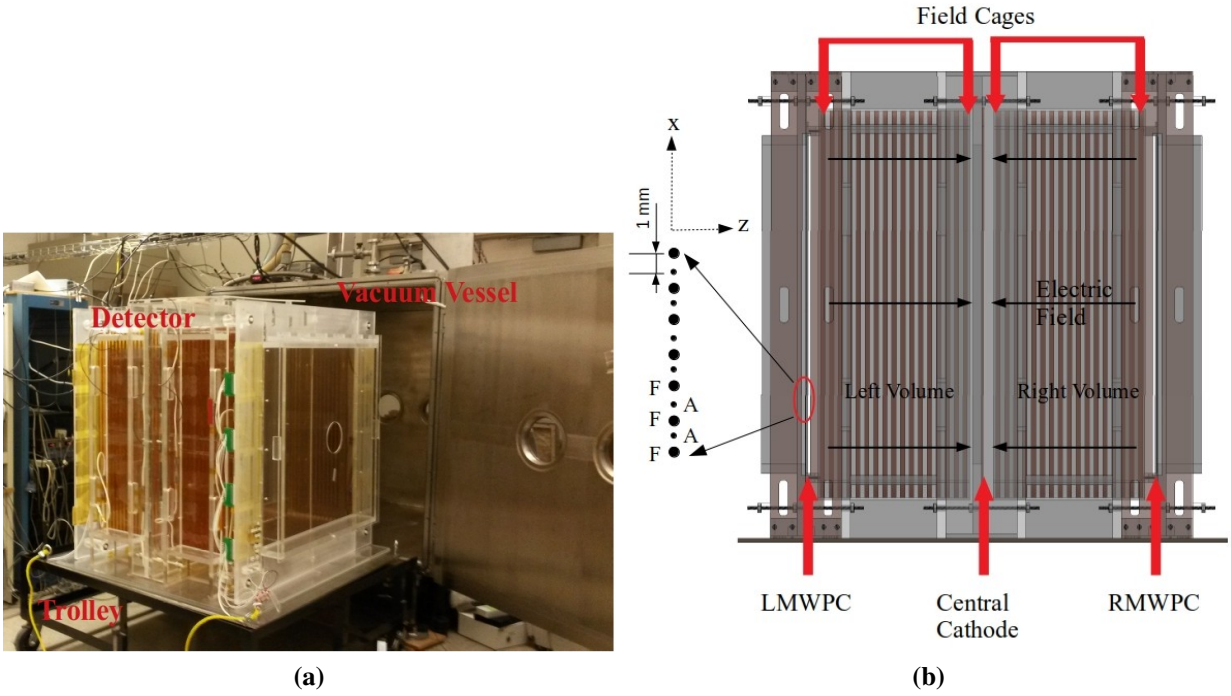

Figure 2.1: (a) Photo of the replica DRIFT-IIe detector located in a surface laboratory at Occidental College. The detector is shown uninstrumented with readout electronics. The detector has been removed from the stainless steel vacuum vessel and is sitting on the detector trolley. On the right side of the photo, the hinged vessel door can be seen. (b) The view of the detector from the front. Sketched along the left side of this panel is an expanded view of a section of MWPC wires. Each MWPC, left and right, is composed of alternating field (F) and anode (A) wires which are parallel to each other and oriented in/out of the page. Adjacent wires are separated by 1 mm. This figure was produced from SolidWorks files that were developed by Eric Lee, a member of the DRIFT collaboration, while at the University of New Mexico.

2.1.1 Physical Description

In reading this section, one should keep in mind that some differences exist between the WIMP-search and replica detector. The focus in this section will be to describe the replica detector, since it was used for this work, while also pointing out some of the differences.

The DRIFT-IIe detector is a low-pressure gas, $\sim$40 Torr, Negative-Ion Time Projection Chamber (NITPC) [91], with the primary component of the gas being CS_2. CS_2 gas is electronegative and quickly captures electrons, such as from a track of ionization resulting from a nuclear recoil. Drifting negative ions, anions, instead of electrons has been shown to suppress diffusion in the track without the need of a magnetic field [92]. These drift under the influence of the electric field of the detector volume towards anode wires of the MWPC resulting in signal formation. Capture, diffusion, and signal formation is discussed in Section 2.1.3.

The specific target gas mixture for this work was 40:1.5 Torr CS_2:O_2. After evacuating the vessel, this mixture was achieved by manually opening valves to allow CS_2 followed by O_2 gas into the vessel. A more detailed description of this process is given in Section 3.2.1. Each fill was static, meaning that the gas was not recirculated or flowed through the detector. Over time the properties of the gas have been observed to degrade, so flow is desirable, further comments on this appear in Section 2.2.1. The DRIFT-IId detector, sited at the Boulby lab, had a custom-built and automated system to control the gas mixing, pressure, and flow rate that was approximately an exchange of one detector volume per day [78] [81]. The nominal gas mixture for DRIFT-IId WIMP searches was 30:10:1 Torr CS_2:CF_4:O_2. A similar gas mix and automated system would be used for DRIFT-IIe WIMP searches. The addition of CF_4 allows for the search for spin-dependent WIMP interactions, some further discussion is provided in Section 2.1.3.

The detector is housed in a cubic 304-grade stainless steel vacuum vessel that is nominally 1/2 inch thick. Support beams are welded along the outside of the cubical shell of the vessel to maintain rigidity. A hinged door, which constitutes the front face of the vessel, allows access to the vessel interior. The inner dimensions of the vessel walls are 1.5 m in length. The detector itself sits on a skate plate that allows the detector to be slid in/out of the vessel onto the detector trolley, see Figure 2.1(a). The detector is not entirely shown surrounded by the acrylic shielding that is used to prevent discharge between the high-voltage components of the detector and the grounded vacuum vessel.

In Figure 2.1(b), the detector is shown as viewed from the front. A central cathode allows for drift volumes on both sides of the cathode. Each drift volume, left and right, is 50 cm in length and spans the region of space between the central cathode and the corresponding Left MWPC (LMWPC) or Right MWPC (RMWPC). For the WIMP-search DRIFT-IIe detector, the cathode would be composed of 0.9 μm thick, texturized aluminized-Mylar [93]. For the replica detector, the cathode was a 1 mm thick aluminum sheet that was held at a voltage of -30 kV during data collection. Each MWPC is composed of 914 alternating stainless steel anode and field wires that are oriented in-and-out of the page in the figure. The anode wires are 20 μm in diameter and held at ground potential. The field wires are 50 μm in diameter and held at $\sim$-900 V. The spacing between adjacent anode and field wires is 1 mm, implying that the spacing between adjacent anode wires is 2 mm. The signals produced on the anode wires were collected and studied in this work, the corresponding field wire signals were not available for all periods of data collection and are not necessary for the analyses presented in the forthcoming sections. The field wires shape the electric field near the anode wires to allow for avalanche, which is described in Section 2.1.3.

Each volume, left and right, is surrounded by a field cage. The field cages each consist of 17 evenly-spaced square rings that surround the drift volume. Each ring is made of 12.7 mm wide copper ribbon. The rings of the field cage are resistively connected to uniformly step the voltage down across the volume. The relative biasing between each MWPC and the cathode allows for a uniform electric field in the detector volume that points horizontally from each MWPC toward the cathode. Negative charges in the detector volume, tracks of ionization, drift opposite the direction of the field lines towards the anode wires.

The three detector axes are defined as shown in the figure. The x axis is vertical and oriented perpendicular to the wires, the z axis coincides with that of the electric field, and the y axis is parallel to the wires of the MWPC. The $\hat{x}$ and $\hat{z}$ directions are shown explicitly and $\hat{y}$ is out of the page and assumes a right-handed coordinate system.

The readout electronics were developed at Occidental College and are only discussed briefly here. The signal for each wire, this includes both anode and field wires, is read out independently.

The readout for a group of wires is controlled by an electronics box, which reads out 60 anode wires plus 60 field wires. With 914 wires per MWPC, a total of eight electronics boxes are required to read out each side of the detector.

For each wire, the signal was first processed by a chip developed at Brookhaven National Laboratory [94]. These shaping electronics were set to produce a semi-Gaussian output of amplitude 25 mV per 1 fC impulse charge input with a peaking time of 3 μs. After an impulse charge input has been shaped, the peaking time is the amount of time it takes the signal to rise from baseline to the peak value of the shaped signal. The peaking time is different than what is typically known as the shaping time. For a Gaussian, shaping time is described by the standard deviation in time about the peak of the shaped signal. In Section 2.2.1 the shaping electronics response is investigated empirically, and the shaping time is found to be $\sigma_{shape} = 1.45 \pm 0.02$ μs. The peaking time can then be related to the shaping time by $\tau_{peak} = n\sigma_{shape}$, where n is a value which tells how many standard deviations wide the shaped signal is. The above values result in $n = 2.07$, for a true Gaussian 95.45% of the distribution lies within $\pm 2\sigma$ of the peak. The signal was then low-pass filtered before being digitized at a rate of 1 MHz. A Linear Technology LTC2365 ADC [95] with 12-bit resolution was used to digitize values over an ADC range measured to be 1807 mV. The filter prevents aliasing from higher-frequency signal components and the time constant was chosen based on the ADC specifications.

Before the low-pass filter described in the previous paragraph, the signal is split. This signal is bandpass filtered by the combination of a high-pass filter in series with a low-pass filter. The time constant of the high-pass filter is 1 ms corresponding to a cutoff frequency of $\sim$160 Hz to filter known electronics noise, and the time constant of the low-pass filter is 10 μs which corresponds to a cutoff frequency of $\sim$16 kHz. This second signal is then compared to a threshold voltage which allows the data acquisition to be run in a triggered mode.

If running in this triggered mode, only the digitized signals which meet this condition, as described in the previous paragraph, are saved to disk. This mode of operation as well as an untriggered mode of operation are further discussed in Section 2.1.5. The upper frequency cut

allows one to avoid triggering on high-frequency components of the signal that do not contribute to the larger-timescale structure expected in nuclear recoil signals[16].

Again, the replica detector is in a surface laboratory space at Occidental College. The WIMP-search detector would be sited $\sim 1.1\ \mathrm{km}$ underground at the Boulby Underground Science Facility to shield from cosmics. A particularly onerous background for the direct detection of WIMPs is neutrons. Nuclear recoils produced from WIMPs scattering off target nuclei in the detector are, in theory, indistinguishable from those produced by neutrons. For this reason, later in this work, neutrons will be used to characterize the directional capabilities of the detector. Even if one is careful to construct a detector of low-radioactivity materials, deep underground ambient neutrons are still present, being emanated from the surrounding rock from spontaneous fission, (α,n) reactions, and muon-induced neutrons [96] [97] [98]. To shield from these ambient neutrons, during WIMP search runs the detector is surrounded with polypropylene pellet shielding (later in the lifetime of DRIFT-IId a combination of water and polypropylene was used). In both cases the shielding is hydrogenous since its constituent hydrogen particles are of similar mass to that of a neutron. Energy can be maximally transferred from a moving object, a neutron, to one at rest, the shielding, when the two colliding objects are of the same size, which is dictated by standard scattering physics. It was determined that with the shielding in place the rate of rock neutron events that would be observed above a detector threshold of 1000 Number of Ion Pairs (NIPs) is $\sim 1\ \mathrm{year}^{-1}$ [99]. NIPs are a measure of energy deposited in the detector. A given recoil species, such as sulfur, will produce an amount of ionization, or in other words electron-ion pairs, that scales with its kinetic energy. Further explanation is provided in Section 2.3. A threshold of 1000 NIPs is consistent with that found in this work for the replica DRIFT-IIe detector.

In this section, the full detector has been described. At the time that data was collected for this dissertation, the readout electronics were in a phase of R&D, and the detector readout was not fully

[16]Nuclear recoil tracks in this detector are expected to be of length of order a few millimeters, for a concrete value let 3 mm be used. The main component of the ionization drifts to the MWPC at a speed of 0.0524 mm/μs, see Section 3.2.4. This implies a length in time for the signal of $\sim$57.3 μs. Taking the previous as the period for this signal results in a frequency of $\sim$17.5 kHz. This calculation is meant only to give a sense of scale. Important factors such as track orientation, diffusion, and convolution with the shaper response have not been considered.

instrumented. That is, data was only collected for part of the detector. The state, over the period for which data was collected, is described in Section 2.1.6.

2.1.2 Minority Carriers

DRIFT gas mixtures are nominally 40 Torr CS_2 or 30:10 Torr CS_2:CF_4 depending on whether a spin-independent or spin-dependent dark matter search is being conducted, respectively. It was discovered that the addition of $\sim$1 Torr of O_2 to the gas mixture results in the formation of three additional charge carriers species when a track of ionization is created in the detector [100]. For a given electric field strength, pressure, and gas temperature these different carriers drift with stable and slightly-different-yet-distinct speeds. The three new charge carriers drift with speeds that are greater than that of the single charge carrier species observed with CS_2 alone. These new carriers are termed minority carriers. The result is that the signal observed on an anode wire from a track of ionization in the detector is composed of four pulses, one for each of the charge carriers, and the shape of this type of signal is shown in Figure 2.2. The four carriers and peaks they produce in the signal have been named D, P, S, and I and move with speeds in the gas in descending order of which they have been listed. That is, D carriers move the quickest and so the D peak is observed first in the signal. In the aforereferenced work it was shown that the I carrier anions are with high probability the same species of carrier anion as those observed with CS_2 only. The identities of the minority carrier species are unknown, however, the preceding statement along with the fact that the drift speeds are similar suggest they are variants of the CS_2 anion.

For the j^{th} carrier anion species, the drift speed of the carrier anion can be specified by Equation 2.1. Where E is the electric drift field strength, P is the gas pressure, T the gas temperature, and $T_0 = 273.15$ K. The reduced mobility μ_0 has been meausured [100] for the P, S, and I carriers as function of the O_2 partial pressure P_{O_2} present in the gas mixture for both 40 Torr CS_2 and 30:10 Torr CS_2:CF_4 and increases linearly with the O_2 content $\mu_{0j} = a_j P_{O_2} + b_j$. For ease of reference, $a_P = 6.8 \pm 0.1$ $\frac{\mathrm{cm}^2}{\mathrm{V{\cdot}s}}$, $b_P = 369.75 \pm 0.08$ $\frac{\mathrm{cm}^2{\cdot}\mathrm{Torr}}{\mathrm{V{\cdot}s}}$, $a_S = 6.9 \pm 0.1$ $\frac{\mathrm{cm}^2}{\mathrm{V{\cdot}s}}$, $b_S = 359.46 \pm 0.08$ $\frac{\mathrm{cm}^2{\cdot}\mathrm{Torr}}{\mathrm{V{\cdot}s}}$, $a_I = 6.5 \pm 0.1$ $\frac{\mathrm{cm}^2}{\mathrm{V{\cdot}s}}$, and $b_I = 350.95 \pm 0.08$ $\frac{\mathrm{cm}^2{\cdot}\mathrm{Torr}}{\mathrm{V{\cdot}s}}$ for the case of 40 Torr CS_2. For P_{O_2} = 1.5

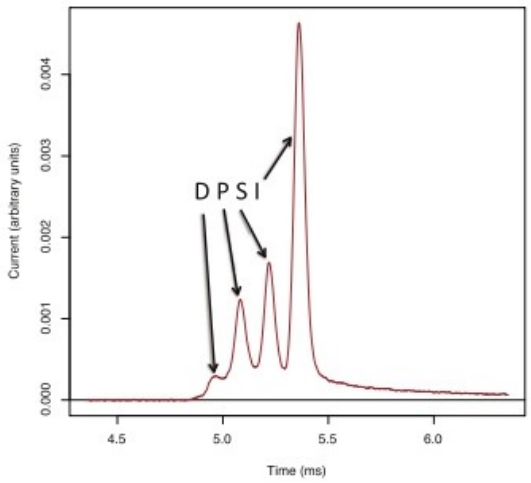

Figure 2.2: The characteristic signal structure due to the D, P, S, and I carrier anions. This figure is a reproduction from [100].

Torr which was used for this work, these result in reduced mobilities of $\mu_{0I} = 360.7 \pm 0.2 \ \frac{\mathrm{cm}^2 \cdot \mathrm{Torr}}{\mathrm{V \cdot s}}$, $\mu_{0S} = 369.8 \pm 0.2 \ \frac{\mathrm{cm}^2 \cdot \mathrm{Torr}}{\mathrm{V \cdot s}}$, and $\mu_{0P} = 380.0 \pm 0.2 \ \frac{\mathrm{cm}^2 \cdot \mathrm{Torr}}{\mathrm{V \cdot s}}$. In [100], the linear trend was observed over the range $0 \leq P_{O_2} \lesssim 1.1$ Torr, so the assumption here is that the trend remains linear up to 1.5 Torr P_{O_2}. The ratios $\frac{\mu_{0S}}{\mu_{0I}} = 1.025$ and $\frac{\mu_{0P}}{\mu_{0I}} = 1.054$ indicate that the S carriers drift 2.5% faster than the I carriers and the P carriers drift 5.4% faster than the I carriers.

$$v_j = \mu_{0j} \sqrt{\frac{T}{T_0}} \frac{E}{P} \qquad j = D, P, S, I \tag{2.1}$$

Since the carrier species drift at well-defined speeds, one can imagine that the separation in time of the peaks is a function of how far from the MWPC along the $\hat{z}$ direction of the detector a track of ionization is deposited; actual events depicting this are shown for the DRIFT-IIe detector in Section 3.2.2. Tracks deposited close to an MWPC will have minimal separation and the peaks may completely overlap making them indistinguishable. Tracks deposited near the cathode will have maximal separation. In other words, the separation in time between two of the peaks allows one to determine how far from the MWPC the recoil interaction occurred within the detector volume.

As will be discussed shortly, the S carriers have a finite lifetime and so the size of the S peak decreases with increased drift distance. In addition, the D peak is relatively small and not always

visible. When comparing the size of the D peak to other peaks, sans the S peak in certain circumstances due to its finite lifetime, the D peak has been observed to be the smallest for a given signal. The D peak is not visible for every track or may be difficult to pick out during analysis. If a track is deposited close to the MWPC the different carriers may not have enough drift time to fully separate, resulting in a shoulder on the signal where the different peak locations are unclear. The farther a track is deposited from the MWPC, the more time carrier populations have to separate and undergo diffusion while drifting to the MWPC, this can cause the D peak to become indistinguishable from noise. It is also possible that for some signals the portion of D peak carriers created in the track is just statistically small making the D peak difficult to observe. For these reasons the separation in time of the I and P peaks is typically used to determine the z distance from the MWPC.

For two carrier species j and k, let t_j and t_k represent the time associated with the peak signal of each and $\Delta t_{jk} \equiv \left|t_j - t_k\right|$. It is assumed that all carrier anion species are distributed on average around the same site of ionization production for a given portion of a track, that is all anion species are created at the same distance from the MWPC and separate as they drift to the MWPC. Let this distance be named z_{jk} to indicate it was measured via the j and k peak separation in time. Supposing the portion of the track was deposited in the detector at time t_0 implies that $t_j = \frac{z_{jk}}{v_j} + t_0$ and $t_k = \frac{z_{jk}}{v_k} + t_0$. Implementing (2.1), taking $t_j - t_k$, and rearranging yields an expression for z_{jk}.

$$z_{jk} = \Delta t_{jk} \frac{E}{P} \sqrt{\frac{T}{T_0}} \left(\frac{1}{\mu_{0_j}} - \frac{1}{\mu_{0_k}}\right)^{-1} \quad j,k = D,P,S,I \; and \; j \neq k \tag{2.2}$$

In Section 3.2.2, this method is applied to determine z_{IP} for nuclear recoil tracks resulting from exposure of the detector to a neutron source. In reality a track has a spatial extent. If the spatial extent is such that the track results in a signal on more than one wire of the MWPC, the wire that has the largest amplitude signal is used to calculate z_{IP}. Depending on the orientation of the track, the tail(start) and head(end) of the track may be different z distances from the MWPC. However, as long as the track length is small compared to the drift length of the detector, using the signal of one wire only is adequate to describe the z position of the track within the detector. Later in this

work, it will be shown that on average the z extent of these tracks is estimated to be less than 3 mm. The full drift length of the detector is 50 cm. So at most one could expect to reconstruct z_{IP} values that are 0.6% different relative to the drift length.

A few other observations have been made regarding the nature of these signals. The I peak has the largest amplitude and accounts for ∼50% of the total signal integral for $P_{O_2} \cong 1$ Torr [101]. As mentioned above, the amplitude of the S peak, relative to the I peak, is known to decrease with increasing drift distance [100]. The integral of the P peak relative to that of the I peak tends to increase with increased drift distance [102] [78]. The resulting suggestion is that there is a conversion between carrier types as a function of time such the total number of anions, energy, is conserved. It is expected that the signals observed in this work should have similar properties, these observations and the formulae contained in this section have been implemented into the analysis of signals for this work.

2.1.3 Negative Ion Drift and Signal Formation

For this dissertation, the gas of interest is 40:1.5 Torr CS_2:O_2. This differs from the nominal DRIFT gas that has been used for previous WIMP searches which is 30:10:1 Torr CS_2:CF_4:O_2. The difference in gas mixtures is due to the fact that a WIMP search was not being performed. Here the goal is to understand the directional detection capabilities of the detector. The F content in the CS_2:CF_4:O_2 mixture allows for the opportunity to search for spin-dependent interactions. The unpaired proton in the ^{19}F nucleus results in net nuclear spin and in theory allows for a spin-dependent interaction between a DM particle and the F nucleus. The spin-independent cross section scales as A^2, with A being the nuclear mass, and is the dominant contribution for detectors with heavy nuclei [103]. For lighter nuclei with net spin, and in particular ^{19}F, the spin-dependent cross section can dominate [104] [105]. In reference [106], some supersymmetric interaction cross sections had been tabulated for WIMPs interacting with ^{19}F, and a comparison of the reported values indicates that the spin-dependent cross section could be ∼2-4 orders of magnitude larger than the spin-independent contribution. This type of theoretical enhancement has historically been

a search motivation, and is desirable for a gaseous and relatively low-mass detector. Within the context of many ongoing WIMP searches, both spin-independent and spin-dependent, as statistical limits further push possible interaction cross sections to smaller values, theories become further constrained.

For this work it is expected that most of the recoils are S recoils. Previously in 40 Torr CS_2 it has been determined that C recoils are suppressed in observation by a factor of $\sim$100 relative to S recoils [88]. This is due to the fact that the energy deposited in the form of ionization per step in path length dE/dx is relatively low for C in comparison to S recoils. Concerning the O content of the gas, the probability of an O recoil occurring relative to S was calculated to be 3.4% in Appendix A. Further, the dE/dx for O recoils is in general less than that of S recoils, assuming the same initial recoil energy, according to SRIM [107] simulations. These two previous statements lead to the expectation that the observation of O recoils is suppressed.

A summary of the principle of operation of the detector is described in the following, details will follow in the subsequent paragraphs. For further information regarding the operating principles of gaseous TPCs, the reader is referred to [108]. Figure 2.3 is a pictorial representation of this textual description. An incoming WIMP scatters off one of the gaseous target nuclei resulting in a nuclear recoil. As the recoiling nucleus travels through the gas other molecules are ionized creating a track of ionization, which is not depicted explicitly. Secondary recoils can also result in branching of ionization from the track of the primary. The deposition of ionization is more dense at the tail(start) of the track compared to the head(end) of the track [68]. The gas mixture is primarily CS_2 with a small addition of O_2, for a net pressure of $\sim$40 Torr. The CS_2 results in the formation of anions, and the addition of O_2 results in three more species of anions being formed, see Section 2.1.2. The different anion species I, S, P, and D drift with different and well-measured speeds for a given gas pressure and electric field. The D anions arrive at the wires of the MWPC first followed by P, S, and I. Once close to an anode wire, where the field strength is high, the electron is stripped from each anion and the electron seeds an avalanche. The avalanche about each wire that is hit results in an electron-ion pair at each site of ionization. The resulting signal on the anode wires is

current due to collection of the electrons as well as induced signal as the ions drift to the neighboring field wires or back to the cathode, the latter is the primary contribution to the signal. The signal from current is converted to voltage and digitized as described in Section 2.1.1.

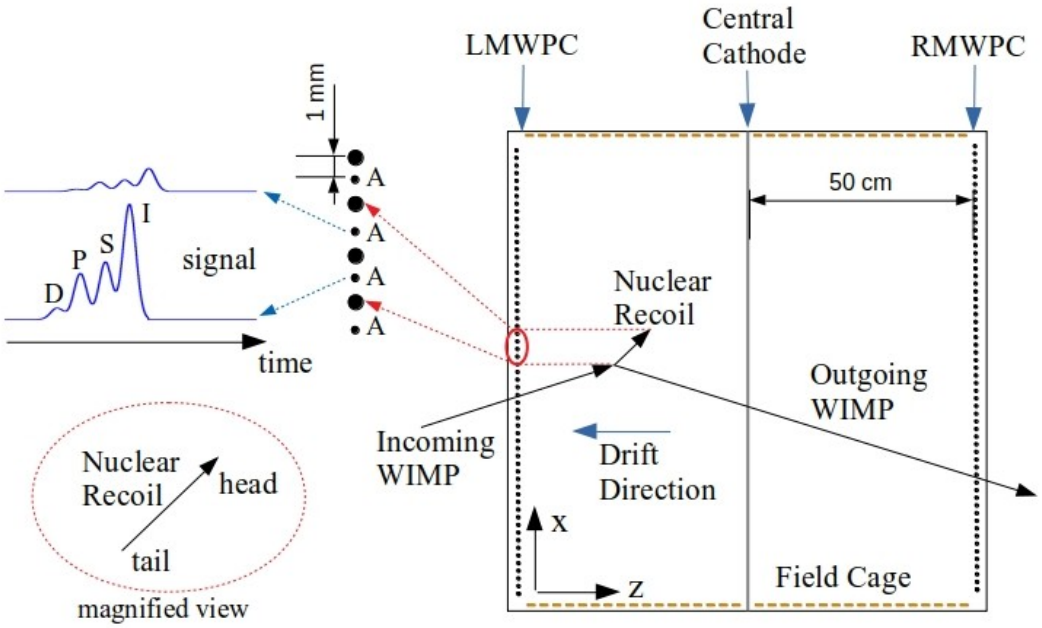

Figure 2.3: This figure describes the operating principle of the detector. It is a view of the detector from the front. The wires of each MWPC are in/out of the page. See the body of the text for further description. This schematic is not drawn to scale. (Thanks is given to the developers of LibreOffice. This figure and some other figures within this dissertation were made using LibreOffice [109].)

A track of ionization is composed of electrons that have been liberated from the gas and are subsequently captured by CS_2 resulting in the formation of anions. As these anions drift toward the MWPC, diffusion is incurred in both the direction of drift (longitudinal) and that transverse to it (lateral). Due to these two effects, capture and diffusion, the spread along the longitudinal and lateral directions is found by the convolution of the position with two Gaussians of widths $\sigma_{capture}$ and $\sigma_{diffusion}$.

$$\sigma_i^2 = \sigma_{capture_i}^2 + \sigma_{diffusion_i}^2 \qquad i = lateral, longitudinal$$

The drift speeds of anions in gas mixtures relevant to this work have been found to be proportional to E/p [110] [111], which is known as the low-field approximation [108][17], with E being the electric field strength and p the gas pressure. In this regime, the variance in the anion position along each dimension is proportional to the anion energy. The average anion energy is a combination of thermal energy, that gained over the mean free path, and that lost in collision. The energy gained is determined by the ratio $E/(\sigma_{a-g}p)$, where σ_{a-g} indicates the interaction cross-section of the anion with the gas. The energy gained increases with E and decreases as either p or σ_{a-g} increases since this will shorten the mean free path resulting in more collisions.

The use of CS_2 gas has been found to suppress diffusion down to the thermal energy level of the gas [110] [111]. This is the result of the nature of elastic scattering for objects of similar mass. CS_2 anions drift in the CS_2 gas, since the anions and gas molecules essentially have the same mass, energy is maximally transferred from anions to the gas during collision. With anion energy reduced to the thermal level, the spread in position is set by a Gaussian variance.

$$\sigma^2_{diffusion_i} = \frac{2k_B T_i z_{IP}}{eE} \quad i = lateral, longitudinal$$

Here T_i indicates the temperature of the gas and z_{IP} is the distance the anion must drift to the MWPC. Measurement of the spread in position due to diffusion along the lateral and longitudinal directions can be used to measure the characteristic temperature, energy, of the gas. Most relevant to this work, these characteristic temperatures have been measured for 40 Torr CS_2 [111], resulting in $T_{lateral} = 295 \pm 15$ K and $T_{longitudinal} = 319 \pm 10\ (stat.) \pm\ 8(sys.)$ K. The capture distances have also been measured to be $\sigma_{capture_{lateral}} = 0.21 \pm 0.07$ mm and $\sigma_{capture_{longitudinal}} < 0.35$ mm at the 90% confidence level. For this work, $E \approx 580$ V/cm, combined with the maximum drift distance of $z_{IP} = 50$ cm implies maximum values of $\sigma_{diffusion_{lateral}} \approx 0.66$ mm and $\sigma_{diffusion_{longitudinal}} \approx 0.69$ mm. The total randomization of position along each direction, due to both capture and diffusion, is $\sigma_{lateral} \approx 0.69$ mm and $\sigma_{longitudinal} \approx 0.77$ mm. It should

[17] See Sections 2.2.2 and 2.2.4 of the referenced work.

be emphasized that these values represent the maximum amounts of randomization expected and only apply to those tracks deposited farthest from the MWPC.

A Garfield++ [112] simulation was developed as part of this dissertation work to further describe the process of signal formation. The simulation utilized ROOT [113] classes. For the simulation, the drift gas was room temperature 40 Torr CS_2, the anode wires were grounded, the field wires held at -900 V, and the central cathode was held at -30 kV. Dissimilar to the detector description in Section 2.1.1, 31 0.5 cm field cage wires were used to step down the voltage over the 50 cm drift volume in order to set up the uniform drift field. Only 100 anode and 100 field wires were included, decreasing the x-length of the volume. The wires shown in any figures that follow are those which were central-most to avoid any edge effects. For this initial simulation, only the I anions were considered since the gas was CS_2 only. In Figure 2.4 a single anion was placed a z distance of 25 cm from the MWPC and allowed to drift. The path of the anion near the MWPC is shown.

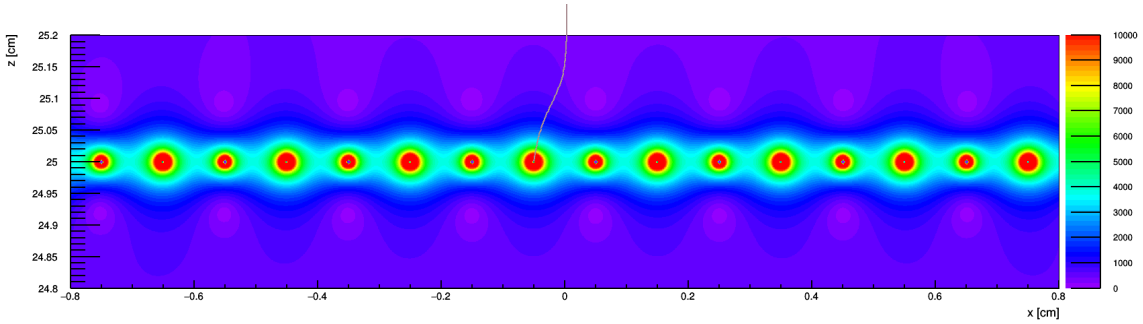

Figure 2.4: The path of a single CS_2 anion as it drifts toward an anode wire of the MWPC. In this plot, vertical is the drift, z, axis. Eight anode and eight field wires are shown oriented in/out of the page. The vertical axis spans 4 mm and the horizontal axis spans 16 mm. A color map of the electric field strength is shown with violet corresponding to low field and red corresponding to large, $\sim$10 kV/cm, field.

Once an anion, of a track, is sufficiently close to an anode wire, the electron can be stripped from the anion resulting in avalanche. Values for this avalanche field are found in the literature to be a few kV/cm [114] [115] to 69.4 kV/cm [116]. Another value can be calculated if one applies the methods of [116] to gas gain data presented in [117] resulting in an avalanche field of 24.4 ± 6.9 kV/cm. In the simulation, as a starting point, the field required for avalanche was set at 10 kV/cm.

This value could be tuned such that the average electron gain returned by the simulation matches the gain results of Section 3.1.2. Figure 2.5, shows the magnitude of the electric field near an anode wire. For a single anode wire, the field strength is plotted as one moves away from the edge, at the cross-sectional center, of the wire along $\hat{z}$. The plot indicates that avalanche initiates at approximately a distance of 12.5 anode wire radii away from the wire.

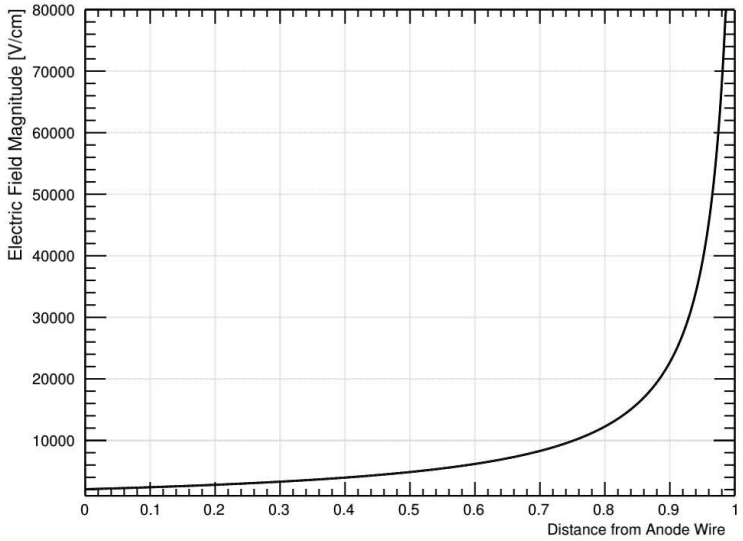

Figure 2.5: A plot of the magnitude of the electric field near the central-most anode wire from 50 anode wire radii along $\hat{z}$ up until the wire edge. The horizontal axis describes a distance of 50 anode wire radii, with 0 being 50 anode wire radii away and 1 being the anode wire location.

The electron, once stripped from the anion, rapidly accelerates due to the electric field. Once it has crossed a potential difference sufficient to gain enough energy to ionize the gas[18], an electron-ion pair is formed. For each liberated electron, this process repeats resulting in an avalanche of electron-ion pairs being formed near the anode wire. The single anion of the simulation was allowed to undergo electron detachment at the first instance along its path that it encountered the previously mentioned avalanche field. The simulated avalanche is plotted in Figure 2.6.

[18]The amount of energy required on average to create an electron-ion pair in the gas is known as the W-value and will be discussed in Section 2.3.

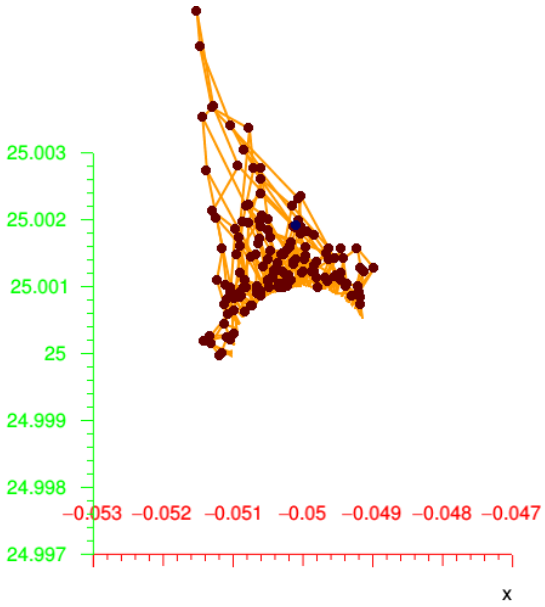

Figure 2.6: A simulated single-electron avalanche is shown. The avalanche resulted in a gain of 145 electrons. Each point represents a site of ionization where an electron-ion pair is created. Upward is along $\hat{z}$ into the drift volume of the detector. Horizontal is the x-axis, with the wire coming in/out of the page. The axes have units of centimeters, and for reference, a partial outline of the wire circumference can be seen which is of diameter 20 μm.

The signal on the anode wire is current from the electrons being collected as well as induced signal as the ions drift towards the nearby field wires or back toward the cathode. The drift paths of the ions is shown in Figure 2.7. In the simulation, it was assumed that ions that were formed during avalanche had the same drift speed as the I species anions. It has been reported [118] that in general anions of a certain gas tend to move more quickly than cations of the same gas. The same work appears to indicate that if the gas number density of CS_2 is $< 3.8\times10^{26}$ m^{-3}, as is the case for 40 Torr (1.317×10^{24} m^{-3}), then the anion and cation mobilities are approximately the same.

Both of these contributions, the electron signal and induced signal from the avalanche ions, produce pulses of negative current. On approach, the single negative ion also produced a negligible amount of induced positive current. Later in this dissertation, signals on the anode wires are shown to be positive while signals on the field wires are shown to be negative which is opposite to this. This is simply a convention of the DRIFT collaboration. The anode wire and field wire pulses are inverted such that the anode wire pulses are positive.

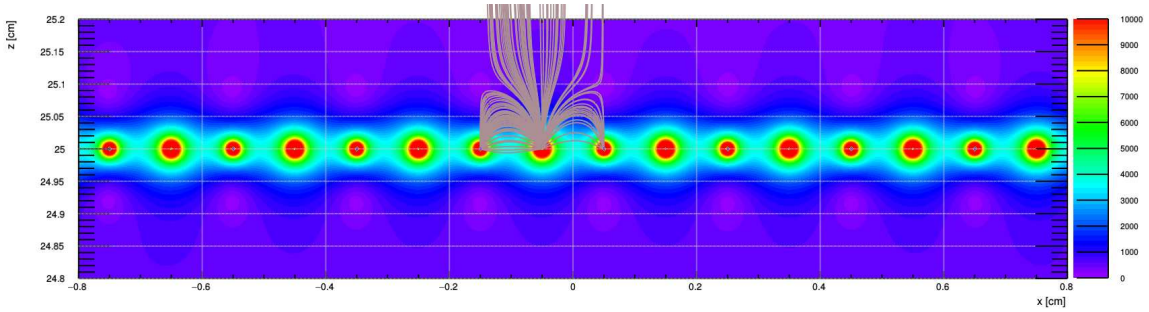

Figure 2.7: After a single-electron avalanche. The ions which were created at each ionization site were allowed to drift. Shown are simulated paths taken by these ions.

In Figure 2.8, the components of the signal produced on the single anode wire were retrieved from the simulation. In (a), the induced signal is shown as the one anion drifts to the anode wire, it is of amplitude $\sim 0.1 \times 10^{-6}$ fC/ns. This should be taken as an upper limit, in reality the contribution should be smaller. Plotted is the induced anion signal as it drifts all the way to the anode wire, one should remove the signal contribution after the point in time that the anion has a reached the position in space where it is at the field required for avalanche and the electron is stripped. The electron signal, shown in (b), is of amplitude $\sim 2 \times 10^{-6}$ fC/ns and is one time bin in duration. The induced-ion signal, shown in (c), is of amplitude $\sim 10 \times 10^{-6}$ fC/ns with a tail that decays exponentially over $\lesssim 10$ μs. These simulations indicate that the majority of the signal is induced as the avalanche ions drift away to the nearby field wires or to the cathode.

2.1.4 Terminology in Regards to Signals

For the analysis presented in this work, several terms are used to describe the signals which are read out from the detector and how they are grouped. Only the signals from the anode wires will be subjected to analysis later in this work, Section 3.2.5. While the signals from the field wires can also be read out, for some of the runs large portions of the field wire data was not read out. Due to this and due to the fact that the field wire data is not essential to proceed, no work will be performed with field wire data. Specifically, five terms will be used which are *trace*, *signal region*, *event*, *track*, and *hit*.

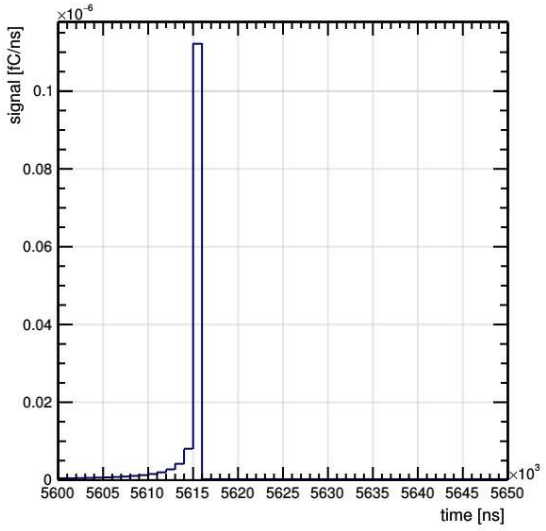

(a) Single anion induced signal

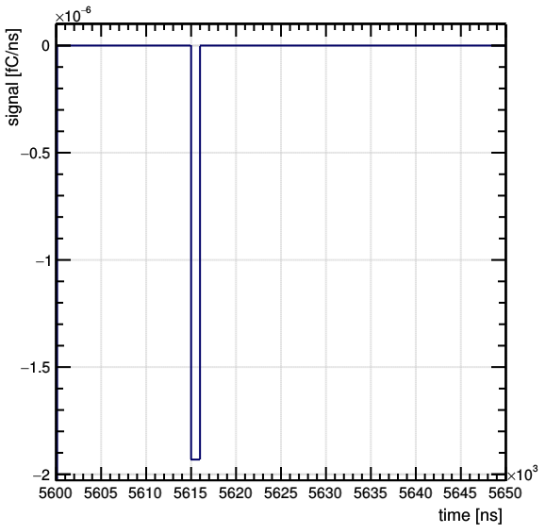

(b) Avalanche electrons signal

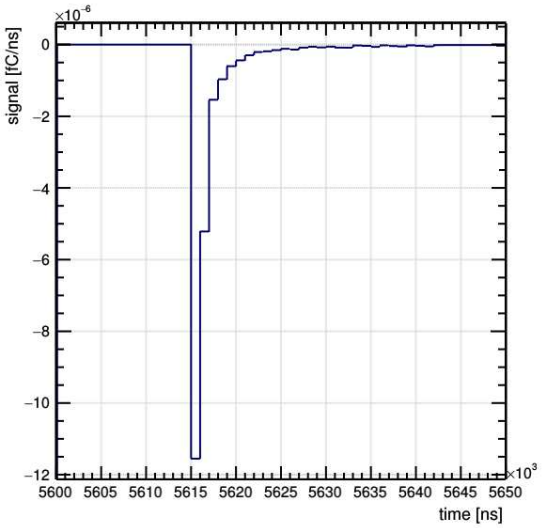

(c) Avalanche ions induced signal

Figure 2.8: The signal, current, on a single anode wire has been simulated using Garfield [112]. Plotted are three contributions to the signal. In (a) the induced signal from a single approaching anion is shown, and it is an overestimate as described in the text. The signal from the avalanche electrons (b) and the induced signal from the avalanche ions (c) are also plotted. The latter constitutes the majority of the overall signal.

To summarize, the detector may be *run* in two different modes, either triggered or untriggered. The data for each *run* is grouped into *events*. Each *event* may be composed of one or more *tracks*. A track nominally corresponds to the trail of ionization deposited in the detector by one incident particle; such as due to a neutron, alpha, or gamma when the detector is exposed to an ^{55}Fe source. A spark, as will be described in Section 2.2.1, can also be classified as a type of track. If, for

instance, two particles deposit trails of ionization relatively close to each other in time, the two tracks could be grouped logically as an event, later in analysis it may then be possible to separate the event into two tracks, one for each particle. Each *track* may *hit* one or more wires. The digitized data values collected for a given wire over a period of time is the *trace* for that wire. If the *hit* results in a signal abovFe a predetermined threshold, then a *signal region* will be determined within the *trace* associated with that *hit*.

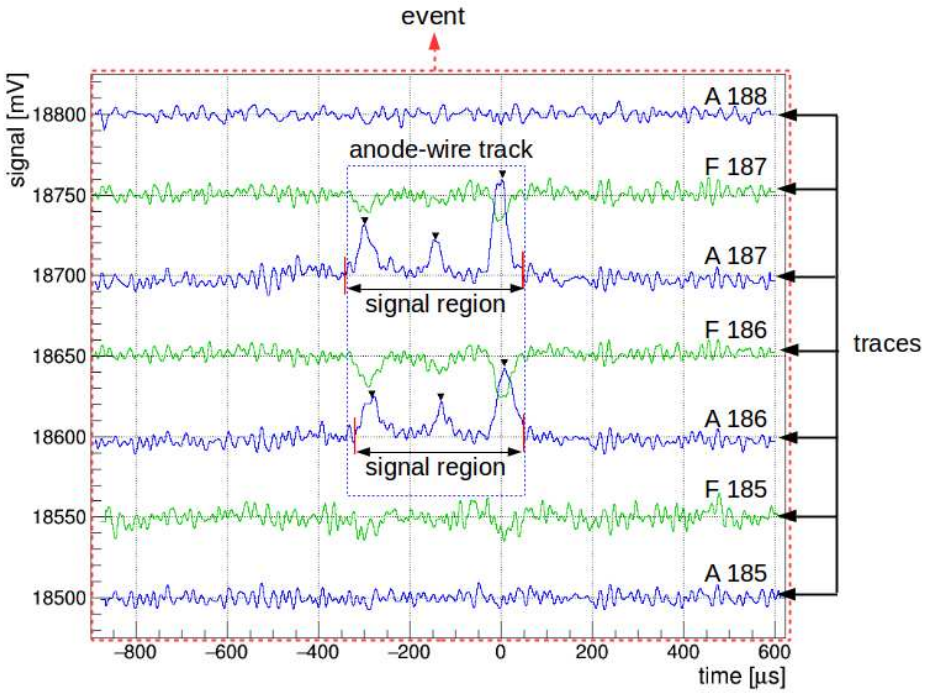

Figure 2.9: An example event is shown. The *event* itself encompasses all that happens within this time window. Seven *traces* are plotted. Anode and field wires are labeled A and F, respectively. *Signal regions* are present for two anode wires implying these two wires were *hit*. Since the two signal regions overlap, this event is a two-anode-wire *track*. For the record, this is event 5461 of drift2e-20170525-05-0001.

As an example, a single event that contains a two-anode-wire track signal is shown in Figure 2.9. The event was collected in triggered mode, see Section 2.1.5, which simply means that at least one of the pulses shown exceeded a fixed hardware threshold. The signals versus time have been offset from each other for clarity. In total seven signal versus time plots are displayed, each one of these is known as a trace. The blue traces correspond to anode wires and the green traces

correspond to field wires. Specifically, starting from the bottom and moving upward, the traces shown were collected for wires: anode 185, field 185, anode 186, field 186, anode 187, field 187, and anode 188. The signals have been processed using the methods described in Section 3.2.5. The combined main peak and minority peak signal regions, as picked out by automated analysis, are marked with red-vertical lines. Upward-going peaks are apparent for anode wires 186 and 187. The signal structure is consistent with the minority peak structure discussed in Section 2.1.2. Corresponding downward-going peaks are apparent for the field wires. These signal regions for these two traces overlap in time, are on adjacent wires, and thus are classified as a track. A dashed-blue outline encompasses the anode-wire track signal. This track was observed when the detector had been exposed to a neutron source. An interpretation of this track is as follows. A source neutron resulted in a nuclear recoil with the target gas within the volume of the detector. A track of ionization was deposited resulting in the formation of at least three varieties of anions. The anion species, of unique drift speeds, arrived at the LMWPC and produced signal pulses separated in time. The signal amplitudes appear slightly larger for anode wire 187. Since more ionization is expected to be deposited at the tail(start) of the track in comparison to the head(end), this track may have been moving downward through the detector. This is consistent with the fact that the source was placed above the detector at this time. Further, the I peak (largest amplitude peak), for anode wire 187 appears to be slightly earlier in time than the I peak of anode wire 187, indicating that the tail of the track may have been oriented such that the tail was slightly closer to the LMWPC. Described here is a single event, the terminology is elucidated further below.

Trace: The signal, read out in units of mV, from a single anode or field wire with respect to time. Each trace is composed of 1500 bins of data sampled at 1 μs intervals. In this work, traces which are blue (and have positive going signals) represent anode wires and traces which are green (and have negative going signals) represent field wires.

Signal Region: A trace may or may not contain an interaction signal. For instance the trace may consist only of the background noise on the line with nothing else. A signal region will be defined as the region in time surrounding the peak value of a signal pulse of a trace.

Signal pulses are in reality negative going for anode wires but inverted to be positive by convention, the converse is true for field wire signal pulses. To be recognized as a signal region, the pulse must surpass a threshold value and is picked out via automated analysis. This value is set in software and requires the pulse peak to be a set number of standard deviations out of the baseline noise level. The signal region extends both left and right of the peak until it sufficiently approaches the baseline (also known as pedestal) of the trace. A trace may contain more than one signal region. For instance, the signal regions about the various minority peaks and main peak may initially be picked out separately by the analysis software. These are later combined into a single signal region. In another scenario, a trace can have more than one signal region if more than one source of ionization results in a pulse on a specific wire over the time window for that trace. For instance, a nuclear recoil and an alpha could be observed in the same time window.

Event: The definition of an event depends on whether the detector is operated in triggered or untriggered mode, which are discussed in Section 2.1.5.

Triggered Mode: Each trace that has a signal region above the detector threshold then has an associated trigger time. Wires which do not produce a signal region above threshold have a time stamp that is the same as the adjacent wire which did trigger. An event is defined as all recorded traces which have time stamps which are within 1 ms of each other consecutively. To clarify, this does not mean that all timestamps must occur over a 1 ms time window, but it does mean the each trace of an event must be within 1 ms of at least one other trace of the event.

One could reasonably advocate for a shorter or longer event grouping time. The track of ionization deposited by a nuclear recoil within the detector is expected to be continuous, and if the track were to hit more than one wire the difference in trigger times depends on the ionization density along the track and the orientation of the track within the detector. Suppose two otherwise equal tracks deposit triggerable signals on more than one wire, if one track is oriented more parallel to the plane of the MWPC the trigger times of adjacent

wires will be closer to each other in time than a track which is more oriented along the drift direction. The ionization density, as observed in a signal, depends on how much of the nuclear recoil energy is deposited as ionization per step in path length and also how much the track straggles[19] as the nuclear recoil moves through the gas. The drift speed of anions in the detector is $\sim$50 m/s and the maximum drift distance for a track is 0.5 m, this implies a maximum drift time for a track is 10 ms. So, one may argue that 10 ms would be an appropriate event grouping time as it would allow one to contain all tracks which may be related in some way but spatially separated to be grouped together. One could alternatively support a shorter event grouping time. WIMP recoils, see Section 3.2.3, are expected to have energies enabling production of $\leq$ 6000 NIPs. The range of 6000 NIP C, O, and S recoils in the gas can be estimated, first one must convert the 6000 NIP ionization energy to recoil energies for each ion species, see Appendix B. This yields 179.5 keVr for C, 194.9 keVr for O, and 252.6 keVr for S. For each recoil species SRIM [107] was used to "fire" 1000 ions of the corresponding energies into 1 cm of 40:1.5 Torr CS_2:O_2 gas. Each ion was fired in the same initial direction (longitudinal) and the average longitudinal and radial ranges were recorded. Since the gas is homogeneous, the 1000 ions follow paths that possess cylindrical symmetry when studied as a whole. The radial range is the distance on average from the initial ion position to the final ion position measured perpendicular to the longitudinal axis. The average ranges were estimated by summing the average longitudinal and radial ranges with the Pythagorean theorem resulting in 6.38 ± 1.26[20] mm for C, 5.91 ± 1.27 mm for O, and 4.37 ± 1.16 mm for S. Adding 3σ to each mean range should account for > 99% of the recoils allowing one to estimate the maximum recoil ranges as 10.16 mm for C, 9.73 mm for O, and 7.87 mm for S. Based upon this, one could support the use of a shorter event grouping time which would correspond to the lengthiest expected recoil of relevant energy.

[19]Nuclear recoil tracks deposited in the gas are not straight.

[20]Uncertainties reported here are standard deviations of each population and not the uncertainty on the mean.

A grouping time of 220 μs would be sufficient and corresponds to an 11 mm drift distance within the detector.

With the above discourse in mind, it can be asserted that the currently used event grouping time is also a reasonable choice. Neutron recoils of interest have been measured with previous DRIFT-II detector iterations to have ranges of order a few millimeters [88] [81]. For the referenced papers, the former used 40 Torr CS_2 as the drift gas and the latter used 30:10:1 Torr CS_2:CF_4:O_2, compared to the 40:1.5 Torr CS_2:O_2 used in this work. Being that all three works use drift gases of similar pressure and gas composition, one can expect recoil ranges to be similar also. The chosen grouping time of 1 ms with a $\sim$50 m/s drift speed corresponds to 5 cm of track extent along the drift axis of the detector. The chosen grouping time is more than adequate to contain tracks which are millimeter-scale even if signal regions produced on some of the wires were to be lost during data acquisition.

Untriggered Mode: During untriggered mode all wires belonging to a given electronics box are read out simultaneously and constitute an event. If all wires are active for a given box this corresponds to 60 anode plus 60 field wires. Events are generated by sequentially reading out each active electronics box and then repeating. Further details, including rate, are provided in Section 2.1.5.

Track: The definition of a track also depends on whether the detector is operated in triggered or untriggered mode.

Triggered Mode: A track is a group of traces which have signal regions above some specified software threshold and are ordered logically in time. Let us consider signal regions on three adjacent anode wires 1, 2, and 3. Let each signal region have start times of t_{0i} and t_{fi}, respectively. If for instance $t_{01} \leq t_{02} \leq t_{03}$, $t_{02} \leq t_{f1}$, and $t_{03} \leq t_{f2}$, this would represent a signal which is ordered logically in time. Signals from nuclear recoils appear in this way. However, if $t_{02} < t_{01}$ and $t_{03} > t_{01}$, this would be indicative that more than one source of ionization and possibly more than one track is present. This could occur if a spark event (see

Section 2.2.1) directly preceded the signal of a recoil for wire 2 causing the identifiable signal region to extend to earlier times. An event may contain more than one track, the signals of which may or may not overlap in time.

Untriggered Mode: Each event is composed of up to 60 anode wires, first all signal regions on all anode wires are found. Those that overlap in time are tentatively tracks, then the same algorithm is applied as for the triggered runs to ensure the relative times of the signals are logical. As discussed in Sections 2.1.5 and 3.1, untriggered mode is used for energy calibration runs. These energy calibration events are known to deposit less energy in the detector than the nuclear recoils which will be of interest. Further it is expected that calibration events should result in tracks of one or two wires in length. As such, the software threshold is lower in comparison to triggered runs and untriggered tracks are only kept if ≤ 3 signal regions on adjacent wires compose the track.

Hit: A track of ionization deposited in the detector will drift toward the anode wires and result in an observable signal for those anode wires which are "hit" by the track. This term is meant to simplify the language associated with signal production, a detailed account of which is provided in Section 2.1.3.

2.1.5 Modes of Operation and Data Persistence

The detector can be operated in two different modes, triggered and untriggered. The mode of operation depends on the type of run being performed with the detector. For calibration runs, discussed in Section 2.3, the detector is operated in untriggered mode. This is done since the observable event rate for calibration runs is relatively high. One may expect to observe several signals from different calibration events occurring in the detector all within the same window of time. It is therefore more efficient to take snapshots in time of the signals for a group of wires within the detector and then search through these snapshots and pick out the signals. For neutron runs or if WIMP search runs are performed, the detector is operated in triggered mode. Here a hardware threshold on the signal amplitude is set such that if this threshold is surpassed the data acquisition

is triggered. Neutron runs are performed to better understand what signals from WIMPs may look like with the detector. For neutron/WIMP runs triggered mode is used since the interaction cross section of these particles in the detector is small hence a low event rate is expected. Operating in an untriggered mode for these runs would result in the collection of an abundance of data that contains no neutron/WIMP events and would be cumbersome to store and analyze.

For each of the two run types, raw-binary-data files, known as ndd files are generated. A full ndd file contains 50,000 anode wires traces with the corresponding 50,000 field wire traces. Once this limit is reached, the current file is saved and a new file is opened for the run. For each trace recorded, information is stored to identify it as an anode or field wire, its wire number within the detector, and the timestamp associated with that trace. The latter will be discussed in more detail below for each of the modes of operation, and how trace timestamps are reconstructed from the raw data data files will also be described.

Untriggered Mode: All 60 anode and 60 field wires belonging to a specific electronics box are read out over the same time period. All 120 wires have the same timestamp which corresponds to the time at which transfer to file is initiated. This timestamp is the TSI timestamp described for triggered mode below. In Section 2.1.6 it is stated that only boxes 0, 1, 2, and 3 have been instrumented on the left side of the detector. The set of four boxes are read out iteratively over a period of $\sim$1-2 ms. This implies that there are four unique timestamps over this couple-millisecond period, one for each box. A period of 1.37 s then elapses, on average, until the set of four boxes is read out again, equivalent to a read out rate of 0.73 Hz per set of four boxes[21].

Triggered Mode: Any anode wires that have signals which cross a hardware trigger threshold, for this work 20 mV, are stored. Triggered data runs are listed in Table 3.5 of Section 3.2.1. For 94.5% of the analyzed triggered runs, this trigger threshold is approximately double the size of the RMS noise. The timestamp of each is associated with the trigger

[21]These periods of time were determined by comparing timestamps from the first 10 files of untriggered run 20170519-05. Each file contained nearly 1120 events.

time[22]. We stored 900 1-μs bins pretrigger and 600 bins at trigger and after. For each anode wire which is triggered the field wire of corresponding number is also stored and receives the same timestamp as the anode wire. The neighboring anode wires which are directly adjacent to anodes which have triggered are also stored along with the corresponding field wire over the same time interval as that closest triggered anode. This triggering scheme is meant to allow for the complete containment of signals produced by tracks of ionization. The triggering scheme also allows one to search these neighboring traces which have not triggered at a reduced software threshold for any parts of the track which may have not crossed the hardware threshold. In this way the energy and range of a track can be best reconstructed.

At the time that data was taken, this triggering scheme was only available for all wires of a given electronics box. For instance, box 0 reads out anodes [0-59] and box 1 reads out [60-119]. If a track deposits enough ionization on anode 59 to trigger but not enough on wire 60 to trigger, the information on wire 60 will be lost since the triggering scheme does not extend across boxes. As such, these types of losses can occur at the three locations of the edge wires for the four boxes. During analysis, see Section 3.2.5, a cut *trackPassUpperAndLowerNeighborsCut* is introduced when classifying recoil-like tracks to ensure the signals that compose a track are well-contained within the traces of the event. This cut, in part, serves to reject tracks where information is lost at the electronics box junctures. As will be shown later, most nuclear recoil tracks of interest hit one or two anode wires; since each box spans 60 anode wires it is not expected that the loss of tracks at the box junctures will greatly reduce the total number of analyzable tracks.

For each triggered trace two timestamps are saved with it to the raw ndd file such that the real time RT at which the trigger happened can be reconstructed. RT is not an absolute timestamp, it is defined to be zero at the start of a run. Each electronics box has its own

[22]The timestamp is not always exactly the time at which the trigger threshold was crossed. This is due to the low-pass filter in the triggering circuit.

clock, these clocks are all synchronized at the beginning of a run. When a wire belonging to a particular electronics box is triggered and the trace is saved to file, a 24-bit timestamp TS, as measured by the clock for that box, is saved for that trace. A 48-bit computer timestamp TSI , at which data transfer to disk for that trace is initiated, is also saved. Each clock tick corresponds to 1 μs, which implies that TS resets every 2^{24} μs (16.78 s) and TSI resets every 2^{48} μs (3258 days).

At the beginning of a run $TS = TSI = 0$. Causally, $TSI \geq TS$. Let $TSI24 \equiv TSI \ modulo \ 2^{24}$, this corresponds to the number of clock ticks which have occurred since TS last reset. The real time of a trace can then be calculated as $RT = TSI - (TSI24 - TS)$. A visual representation of this calculation is provided in Figure 2.10.

As stated previously, RT is not absolute it is relative to the start of run. As of now, an absolute time for each trace can be estimated by using the creation time of the first file of a run as set by the file system of the computer writing the data to disk. However, this method is not robust, for instance this information could be lost if an original file is deleted, even if it has been backed up, since the creation time of the two files will not agree. As an improvement, one could instead write an absolute time stamp into the header of each raw data file that corresponds to the UTC date and time at which the file was created. For WIMP searches, absolute times are needed so that the direction of any ionization tracks which are deposited in the detector can be mapped onto the sky, if the WIMP wind exists one may expect a recoil distribution that points back to the constellation Cygnus.

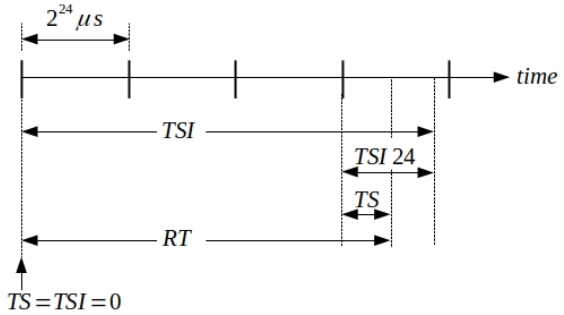

Figure 2.10: A visual representation of the trigger time stamp calculation for a trace.

2.1.6 Development Status of Detector

The DRIFT-IIe detector, which was in a phase of R&D, was not fully instrumented over the time period for which data was collected for this dissertation. Only the central 240 anode and 240 field wires were instrumented for readout as shown in Figure 2.11. Four electronics boxes were used to read out the wires. The electronics and readout modes are described briefly in Sections 2.1.1 and 2.1.5. Each box was capable of reading out 60 anode and 60 field wires. The wire numbering starts from zero from the bottom of the instrumented region. Anode wire 0 is bottom-most followed by field wire 0 above it, wire numbers increment as one moves upward with field wire 239 being top-most.

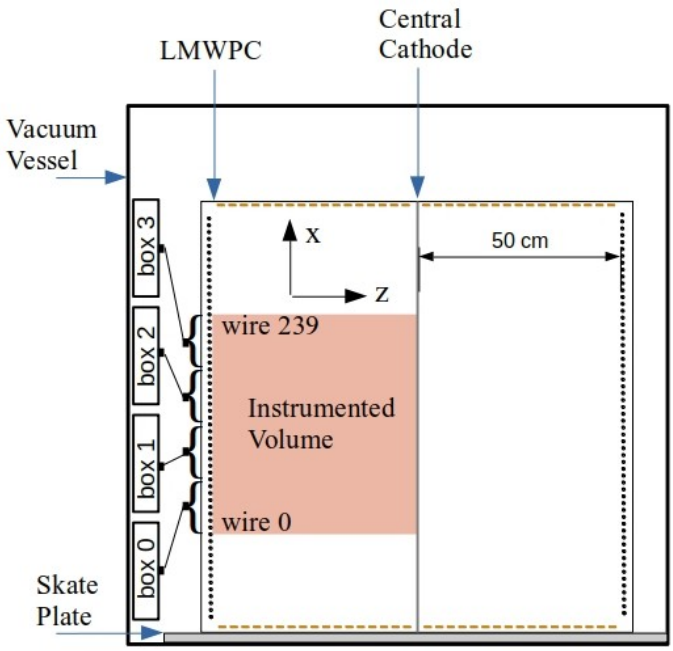

Figure 2.11: This schematic describes the state of the detector during the time data was collected for this dissertaton. It is not drawn to scale. Shown is a front view of the detector such that the wires of the MWPC are in/out of the page. The shaded region indicates the portion of the detector volume for which read out electronics were instrumented.

A loss in this target volume was incurred since not all electronics boxes were active for each run, in addition an active electronics box may have specific wires that were not active. Four wires of the LMWPC had broken and were removed. The readouts of several additional wires were masked

via software due to noise resulting in high trigger levels. These types of wires are termed dead wires, they are those for which readout is not available. Any wire for which readout is available, but is directly adjacent to a dead wire is flagged as a veto wire. Any track which deposits signal on a veto wire is cut since it is not known if the track extends to the adjacent dead wire. Any wires which are not dead wires or veto wires are termed active wires. This is discussed in more detail in Section 3.2.5. The electronics boxes that were active and the number of active wires for each run are listed, along with other run statistics, for triggered runs in Table 3.5, and for untriggered runs in Tables 3.1 and 3.2.

The active detector volume and target mass scales with the number of active anode wires n_{wires}. Each active anode wire is used to read out a volume of the detector that is approximately 0.002 m along $\hat{x}$ (the anode wire spacing), 1 m along $\hat{y}$ (the wire length), and 0.5 m along $\hat{z}$ (the length of the drift volume), netting a volume of 0.001 m^3. If all 240 anode wires were active this would correspond to an active volume of 0.24 m^3. For the triggered runs discussed later in this work, and reported in Table 3.5, it is shown that the number of active wires was 143 for several of the runs. So a more realistic estimate of the active volume is 0.143 m^3. For room temperature 40:1.5 Torr CS_2:O_2, the gas density is 0.169 kg/m^3 with constituent mass fractions of 0.828 for S, 0.156 for C, and 0.016 for O. For $n_{wires} = 143$, this results in a S target mass of 20.0 g, C target mass of 3.77 g, and an O target mass of 0.39 g.

2.2 Background Signals

Any non-WIMP interaction that can result in an amount of ionization that triggers the detector in WIMP-search mode is a potential background. Backgrounds have been well-studied and mitigated by the DRIFT collaboration over the years. It is assumed that the same technologies that allowed for DRIFT-IId to run in this low-background state can be applied to DRIFT-IIe. Understanding backgrounds is of essential importance when searching for rare events such as WIMP recoils. The study and mitigation of these backgrounds is not the main focus of this dissertation, as such, backgrounds will be discussed only briefly.

During a WIMP search run, DRIFT-IIe would be located deep underground to shield from cosmics. The detector would also be surrounded by polypropylene or water to shield from ambient neutrons. Both of these points have been discussed in Section 2.1.1. Running in a triggered mode, DRIFT-IId has been found to have a gamma rejection factor of 1.98×10^{-7}, assuming Poisson counting, at a confidence level of 90% [78]. The rejection factor was determined by exposing the detector to ^{60}Co sources, observing no events, and comparing to the number expected from GEANT4 [119] simulations. The distribution of energy deposited per unit of path length for gammas is differently shaped when compared to nuclear recoils, and not sufficient to trigger the detector.

Other backgrounds are the result of radioactive materials, such as uranium, contaminating components that comprise the detector and housing. The decay chain can lead to radon emanation into the detector volume. When an α decay occurs its partner nucleus can result in a nuclear recoil signal, which can be indistinguishable from that expected from a WIMP. These are termed Radon Progeny Recoils (RPRs) [99]. RPRs that are accompanied by an observed α particle are easily rejected since they leave tracks of lengths $\sim$200-600 mm in the detector [120], which are much longer than the millimeter-scale tracks expected from WIMPs.

Some RPRs were problematic. For example, ^{222}Rn can α decay to ^{218}Po within the volume of the detector. This particular decay can be identified by the accompanying α. The majority of the time after the previous decay, ^{218}Po is positively charged and will drift towards and deposit onto the central cathode. ^{218}Po will then α decay to ^{214}Pb. If the α is observed, the event can be identified as background. If the α ranges out in the material of the cathode and only the ^{214}Pb recoil is observed, it is a background indistinguishable from a possible WIMP event. The installation of a 0.9 μm thick thin-film central cathode, in DRIFT-IId, reduced the RPR background by reducing the probability of an alpha ranging out in the cathode material [93]. Following this, the RPR background was eliminated after O_2 was introduced to the DRIFT gas mixture. The presence of minority peaks in nuclear recoil signals and the resulting ability to fiducialize the detector volume along the drift direction, z, allows one to cut any events that occur close to the central cathode or

MWPCs. This discovery resulted in the first background-free operation of a directional DM search detector [77]. This search included 46.3 days of live time. Additional information in regard to DRIFT collaboration studies on backgrounds can be found in references [121] [122] [123].

Another background, sparks, are common in gaseous TPC detectors. Sparks were analyzed in this dissertation in order to understand properties of the DRIFT-IIe shaping electronics. This will be discussed in the following section.

2.2.1 Sparks and Study of the Shaping Electronics

Sparks: Any events that result in the deposit of ionization in the high-field region of the MWPCs result in signals distinguished by a sharp risetime due to the relatively instantaneous[23] avalanche of that charge; these are spark-like events. Spark-like events have more than one mechanism for production. Sparks are caused by electrical discharge within a MWPC. Other spark-like events are due to any particles which traverse a MWPC and result, at least partially, in a track of ionization in the vicinity of the wires. In this way, spark-like events are useful. The sharp risetime of signal provides a way to veto events which have passed through the MWPC and were not fully contained in the detection volume. Since these events are easily distinguished, they are not a problematic background for the DRIFT experiments and can be rejected during analysis. In this dissertation the term *spark* may be used loosely to encompass all *spark-like* events regardless of production mechanism.

A few typical spark-like events are shown in Figure 2.12. For each event, a likely assessment is given as to the identity of the event. Anode wires are shown in blue and field wires are shown in green. In (a), there are two sharp-upward-going anode pulses with risetimes of 3 μs. They are accompanied by a downward-going field wire pulse. The polarities on the anode and field wires are as expected for a real ionization event, so, this appears to be ionization that was deposited in the high-field region of the MWPC and quickly underwent avalanche. In (b), there is a large-upward-

[23]For wires of a proportional counter, avalanche typically occurs over fractions of a nanosecond. Subsequently, the avalanche electrons will move toward the anode wires also on time scales less than a nanosecond [108]. In comparison the shaping amplifiers for this detector have a peaking time of 3 μs.

going anode pulse, the flat top on this signal is indicative of the ADC being saturated. The two surrounding anodes have downward-going-induced pulses as do the field wires. This appears to be a spark event. In (c) all pulses on both the anode and field wires are upward-going. This is a hit to ground event in which a spark deposited current on ground changing the ground potential, as such amplifiers for all wires are temporarily biased in the same direction. In (d), a real ionization track crosses the bottom wires shown for this event, one will notice three upward-going-and-adjacent anode wires that have been saturated. All three of these traces have risetimes of 3 μs. Long tracks such as this are indicative of α particles. No minority peaks are visible due to the close proximity of the track to the MWPC.

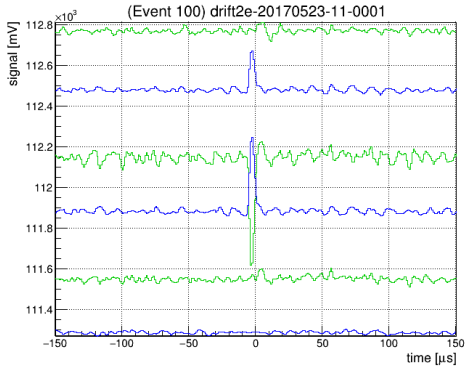

(a) Ionization Track Deposited Near the MWPC

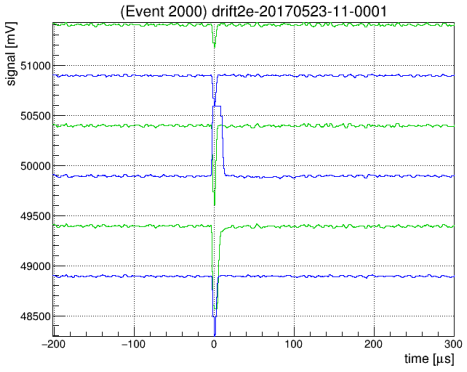

(b) Spark

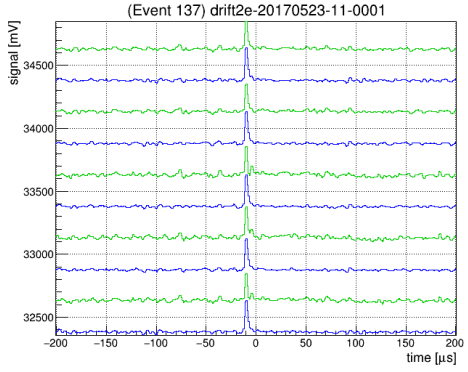

(c) Hit to Ground

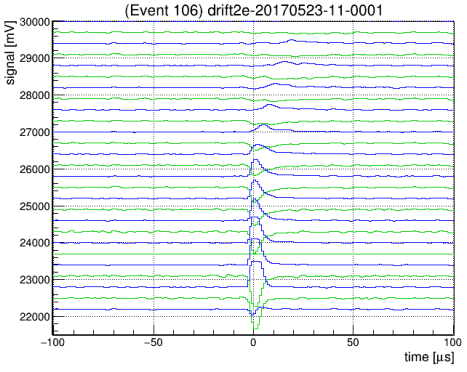

(d) α Particle Crossing the MWPC

Figure 2.12: Events which exhibit features that are spark-like. Further exposition for these events is provided in the text. The ranges on the vertical and horizontal axes are not the same for all plots and were chosen to best showcase the nature of each event.

Spark Selection and Analysis Method: Spark events which primarily deposit their charge near the wires of the MWPC will avalanche and result in a pulse of current for that wire which is much shorter in duration than the peaking time of the shaping amplifiers. These events approximate a delta function current input which can be used to measure the response of the shaping amplifiers. The peaking time of the shaping amplifiers is 3 μs, but the exact relationship between the between the peaking time and shaping time for the amplifiers was not provided in the electronics specifications [94]. The distinction between peaking time and shaping time was previously discussed in Section 2.1.1. Spark events of this type recorded during triggered background runs can be used to measure the shaping time of the amplifiers. Signals from these spark events are selected by only accepting those which have a full duration in time consistent with the 3 μs peaking time of the amplifiers. The measurement of the amplifier shaping time is necessary to later understand the gas gain achievable by this detector.

A single spark event may occur over several wires, producing signals in the traces for each of those wires. This can occur in different ways, for example, if electrical discharge extends over the region of more than one wire or if a particle traverses and leaves a trail of ionization in the MWPC in a plane which is $\sim$parallel to the MWPC and $\sim$perpendicular to its wires resulting in spark-like signals on more than one wire. For this particular analysis, traces which have signals that overlap in time are not grouped into tracks. The shaping times are parameters individual to each wire. As such, one need not consider the fact that a single spark event may extend across several wires. It is the signal produced on each wire individually which should be analyzed, not the summed signal from all of those in the event. For simplicity, only those traces which were found to have a single identifiable signal region were analyzed. For instance, it is possible to observe a signal from an alpha event later followed by a spark which would produce two separate signal regions on the same trace. Traces of this type with multiple signal regions are ignored and doing so should not affect the results other than in a mild loss of statistics.

A simple analysis to measure the shaping time of the amplifiers proceeds in the following manner for each trace recorded to file during a triggered background run. Only the signals produced

on the anode wires are considered. The pedestal, also known as baseline, is identified and subtracted and the standard deviation of the noise about the pedestal value, σ_{noise}, is determined. For clarity, the pedestal is defined by the regions of the trace outside of any identified signal regions. A trace with no signal pulses is baseline, or pedestal, only. Signals on the anode wires are positive by convention. The max value belonging to the trace is found and identified as a peak if its amplitude is $\geq 5\sigma_{noise}$. The signal region about the peak is identified by moving bin-by-bin on each side of the peak until the zero level of the trace is found. With a first peak and signal region identified, the process is repeated until all signal regions within the trace are found. As discussed in the preceding paragraph, only those traces with a single signal region are analyzed. Next, the risetime and falltime of the signal are calculated. The risetime here will be defined as the time it takes the signal to rise from 10% of the peak value to the full peak value. Similarly, the falltime is defined as the time it takes for the signal to fall from the full peak value to 10% of the peak value. Both risetime and falltime are measured from bin-center to bin-center. The shapers are reported to have a semi-Gaussian response and peaking time of 3μs. The tails of a Gaussian integrated beyond which the signal has fallen below 10% of the peak value only contain a combined 3.2% of the area, so, a choice of 10% should guarantee that most of the signal is captured. For those signals which are similar in amplitude to the analysis threshold of $5\sigma_{noise}$, the signal level at 10% of the peak height will have already dropped below the point where the signal will be distinguishable from the noise and thus the search for the boundaries of the risetime and falltime will be halted.

The summed risetime and falltime will be used as the total width in time of the signal. For a peaking time of 3 μs, it is reasonable to expect the signals of interest to be about double this value. Since the data has 1 μs bins, which is rather coarse for this particular measurement, it was decided to cut signals which are > 8 μs in total width.

Measurement of Shaping Time and Pulse Gaussianity: For each triggered background run, the first file for that run was analyzed using the method outlined above. The results are reported in Table 2.1. It can be seen for all runs that the measured risetime of these signal regions is on average $\sim$1 μs less than the falltime, showing that the impulse response is not exactly Gaussian.

It is seen that the average risetime across all runs is 3.03 $\pm$ 0.03 μs which is consistent with 3 μs peaking time reported in the specifications for the shaping amplifiers. With the peaking time of the amplifiers confirmed, it shows that the signals which have been selected for analysis here are good approximations to impulse inputs to the readout electronics. These signals will therefore be used to measure the shaping time of the electronics.

Let each time bin of the signal be indexed by i, the integral of each bin of the signal be designated by S_i, and the total integral of the signal be S. The mean in time $\langle i \rangle$ of each signal and standard deviation, shaping time, σ_{shape} were then found in the following way.

$$\langle i \rangle = \frac{\sum_i S_i i}{S} \qquad \sigma^2_{shape} = \frac{\sum_i S_i (i - \langle i \rangle)^2}{S}$$

This method was chosen over a measurement of the FWHM of each signal since the width of the time bins are rather coarse in comparison to the value being measured. The measured shaping times are also reported in Table 2.1.

Table 2.1: The first file of each run reported in the first column was analyzed using the method described in the text. The number of spark-like signal regions, average risetime, average falltime, and mean shaping time are reported. Values in parentheses indicate the standard deviation associated with each distribution and not the uncertainty on the mean[24].

Run	$\Delta_{t_{run}}$ [s]	N	t_{rise} [μs]	t_{fall} [μs]	σ_{shape} [μs]
20170511-27	754	2968	2.89 (0.73)	3.66 (0.89)	1.36 (0.24)
20170517-45	3413	507	3.09 (0.57)	4.03 (0.79)	1.46 (0.20)
20170523-11	2331	9492	3.00 (0.32)	4.10 (0.47)	1.44 (0.09)
20170525-04	2864	4726	3.02 (0.32)	4.12 (0.47)	1.45 (0.10)
20170526-21	1436	343	3.07 (0.58)	4.33 (0.76)	1.52 (0.18)
20170530-05	3359	1027	3.13 (0.48)	4.23 (0.78)	1.51 (0.17)
20170531-04	3213	3375	3.03 (0.33)	4.16 (0.56)	1.46 (0.12)
20170601-02	2290	5296	3.01 (0.34)	4.03 (0.50)	1.43 (0.11)
$average$			3.03	4.08	1.45
σ			0.07	0.20	0.05
$\frac{\sigma}{\sqrt{8}}$			0.03	0.07	0.02

With the amplifier shaping time tabulated, the focus is now to further scrutinize the impulse-input signal shape and the the amplifier gain. Two effects may contribute to the shape of the signals here, both the semi-Gaussian nature of the shaping electronics and how the signal actually formed must be considered. Electrons created during avalanche will move toward the anode wire typically on timescales $\ll 1$ ns. However, the majority of the signal on the wires is induced, as previously discussed in Section 2.1.3, by the ions created in the avalanche drifting away over much longer timescales. This will cause the induced signal to decay with time yielding a signal which is asymmetric in shape. Being that the peaking time measured here is consistent with what is expected from the shaping amplifiers alone seems to suggest that the majority signal production mechanism occurred over a time scale small enough to approximate a delta function input. For this work, instead of investigating how much each of these two effects contribute to the non-Gaussian shape of the signal, first it will be shown that the integral of each signal while not Gaussian is well approximated by that of a Gaussian, and second the spark signals measured here will be used to understand the response kernel from these two effects combined. The kernel potentially provides a useful starting point for investigations into deconvolution of real data traces as well as providing a measure of the electronics response which could be applied in simulation work.

Let A_S be the amplitude or maximum value of each signal. Using A_S along with the standard deviation of the signal σ_{shape} the expected integral of the signal can be calculated assuming that the signal is Gaussian.

$$S_{Gaussian} = A_S\sqrt{2\pi}\sigma_{shape}$$

For each signal in a run several quantities were calculated to understand how the measured integral compares to that expected from a Gaussian signal. For these quantities S_{rise} is the integral of a signal over its risetime and S_{fall} the integral over the falltime such that $S = S_{rise} + S_{fall}$. The averages of all calculated quantities for each run are reported in Table 2.2.

[24]For instance, the t_{rise} distributions are skewed right. This is not remarkable because the lower bound is fixed by the expected risetime minus the spread due to manufacturing tolerances. However, not all sparks selected by the analysis will be equal in how well they approximate an impulse current input to the amplifiers. So, one would expect to observe a tail on the right of the distribution.

Table 2.2: Comparisons of the actual integral of a spark signal in comparison to that of a Gaussian which has the same amplitude and standard deviation as that spark signal. All values are described in the text. Values in parentheses indicate the standard deviation associated with each distribution and not the uncertainty on the mean.

Run	$\frac{S}{S_{Gaussian}}$	$\frac{S_{fall}}{S_{rise}}$	$\frac{S_{rise}}{S_{Gaussian} \div 2}$	$\frac{S_{fall}}{S_{Gaussian} \div 2}$
20170511-27	1.080 (0.072)	1.326 (0.475)	0.969 (0.214)	1.192 (0.210)
20170517-45	1.048 (0.050)	1.306 (0.415)	0.940 (0.183)	1.156 (0.176)
20170523-11	1.023 (0.035)	1.300 (0.419)	0.917 (0.159)	1.128 (0.164)
20170525-04	1.028 (0.037)	1.327 (0.387)	0.906 (0.144)	1.150 (0.158)
20170526-21	1.058 (0.050)	1.423 (0.436)	0.902 (0.167)	1.215 (0.184)
20170530-05	1.051 (0.052)	1.318 (0.420)	0.937 (0.177)	1.165 (0.176)
20170531-04	1.028 (0.046)	1.314 (0.386)	0.911 (0.146)	1.145 (0.157)
20170601-02	1.035 (0.045)	1.287 (0.378)	0.928 (0.147)	1.143 (0.165)
$average$	1.044	1.325	0.926	1.162
σ	0.019	0.042	0.022	0.029
$\frac{\sigma}{\sqrt{8}}$	0.007	0.015	0.008	0.010

The three rightmost columns of Table 2.2 accentuate the non-Gaussian nature of the signals. For all runs the integral over the falltime is on average larger than that over the risetime by 32.5%. It is also shown that the integral of the signals over the risetime is on average 92.6% of that you would expect from Gaussian signals, similarly, the integral of the signals over the falltime is on average 116.2% of what you would expect from Gaussian signals. The results show that signals measured here are in general skewed right. Despite this fact, the second column of the table indicates that $S_{Gaussian}$ is a good approximation for the integral of each signals. Across all runs, the measured integrals S are on average 4.4% larger than $S_{Gaussian}$.

Shaping Response Kernel: The spark signals can also be used as a measure of the shaping electronics response kernel to an impulse charge input. This is particularly useful for purpose of simulation. Measurement of each kernel bin or weight w_i for a spark signal is the the integral of each bin of a spark signal S_i relative to the total integral of the spark signal S, $w_i \equiv \frac{S_i}{S}$. The kernel was measured to be eight bins in length and will be labeled with $0 \leq i \leq 7$. The average w_i were determined for each run with values reported in Table 2.3. The best estimate of the response kernel is given by the average of each w_i over all runs, resulting in $w = [0.015, 0.085, 0.210, 0.267, 0.220, 0.126, 0.053, 0.025]$. It can be seen that the weights sum to a

value of 1.001 which is consistent with unity within uncertainty. For purposes of simulation, one may choose to adjust the value of $w_0 = 0.015 \rightarrow 0.014$ since it has the largest relative uncertainty and would allow the kernel weights to sum to one.

Table 2.3: Measurement of the average bin-by-bin response of the shaping electronics to spark inputs. Each w_i represents one bin of the response kernel. The sum of all kernel weights is given in the rightmost column.

Run	w_0	w_1	w_2	w_3	w_4	w_5	w_6	w_7	$\sum_i w_i$
20170511-27	0.020	0.079	0.212	0.279	0.231	0.125	0.042	0.027	1.015
20170517-45	0.020	0.086	0.208	0.267	0.219	0.124	0.053	0.026	1.003
20170523-11	0.011	0.085	0.215	0.273	0.219	0.122	0.049	0.023	0.998
20170525-04	0.012	0.084	0.211	0.269	0.221	0.126	0.053	0.023	0.998
20170526-21	0.019	0.085	0.197	0.252	0.218	0.135	0.066	0.028	0.999
20170530-05	0.017	0.091	0.208	0.256	0.213	0.127	0.059	0.028	0.998
20170531-04	0.012	0.086	0.211	0.267	0.220	0.125	0.052	0.024	0.997
20170601-02	0.012	0.086	0.215	0.272	0.221	0.123	0.049	0.022	1.000
$average$	0.015	0.085	0.210	0.267	0.220	0.126	0.053	0.025	1.001
σ	0.004	0.003	0.006	0.009	0.005	0.004	0.007	0.002	
$\frac{\sigma}{\sqrt{8}}$	0.001	0.001	0.002	0.003	0.002	0.001	0.003	0.001	

Shaper Gain: The total amplification of an observed signal is the product of the gain during avalanche with that of the shaping electronics. To understand the gas gain one must first know how much amplification the shaping electronics contribute to the measured signal. This is the reason σ_{shape} has been measured here. Since the measured peaking time of the signals here matches that reported for the shapers and since $S_{Gaussian}$ closely approximates the measured integrals shown in Table 2.2, σ_{shape} = 1.45 $\pm$ 0.02 μs will be used as the as the shaping time of the amplifiers for any further calculations that require this value.

The shaping electronics were set to produce a signal of amplitude 25 mV per 1 fC impulse charge input. The gain of the shaping electronics can be estimated by assuming that signal produced by the shapers is Gaussian, and using the value measured for σ_{shape} to calculate the integral.

$$G_{shape} = (\frac{25 \text{ mV}}{\text{fC}})\sqrt{2\pi}\sigma_{shape} = 90.9 \pm 1.3 \frac{\text{mV}\cdot\mu\text{s}}{\text{fC}}$$

The measured spark kernel weight when the signal is at maximum amplitude is $w_3 = \frac{S_3}{S} = 0.267 \pm 0.003$. Let S_3 have an integral of 25 mV·μs to correspond to the known shaper signal amplitude for a 1 fC input. Comparing to the calculation of G_{shape}, this implies[25] $\frac{1}{w_3} = \sqrt{2\pi}\sigma_{shape}$. Using the values measured above, $\frac{1}{w_3} = 3.75 \pm 0.04$ and $\sqrt{2\pi}\sigma_{shape} = 3.63 \pm 0.05$. The latter calculation was made unitless by absorbing the units of time into that of the amplitude term for the calculation of an integral. These two values are consistent just outside of 1σ, neglecting any uncertainty in the 25 mV/fC shaper amplitude gain, with the former being larger by 3.3%. This reaffirms that the shaper response can be sufficiently modeled as Gaussian. Calculation of the gas gain further involves knowing the size of signals produced on average by a calibration source. For the DRIFT experiments calibration is performed with gammas emitted from an ^{55}Fe source. Gas gain will be the topic of Section 3.1.2.

Concerning Table 2.1, rates were purposely not tabulated. Several factors can affect the rate of sparks observed in the detector. Firstly, the number of wires active for each run was not constant among runs. This is partly due to the fact that the detector was still in development during the runs and the four electronics boxes, previously discussed in Section 2.1.6, were not all active for each run. Further, readout for wires of particular run can be masked via software, for instance if they were triggering more frequently than other wires, and this set of masked wires was not the same among runs. Differences in the gas mixture between runs could also influence the spark rate. For actual dark-matter-search runs, the control of the gas mixture in the vessel would be automated and the gas would actually flow through the detector at a slow rate to avoid any degradation of its properties. For these runs the vessel was filled manually by letting 40 Torr of CS_2, followed by 1.5 Torr of O_2, into the vessel and monitoring each of these changes in pressure by eye. This gas was then used without any flow for the duration of that run. Even though efforts were made to do this carefully, one would expect more variation among gas fills than if an automated system specifically designed to monitor the gas was in use. The quality of the gas is also affected by how

[25]This equality is not strictly true since the amplitude A_S of a signal which is assumed to be continuous is essentially being equated to the height of a discrete bin of integral S_3.

long the detector has been allowed to outgas inside of the vessel and how many times the vessel has been pumped out compared to other runs. For instance some of these runs were performed the day following the vessel being opened and others were performed a few days after being opened and had been filled with gas and pumped out a few times. Variations in the gas may affect how often it breaks down and leads to sparking. Variation of the cathode and field wire voltage will also affect the spark rate. The cathode voltage was held constant at -30 kV to within one volt and the field wire voltages for these runs were in the range of -894 to -900 V. Finally, since the detector was opened a few times over the course of these runs for repairs, physical changes within the detector, for instance an unintentional introduction of dust, could affect the spark rate. For the reasons above, rates here should not be compared directly without carefully trying to understand the differences in the conditions between runs.

2.3 ^{55}Fe Energy Calibration

To calibrate the end-to-end response of the detector to ionization, it is exposed to a source of photons of known energy. ^{55}Fe is utilized as the source of calibration photons for the DRIFT-IIe experiment. The distribution of signals observed corresponds to the energy of the photons folded with the detector response. DRIFT-IIe signals are read out in units of mV, and the width of each signal bin is 1 μs, so, each ^{55}Fe event deposits a certain amount of energy in the detector collected in units of mV$\cdot\mu$s. The calibration constant which relates the mean energy of the photons entering the detector to the area of the signals in units of mV$\cdot\mu$s can be determined. One can then apply this constant to the integral of the signal produced by a nuclear recoil to determine how much energy was deposited in the detector. This energy is the amount of energy deposited in the detector in the form of ionization only. It is typical to label the amount of electron equivalent energy deposited from a nuclear recoil in the detector with units of keV$_{ee}$ to distinguish it from the full recoil energy of a nucleus with units keV$_r$. A nuclear recoil within the gas has some true initial energy keV$_r$. However, in this detector energy is measured by the amount of ionization produced along a nuclear recoil track. So, the detector can only observe a portion of the initial energy keV$_{ee}$.

Energy that is deposited in the form of scintillation light is not detected. The ratio of keV$_{ee}$ to the total recoil energy keV$_r$ is known as the quenching factor and will be discussed later. The rest of the energy is lost to atomic motion or heat during collisions. A fraction of the ionization is also lost to recombination of ionization electrons with ions they were liberated from. This latter effect need not be considered here as the loss of ionization due to recombination could be folded into a measurement or careful simulation of the quenching factor.

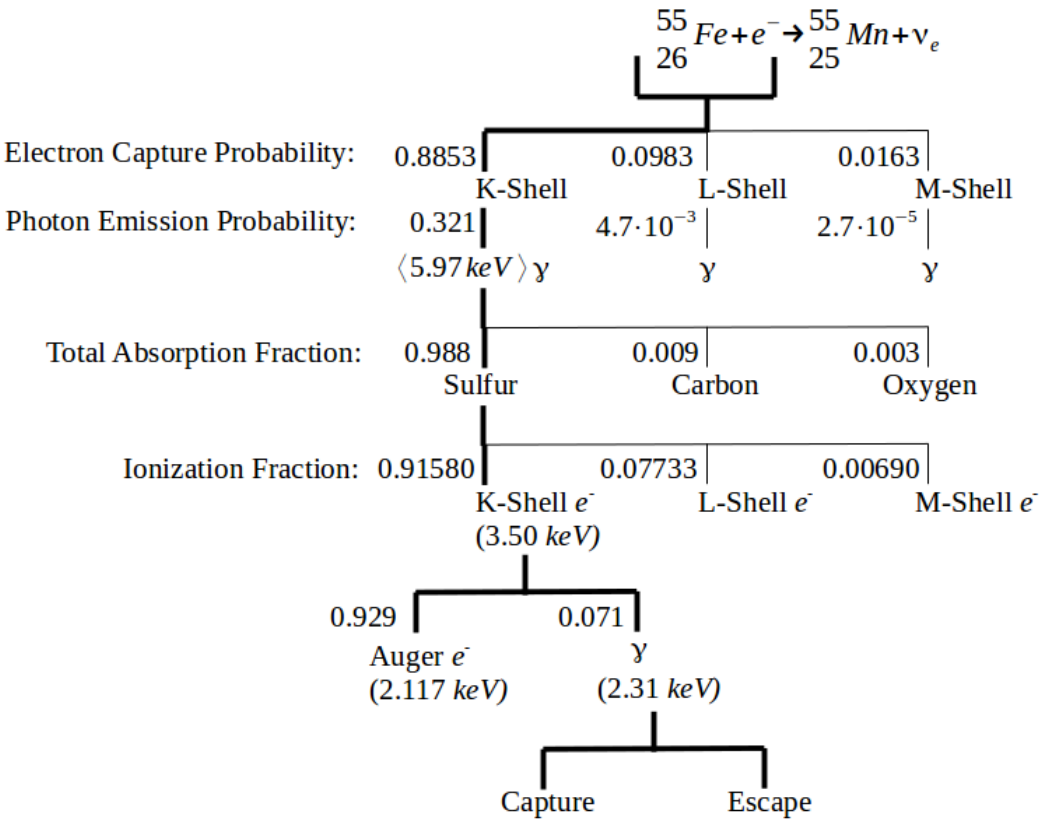

Figure 2.13: A tree diagram describes the processes by which signals are produced during ^{55}Fe energy calibration runs with the detector. The path that has been made bold corresponds to the primary process.

^{55}Fe decays by electron capture to ^{55}Mn with a half life of 2.747 years [124]. Figure 2.13 explains how this decay leads to the deposit of calibration energy within the detector. Previous works [125] [126] by DRIFT collaboration members contributed to the understanding of these

processes. The remainder of the section will provide the necessary context for the figure. The bold path of the figure follows the line of assumptions which are made.

K-shell capture is dominant with a probability of 0.8853. The filling of the vacant K-shell by an outer-shell electron is accompanied by the emission of one of a few possible x-rays with a probability[26] of 0.321 and of energies too similar to be resolved separately by DRIFT-IIe. The total emission probability resulting from K-shell capture is $0.8853(0.321) = 0.284$ per ^{55}Fe disintegration, and the mean[27] x-ray energy is 5.97 keV. The combined L-shell and M-shell electron capture probabilities are 0.0983 and 0.0163 with subsequent fluorescence probabilities of 4.7×10^{-3} and 2.7×10^{-5}, respectively. This nets a total probability[28] of L or M-shell fluorescence production of 4.6×10^{-4} per ^{55}Fe disintegration [124]. It is therefore a reasonable assumption that all photons result from K-shell capture and the source can be assumed to constitute, effectively, a monoenergetic x-ray source of mean energy 5.97 keV. It is common to see the emission energy of ^{55}Fe x-rays reported as 5.90 keV. This energy corresponds to that of the x-rays with the largest emission probability. Here it has been chosen to report the mean energy of 5.97 keV.

The 5.97 keV x-ray can interact with the gas in three ways. It can scatter coherently by which only the direction of the photon is changed, it can scatter incoherently otherwise known as Compton scattering, or photoelectric absorption can occur. Table 2.4 provides the interaction cross sections for an x-ray of this energy for each of the elements present in the gas. The dominant interaction that occurs is photoelectric absorption, made apparent by the absorption fractions.

The 40:1.5 Torr CS_2:O_2 gas mixture has a total density of 0.169 kg/m^3 with constituent mass fractions provided in Table 2.5. A total absorption fraction of 0.988 for S indicates that nearly all of the 5.97 keV photons that interact in the gas do so by means of photoelectric absorption with S.

---

[26]In the literature the term yield is often used instead of probability.

[27]A few different K-shell photons can be emitted, to find the average energy each K-shell photon energy was multiplied by its emission probability, all of these values were summed and then divided by the total emission probability of 0.284, resulting in a mean photon energy of 5.97 keV. Typically, an energy of 5.90 keV due to Kα x- rays only is reported as they are of similar energy and have the dominant emission probabilities.

[28] For clarity, 4.7×10^{-3} and 2.7×10^{-5} are the probabilities that a photon will be emitted after either L-shell or M-shell capture, respectively. The total probability of L or M-shell fluorescence is $0.0983(4.7\times10^{-3}) + 0.0163(2.7\times10^{-5}) = 4.6\times10^{-4}$.

Table 2.6 further indicates that the majority of photoelectrons produced in the process result from the K-shell ionization of S and account for a fraction of 0.9158 of the total ionization produced. For simplicity and by justification of the large K-shell ionization fraction, photons resulting from L and M-shell ionization will be neglected. Since the binding energy of the S K-shell electron is 2.472 keV [127], the photoelectrons are of energy 3.50 keV.

Table 2.4: Interaction cross sections for a 5.97 keV photon [128] and absorption fraction found by the ratio of the photoelectric absorption cross section for each element relative to the sum of all three interaction cross sections for that element. Cross sections are reported in units of cm^2/g which is the interaction probability per unit of target mass rather than per particle of target material where a cross section would be reported in units of cm^2. Multiplication by the density of the target material and taking the reciprocal conveniently nets the attenuation length.

Element	Coherent Scatter Cross Section $[\frac{cm^2}{g}]$	Incoherent Scatter Cross Section $[\frac{cm^2}{g}]$	Photoelectric Absorption Cross Section $[\frac{cm^2}{g}]$	Absorption Fraction
S	1.176	0.07922	213.3	0.994
C	0.2934	0.1101	10.71	0.964
O	0.5011	0.09997	27.52	0.979

Table 2.5: Elemental mass fractions for 40:1.5 Torr CS_2:O_2 gas mixture, weighted absorption cross sections calculated by multiplying each elemental mass fraction by the corresponding photoelectric absorption cross section of Table 2.4, attenuation lengths calculated by multiplying the weighted absorption cross section by the gas density and taking the inverse of that quantity, and total absorption fraction calculated by the ratio of the weighted absorption cross section for a given element relative to the sum of all three weighted absorption cross sections.

Element	Mass Fraction	Weighted Absorption Cross Section $[\frac{cm^2}{g}]$	Attenuation Length $[cm]$	Total Absorption Fraction
S	0.828	177	33.4	0.988
C	0.156	1.67	354	0.009
O	0.016	0.440	1.34×10^4	0.003
Totals		179	33.1	

Following photoelectric absorption in the K-shell, the S atom will quickly relax to a lower energy state in one of two ways, by the emission of an Auger electron with a probability of 0.929 [130] and mean energy 2.117 keV [131] [132] or by fluorescence with a probability of 0.071 and

Table 2.6: Theoretical ionization cross sections for a 6 keV photon interaction with sulfur [129].

	S K-shell Ionization Cross Section [b]	S L-shell Ionization Cross Section [b]	S M-shell Ionization Cross Section [b]	S Total Ionization Cross Section [b]
	1.0256×10^{4}	8.6602×10^{2}	7.7247×10^{1}	1.1199×10^{4}
Fraction of Total	.91580	0.07733	0.00690	

mean energy 2.31 keV [127]. Therefore, $\sim$93% of the ^{55}Fe x-ray interactions will result in the production of a 3.50 keV photoelectron followed by the emission of a 2.117 keV Auger electron. The sum of photoelectron energy (3.50 keV) and Auger electron energy (2.117 keV) does not sum to the total incident x-ray energy of 5.97 keV. This is due to binding energy. The S K-shell photoelectron kinetic energy is limited by its binding energy, 2.472 keV. Auger electrons from the $KL_{2,3}L_{2,3}$ process are emitted dominantly for S [133]. This denotes that the original vacancy left in the K-shell is filled by a second electron from the L_2 or L_3 shell and the energy difference from the relaxation process is transferred to a third electron also in the L_2 or L_3 shell which is then liberated from the atom. The kinetic energy of the emitted electron can be estimated from the difference in binding energies. That is, $KE = (E_K - E_{L_{2,3}}) - E_{L_{2,3}} = (2472\ eV - (\sim 163\ eV)) - (\sim 163\ eV) \simeq 2146\ eV$. In the preceding calculation, the leftmost term in parentheses corresponds to an electron from the L_2 or L_3 shell filling the K-shell vacancy. In doing so, the atom is an a lower energy state than previous to the transition, and this accounts for the energy to drive the Auger process. The kinetic energy available to the ejected Auger electron is the energy made available from the L_2 or L_3 shell to K-shell transition electron minus the binding energy of that Auger electron which is ejected. Binding energies are tabulated in [127].

The photoelectron and Auger electron will deposit their energy via tracks of ionization in the gas and since they are not spatially separated will appear as a single event. The measurement of these events nets a distribution of signals which correspond to the 5.97 keV ^{55}Fe x-ray energy being deposited in the detector and can be utilized for energy calibration. The remaining $\sim$7% of the ^{55}Fe x-ray interactions will result in the production of the 3.50 keV photoelectron followed by

the emission of a 2.31 keV x-ray with attenuation length[29] 23.4 cm. Since the 23.4 cm attenuation length is of order the dimensions of the detector two scenarios can follow. Firstly, the x-ray could leave the active volume of the detector and only the energy of the 3.50 keV photoelectron may be detected, resulting in a low energy escape peak in the ^{55}Fe signal distribution. Secondly, it is possible that the 2.31 keV x-ray will interact in the active volume of the detector and lead to a second track of ionization spatially separated from that of the 3.50 keV photoelectron producing a low energy capture peak. The escape and capture peaks typically overlap and have not been resolved separately in previous DRIFT experiments [126].

From the discussion above, one would expect the distribution of observed ^{55}Fe signals to be composed of a main peak corresponding to the 5.97 keV x-ray energy being deposited in the detector due to the K-shell ionization of S followed by the emission of an Auger electron. One may also expect to observe a second peak on the low-energy side of the distribution due to the escape and capture processes which should account for < 7% of the integral of the distribution.

The amount of energy deposited in the detector from ^{55}Fe x-rays can be measured in units of the Number of Ion Pairs (NIPs) produced on average. As a track of ionization is formed in the detector, each liberated electron results in an ion in the gas. Subsequently, the electronegative gas captures the electron resulting in an anion. This can be defined as an ion pair being formed in the gas. Since it is the anions which are drifted and result in signal production for the detector, it best to think of NIPs as the number of anions which are formed in the track. The NIPs formed is then proportional to the amount of energy deposited in the gas. The NIPs produced on average by ^{55}Fe x-rays in 40 Torr CS_2 has been measured [117].

$$NIPs_{^{55}Fe} = 237 \pm 7$$

[29]This value is the attenuation length of a 2.31 keV photon in 40:1.5 Torr CS_2O_2 considering photoelectric absorption only. Only photoelectric absorption was considered as it accounts for ∼99% of the total interaction cross section. This value was calculated in the same fashion as the total attenuation length of a 5.97 keV photon described in Table 2.5.

It will be assumed that this value is representative of the average NIPs one also expects to observe in a 40:1.5 Torr CS_2:O_2 gas mixture. This is justified in part by the fact that O_2 comprises only 1.6% of the gas by mass. More work needs to be done to understand the size of the effect that the addition of O_2 introduces. It has been suggested [77] that the addition of 1 Torr of O_2 to a 30:10 Torr CS_2:CF_4 gas mixture may result in a 1% change on the NIPs observed[30].

The average amount of energy that needs to be imparted to the gas to produce an ion pair is known as the W-value [134]. For a given target gas the W-value is dependent on both the particle type and energy of this particle incident on the gas. This can be understood since the cross section to produce ionization in the gas by liberating an electron from a particular atomic shell is energy dependent. For photons, of various energies and incident upon particular gases, it is suggested W-values are $\sim$constant [135] if the photon energy is much larger than the ionization potential of the gas. The 5.97 keV x-ray from the calibration source results in two electrons of energies 3.50 and 2.117 keV as stated previously. For comparison the ionization potential of CS_2 is 10.07 eV [136]. The W-value for ^{55}Fe x-rays in 40:1.5 Torr CS_2:O_2 can then be found by dividing the mean x-ray energy by the mean NIPs observed.

$$W_{55_{Fe}} = 25.2 \pm 0.8 \, \frac{\text{eV}}{\text{NIP}}$$

Let $\langle S_{55_{Fe}} \rangle$ represent the average signal integral collected by the detector in units of mV$\cdot\mu$s for ^{55}Fe x-ray events. Let S_r represent the signal collected for a single nuclear recoil. A calibration constant can be determined which relates the integral of a signal to a corresponding quantity of NIPs. The measurement of calibration constants is presented in Section 3.1.1.

$$NIPs_r = \frac{NIPs_{55_{Fe}}}{\langle S_{55_{Fe}} \rangle} S_r$$

[30]The value discussed in the referenced work [77] is actually the W-value, which is directly related to the NIPs observed on average

To determine the electron equivalent energy the NIPs collected for a recoil is multiplied by the W-value.

$$E_{ee} = W_{^{55}Fe} NIPs_r$$

Not all energy deposited in the detector from a nuclear recoil goes into the production of ionization. Only the component of the energy that does yield electrons can be measured by the detector. The remaining energy is not observed and goes into heat and scintillation. To reconstruct the true initial energy of a nuclear recoil E_r one must scale by the quenching factor q_r. In general, the quenching factor is dependent on the identity of the incident particle that leads to the production of ionization/scintillation in a medium as well as its energy.

$$q_r = \frac{E_{ee}}{E_r}$$

The amount of quenching is dependent upon the nuclear recoil species, the kinetic energy of the recoil, and the gas in which the recoil is traveling. In this work, the gas mixture is 40:1.5 Torr CS_2:O_2. The quenching factor as a function of nuclear recoil energy has been studied for sulfur recoils in 40 Torr CS_2 by measurement/simulation [137] and calculation [138]. Agreement between the two methods is reported in reference [138]. It is assumed that an approximate form of this quenching factor will provide reasonable values for this work since O_2 only accounts for 1.6% of the mass of the gas. The conversion of NIPs to nuclear recoil energy is further described in Appendix B.0.2. From the relationships above the energy of a recoil can be determined.

$$E_r = \frac{W_{^{55}Fe} NIPs_r}{q_r}$$

Chapter 3

Analysis of Data and Results

3.1 ^{55}Fe Runs

^{55}Fe runs used for energy calibration were performed in untriggered mode as described in Section 2.1.5. When possible, each neutron run performed was accompanied by a calibration run that occurred either directly before or after the neutron run. The amount of time available for the collection of the data was limited and thus it was not always possible to perform corresponding calibration runs. Also when possible, each calibration run was accompanied by an untriggered background run. One can compare events rates between untriggered background runs and the untriggered ^{55}Fe runs to verify that the events observed during calibration are in fact a result of ^{55}Fe exposure.

An isotropically emitting ^{55}Fe source was contained inside a shuttered enclosure. The enclosure was mounted inside the vacuum vessel such that it was approximately centered on the x-y dimensions of the detector and it was located $\sim$15 cm left of the LMWPC. Application of a voltage raised the shutter allowing x-rays to enter the detector volume.

3.1.1 Untriggered Data and Results

Two typical ^{55}Fe events collected in untriggered mode are shown in Figure 3.1. All observed tracks in the runs to be discussed hit one or two wires, with the vast majority of tracks hitting one wire. The raw signals are shown for each event as well as the signals after smoothing. The analysis chain that is applied to untriggered runs is presented in Section 3.1.3.

Results of untriggered background runs and ^{55}Fe runs are presented in Tables 3.1 and 3.2, respectively. Each run is designated by the date on which the run was performed followed by the run number for that day. The date format is YYYYMMDD. Each pair of runs with the same date were performed directly adjacent to another in time and for the same fill of gas mixture in the

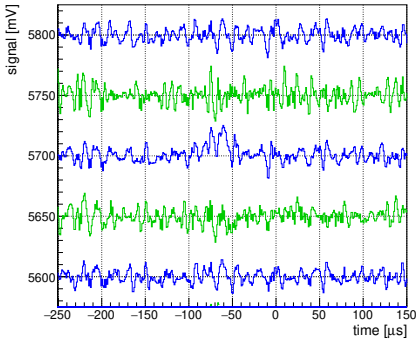

(a) Raw one-wire ^{55}Fe event.
(run 20170525-03-0002 event 87)

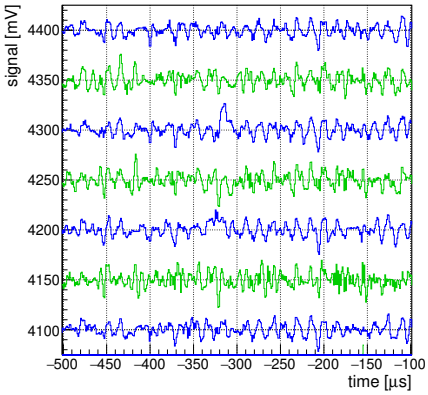

(b) Raw two-wire ^{55}Fe event.
(run 20170525-03-0002 event 195)

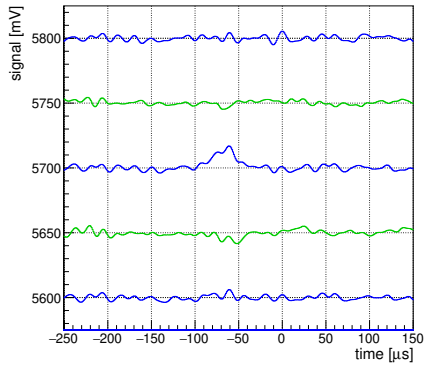

(c) Smoothed one-wire ^{55}Fe event.
(run 20170525-03-0002 event 87)

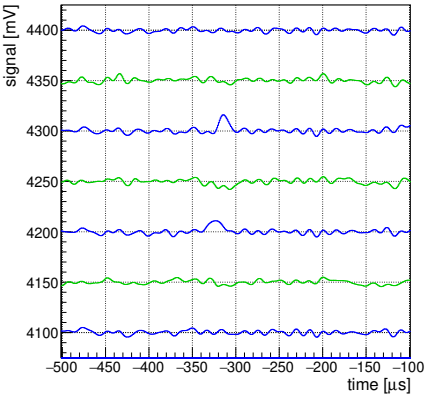

(d) Smoothed two-wire ^{55}Fe event.
(run 20170525-03-0002 event 195)

Figure 3.1: Two example ^{55}Fe events collected in untriggered mode. (a) and (b) show raw one-wire and two-wire events, respectively. Each event after smoothing is shown in (c) and (d). The blue lines correspond to anode wire signals and green the field wires. For clarity the traces have been offset vertically with respect to one another.

vacuum chamber. Care was taken to keep the cathode and field-wire voltages consistent among runs. Only a fraction of the 240 wires which were instrumented for readout were active for these runs. The number of active wires was not constant for all runs.

Table 3.1: A listing of untriggered background runs. The field-wire voltage, number of active wires, run duration, number of events, number of events that hit only one wire, event rate, and average baseline rms noise are tabulated. For every trace of a run, the baseline RMS noise is determined, all of these are then averaged for the run to determine $\langle\sigma_{noise}\rangle$.

Run	V_{FW} [V]	n_{wires}	$\Delta_{t_{run}}$ [minutes]	N	N_{1-wire}	$\frac{N}{\Delta_{t_{run}}}$ [minute^{-1}]	$\langle\sigma_{noise}\rangle$ [mV]
20170519-04	-900	160	94	6	3	0.06 ± 0.03	11.0
20170525-02	-895	143	45	0	0	0	8.29
20170526-05	-894	144	44	0	0	0	10.5
20170530-02	-894	143	46	2	2	0.04 ± 0.03	8.71
20170531-02	-896	143	28	3	2	0.07 ± 0.05	8.56
20170601-04	-896	143	74	5	5	0.07 ± 0.03	8.49

Table 3.2: A listing of untriggered ^{55}Fe runs. The field-wire voltage, number of active wires, run duration, number of events, number of events that hit only one wire, event rate, ratio of each ^{55}Fe rate to the corresponding background rate, and the average baseline rms noise are tabulated.

Run	V_{FW} [V]	n_{wires}	$\Delta_{t_{run}}$ [minutes]	N	N_{1-wire}	$\frac{N}{\Delta_{t_{run}}}$ [minute^{-1}]	Rate Ratio	$\langle\sigma_{noise}\rangle$ [mV]
20170519-05	-896	160	917	4344	4189	4.74 ± 0.07	79	10.8
20170525-03	-895	143	93	1445	1370	15.5 ± 0.4		8.35
20170526-06	-894	144	77	502	492	6.5 ± 0.3		10.2
20170530-04	-894	143	90	1117	1076	12.4 ± 0.4	310	8.70
20170531-03	-896	143	52	751	716	14.4 ± 0.6	206	8.70
20170601-03	-896	143	91	913	873	10.0 ± 0.4	143	8.70

The two 20170519 runs had $\sim$16 more wires active than the other runs. In the time between this run and the other five, the vacuum vessel housing the detector had been opened in order to make some repairs to the readout electronics. After repair, the vessel was filled with gas and detector started. Readout for each wire can be manually masked via software. Efforts were made at this

point to mask wires that were triggering at significantly higher rates than the others. Therefore, fewer wires are active in runs following 20170519-05. All six runs had 143 wires in common.

The event rates observed for ^{55}Fe runs are significantly higher than those for untriggered background runs, this is indicated by the rate ratios in Table 3.2. However, the event rate in background runs is non-zero. This indicates that at present the analysis software is not sufficient to suppress all backgrounds, or that some ^{55}Fe-like events are being observed in these runs. The clear difference between the background and ^{55}Fe rates suggests that the events observed for the latter runs do result from the ^{55}Fe source. For a statistical comparison, let it be assumed that exposure of the detector to the source has no effect on the observed event rate. Poisson statistics can be used to compare two of the untriggered runs, for instance the two 20170519 runs. The average number of events observed per minute for the untriggered background run was 0.06 which will be used as the mean for the Poisson distribution. The average number of events observed per minute for the untriggered ^{55}Fe run was 4.74. The Poisson probability of observing greater than or equal to four events over a minute is 5.1×10^{-7}. In order to interpret the significance of this value, for a Gaussian random process, sampling a value at least 5σ above or below the mean equates to a p-value of 2.87×10^{-7}. This result is inconsistent with the assumption that exposure of the detector to the source does not effect the observed event rate.

With regard to the ^{55}Fe runs, run 20170519-05 has an event rate lower than all other runs despite the fact that it had more active wires than the other runs. In addition, for the runs that do have the same number of wires, the event rates do not agree. It is likely that this disparity can be attributed to differing amounts of noise present in the system for the various runs. This is exemplified in Figure 3.2. A comparison of the RMS noise calculated for each anode wire for the two runs of highest and lowest observed event rate are shown. The noise for most wires of run 20170525-03 is smaller than for run 20170519-05. Since care was taken to keep the gas mixture, drift field, and field-wire voltages consistent between runs, one would expect the size of ^{55}Fe signals to be the same between runs. The analysis relies on the peak height of a potential signal in comparison to

that of the noise to be identified as a signal. Therefore, more ^{55}Fe events are missed for those runs which have more noise and the observed rates are smaller.

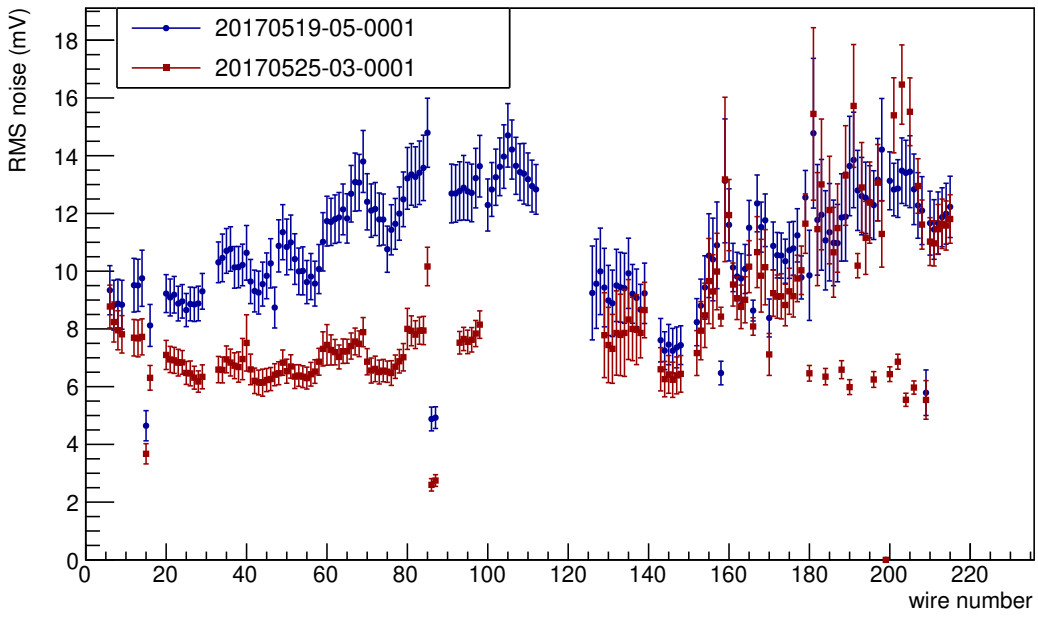

Figure 3.2: The RMS noise observed for each anode wire for runs 20170519-05 and 20170525-03 is shown. For run 20170519-05 each data point(set of error bars) represents the average(standard deviation) of the RMS noise found from the first 279 traces written to file for that particular wire. The same is true for the data points for run 20170525-03 except the results of 310 traces were averaged for each wire.

The distributions of observed signal integrals for all ^{55}Fe runs are shown in Figure 3.3. The distributions do not appear to be simply Gaussian. This can be understood, at least in part, by looking at the width in time of the signals at half maximum versus the total integral of the signals. To do this, *trackHalfMaxTimeCut* and *trackRiseTimeCut* as described in Section 3.1.3 have been removed from the analysis.

In Figure 3.4 two populations of events are seen and are separated by the horizontal dashed line which is drawn for a signal width at half maximum of 16 μs. The population of events that extends to large integrals and has half-maximum widths in time below 16 μs is spark-like events and may include MWPC events, which are events that occur in the high-field region near the MWPC. These events will necessarily be short in time since charge deposited in the high-field

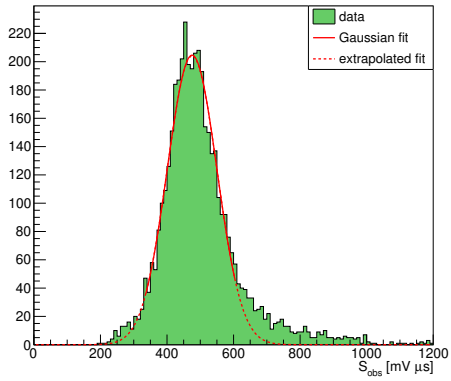

(a) 20170519-05

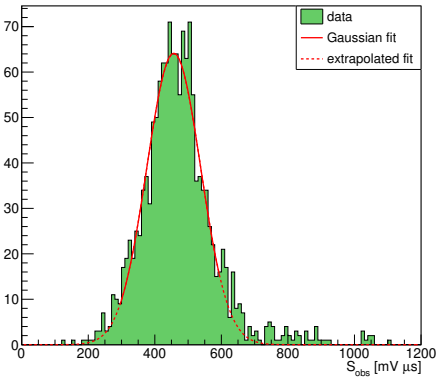

(b) 20170525-03

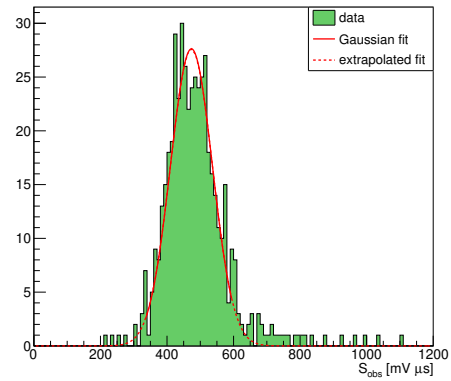

(c) 20170526-06

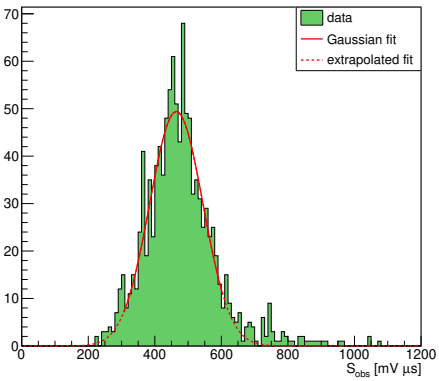

(d) 20170530-04

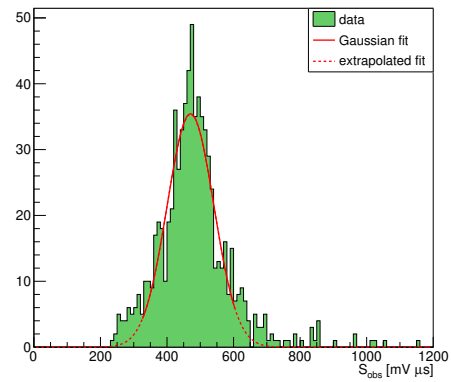

(e) 20170531-03

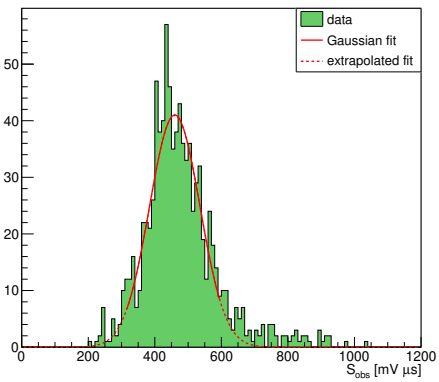

(f) 20170601-03

Figure 3.3: The distributions of observed signal integrals for each of the ^{55}Fe runs. Each distribution was fit via an automated routine. First a boxcar smooth of width 7 bins was applied to generate a smoothed histogram (not shown). The smoothed histogram was used to identify where the peak and quarter-maximum values on each side of the peak occur. After identifying the quarter-max width of each distribution, only this region of the unmodified histogram was fit with a Gaussian (solid-red curve). The fit extrapolated outside of the fit region is shown by the dashed-red curve.

region will rapidly undergo avalanche resulting in signal formation. When ionization is deposited in the high-field region, the avalanche process may not proceed in the same manner as it does for events that deposit ionization in the rest of the detector volume. For events that occur in the main detector volume, each electron liberated in the track is quickly captured by the electronegative gas and it is these anions which drift toward the MWPC. For avalanche to occur, the electron must be stripped from the anion once it reaches a region of large enough electric field near an anode wire. MWPC events which liberate electrons in the high-field region near the MWPC can begin avalanche before they are ever captured by the gas. The required field for avalanche is less than that required to strip the electron from one of the anions, and since the field near the wires drops off approximately inversely with the radial distance away from the wire, electrons deposited by MWPC events can initiate avalanche farther from the wire than an electron that is stripped from an anion. Therefore, avalanches initiated by MWPC events can have more doubling distances and hence more gain resulting in larger observed integrals for those events.

The two populations of events are seen with lower bounds on both half-maximum width and integral. The lower bound on the width in time can be understood as the convolution of the Gaussian shaping time of the electronics and the width of the Gaussian smooth performed during analysis. The electronics shaping time is 1.45 μs and the smooth has a standard deviation of 4.0 μs. Addition in quadrature results in a value of 4.25 μs. To scale this value to a FWHM, multiplying by $2\sqrt{2\ln 2}$, nets a value of 10.0 μs, which closely matches the lower vertical-axis edge of Figure 3.4. The integrals also have a lower bound which is sloped positively. This can be interpreted in the following way. All ^{55}Fe interactions in the gas deposit about the same amount of charge per track produced. Signals that are wider at half maximum are smaller in amplitude. Since the analysis relies on the signal amplitude for identification, those tracks which do have less charge than average and produce signals that are wider in time are missed by the analysis. Both the orientation of the track in the detector relative the MWPC and how far away from the MWPC the event occurs affect the signal width in time. Tracks which are directed primarily along the z-axis will be longer in time since this is the drift axis. Tracks which are deposited farther away from the MWPC along

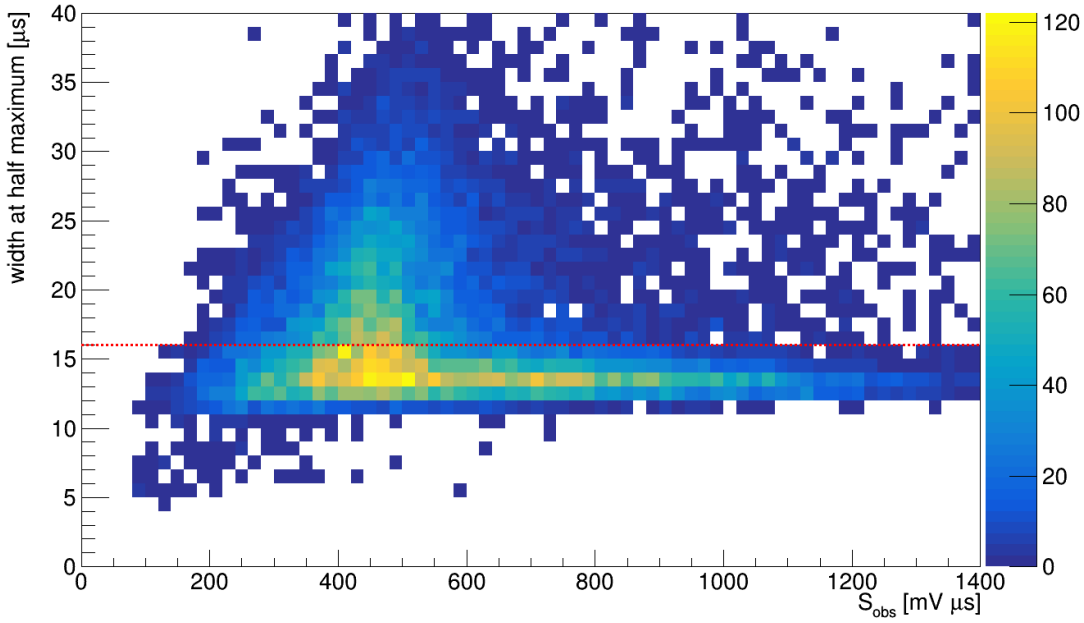

Figure 3.4: A two-dimensional histogram of events for ^{55}Fe run drift2e-20170519-05. The vertical axis is the width in time, measured at half maximum, for each signal. The horizontal axis shows the integral of each signal. 19360 tracks were observed for this run with ∼19080 plotted over the ranges shown. The number of tracks here is larger than reported in Table 3.2 since *trackHalfMaxTimeCut* and *trackRiseTimeCut* have been relaxed. The horizontal-dashed line represents the value, 16 μs, used for *trackHalfMaxTimeCut* during analysis. Each cell is 1 μs tall and 20 mV·μs (∼10 NIPs) wide.

the z-direction must drift a longer distance before reaching the MWPC. In doing so more diffusion is incurred, broadening the signal in time.

Several effects may contribute to the non-Gaussian shape of the integral histograms of Figure 3.3. As described above, ^{55}Fe events which produce small signal integrals and are short in duration may be lost in the noise. This would contribute to a difference in shape in the rising and falling edges of the integral histograms. Secondly, for the *trackHalfMaxTimeCut* chosen, spark-like events are not completely removed from the analyzed events. Since the spark-like events can result in much larger integrals than events which occur in the detector volume, this in part can explain the skewed-right appearance of the histograms. Thirdly, Figure 3.5 shows the average signal integrals observed for all one-wire events of run 20170519-05. The average integrals of some wires are distinctly larger than that of the majority. In comparing to the noise levels for these wires, Figure 3.2, it is possible for some wires that this is a noise-related issue. For instance, the events observed

for a wire of high RMS noise may also be the events which are larger in energy than average, the lower energy events being lost due to the signal-to-noise ratio. Other effects may contribute to the shape of the integral histograms. The electronics shaping time may vary from the norm for some of the wires. If this was the case more spark-like events may evade the analysis cuts and push the average signal integral to larger values for those wires. Another possibility is variance in gain among the wires. Since the total integral distributions of Figure 3.3 include entries for all wires of a given run, the skewed-right appearance may be partially attributed to the fact that some wires contribute larger than average integrals, regardless of cause.

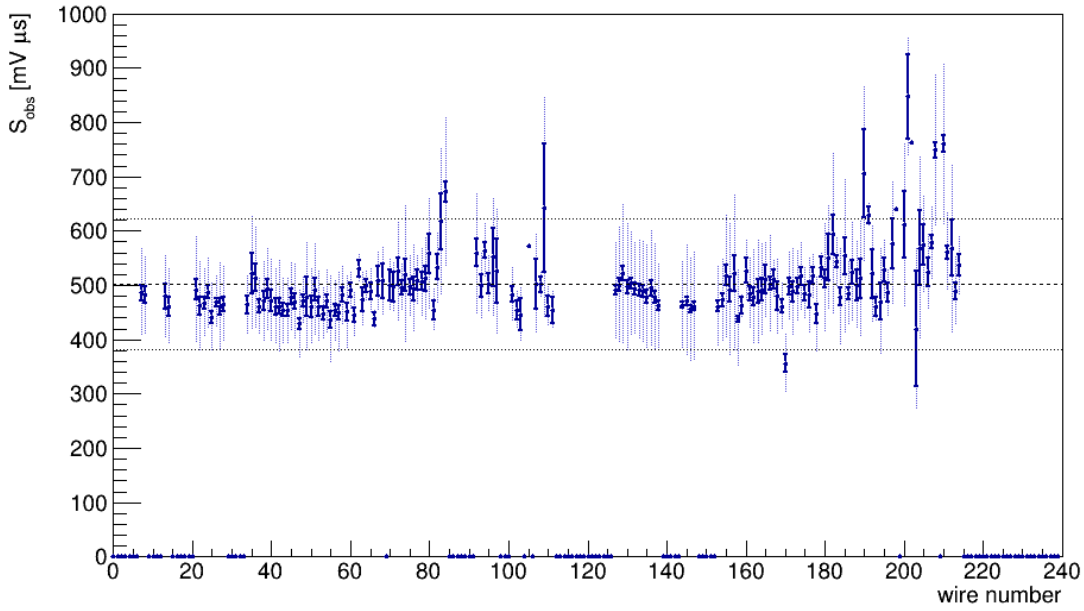

Figure 3.5: For the 4189 one-wire events of run 20170519-05, all signal integrals collected for each active wire were averaged. Each point and error bar is the average and the standard deviation over the square root of the number of events for a specific wire. The vertical-dashed line behind each point represents the standard deviation for that wire. The horizontal-center-dashed line is the overall average signal integral for the run $\langle S_{obs} \rangle = 502$ mV·μs as shown in Table 3.3. The horizontal-dashed lines above and below the central line is the standard deviation about this average. For a few wires (105, 198, 202), only one event was observed and no error bars are plotted.

The final, and potentially most concerning, reason the ^{55}Fe integrals may not appear Gaussian in nature comes from comparing the number of tracks which hit one wire versus those that hit two

wires. For a previous iteration of the DRIFT detectors, DRIFT-IIb, it was reported [126] that the range of an ^{55}Fe track in 40 Torr CS_2 is of order the 2 mm wire spacing of the MWPCs and that 54% of the tracks observed in that work hit two wires. Table 3.2 indicates that for all runs of this work $\geq$ 95% of tracks hit only one wire. If it is the case that a much larger percentage of the tracks should be expected to hit two wires, the integrals reported here may be systematically low. This would likely be due to the signal-to-noise ratios for the anode wires. If the charge is spread across two wires it may be the case that only the largest signal of the two wires is identified during analysis while the other smaller signal cannot be distinguished from noise, leading to only a partial measurement of the total charge for that ^{55}Fe event. Figure 3.6 may corroborate this assessment, which for run 20170519-05 shows the distributions of integrals for one-wire and two-wire tracks. On average, the relatively few two-wire tracks which are observed result in larger integrals. For run 20170519-05, there are 4189 one-wire tracks and 155 two-wire tracks. The averages for the distributions are 496.3 and 659.7 mV·μs with standard deviations of 114.5 and 184.2 mV·μs for one-wire and two-wire tracks, respectively. Naively assuming the uncertainty on each mean scales as typical for Gaussian distributions results in ± 1.8 and ± 14.9 mV·μs for one-wire and two-wire tracks. This implies that the means are different by $\sim$10 standard deviations.

Assuming that the number of observed one-wire tracks is elevated in comparison to the number of two-wire tracks and also assuming that the measured averages are representative of the actual distribution averages, a systematic uncertainty on the average integral, energy, can be calculated. Run 20170519-05 is comprised of 96.4% one-wire tracks and 3.6% two-wire tracks with averages of 496.3 and 659.7 mV·μs, respectively. This results in a combined average of $0.964(496.3\ \mathrm{mV}\cdot\mu\mathrm{s}) + 0.036(659.7\ \mathrm{mV}\cdot\mu\mathrm{s}) = 502\ \mathrm{mV}\cdot\mu\mathrm{s}$, which matches the overall average reported in Table 3.1. Let it now be assumed that the true fraction of two-wire tracks should be 54% in accordance with the observations in reference [126]. This results in a combined average of $0.46(496.3\ \mathrm{mV}\cdot\mu\mathrm{s}) + 0.54(659.7\ \mathrm{mV}\cdot\mu\mathrm{s}) = 585\ \mathrm{mV}\cdot\mu\mathrm{s}$. This implies that the average energy measured in this work may be 14% low. Ignoring other effects, this estimate may be somewhat conservative since partial two-wire tracks for which signal on only one wire was detected are ex-

pected to have the effect of driving the one-wire integral average to a lower value, increasing the spread in means between the one-wire and two-wire integrals. It is also reasonable to assume that the two-wire tracks that were observed were the more energetic of the two-wire tracks which also should increase the spread in one-wire and two-wire means. A more conservative estimate on this systematic can be arrived at by assuming that the measured two-wire average is most comparable to the expected overall average. The measured overall average of 502 mV·μs is 24% lower than the measured two-wire average of 659.7 mV·μs. The main focus of this dissertation is to understand the directional detection capabilities of the detector. This understanding comes from measuring parameters of nuclear recoil signals such as width in time of signals and counting the number of wires hit by a nuclear recoil. A systematic offset in energy calibration does not impact these values. This provides a justification for not carefully quantifying the size of the systematic uncertainty on energy in this work but is not a justification that can diminish the importance of calibration overall. Proper calibration is essential for accurate track energy reconstruction and for the capability of discrimination of particle types based on energy spectra as well as understanding what WIMP masses the detector may be sensitive to.

For this dissertation, energy calibration constants have been calculated with the data at hand and with acknowledgement that systematic uncertainties may be present. Future studies are required to understand these systematics. These studies are not pursued here, but two suggestions are mentioned in passing for the purpose of laying out how one could proceed. Firstly, simulations should be done to more accurately understand the expected range of ^{55}Fe tracks for this gas mixture and the expected ratio of the number of two-wire to one-wire events. Secondly and in regards to actual experimentation, one would want to try and increase the signal-to-noise of the detection system and see if the integral distribution shifts to larger values and the tail on the right side starts to fill in. With the possibility of a systematic discussed, discussion of calibration constants will proceed with only considering statistical uncertainty.

The signal integrals that have been discussed are a measure of energy in units of mV·μs, and since it is known on average how many NIPs are produced by ^{55}Fe tracks a proportionality con-

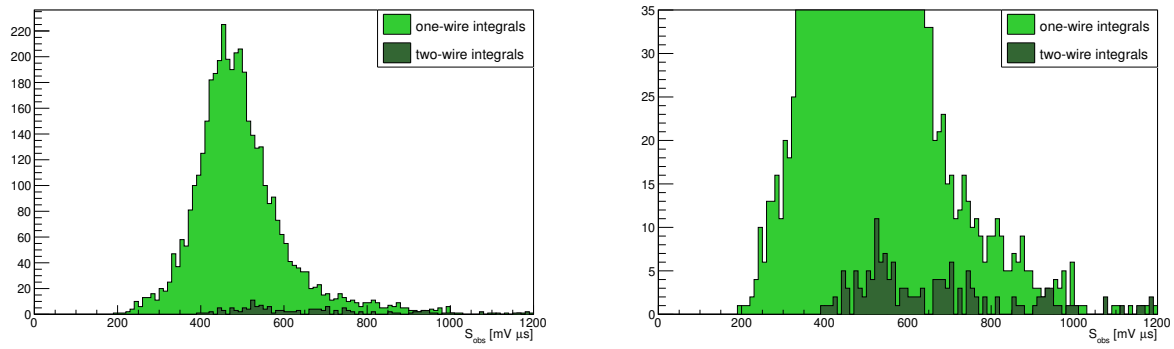

(a) **(b)**

Figure 3.6: Distributions of observed integrals for one-wire (light green) and two-wire (dark green) ^{55}Fe tracks. Two-wire tracks span a range over larger integral values than do one-wire tracks. The distributions are shown with a full-scale vertical axis (a) and truncated vertical axis (b).

stant relating the two units can be determined. This has been described in detail in Section 2.3. For each ^{55}Fe run presented in this section, the corresponding integral histogram of Figure 3.3 can be used to determine the calibration constant that can be applied for neutron and background runs which took place for the same gas fill. The evaluation of calibration constants is presented in Table 3.3. For each integral histogram the average $\langle S_{obs} \rangle$ and standard deviation σ_{obs} were calculated. These values are not the results of fitting. It is believed that the skewed-right appearance of the integral histograms is due in part to the contamination of each sample population with spark-like events. Under the assumption that the main contributor to the non-Gaussian appearance is spark-like events, the two aforementioned values would not be good estimators for the average and dispersion in energy. The spark-like events, which can be larger in energy, will pull the average to a value larger than should be observed for ^{55}Fe tracks which occur in the detector volume. Further, σ_{obs} is not a good measure of uncertainty because the distributions are asymmetric and also because the tail on the right of each histogram will inflate the measure of this value. For these reasons, each distribution was fit with a Gaussian over a region about the peak which extended to one quarter of the peak value on each side. This is described in the caption of Figure 3.3. The fit results are presented in Table 3.3. All average values as determined by the fit S_{fit} are smaller, as had been expected, than each corresponding $\langle S_{obs} \rangle$ as is the case for the variance. For most fits

though, it is indicated by the reduced chi-squared values that the fits do not well capture the data. For convenience the corresponding p-value for each reduced chi-squared $P(\tilde{\chi}^2 \geq \tilde{\chi}^2_{fit})$ is given, which represents the fraction of the $\tilde{\chi}^2$ distribution which lies at values larger than the one that has been measured. For a reasonable fit, just about as much of the $\tilde{\chi}^2$ distribution should lie above the measured value as below resulting in a p-value of $\sim$0.5. Since most of the fits do not well describe the data, σ_{fit} should not be used to estimate the uncertainty on S_{fit} nor should one use the uncertainty on S_{fit} which can be extracted from the covariance matrix of the fitting routine (not reported here). Each S_{fit} however, does provide a reasonable measure of the peak[31] value of each integral distribution. Even though each integral distribution is itself not Gaussian, repeated measurement of the peak values should net a distribution that is Gaussian. Therefore, the uncertainty on each individual S_{fit} can be reasonably estimated by finding the standard deviation of the S_{fit} values for all six runs and dividing by $\sqrt{6}$ resulting in a value of $\pm$ 2.99 mV$\cdot\mu$s. The calibration constants in the right-most column of Table 3.3 have been calculated by dividing $NIPs_{^{55}Fe} = 237 \pm 7$ by S_{fit} for each of the six runs.

Table 3.3: Calculation of the energy calibration constants for each of the ^{55}Fe runs. The calibration constants appear in the right-most column. All other values are described in the text.

Run	$\langle S_{obs} \rangle$ [mV$\cdot\mu$s]	σ_{obs} [mV$\cdot\mu$s]	S_{fit} [mV$\cdot\mu$s]	σ_{fit} [mV$\cdot\mu$s]	$\tilde{\chi}^2_{fit}$	$P(\tilde{\chi}^2 \geq \tilde{\chi}^2_{fit})$	$\frac{NIPs_{^{55}Fe}}{S_{fit}}$ [$\frac{\text{NIPs}}{\text{mV}\cdot\mu\text{s}}$]
20170519-05	502	121	475	75	1.30	0.146	0.499 $\pm$ 0.015
20170525-03	473	116	457	81	0.834	0.715	0.519 $\pm$ 0.016
20170526-06	489	102	473	63	1.04	0.412	0.501 $\pm$ 0.015
20170530-04	478	110	465	80	1.53	0.0368	0.510 $\pm$ 0.015
20170531-03	482	112	471	70	1.52	0.0424	0.503 $\pm$ 0.015
20170601-03	479	114	460	76	1.65	0.0201	0.515 $\pm$ 0.016
σ			7.33				
$\frac{\sigma}{\sqrt{6}}$			2.99				

[31]Each integral distribution was fit with a Gaussian distribution over the quarter-max region about its peak value. The mean value returned by the fit is a measure of the peak location. The actual average of the distribution will be larger since the distributions are skewed right.

The escape/capture peak described in Section 2.3 has not been observed for the integral distributions reported for each run here. It is suspected that this is due to the noise present on the wires. The amplitude of signals produced by these smaller deposits of charge are likely not distinguishable from the noise. This is also consistent with a lack of two-wire events being observed. If it is the case that most two-wire ^{55}Fe events are being missed where the total charge of the track is split between two wires, one would not expect to see the escape/capture tracks which produce $\sim$40 to $\sim$60% of the charge of a full track.

Signals collected during ^{55}Fe exposures have been scrutinized visually. Minority peaks, as will be discussed and analyzed for neutron runs, were not observed in ^{55}Fe run data. As discussed in Section 2.1.2, this is likely due to the various charge carrier species not having sufficient time to separate over short drift distances. It is believed that those x-ray events which do occur far enough into the detector for minority peak separation to occur result in deposits of charge too sparse to produce signals that can be distinguished from the baseline noise. The distance, along the z axis of the detector, from the MWPC to where the track is deposited in the detector volume is called z_{IP}. The shortest z_{IP} reconstructed for the neutron runs presented in Section 3.2.2 was $\sim$4 cm. Of all 2089 reconstructed neutron-run track z_{IP} distances, 5.0% of these distances[32] were $\leq$ 7 cm. The ^{55}Fe source was located $\sim$15 cm behind the MWPC and in Section 2.3 the attenuation length of x-rays in the gas was calculated to be 33.1 cm. A simple Monte Carlo simulation was developed to understand the distribution of 5.97 keV x-ray interaction distances from the MWPC along the z axis. The active volume of the detector was limited to the 480 central-most wires of the detector as described in Section 2.1.6. In total, 1,000,000 x-rays were emitted isotropically from the source location. Of these 88,910 interacted in the active volume. The interaction distances were randomly sampled from an area-normalized exponential distribution, which decayed with the attenuation length already described. The result was 40.4% of the interactions occurred $\leq$ 7 cm from the MWPC. This indicates that a substantial portion of the interactions occur above

[32]The total number of tracks remaining after applying the $TracksCPA$ cuts of Section 3.3.3 is 1907, of which 3.8% of the tracks have a $z_{IP} \leq$ 7 cm.

the distance threshold for which one may expect minority peaks to be observable. Half of the ionization typically belongs to the main I peak of a signal with the other half distributed among the minority peaks. Additionally, more diffusion is incurred for tracks deposited farther from the MWPC. It is thought that the reduction in signal-to-noise, due to the peaks of charge separating and additionally diffusion, results in these tracks being lost in noise.

3.1.2 Measurement of Gas Gain

With energy calibration complete in Section 3.1.1, one can determine the gas gain of the detector. The gas gain depends on the drift gas pressure, anion species carrying the charge to the wires, and the field wire voltage relative to the anode wires. The amount of gain depends on how tightly bound the electrons are to the carrier anions and how strong the electric field is near the MWPC. Multiple carrier anion species are present for the gas mixture, see Section 2.1.2, which implies that the gas gain is an average that is weighted according to the proportions of carrier anion species that reach the MWPC for calibration run tracks. For the same carrier anions in the same drift gas, the farther the field at which electrons are detached from the anions extends from the MWPC the more collisions will happen for those electrons as they are accelerated toward the anode wires and the more gain will be achieved.

The total gain for a signal is a product of the shaping electronics gain and the gas gain. In Section 2.2.1 a value of $G_{shape} = 90.9 \pm 1.3 \ \frac{\text{mV}\cdot\mu\text{s}}{\text{fC}}$ was measured for the shaper gain. In Section 3.1.1 the average signal integral S_{fit} was determined for each ^{55}Fe calibration run. Since it is known that each S_{fit} corresponds to $NIPs_{^{55}Fe} = 237 \pm 7$, the gas gain G_{gas} for each calibration run can be determined. G_{gas} will be reported in units of $\frac{\text{e}^-}{\text{NIP}}$ and corresponds to how many electrons are produced on average during avalanche per charge carrier anion of a track incident on the anode wires.

$$G_{gas} = \frac{S_{fit}\cdot(6241.5 \ \frac{\text{e}^-}{\text{fC}})}{G_{shape} NIPs_{^{55}Fe}}$$

Table 3.4: Calculation of the average gas gain for each of the ^{55}Fe runs. Each S_{fit} value has an estimated uncertainty about the mean of ± 3 mV·μs from Table 3.3.

Run	S_{fit} [mV·μs]	G_{gas} [$\frac{\mathrm{e}^-}{\mathrm{NIP}}$]
20170519-05	475	138 ± 5
20170525-03	457	132 ± 4
20170526-06	473	137 ± 5
20170530-04	465	135 ± 4
20170531-03	471	137 ± 5
20170601-03	460	133 ± 4
$average$		135 ± 2

The mean gas gain $G_{gas} = 135 \pm 2$ $\frac{\mathrm{e}^-}{\mathrm{NIP}}$ when averaging all runs. The gas gain is an important parameter to understand for the detector because it factors into the signal-to-noise ratio. The uncertainty reported here is statistical only. In Section 3.1.1 it was proposed that the average calibration run signal integrals may be systematically low, by an estimated value of up to 24%. This would imply that S_{fit} and G_{gas} may be systematically low by a similar factor.

Since untriggered run 20170519-05 was the longest in duration by an order of magnitude, it was used to investigate the stability of the gas gain over time. The gas was not being flowed through the detector, so it is of interest to understand if the aging of the gas has an observable effect on the gain. This specific run had a recorded run time of 917 minutes[33]. In total 83 files were recorded to disk. For untriggered runs, traces are read out box-by-box at a fixed rate as described in Section 2.1.5. The first 82 files use a disk space of 291 MiB and the 83^{rd} file uses 103 MiB. This implies that each files corresponds to $(917 \text{ minutes})/(82 + \frac{103}{291}) = 11.1 \text{ minutes}$. The first 80 files were grouped chronologically into 10 groups of eight files each. For each file group, distributions of the observed signal integrals S_{obs} were generated and fit in the same manner as described in Section 3.1.1. Each distribution was fit, using ROOT [113], with a Gaussian. The fit value S_{fit}, which corresponds to the mean, and the uncertainty from the fit routine represent the points and error bars in Figure 3.7. The mean $\pm$ standard deviation of the 10 values is 477.7 ± 7.6 mV·μs,

[33] Regarding the gas fill for this day, the vessel was pumped down at 09:20 Pacific Standard Time. The vessel was then filled with 5 Torr of CS_2 at 11:15 to flush the vessel. The first recorded run for the day started at 15:25. At some time in this $\sim$4 hour window the vessel was filled with 40:1.5 Torr CS_2:O_2. Run 20170519-05 was then started at 17:22.

indicating that the average gas gain fluctuated by 1.6% over the course of the run. No overall trend is apparent, although the spread in the last four points appears to be less than in those previous.

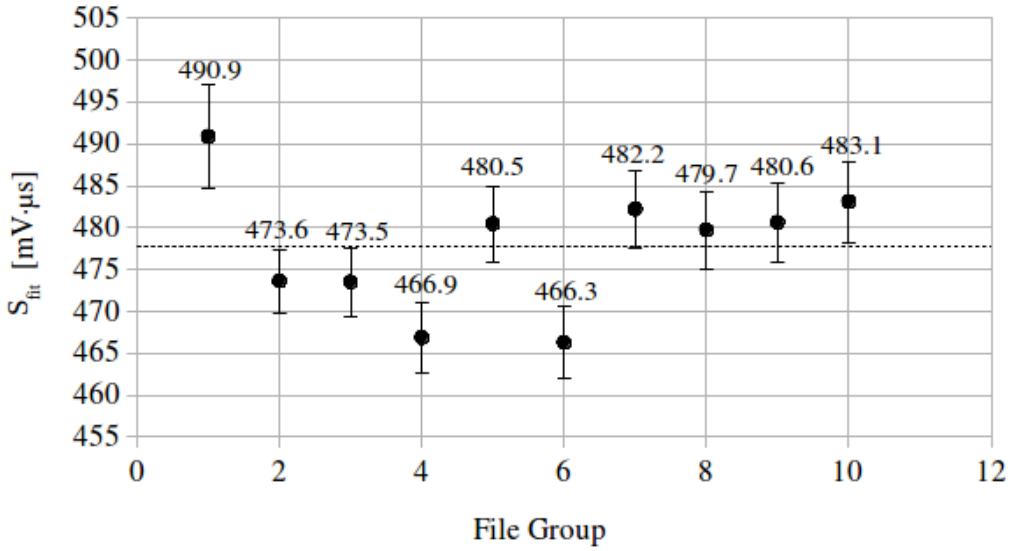

Figure 3.7: The average signal integrals for untriggered run 20170519-05, as determined by fitting, are plotted as a function of time. Each file group represents ∼89 minutes of run time. A detailed description is provided in the text. The horizontal-dashed line represents the average of the 10 points.

3.1.3 Analysis of Untriggered Runs

The collection of data in untriggered mode has been described in Section 2.1.5. The analysis chain for untriggered runs is described here. The majority of this analysis chain is the same as was applied for the triggered runs and it is discussed in Section 3.2.5. One should read through the triggered run analysis, which was used to search for nuclear recoils, before reading this section. Instead of repeating all steps of the chain that have been described, I will simply list what is different for the untriggered analysis when compared to the triggered analysis. The discussion below applies mostly to Stage 4 of the analysis chain.

A difference between untriggered runs and triggered runs was the observation of one-bin spikes on traces, Figure 3.8(a). These one bin spikes were not observed in triggered runs, but were observed in both untriggered background and ^{55}Fe runs. These one-bin spikes are not consistent

with ionization hitting a wire since the one-bin duration in time is shorter than the width in time of the shaping electronics. The peaking time of the of the semi-Gaussian shaping electronics was set at 3 μs and the shaping time measured in this work, Section 2.2.1, was $\sigma_{shape} = 1.45 \pm 0.02$ μs. These one-bin spikes were removed from the traces.

To remove one-bin spikes, one must first select a window that is n_w trace bins in length. This window length is required to be odd. One initially positions this window with its left edge in line with the left bin edge of the earliest bin in a trace. This window is then slid rightward bin-by-bin in time across the trace until the right edge of the window is in line with the right bin edge of the latest bin in the trace. The i^{th} bin of a trace is checked for a one-bin spike by first computing the average and standard deviation of the nearest $n_w - 1$ trace bins. For clarity, these are the $(n_w - 1)/2$ bins that lie both left and right of bin i. Let s_i be the bin value associated with bin i and the average of the nearest neighboring bins be named $\langle s_{\shortparallel i} \rangle$.

$$\langle s_{\shortparallel i} \rangle = \frac{(\sum_{j=i-\frac{n_w-1}{2}}^{i-1} + \sum_{j=i+1}^{j=i+\frac{n_w-1}{2}}) s_i}{n_w - 1}$$

The standard deviation is computed over the same bins and let it be named $\sigma_{\shortparallel i}$. For this dissertation, the window length $n_w = 7$ and if $s_i \geq 7\sigma_{\shortparallel i}$ then this bin indexed by i was considered to contain a one-bin spike. To remove the one-bin spike, the value of this bin was set to the average of its neighboring bins $s_i = \langle s_{\shortparallel i} \rangle$. One cannot apply this to the first and last $(n_w - 1)/2$ bins of a trace since the window would slide past the trace boundaries. These bins were set to the trace average, since $n_w = 7$, this implies the first and last three bins of a trace were essentially discarded. The effect of this algorithm can be seen by comparing the left and right panels of Figure 3.8.

Recall, see Section 2.1.4, that the definition of an event differs between triggered and untriggered runs. All 60 anode and 60 field wires belonging to one of the electronics boxes are all read out simultaneously and constitute an event for an untriggered run. Also, minority peaks have not been observed in ^{55}Fe signals, this is discussed in Section 3.1.1. Additionally, ^{55}Fe signals are

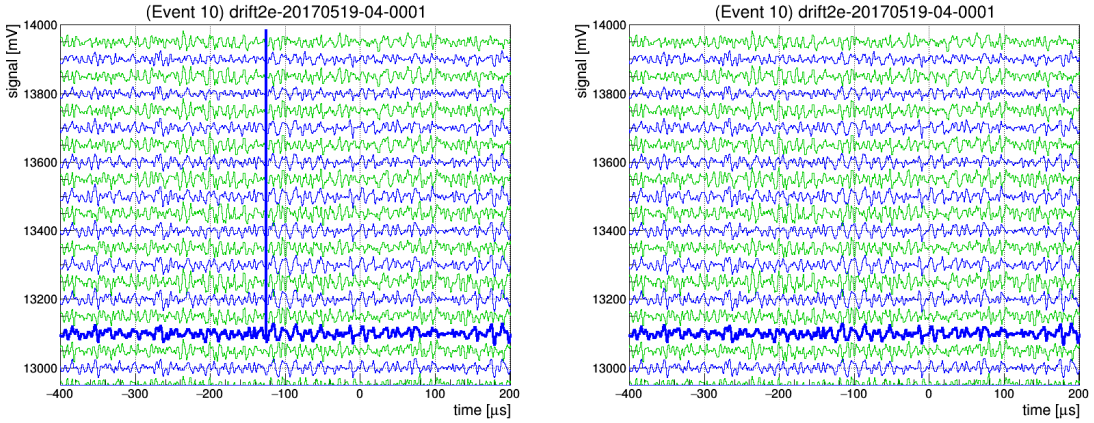

(a) One-Bin Spike

(b) One-Bin Spike Removed

Figure 3.8: (a) For an untriggered background run event, an example one-bin spike is shown. (b) The same traces are shown after the one-bin spike has been removed.

smaller in amplitude and occur at greater rate compared to recoils resulting from neutron exposure. Due to these factors, the analysis for untriggered runs differs in some steps in comparison to triggered runs.

Again, for the following discussion, the reader should refer to Section 3.2.5. The removal of one-bin spikes was performed between Trace Analysis 01 and 02. Trace Analysis 03 to 08 were then applied. Trace Analysis 09 was applied but at a reduced peak finding threshold. The peak and signal region finding parameters were respectively, $n_{peak} = 2.0$ and $n_{SR} = 0$. Trace Analysis 10 was applied and Trace Analysis 11 omitted since the ^{55}Fe signals are of relatively small amplitude, thus one does not want to increase the peak finding threshold. In Trace Analysis 12, any traces for which signal regions were found and additionally the traces that neighbor these directly were searched at a reduced peak finding threshold, this was done with $n_{peak} = 1.5$ and $n_{SR} = 0$. Since minority peaks were not observed in ^{55}Fe signals, step Trace Analysis 13 was not applied, where signal regions of a trace are combined. Trace Analysis 14 was applied and Trace Analysis 15 omitted, step 15 is the search for minority peaks within a signal region.

Tracks were grouped using Track Analysis 01 and were filled using Track Analysis 02. A difference exists in the latter, since no minority peak analysis was done, the parts of Track Analysis 02 that involve minority peak analysis were not applied here. Track Analysis 03 through 06 were

applied without change. Track Analysis 07 and 08 were both omitted. The former is a check to ensure a track is well-contained within an event and was not performed since all wires of a given box are read out for an event. The latter, Track Analysis 08, was a check to ensure that only a single track existed within an event, one does not want to apply this here since the event structure is different and one is more likely to observe multiple ^{55}Fe tracks within an event. Two additional steps are applied for untriggered runs after Track Analysis 08. A boolean flag *trackPassNumWiresCut* was set to false if greater than three wires were hit for the track. It was expected that ^{55}Fe tracks would extend across one or two wires [126]. Looking at Table 3.2 $\geq 95\%$ of tracks hit one wire. A final boolean flag is introduced for untriggered runs, *trackPassReducedThresholdCut* is set to true if a track has at least one track component, that is signal region, picked out in Trace Analysis 09. For clarity, a track does not pass this cut if it is composed only of signal regions identified in the lower peak finding threshold applied to neighboring wires in Trace Analysis 12.

The output is a file in ROOT [113] format. Each event was written to file in its custom event class structure. Stage 5 accumulation of event, track, or trace statistics proceeded on file-by-file and additionally run-by-run bases. Two other cuts were required while generating plots. Since minority peak structure is not available to cut on, sparks can make it through this analysis. For this reason, cuts were made on the risetime and half-maximum width of a track. All signal regions of the track were added together in time. Starting at the global maximum of the track signal, one iterates both left (earlier in time) and right (later in time) of this peak bin-by-bin until the first instance of bins are found that are less than or equal to half the peak value. This defines the half-maximum width in time. To find the risetime, one again starts at the peak of the track signal. Iterating left of the peak bin-by-bin, the first bin that has a value less than or equal to 0.9 of the peak value defines the later edge of the risetime. Continuing to iterate left bin-by-bin, the first bin that has a value less than or equal to 0.1 of the peak value defines the earlier edge of the risetime. For this dissertation untriggered tracks were required to have a risetime > 12.0 μs and a half-maximum width in time of > 16.0 μs, let these be named *trackRiseTimeCut* and *trackHalfMaxTimeCut*, respectively. Recall,

this is subsequent to signals passing through hardware and software shaping. More information about these cuts appear in Section 3.1.1.

3.2 Neutron Runs

3.2.1 Description of Collected Data

In this section the process of data collection will be described as well as some basic results of the runs to be discussed. The term *analysis* will refer to the algorithm described in Section 3.2.5. In Section 2.1.4, a distinction was made between the terms *event* and *track*. An event can consist of more than one track if the signal regions composing the tracks occur within specified timing constraints. The analysis has some capability to pick out multiple tracks that occur within the same event. For simplicity, for this work the analysis was set to only accept those events containing single tracks.

An isotropically emitting ^{252}Cf source, which produces neutrons via spontaneous fission, was used for the neutron runs described in this section. The energy spectrum of these neutrons is assumed to have a mean of 2.31 MeV and mode of 0.90 MeV, see Appendix A. The calculated source activity was 69360 neutrons/second as of 08-May-2017. To attenuate gammas, the source was housed in a cylindrical lead container. The container is composed of two pieces, a bucket and lid. The outer dimensions of the bucket are 11.0 cm tall by 10.0 cm in diameter. The inner dimensions of the bucket are 8.31 cm tall by 4.45 cm in diameter. The walls of the bucket are 2.79 cm thick. The lid is 2.10 cm thick around the outside and $\sim$2.69 cm thick for the central-cylindrical portion which mates with the bucket. Each value, except the last one, is reported to the number of significant figures allowed by the measurement precision that was recorded. The last value is more uncertain, it was not measured directly but estimated assuming it was the same thickness as the bottom of the bucket.

The source itself is relatively small compared to the size of the lead container. The source is suspended from a thin string. For each run the source was put into the bucket with the string remaining partially out of the bucket. The lid was placed on top of the bucket resulting in the source

being held in place near the wall of the bucket. For all runs this makes the actual source position uncertain to within the inner dimensions of the lead container. This corresponds approximately to uncertainties on the source position within the lead container of $\pm$ 2.23 cm for y and z dimensions, which correspond to the diameter, and $\pm$ 3.85 cm for the x dimension, which is along the axis of the cylinder.

Seven different types of runs were conducted as described below, corresponding to the seven different source positions. For each position, one is to imagine viewing the detector from the front, or opening, of the vacuum vessel, see Figure 3.9. Since only the centermost 240 anode wires of the left MWPC were instrumented to be read out, see Section 2.1.6, efforts were made to place the source at positions measured relative to the volumetric center of the left detector. The placement of detector within the vessel and the location of the volumetric center of the left detector are described first.

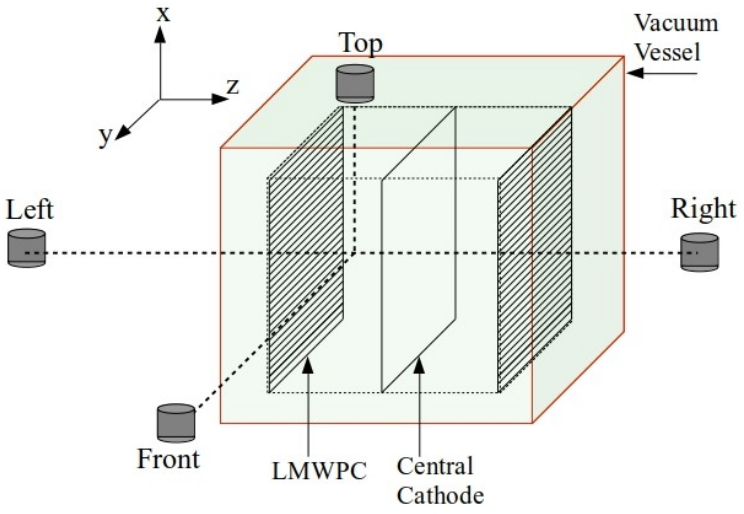

Figure 3.9: A three-dimensional view of the detector and the neutron source positions that will be analyzed in this dissertation. Details regarding the source positions appear in the body of the text. This schematic is not drawn to scale.

The detector was not centered within the vacuum vessel[34], the positioning of the detector inside of the vessel was taken into account when placing the source. All measurements of the position of the detector within the vessel were performed prior to any of the data runs. Over the period in which all runs were performed, it was necessary to remove the detector from the vessel twice for repair. This introduces some uncertainty on the position of the center of the left detector volume. As described in Section 2.1, the detector itself sits on a skate plate. When it is required to remove the detector from the vessel, the skate plate is used to slide the detector out of the vessel onto a custom built trolley such that the position of the detector does not change relative to the skate plate. Each time the detector was removed from the vessel and then reintroduced, it was positioned such that right side of the skate plate was pushed against the inside-right wall of the vessel and also so that the spark shielding on the back of the detector was approximately touching the inside back wall of the vessel. Due to this, it is believed that the measurements of the left detector center relative to the inside of the vessel remain accurate, even after the detector has been removed and then reintroduced to the vessel. Only the horizontal, or y and z, positions of the center position of the left detector can be affected by removing and then reintroducing the detector to the vessel.

The center of the left detector volume was located 58.8 cm from the inside-left face of the vessel (z position), 69.2 cm from the inside-back of the vessel (y position), and 71.8 cm from the inside-bottom of the vessel (x position, correspondingly this is 122.6 cm from the lab floor). An uncertainty of $\pm$ 1.0 cm is reasonable for the x position, larger uncertainties of $\pm$ 2.0 cm are reasonable for the y and z positions since the detector had to be removed and reintroduced to the vessel on a couple of occasions. The source positions are listed below, for which the uncertainties on all measured values are $\pm$ 1.3 cm.

Left (L): The center of the lead container was placed left of the vessel 147.7 cm from the volumetric center of the left detector. It was 123.4 cm above the lab floor and 68.0 cm forward from the plane defined by the inside-back wall of the vessel. It was approximately centered

[34]Normally, the detector would be centered within the y and z dimensions of the vessel. However, for these runs this was not possible due to the space required for this initial version of the readout electronics.

on the x-y dimensions of the detector. In comparing to the location of the volumetric center of the left detector, the center of the lead container was 1.2 cm behind and 0.8 cm above.

Right (R): The center of the lead container was placed right of the vessel 153.3 cm from the volumetric center of the left detector. It was 123.4 cm above the lab floor and 68.0 cm forward from the plane defined by the inside-back wall of the vessel. It was approximately centered on the x-y dimensions of the detector. In comparing to the location of the volumetric center of the left detector, the center of the lead container was 1.2 cm behind and 0.8 cm above.

Top (T): The lead container was placed directly on top of the vacuum vessel, which makes the center of the lead container 87.8 cm above the volumetric center of the left detector. It was 62.2 cm from the plane defined by the inside-back wall of the vessel and 59.7 cm from the plane defined by the inside left wall of the vessel. It was approximately centered on y-z dimensions of the left detector volume. Due to limitations in physical space, it was not possible to place the source such that it was $\sim$1.5 m away from the volumetric center of the left detector as was done for the other runs. In comparing to the location of the volumetric center of the left detector, the center of the lead container was 7.0 cm behind and 0.9 cm right.

Front (F): The center of the lead container was placed 159.4 cm in front of the volumetric center of the left detector. It was 123.4 cm above the lab floor and 56.6 cm right of the plane defined by the inside-left wall of the vessel. It was approximately centered on the x-z dimensions of the left detector volume. In comparing to the location of the volumetric center of the left detector, the center of the lead container was 2.2 cm left and 0.8 cm above.

Back-Left-Edge-Center (BLEC): The center of the lead container was 123.4 cm above the lab floor. It was placed 50.8 cm from the outside edge of the vessel where the left and back walls meet, it was placed such that it was along a line that extends from the vessel center through the back-left edge of the vessel.

Back-Left-Bottom-Corner (BLBC): The center of the lead container was 42.1 cm above the lab floor. It was placed 17.8 cm from the outside-back-left-bottom corner of the vessel, it was placed such that it was along a line that extends from the vessel center through the previously defined corner.

Background (BG): The neutron source was not present. The source was placed in a shielded container and moved several meters away from the detector. The background events as observed by the detector are recorded.

The detector was exposed to neutrons with the source located at these various positions around the vessel so that one may observe differences in the signals that are dependent on the incident direction of the neutrons. This is done to mimic the WIMP wind, which changes in direction relative to the detector axes over the course of a sidereal day. Optimally, one would want to place the source far from the detector such that the neutrons which reach the detector have incident directions which are all approximately parallel to each other in order to better approximate the WIMP wind. Due in part to space that was physically available, but more so due to the fact that the source intensity drops off as the inverse of distance squared and a limited time window was available to perform the runs, the source was not placed far from the detector. The opening angle of neutrons incident on the active volume of the detector is determined by the relative source-to-detector positioning and geometry. For the L runs, the half-angle spread of incident neutrons at the center of the left detector along the vertical direction $\hat{x}$ is 9.1° since only the central-most 240 anode wires were read out.

Neutron recoil data are collected via triggered mode and recorded to disk as described in Chapter 2.1.5. As stated in Chapter 2.1.6, only the 480 central-most anode and field wires of the left MWPC were instrumented to be read out. For the data presented here, the central cathode was held at -30 kV and the detector trigger threshold was set at 20 mV.

The target gas mixture for each run was 40:1.5 Torr CS_2:O_2. To achieve this for each gas fill, the vessel was first pumped out. The digital pressure gauge used for these runs had 0.1 Torr precision. Further it is thought that the pressure reading had a positive offset of 0.4 Torr. So, the

base pressure before adding any gas read $\leq$ 0.5 Torr and was believed to correspond to a value of $\leq$ 0.1 Torr. A few Torr of CS_2 was then added to the vessel and pumped out to further reduce the amount of undesired contaminant gas within the vessel, this will be referred to as flushing the vessel. After the flush, 40.5 Torr of CS_2 was added. This value is 0.5 Torr above the target value since the pressure tends to drop for the first couple of hours after a CS_2 fill due to adsorption of gas on the detector and vessel. 1.5 Torr of O_2 was then added. Over time the pressure increased at a rate of 0.02 to 0.05 Torr/hour as air leaked into the vessel. All additions of gas to the vessel were performed manually by opening valves and watching the digital pressure display. Efforts were made to stop each fill at the desired values within the precision of the display.

To minimize the number of variables present one would want to keep the experimental conditions for each of the runs constant barring the source position. Since the detector was still in development at the time of data taking, some differences in experimental conditions between runs were unavoidable. The number of active electronics boxes, and hence number of active wires, able to read out data varied between runs. The voltage applied to the field wires varied slightly between runs. Later runs had field wire voltages that were a few volts less in magnitude than earlier runs. The adjustment was done to mitigate spikes in current that had been observed, likely due to sparking. Further differences such as the size of the background noise for each wire and number of gas fills since the vessel had last been open to air were also different between runs. After the vessel has been filled with gas and pumped out several times, the physical state of the detector/gas may tend to stabilize and be in some ways different than a run which is performed after just one gas fill preceded by the vessel being opened to air.

Table 3.5 lists information about each run that was used for analysis. The different run types were defined earlier in this section. To view example recoil tracks the reader is directed to Section 3.2.2. A description of the electronics boxes can be found in 2.1.6. For now only the L, R, T, F, and BG runs will be analyzed. The BLEC and BLBC runs are not analyzed in this dissertation[35]. While

[35]The main reason for neglecting these runs is due to time constraints. The intention was to leave these runs blinded until a full end-to-end simulation for the runs had been built. Since the previous has not fully come to fruition, these files were left unanalyzed.

the BLEC and BLBC runs provide additional information, they are not essential to investigate the directional sensitivity of the detector. These runs are mentioned here to keep record of the fact, especially for those within the collaboration, that these unanalyzed runs exist.

In looking at Table 3.5, one may notice that the rates observed for neutrons runs which occurred on 20170511 are considerably lower than rates on other days. The last column of the table shows the average RMS noise on the wires for all traces of the run. The noise observed on 20170511 was about twice the size of the noise on subsequent days. Since the analysis requires the amplitude of a signal to be a specified factor larger than the noise, fewer tracks pass through the analysis for this day resulting in a lower rate.

Before trying to extract any information regarding directionality from the signals, one should first be convinced that they are observing recoils due to source neutrons. A comparison of rates when the source is present to when it is not present will suffice to show this. If the detector conditions had been the same for each run, this could be easily achieved by summing the number of tracks observed as well as live time for all background runs, calculating an overall rate, and then comparing this value to a similar calculation when the neutron source was present at one of the specific positions. This however, cannot be done since conditions differed between runs. Owing to this fact, it is chosen to instead look at the difference in rates for a background run which was followed by a right neutron run for the same fill of gas in the vessel and for the same active wires being read out. Specifically, runs 20170523-11 (BG), 20170523-14 (R), and 20170524-02 (R) will be compared. The latter R run was a continuation of that previous, the data acquisition system had crashed and was restarted $\sim$50 minutes after the crash. In the table, rates are shown along with uncertainties which were calculated assuming Poisson statistics and that the relative uncertainty in the duration of each run is negligible in comparison. The two R rates are not consistent with each other under the assumption that the rate is constant. Under the assumption of Poisson statistics, their difference over combined uncertainty is 7.4σ. At face value, this seems like a major discrepancy but it will be shown below that is in fact not.

Table 3.5: A listing of triggered runs. The field-wire voltage, number of active wires, list of active electronics boxes, run duration in minutes, number of tracks, number of tracks that hit only one wire, track rate, and average RMS noise for each run are tabulated. For every trace of a run, the baseline RMS noise is determined, all of these are then averaged for the run to determine $\langle\sigma_{noise}\rangle$. Uncertainty on the rate assumes Poisson statistics and that uncertainty on the run duration is negligible. All runs enclosed between two horizontal lines were performed with the same fill of gas in the vessel. On some dates the vacuum vessel was opened for repairs, these dates are noted since any physical changes may have an affect on the detector behavior.

Run	V_{FW} [V]	n_{wires}	$boxes$	$\Delta_{t_{run}}$ [minutes]	N	N_{1-wire}	$\frac{N}{\Delta_{t_{run}}}$ [minute^{-1}]	$\langle\sigma_{noise}\rangle$ [mV]
20170510	opened vacuum vessel							
20170511-27 (BG)	-899	121	0,2,3	59.4	0	0	0	27.6
20170511-32 (L)	-898	121	0,2,3	33.6	2	2	0.06 ± 0.04	27.3
20170511-37 (L)	-898	83	0,2	38.4	5	5	0.13 ± 0.06	22.4
20170511-41 (R)	-898	123	0,1,2	40.6	3	2	0.07 ± 0.04	21.0
20170511-42 (F)	-898	123	0,1,2	118.8	10	6	0.08 ± 0.03	21.0
20170511-43 (T)	-898	123	0,1,2	55.0	5	4	0.09 ± 0.04	20.7
20170512-03 (BLEC)	-898		0,1,2	467.3	not analyzed			
20170513-09 (BLBC)	-900		0,1,2	361.6	not analyzed			
20170513-10 (BLBC)	-900		0,1,2	58.8	not analyzed			
20170516	opened vacuum vessel							
20170517-45 (BG)	-900	106	0,1,2	440.7	10	8	0.02 ± 0.007	10.3
20170518-48 (L)	-900	157	0,1,2,3	90.0	78	57	0.87 ± 0.10	9.56
20170518-49 (L)	-900	157	0,1,2,3	69.9	56	46	0.80 ± 0.11	9.56
20170518-50 (L)	-895	157	0,1,2,3	181.9	106	90	0.58 ± 0.06	10.2
20170522	opened vacuum vessel							
20170523-11 (BG)	-896	143	0,1,2,3	103.4	3	3	0.03 ± 0.02	9.22
20170523-14 (R)	-896	143	0,1,2,3	740.3	265	218	0.36 ± 0.02	9.30
20170524-02 (R)	-896	143	0,1,2,3	275.3	40	36	0.15 ± 0.02	9.17
20170524-04 (F)	-896	144	0,1,2,3	1167.0	587	434	0.50 ± 0.02	9.89
20170525-04 (BG)	-895	143	0,1,2,3	90.8	2	0	0.02 ± 0.02	10.2
20170525-05 (T)	-895	143	0,1,2,3	379.0	336	243	0.89 ± 0.05	9.28
20170526-01 (T)	-895	143	0,1,2,3	460.5	194	161	0.42 ± 0.03	9.28
20170526-21 (BG)	-894	103	0,1,3	23.9	1	1	0.04	11.8
20170526-22 (L)	-894	103	0,1,3	166.0	74	65	0.45 ± 0.05	10.1
20170526-23 (L)	-894	103	0,1,3	1057.8	286	231	0.27 ± 0.02	10.1
20170530-05 (BG)	-894	144	0,1,2,3	93.1	1	1	0.01	11.0
20170530-06 (BLEC)	-894		0,1,2,3	979.2	not analyzed			
20170531-04 (BG)	-896	143	0,1,2,3	106.4	6	5	0.06 ± 0.02	10.1
20170531-05 (BLBC)	-896		0,1,2,3	983.6	not analyzed			
20170601-01 (BLBC)	-896		0,1,2,3	127.4	not analyzed			
20170601-02 (BG)	-896	144	0,1,2,3	68.2	0	0	0	9.83
20170601-05 (F)	-896	144	0,1,2,3	481.9	42	40	0.09 ± 0.01	9.77

To investigate the discrepancy in R rates, the runs will be broken up into smaller pieces such that rates can be tracked over time. As previously described in Section 2.1.5, data storage for a run may be composed of several files. Each file contains 50,000 anode wire traces (plus the corresponding 50,000 field wire traces), and once that limit is reached a new file is started. Run 20170523-14 is composed of 28 files and 20170524-02 is composed of 14 files. The 28th and 14th files, respectively, will be ignored since they do not contain a complete 50,000 anode traces such that 40 files in total were studied. The mean-RMS-baseline noise observed for the anode traces of the 40 files were averaged resulting in a value of 9.26 ± 0.15 mV. The latter value is the standard deviation and indicates the noise was relatively constant across these runs, varying by 1.6%. Figure 3.10 is composed of three plots that describe the evolution of the content of the files over time. Figure (a) shows the event rate for each file. The total number of events was divided by the run time for each file, which was determined via the timestamps associated with the first and last traces of the file. An event is a grouping of traces that have timestamps that are consecutively within 1 ms of each other, see Section 2.1.4. The plot appears to show a trend of increasing event rate with file number, implying an increase in event rate with time. The next two plots provide some information about the content of these events. Figure (b) shows the rate of recoil-like tracks that are contained within the events and pass through the analysis. This track rate appears to decrease with time. In Figure (c), the rate that spark-like signal regions appear within the anode traces is plotted for each file. This spark rate was determined by counting each signal region that contained a peak that was at least three standard deviations out of the noise and rose from baseline to the peak value in ≤ 4 μs. This value was chosen based on the peaking time of the shaping amplifiers which is 3 μs. Overall, this spark rate appears to increase over the course of the run time, although it appears a dip is present about file 24. Cumulatively, these three plots indicate that the event rate increased with time while the number of recoil tracks identified within these events decreased per unit of time, and the number of spark-like signal regions identified within the traces of the events increased per unit of time. The neutron source strength does decrease over time; one would expect a decrease in source strength of $\sim$1.7% over the 24 days over which runs

were performed. Assuming the observed recoil rate scales proportionally with the neutron source strength, this cannot account for the decrease in rate observed in (b) which was $\sim$80% over the course of $\sim$18 hours.

A plausible explanation is that the increase in spark-like signal regions results in a decrease of recoil-like tracks passing through the analysis. The gas was not being flowed through the detector and so it is thought that the properties of the gas change over time. After a gas fill, air slowly leaks into the vessel. This will, over time, change the dielectric properties of the gas and possibly lead to break down and hence sparking more frequently in the MWPC. This can impact the identification of recoil tracks in a couple of different ways. Firstly, a recoil may be missed completely due to dead time. Dead time is incurred on a per wire basis. Each time trigger occurs and a wire is read out, this is followed by some dead time. An upper limit of 27.7 ms was determined for the dead time. This value was found by studying the timestamps of 7,325,104 anode wire traces, which were accumulated for the L, R, F, and T runs. Each timestamp was the real time (RT), as described in Section 2.1.5. For each file of a run, the differences in time were found between all consecutive timestamps that belonged to the same anode wire, and this was done for all active anode wires. The lower bound of the resulting distribution of time differences corresponds to the upper limit on the dead time reported above. Secondly, as sparking increases the rate at which spark signal regions appear on the same trace as recoil signal regions will also increase. If spark and recoil signal regions overlap, these tracks may not pass through the recoil analysis. If a spark creates a separate track from that of a recoil within the same event, this recoil will also be missed since only single-track events were analyzed in this work. It is thought that the apparent disagreement of recoil track rates for runs 20170523-14 and 20170524-02 can be attributed, at least in part, to the increase in spark rate as explained above. It should be cautioned, the rate uncertainties reported in Table 3.5 had assumed Poisson statistics which further assumes tracks occur at some constant average rate, since the rate is clearly changing these uncertainties may not be accurate. Looking at the table, one can observe this same type of behavior for other neutron runs of the same source

position and common gas fill. That is, a decrease in rate for runs which were performed sequential to each other and otherwise appear equal.

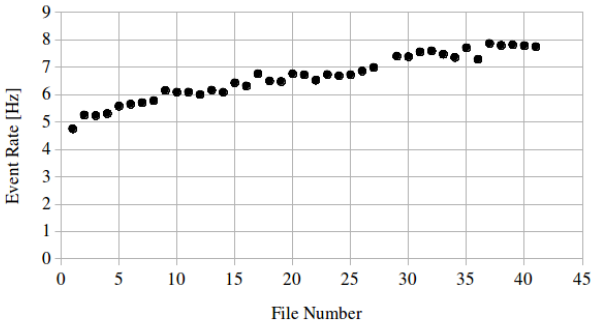

(a)

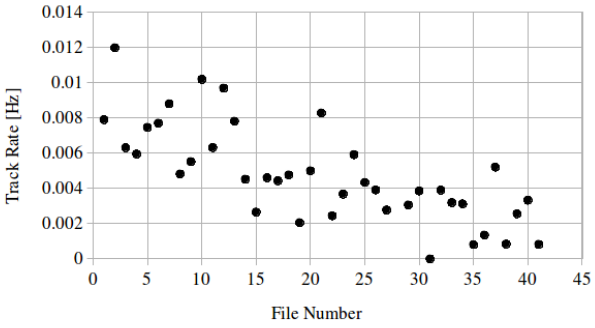

(b)

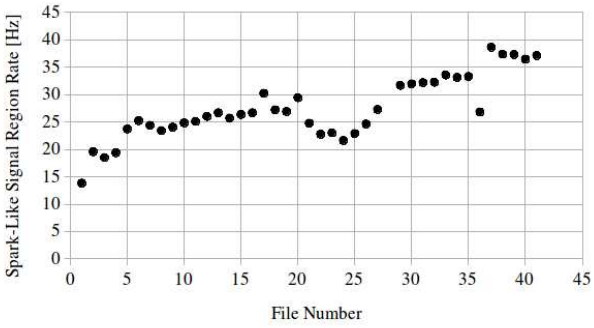

(c)

Figure 3.10: The event rate, recoil track rate, and spark-like signal region rate for the files which compose runs 20170523-14 and 20170524-02. Further explanation appears in the text.

Poisson statistics can be used to compare the recoil track rates for BG run 20170523-11 and R run 20170523-14. There was a gap in time of $\sim$1.75 hours between these two runs in which the field wires were ramped down in a controlled manner by a safety mechanism and the ramp down occurred due to a faulty 9 V power supply. After addressing the issue, the field wires were ramped back up to the same voltage previous to being brought down. The same gas fill remained and it is not believed that this had any significant effect on the state of the detector other than aging of the gas over this time period. Since the BG run preceded the R run, the assumption will be that the exposure of the detector to the neutron source does not influence the track rate. The BG rate from Table 3.5 is 0.87 tracks per half hour. For the first three files of the R run, 52 tracks were observed

over 100.14 minutes as shown in Table 3.6. Only the first three files were used since it is known that the rate changes with time and since the combined run time for these three files is similar to the 103.4 minute BG run time. Rounding down, this corresponds to 15 tracks per half hour on average for the R run. The Poisson probability of observing greater than or equal to 15 tracks when 0.87 are expected on average is 4.2×10^{-14}. For a Gaussian random process, this p-value would be representative of a significance beyond 5σ. This indicates that the result is inconsistent with the assumption that exposure of the detector to the neutron source does not affect the track rate.

Table 3.6: Average analyzed track rate for the first few files of run 20170523-14.

File	$\Delta_{t_{run}}$ [minutes]	N	$\frac{N}{\Delta_{t_{run}}}$ [minute^{-1}]
20170523-14-0001	37.92	18	0.475
20170523-14-0002	30.58	22	0.719
20170523-14-0003	31.64	12	0.379
average			0.524 ± 0.175

Since the number of active wires varied between runs, effectively the size of the active volume and how it is split up changes from one run to another. The runs of 20170511 do not contribute significantly to the total number of tracks for each run and therefore the fact that the number of wires active for these runs being different than others also should not be of great consequence. All runs after 20170511 have at least 103 wires active wires in common. The previous piece of information is not obvious from Table 3.5 since only the number of active wires for each run is listed without reference to which wires specifically in the detector were active. It was verified that the same 103 wires were active for all runs after 20170511. Similarly, all runs with 143 active wires have those specific wires in common with all runs with greater than 143 wires. The largest number of active wires was 157. This means that the active detector volume is at largest $1 - \frac{103}{157} = 0.34$ different from one run to another. Ideally one would want the same active volume for each run, this could have been achieved by only keeping those tracks which hit wires that are common to all runs. However, the fact that track numbers are low led to the decision to keep all tracks which pass

the analysis. Since the source is placed in close proximity to the detector and has an appreciable angular spread of incident neutron directions having different sets of active wires for runs, even of the same source, could possibly lead to a difference in results. For example, consider a run where the neutron source is placed on top of the vessel. The wires at the top of the detector are closer to the source and so the incident neutrons will have a larger angular spread in incident direction than for those wires farther from the source. This will result in a difference in nuclear recoil directions for wires closer to the source when compared to those farther from the source. So, if two top runs had been performed where the first had only the top half of the wires being read out and the second had only the bottom wires being read out, one may expect to observe difference in the directionality present in those two populations.

Table 3.7 shows the fraction of tracks that are observed for each neutron source position and for each combination of active detector wires for that particular run type. It is seen that for the R, F, and T runs that the same 143 active wires account for $\gtrsim 98\%$ of the tracks observed for each of those run types. This is not the case for L runs in which for 39.5% of the data 157 wires were active and for 59.3% of the data 103 wires were active.

In the subsequent sections the 607 L, 308 R, 639 F, and 535 T tracks will be combined into four populations respectively. The difference in the size of the active detector volume when comparing the L population to the other three populations should be kept in mind for the analysis of results.

3.2.2 Fiducialized Events Along $\hat{z}$

In Section 2.1.2 it was shown that the addition of O_2 gas to the nominal CS_2 DRIFT gas allows one to determine the distance z_{IP} from an MWPC that a nuclear recoil event took place within the detector volume. Some resulting signals for nuclear recoils which hit one or two wires are shown in Figures 3.11 and 3.12, respectively.

[36]Here it is also assumed that systematic uncertainty does not exist in measurement of the calibration constants. As described in Section 3.1.1 if a substantial fraction of 2-wire ^{55}Fe events have been missed the calibration constants may be systematically high.

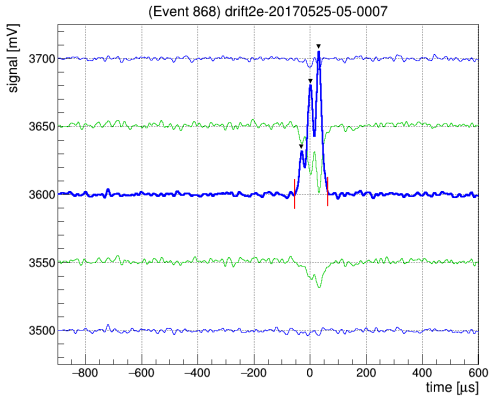

(a) z_{IP} = 6.3 cm, NIPs = 2582

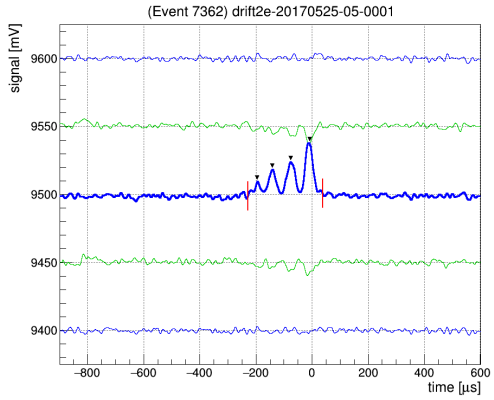

(b) z_{IP} = 13.6 cm, NIPs = 1478

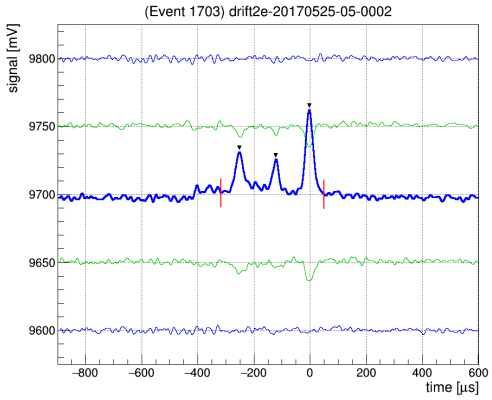

(c) z_{IP} = 25.7 cm, NIPs = 2348

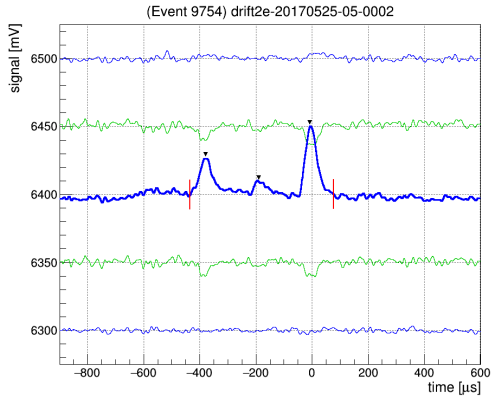

(d) z_{IP} = 38.3 cm, NIPs = 2424

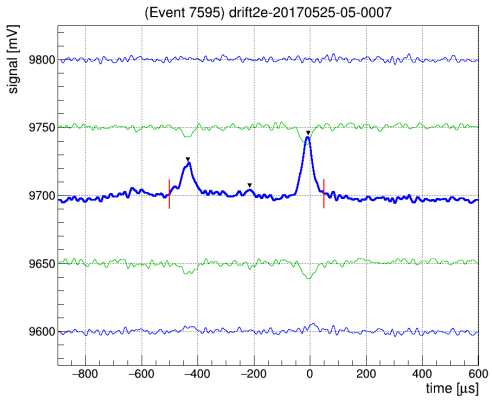

(e) z_{IP} = 44.2 cm, NIPs = 1766

Figure 3.11: Example 1-wire neutron recoil signals. Traces have been vertically offset for clarity and smoothed per the analysis algorithm of Section 3.2.5. The calibration constant calculated for ^{55}Fe run 20170525-03 from Table 3.3 was used to calculate the energy in NIPs for each event, which results in an uncertainty $\sim$0.016/0.519 = 0.0308 $\rightarrow$ 3.1% under the assumption that the size of the noise on the wires for these runs is similar to that of the calibration run[36]. The vertical lines about each signal indicate the signal region of the event as determined by the analysis algorithm. Triangular markers also indicate the peaks in the signal as determined by the analysis algorithm. Uncertainty on z_{IP} is discussed in the text.

Table 3.7: A comparison of the active detector wires for the L, R, F, and T runs. For each run the number of active wires n_{wires} and number of tracks observed for that run N are listed. The total number of tracks for each run type are shown in bold and the fraction of tracks that were observed for each combination of active wires is shown in the bottom row of each run type.

L	n_{wires}	121	83	157	157	157	103	103	
	N	2	5	78	56	106	74	286	**607**
		0.012		0.395			0.593		
R	n_{wires}	123	143	143					
	N	3	265	40	**308**				
		0.010	0.990						
F	n_{wires}	123	144	144					
	N	10	587	42	**639**				
		0.016	0.984						
T	n_{wires}	123	143	143					
	N	5	336	194	**535**				
		0.009	0.991						

The shape of observed signals appears to be in accordance with what has been previously observed and discussed in Section 2.1.2. For each signal shown, the peaks are termed I, S, P, and D from right to left. For all signals shown, the I peaks have the largest amplitudes. The D peaks are of relatively low amplitude and are not clearly visible in all signals. For low-z_{IP} events, the peaks merge while for high-z_{IP} events the peaks are more spread out. It is also apparent that the size of the S peak decreases with increased z_{IP}, indicating that the S charge carriers have a finite lifetime.

The mean free path for elastic scatters of ^{252}Cf neutrons in 40:1.5 Torr CS_2:O_2 is $\sim$1124 m, see Appendix A. Since this is much larger than the dimensions of the detector one may naively expect a flat distribution of event locations along $\hat{z}$. A track of ionization deposited far from the MWPC will result in a signal with the charge carrier peaks more spread out and will undergo more diffusion during drift than an equal track deposited close to the MWPC, which can have the peaks overlap and result in an overall larger amplitude signal. Therefore, the latter track may trigger the acquisition system and be saved to file while the former will be missed. Further, due to the geometry of the source placement for each run, the angular distributions of tracks from source

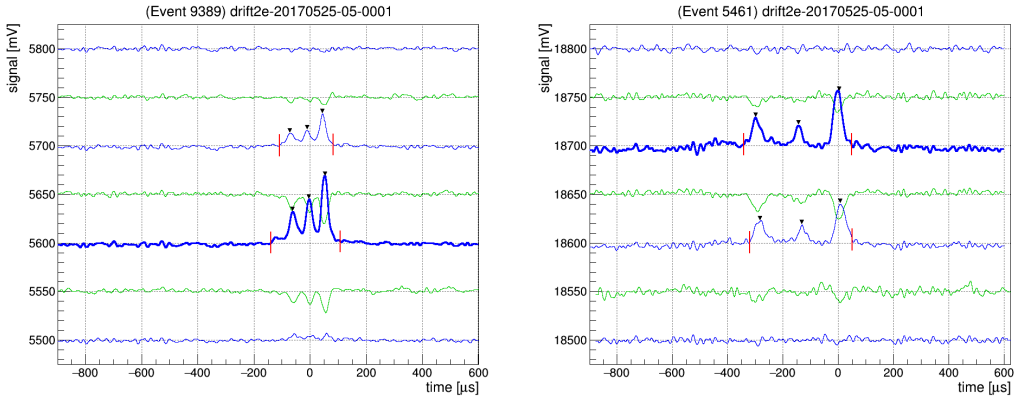

(a) z_{IP} = 12.0 cm, NIPs = 3584

(b) z_{IP} = 31.0 cm, NIPs = 4194

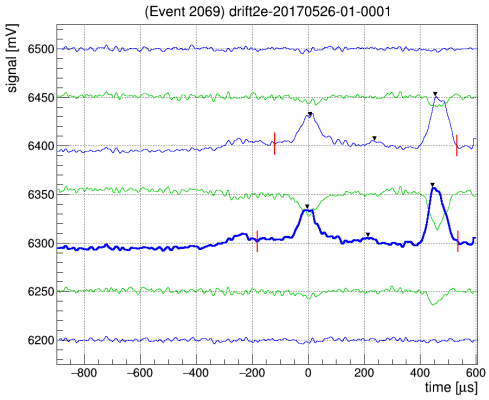

(c) z_{IP} = 46.2 cm, NIPs = 7472

Figure 3.12: Example 2-wire neutron recoil signals. Traces have been vertically offset for clarity and smoothed per the analysis algorithm of Section 3.2.5. For further details refer to the caption of Figure 3.11.

neutrons will be distinct per step in z_{IP} in the detector volume. For instance, even though the L and R runs were set up symmetrically, the angular spread of neutrons at low-z_{IP} is greater than at high-z_{IP} while the opposite is true for R runs. Efficiencies for triggering and analysis of tracks that occur at the same z location but have differing orientations may not be equal. Further, the amounts and types of material a neutron must pass through before reaching the left detector volume was not identical for each source position. So, in actuality one may not expect a flat distribution of tracks along $\hat{z}$, and further one should not expect distributions from different run types to be identical.

After the analysis of Section 3.2.5 was applied, all tracks which passed the analysis were visually inspected. In doing so it was found that the analysis, in its current incarnation, is not totally

efficient at only passing tracks that appear to be recoil-like, and sometimes fails to correctly determine z_{IP} for a recoil track, see Section 3.3.3. These types of tracks are termed *TracksCPA*. The distributions of z_{IP} for each of the runs both before and after identifying *TracksCPA* are shown in Figure 3.13.

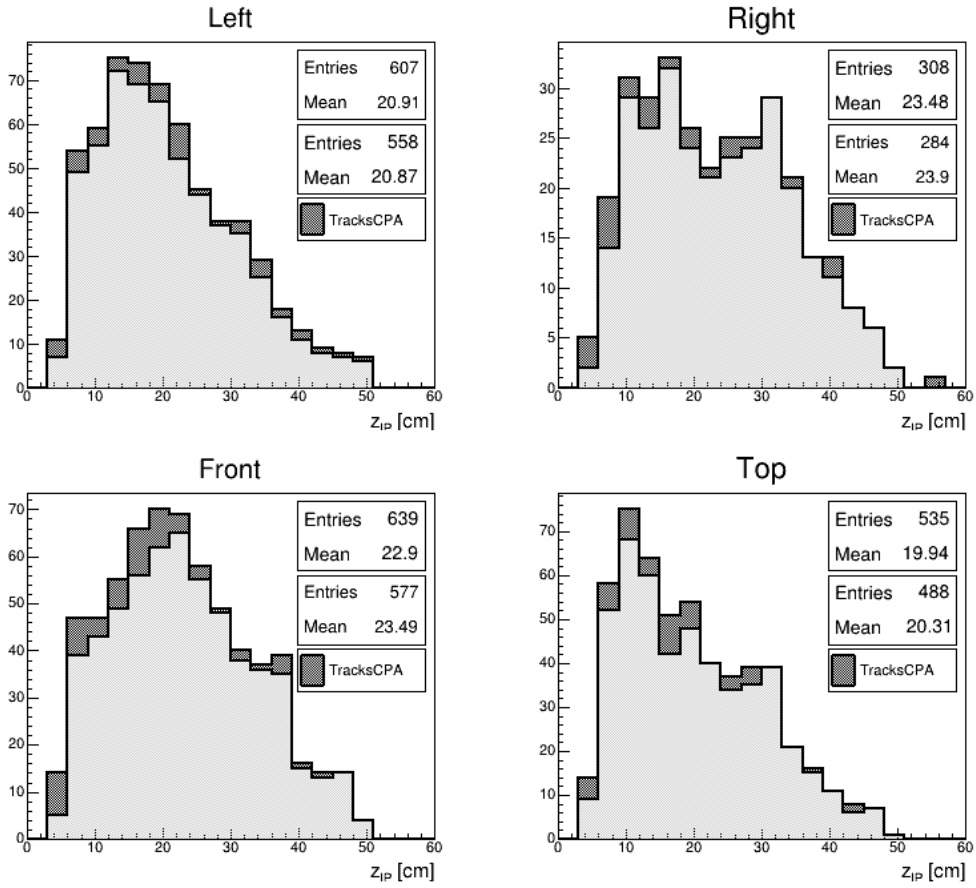

Figure 3.13: Distributions of z_{IP} are shown for each neutron source position both before (sum of light and dark entries) and after (light entries only) removing *TracksCPA*, which are described in the accompanying text and Section 3.3.3. Statistics are given for the former(latter) in the top(bottom) box of each histogram. The comparison is to provide one with information as to where *TracksCPA*, which lead to contamination within each sample, fall within each distribution. Tracks were histogrammed for $0 \leq z_{IP} \leq 60.0$ in bins of width 3 cm.

The distribution of events in z_{IP} for the right run exemplifies the necessity for studying *TracksCPA* since an event was identified as having a z position on the opposite side of the cathode from the LMWPC; the cathode is located 50 cm from the MWPCs. Since the size of the S peak becomes

small with increased drift distance, the S peak for this event was missed during analysis. When this occurs it is then possible for the D peak to be misidentified as the P peak and the P peak to be misidentified as the S peak. In doing so, the P to I distance is erroneously found to be larger than in reality and so an incorrect z_{IP} value is returned. From the distributions it is clear that a combined detection plus analysis efficiency per step in z_{IP} exists, and the mode values for the L, R, F, and T runs after *TracksCPA* are 13.5, 16.5, 22.5, and 10.5 cm, respectively.

For each track, each z_{IP} was calculated using the method outlined in Section 2.1.2. The reduced mobilities in 40:1.5 Torr CS_2:O_2 were calculated under the assumption that the relationship between reduced mobility for each carrier type and partial pressure of O_2 remained linear above $\sim$1.1 Torr. The maximum z_{IP} values for the L, R, F, and T runs are 50.4, 49.0, 51.0, and 48.1 cm, respectively, resulting in a mean of 49.6 $\pm$ 1.3 cm. The minimum values are 5.1, 4.0, 4.0, and 4.2 cm, resulting in a mean of 4.3 $\pm$ 0.5 cm. The preceding assumption appears to be reasonable since the mean of the maximum z_{IP} is consistent with the 50 cm LMWPC-to-cathode distance. Since the position of the cathode is fixed and since the maximum z_{IP} can serve as a measure of the LMWPC-to-cathode distance a reasonable estimate of uncertainty on individual z_{IP} measurements is $\pm$ 1.3 cm. This value is conservative in that it is improbable that all four tracks that were used for this calculation were deposited at the same exact distance from the MWPC, so, the value reported here is a convolution of the spread one might expect in the measured z_{IP} due to inherit randomness for a given true deposition location plus the actual physical spread in the four individual true positions of each track. In contrast, if one were able to deposit four identical tracks in the detector at the same location at different times one would measure a spread in z_{IP} values due to randomness alone.

3.2.3 Neutron Recoil Energy Distributions

The energy in NIPs associated with each track is calculated by multiplying the integral of each track signal region by an appropriate calibration constant from Table 3.3. The signal regions for several example tracks are shown in Figures 3.11 and 3.12. If an ^{55}Fe energy calibration run was

performed for the same gas fill as a neutron run, then the calibration constant of the ^{55}Fe run was applied to the integrals of the neutron run. If an energy calibration run had not been performed for a certain gas fill, then the average calibration constant across all ^{55}Fe runs of Table 3.3 was applied for neutron runs of that gas fill. The application of these constants assumes no systematic uncertainties in their values, however, as it was discussed in Section 3.1.1, the lack in number of two-wire tracks observed in calibration runs may indicate that part of the upper side of the calibration energy spectrum was not observed, which would lead to evaluated calibration constants which are systematically larger than in reality. The observed energy spectra, calculated via the method described above, for the L, R, F, and T neutron runs are shown in Figure 3.14. Energy spectra are shown both before and after *TracksCPA*, described in Section 3.3.3, has been applied. One of the track types which are cut with *TracksCPA* are those which were not well-contained, meaning that clearly some charge was visible on a wire adjacent to the rest of the track. Since tracks which are not well-contained will not provide a good energy measurement, the remainder of this section will not involve those which did not pass *TracksCPA*.

The smallest track energies in NIPs were 917, 1132, 965, 955 for the L, R, F, and T runs, respectively. An average of 992 NIPs gives an estimate of the effective energy threshold for ^{252}Cf neutron track detection, where any efficiencies due to hardware (triggering) and software (analysis) have been folded in. 1000 NIPs corresponds to an energy of 60 keVr for an S recoil and 40 keVr for a C recoil. The conversion from NIPs to keVr is discussed in Section 2.3 and Appendix B.0.2.

These ^{252}Cf neutron-induced recoil energy spectra can now be compared to a modeled recoil energy spectrum one may expect to observe from WIMPs of a given mass in order to determine how representative of a proxy the neutrons are. WIMP-induced recoils have been modeled as described in Appendix B. WIMPs in the mass range of 1 to 1500 GeV are considered here. For all WIMPs in this range it was found that $\geq 99.8\%$ of WIMP-induced recoils have energies of $\leq$ 6000 NIPs. The recoil energies observed for the four neutron runs were combined into six 1000 NIP bins up to 6000 NIPs. The recoil energy spectra for WIMPs of mass 1000 GeV and for the observed neutron recoils are shown in Figure 3.15(a). Both histograms have been normalized to

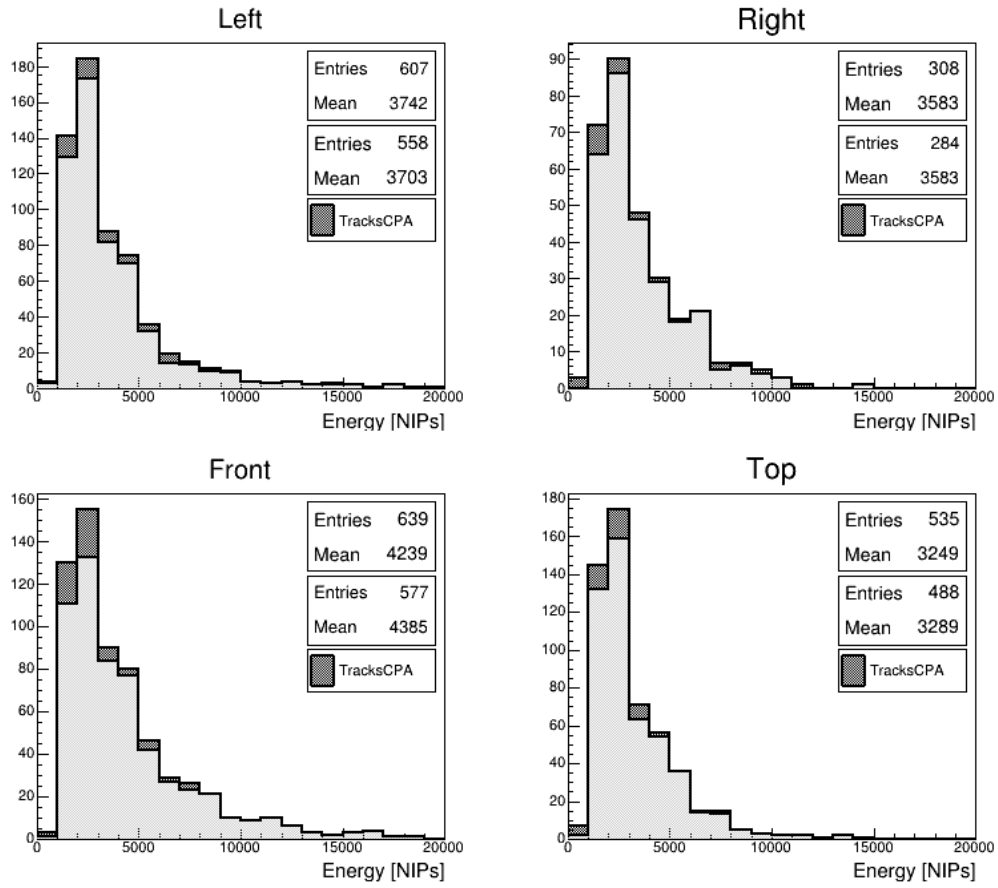

Figure 3.14: Distributions of track energies are shown for each neutron source position both before (sum of light and dark entries) and after (light entries only) removing *TracksCPA*, which are described in Section 3.3.3. Statistics are given for the former(latter) in the top(bottom) box of each histogram. The comparison is to provide one with information as to where *TracksCPA*, which lead to contamination within each sample, fall within each distribution. Tracks were histogrammed for $0 \leq$ NIPs ≤ 20000 NIPs in bins of width 1000 NIPs. $489/558 = 0.88$, $243/284 = 0.86$, $448/577 = 0.78$, $446/488 = 0.91$ of the recoil energies are $\leq$ 6000 NIPs for the L, R, F, and T runs, respectively.

the number of entries in each respective histogram. In doing so, the fraction of overlap between the two histograms serves as a measure of how representative the neutron recoil spectrum is of the WIMP recoil spectrum. Complete overlap results in an overlap fraction of one and no overlap results in an overlap fraction of zero. For 1000 GeV WIMPs, the overlap fraction is $\sim$0.2. This can greatly be attributed to that fact that the detector plus analysis is insensitive to those WIMP recoils of energies < 1000 NIPs. To understand which WIMP masses may result in the largest sensitivity, the overlap fraction versus WIMP mass is shown in Figure 3.15(b). It is apparent that the largest

overlap fraction occurs for WIMPs of masses $\gtrsim$ 1000 GeV where the overlap fraction begins to flatten out to a value of $\sim$0.2.

The overlap plot implies that it would take more detector exposure to accumulate statistics for lower mass WIMPs in comparison to larger mass WIMPs. In principle, any WIMP mass that can produce recoils above the threshold energy at $\sim$1000 NIPs can be modeled by neutron source recoils. After neutron recoil data has been gathered, this can be achieved by selecting the correct proportions of neutron recoil tracks from each energy bin, which the detector is sensitive to, in such a way to force the energy spectrum to match that expected for a certain WIMP mass. This is done in Section 4.

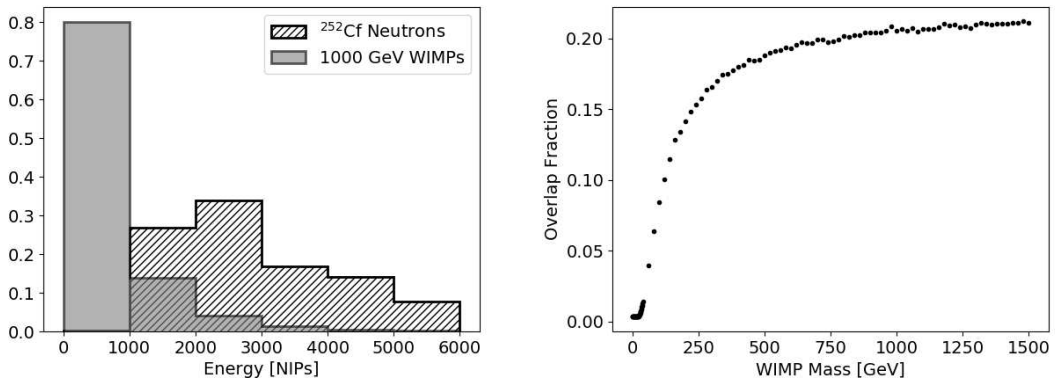

(a) **(b)**

Figure 3.15: (a) The combined ^{252}Cf neutron recoil energy spectrum and that for WIMPs of mass 1000 GeV. 10^5 WIMPs were simulated and the six energy bins for neutron recoils contained 6, 436, 551, 275, 230, and 128 entries, respectively. Each spectrum is normalized to its number of entries. The region of overlap between the two histograms serves as an estimate of how similar the two spectra are. (b) The overlap fraction is presented as a function of WIMP mass. For each WIMP mass 10^5 recoils were generated.

3.2.4 Range Components

One measure of directionality is found from the range components of the track along each of the axes of the detector, which nets the orientation of the track in the detector. Other iterations of the DRIFT-II experiment have been shown to provide the track length in three dimensions [88] [81].

DRIFT-IIe is designed to provide only the length of the track along the x and z directions. This is due to differences in MWPC design for the two cases. Other iterations of DRIFT-II had MWPCs composed of three planes of wires [90] [78]. One plane of anode wires which are orthogonal to and sandwiched between two planes of wires which shape the electric field within the MWPC. The orthogonal planes allow for the reconstruction of both x and y measurements of the track length. The single wire plane of DRIFT-IIe MWPCs can only provide a length measurement for the component of the track length which is perpendicular to the wires of the MWPC. The z length for both cases is reconstructed from the length in time of collected signals.

The loss of one dimension of the track, while not ideal, allows for other pragmatic features. An MWPC consisting of one plane of wires is mechanically simpler and requires less materials than an MWPC composed of three planes. This results in an MWPC which costs less to build and is also easier to repair. These features are especially important if one were to scale up the size of the detector volume.

The x and z lengths of the track will be termed Δx and Δz, respectively. Δx is essentially the number of anode wires which result in an observable signal due to the track of ionization. To simplify this language, it is the number of anode wires which are *hit* by the track. Δz is proportional to the width in time of the signal from one of the charge carrier types. While directionality has previously been measured from the range components of tracks in previous iterations of the DRIFT experiment, the tracks of ionization are known to not be completely straight on account of straggling [68]. Therefore, components of the track along each dimension result in the straight line distance or range along that direction. The full path length of the track is not measurable with this detector.

The pitch or distance between anode wires is Δx_{wires} = 2 mm. Let n_{wires} represent the number of anode wires hit by a track. Figure 3.16 shows what the electric field looks like near the anode and field wires of the MWPC. That is, it shows the paths which carrier anions will follow as they approach the anode wires. The number of anode wires which a track hits depends upon where the track was deposited relative to the anode and field wires. For instance let us consider a track that

has a true x extent of just less than 2 mm. If the orientation of the track is such that it is centered horizontally along $\hat{x}$ directly above of one of the anode wires in the figure, then all of the charge will follow the field lines to a single anode wire. If instead, the same track were deposited such that it is centered horizontally along $\hat{x}$ directly above of one of the field wires, then charge will follow the field lines to two anode wires.

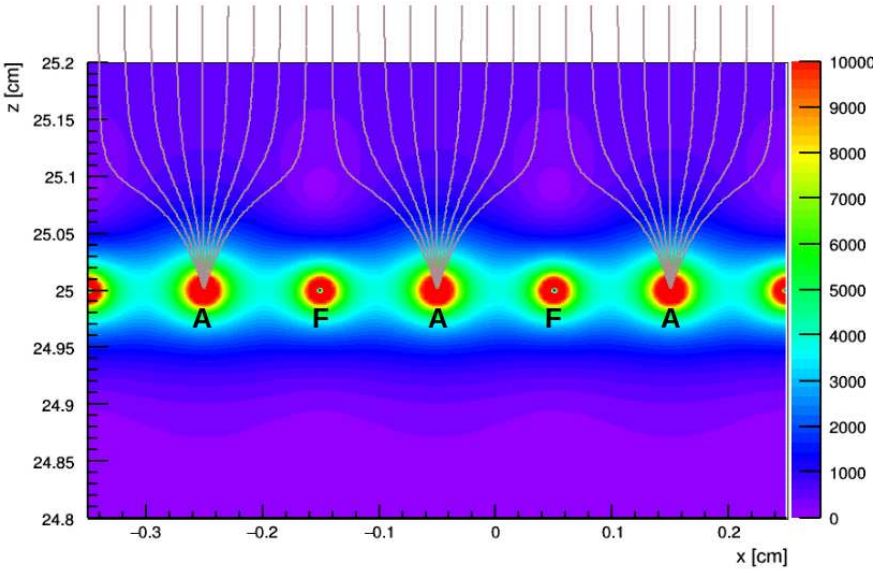

Figure 3.16: The electric field strength near the wires of the MWPC and paths of anions as they approach the anode wires are shown. Three anode wires (A) and two field wires (F) are oriented in/out of the page. Twenty-seven CS_2 anions were placed evenly spaced $\sim$1 cm away from these wire and allowed to drift. The electric field strength has units of V/cm. The simulation was performed with Garfield++ [112]. For the simulation, the drift gas was room temperature 40 Torr CS_2, the anode wires were grounded, the field wires held at -900 V, and the central cathode was held at -30 kV. Dissimilar to the detector description in Section 2.1.1, 31 0.5 cm field cage wires were used to step down the voltage over the 50 cm drift volume to set up the uniform drift field; also, only 100 anode and 100 field wires were included, decreasing the x-length of the volume. The wires shown are those which were central-most to avoid any edge effects.

In general, if a track hits n_{wires} then the maximum Δx it could have spanned is given by 2 mm multiplied by n_{wires}. Quantifying the minimum distance a track could have spanned depends on the number of anode wires which were hit. If $n_{wires} \leq 2$, then the minimum possible Δx could approach zero. For instance a track could hit two wires if all the charge of the track approaching the MWPC is along a line parallel with the $\hat{z}$ of the detector and is also directly in line with one of the field wires. If $n_{wires} > 2$, the minimum possible Δx is found by multiplying 2 mm by the

quantity $(n_{wires} - 2)$. For instance a track could hit three wires if the ionization has an x extent that is approximately centered on an anode wire and just surpasses the two adjacent field wires. To conform with previous definitions within the DRIFT collaboration the x length of a track will be calculated with Equation (3.1). This will assign a length of 1 mm to all tracks which hit one wire. For perspective, the total length of WIMP recoils are expected to be a few mm in length [137] [88], and therefore by geometry one would expect to see predominantly 1-wire or 2-wire WIMP recoil tracks. A 3 mm track can only hit 3 wires if the beginning and end of the track both extend past a region that spans two field wires. A simple Monte Carlo was written in which a straight 3 mm track was randomly oriented in three dimensions and randomly positioned within the detector volume. The number of wires which the track would hit was then calculated, and 10^5 trials were performed. For this simple MC, any affects such as diffusion or whether or not a certain portion of the track had enough ionization density to actually trigger a specific wire were ignored. In doing so, it was found that 44.89% of tracks hit one wire, 49.52% hit two wires, 5.59% hit three wires, and no tracks hit greater than three wires.

$$\Delta x = \Delta x_{wires} n_{wires} - 1 \text{ mm} \tag{3.1}$$

From the preceding discussion it is clear that the relative uncertainty in an individual Δx measurement is quite large. For a 1-wire track the range of possible Δx lengths in mm is (0,2][37]. For 2-wire tracks that range of possible Δx lengths is (0,4] mm, for 3-wire tracks the range is [2,6] mm, and so forth. However, one is really concerned as to how the distribution of Δx lengths for a particular neutron run will compare to that of another neutron run. For a T neutron run one may expect the recoils on average to have a larger Δx than for a L or R run. It is the difference in comparing the distributions of each population in which one is interested.

The details of minority peak formation in the signals was previously described in Section 2.1.2. To measure Δz the width in time of one of the three peaks of the signal I, S, or P must be used.

[37]Here typical mathematical notation is used where "(0" indicates that the range of possible values begins with a value just larger than 0 but excludes 0 itself. The end of the range of possible values is 2, inclusive.

The I peak will be used for this purpose. It is chosen because it is always the largest amplitude peak. The S peak in particular would not be a good choice since the S carriers are known to have a finite lifetime and therefore the size of this peak is relatively small for events that occur far from the MWPC. The length in time of the I peak signal is proportional to Δz since the drift speed of the I carriers is $\sim$constant in the drift volume[38]. This is true as long as the electric field is uniform over the volume and as long as the pressure and temperature of the gas are also constant. Since all parts of the track drift at the same speed, knowing the length in time of the signal from a track along with the drift speed results in Δz.

The speed at which the I carriers drift to the MWPC is calculated with Equation (3.2) where $p = 41.5$ Torr, $E = \frac{|V_{FW} - V_{cathode}|}{50 \text{ cm}}$, V_{FW} is the field wire voltage for a particular run, $V_{cathode} = -30.0$ kV, $T = 293$ K was used for the temperature of the gas although this was not measured for each run, and $T_0 = 273.15$ K. The reduced mobility μ_{0I} can be calculated from [111] using an O_2 partial pressure of 1.5 Torr which results in $\mu_{0I} = 360.7 \pm 0.2 \frac{\text{cm}^2 \cdot \text{Torr}}{\text{V} \cdot \text{s}}$. $V_{FW} = -896$ V yields a drift speed of 52.4 m/s which is equivalent to 0.0524 mm/μs; the latter is particularly useful since the tracks are millimeter scale and the signals are digitized with microsecond precision. This implies a Δz spatial resolution of 0.0524 mm for the conditions stated above.

In the preceding paragraph, it was assumed that the gas temperature and pressure were constants. In reality, the gas temperature will fluctuate with the room temperature. The lab space that housed the vessel was air conditioned and so the assumption of constant temperature is likely sufficient even though the true temperature likely oscillated between air conditioning cycles. Additionally, there may have been an offset between runs performed during the day versus night. Assuming an uncertainty of ± 5 K, which would imply a room temperature range of 15°C to 25°C, results in a relative uncertainty on temperature of $(5 \text{ K})/(293 \text{ K}) = 0.017$, as an estimate. Also,

[38] In reality the size and width of the I peak may be in part affected by the existence of the other peaks. For instance at low-z_{IP} the peaks overlap which may increase both the height and width of the I peak. The S peak is also known to have a finite lifetime. In Figure 3 of [78], it is shown that for increased drift distance the integral of the S peak relative to I decreases, as it does so, the integral of the P peak relative to I and the integral of the D peak relative to I increase. It may be that the integral of the I peak also changes as that of S decreases which could affect the height and width of the I peak.

for a given gas fill the pressure tends to first drop by $\lesssim$ 0.5 Torr as gas adsorbs on to the detector and vessel materials. As time goes on the pressure tends to then increase as air leaks into the vessel. A maximum value of $\sim$0.05 Torr/hour was observed over all runs in which the leak rate was recorded. The gas fill of longest duration was $\sim$36 hours which would result in at most 1.8 Torr of air leaking into the vessel. Addition with the 0.5 Torr of gas adsorption results in a maximal range of 2.3 Torr of pressure fluctuation which is 5.5% of the 41.5 Torr target pressure.

$$v_I = \mu_{0I}\sqrt{\frac{T}{T_0}}\frac{E}{p} \tag{3.2}$$

To calculate Δz it is left to define what is meant by the length in time of the I peak signal. A track can be composed of signals on more than one wire. The length in time is found by summing in time the signals from all wires of a track, and using the half maximum width of the summed I peak signal as the width in time Δt_I. For single wire tracks no summing needs to be performed. For clarity, the determination of Δt_I is exemplified for a 1-wire track and a 2-wire track in Figures 3.17 and 3.18, respectively.

The z component of the track is then defined by Equation (3.3). It should be emphasized that it was chosen to define the length in time of the I peak signal by its half max amplitude. It is not necessarily the goal in this work to measure the true z extent of the tracks, but instead to apply a consistent definition for all observed tracks to calculate a Δz value and then to compare the Δz distributions from one neutron exposure to another. One could have chosen to define the length of a signal by the width in time, for example, at 1/4 of the maximum amplitude, which would then return in general larger z values. There are a couple of reasons for the choice that was made. Historically, it has been convention within the DRIFT collaboration. With the choice one needs to remember the behavior of the minority peaks. If a track is deposited close to the MWPC the minority peaks of the signal do not have sufficient time to separate from one another and the result is that they overlap. If one wants a single consistent definition of the width in time of a signal they must decide how much of the signal left of the I peak must be present for the calculation to be made. The farther left from the I peak one chooses to set this value results in more low-z_{IP} events

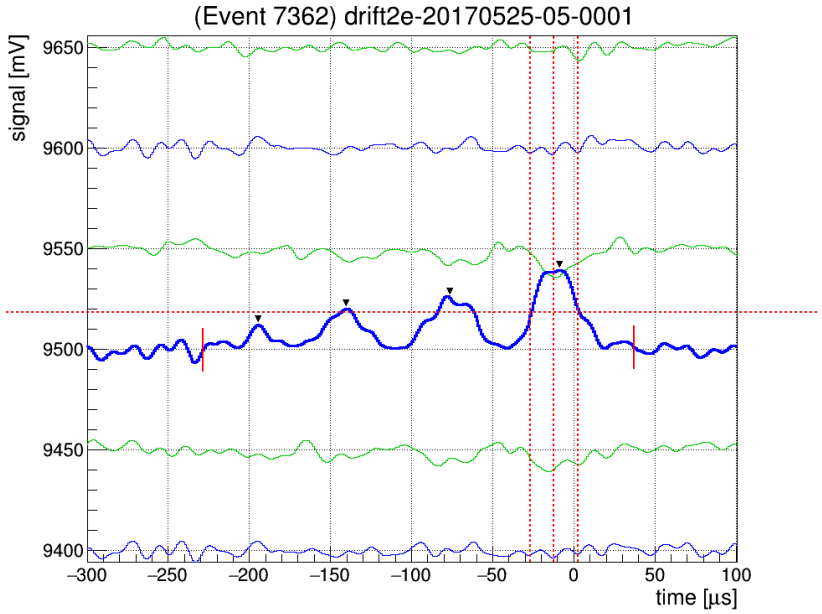

Figure 3.17: A 1-wire recoil signal is shown. The two outermost vertical-dashed-red lines about the I peak (the rightmost peak) indicate the width in time of the peak at half of its maximum amplitude. This width is defined as Δt_I.

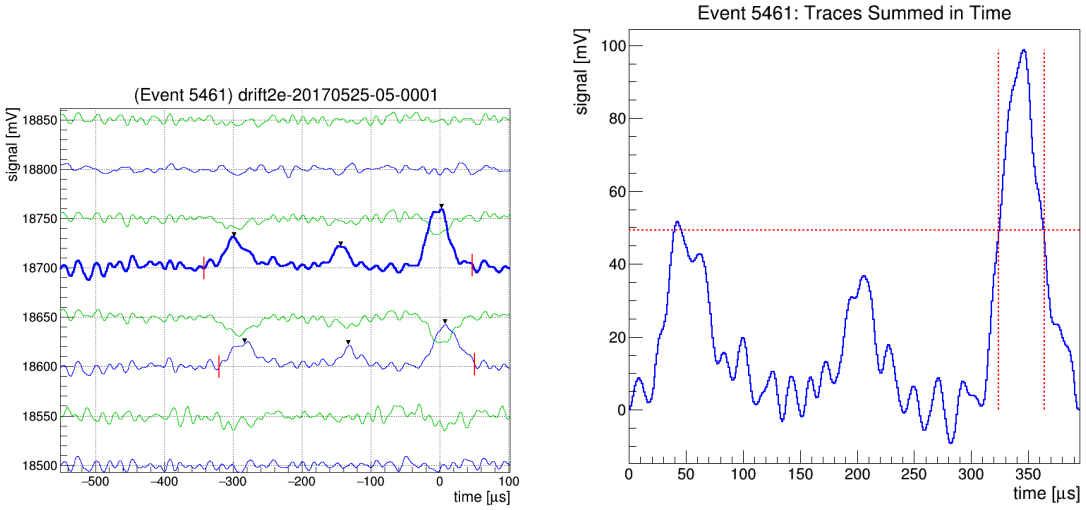

(a) **(b)**

Figure 3.18: (a) A 2-wire recoil signal is shown. (b) The two individual signals have been summed together in time. The two vertical-dashed-red lines about the summed I peak indicate the width in time of the peak at half its maximum amplitude. This width is defined as Δt_I.

being lost. Further, one does not want to use all of the signal that is right of the I peak to calculate the length in time. This is due to how the signals are formed. Most of the signal is formed by the positive ions which are created in avalanche and drift away from the MWPC, see Section 2.1.3. These ions can result in long tails on the signals.

$$\Delta z = v_I \Delta t_I \tag{3.3}$$

Two factors further influence the measured Δz values. First the average electronics shaping time was measured to be 1.45 $\pm$ 0.02 μs in Section 2.2.1 and the Gaussian smooth applied during analysis has standard deviation 4.0 μs. This implies that the true width in time of a signal is in reality shorter than the width in time as measured during analysis. The result is that the measured Δz values are likely larger than if the width in time at half maximum of the unshaped signals had been used to determine Δz values. Second, tracks of ionization which are deposited farther along $\hat{z}$ from the MWPC incur more diffusion as they drift to the MWPC, which widens a signal in time. A possible improvement, not implemented in this dissertation, could be made to the determination of Δz values. In Section 2.1.3 it was discussed that the amount of diffusion-induced randomization incurred along the longitudinal, $\hat{z}$, drift direction $\sigma_{diffusion} \propto \sqrt{\frac{T_{longitudinal} \cdot z_{IP}}{E}}$. In references [111] [110], 40 Torr CS_2 gas and some other drift gas mixes are considered which could serve as approximations for the 40:1.5 Torr CS_2:O_2 gas used in this work. In the previous expression, z_{IP} is the distance the track has drifted, E is the electric field strength, and $T_{longitudinal}$ is a factor related to the energies of the drifting anions and has been studied. The addition of O_2 to the drift gas allows for the measurement of z_{IP}, and with $T_{longitudinal}$ and E known it would be possible to calculate values for the longitudinal diffusion and adjust the Δz values on a track-by-track basis.

3.2.5 Analysis of Triggered Runs

This section describes the full analysis chain which is used from the time raw data is saved to file up until tracks are selected from the data and determined to be nuclear-recoil like. This

analysis was written in code, from the ground up, by the author of this dissertation[39]. The reader is reminded of the terminology laid out in Section 2.1.4 and the two different modes of detector operation, triggered and untriggered, as well as the calculation of timestamp values as presented in Section 2.1.5.

Raw data files, discussed in Section 2.1.5, are suffixed with the tag "ndd". The raw data files are set to contain up to 50,000 anode wire traces along with the 50,000 correspondingly numbered field wire traces. This is the maximum file size, but for instance if a run is stopped mid-file, these raw files can be of a lesser size. After the data have been saved to file, the raw data files are processed in a series of six stages, some of which are further divided into substages. The analysis chain can be run in a fully-automated mode, in that Bash [139] scripts are used to control the flow of input and output files from one stage to the next. The analysis chain of this section only fully applies to runs collected in triggered mode. There are differences to the analysis of untriggered runs which are described separately in Section 3.1.3.

The analysis code is written in the C++ language. The code was written as a group of custom-made classes, some of which depend on ROOT [113] classes. ROOT can be understood as a set of classes, written in the C++ language, for the purpose of storing and analyzing data. Different main programs can then be written using these custom classes. The custom classes were written in a way that the full class structure can be filled and output in ROOT file format. All code was built using CMake [140]. Writing C++ classes that are compatible with ROOT allows those classes to be used in three ways. First the individual C++ classes can be declared at the beginning of other pieces of C++ code and be used when writing further code just like any other native C++ class. Second, one can write standalone ROOT scripts which import and use the classes. Thirdly, one can use the custom classes in real time within the ROOT terminal. The first allowed for the production of a fully-automated analysis chain as well as the production of an event browser that has a graphical user interface and can be used to view and analyze events in real time. All figures

[39]I would like to thank Alexei Dorofeev, a former Research Scientist at Colorado State University. Things that I learned from Alexei were applied to the development of this code.

in this dissertation that display traces for an event or track, for example Figures 3.11 and 3.12, were output from this event browser. The second allows one to write up other analysis algorithms that either need to be tested or do not necessarily need to be part of the standard analysis chain. For instance, the analysis chain is only meant to identify recoil-like tracks within events. Once these have been identified and output statistical analysis of these populations can be performed with standalone ROOT scripts. The third form of implementation allows, for instance, one to load events and identified tracks and perform any desired manipulations to them in real time.

Stage 1: Sort Traces and Group Traces into Events

The input to this stage is a raw ndd file. This file contains a main header that stores information about the run. The sampling frequency (1 MHz), ADC resolution (12 bits), ADC range (1807 mV), threshold voltage for triggering (20 mV for this work), the length in bins of each trace (1500), the number of trace bins which are pretrigger (900), and any comments for the run are stored in the header.

Following the main header, traces are iteratively stored. Each trace has its own header and is followed by 1500 bins of ADC counts. The trace header stores information concerning the wire type (anode or field), absolute wire number within the detector, and two timestamps which can be combined to reconstruct the real timestamp for the trace, see Section 2.1.5.

Each electronics box of the detector, Section 2.1.1, can read out 120 channels 60 of which are anode wires and 60 of which are field wires, let $N_{CPB} \equiv 120$. If the detector were fully active, there are two MWPCs each of which has 457 anode wires and 457 field wires. This implies that eight boxes are needed to read out each MWPC, let $N_{BPM} \equiv 8$. Two pieces of information in the trace header uniquely identify which wire it belongs to. The first is the boxID and the second is the channelID. The boxID ranges from [0-7] for boxes of the left MWPC and [8-15] for boxes of the right MWPC. The channelID ranges from [0-59] for each box. For an anode wire its unique position in the detector is found by first determining which MWPC it belongs to followed by which wire number it is within the MWPC. Let the left MWPC be enumerated as MWPC 0 and the right MWPC be enumerated as MWPC 1.

$$MWPCID = \frac{boxID - boxID\ modulo\ N_{BPM}}{N_{BPM}}$$

$$wireID = channelID + \frac{N_{CPB}}{2}(boxID\ modulo\ N_{BPM})$$

Field wires have boxIDs that are offset positively by 16. That is the boxID for a field wire will appear in a trace header as [16-23] for a left MWPC field wire and [24-31] for a right MWPC field wire. Once it has been determined that a trace is that of a field wire, 16 can be subtracted from the boxID and the same two calculations as shown above can be used to determine its MWPCID and wireID within the detector.

For this work only the central half of the left MWPC was read out, it was instrumented with boxes 0 to 3. The wire numbering starts from zero from the bottom of the instrumented region, anode wire 0 is bottom-most followed by field wire 0 above it, wire numbers increment as one moves upward. With this understanding, the same calculations as described above can still be used to uniquely identify a wire, the point at which one labels wire 0 and starts counting has just been shifted upward from the case of a fully instrumented left MWPC.

Once the real timestamp of each trace has been determined they are sorted chronologically, they are not always written to the raw data file chronologically. Once sorted, any traces with real trigger timestamps which are within 1 ms of any other traces are all grouped together as an event. Any trace of an event only needs to have a trigger time that is within 1 ms of at least one other trace of the event, not all traces must be within 1 ms of each other.

This was needed for a couple of reasons, firstly it had been observed that some traces had incorrect timestamps which were written to file, this problem has since been addressed, sorting was kept in part to maintain a safeguard against this problem which had occurred before. Secondly, it was not always guaranteed that traces were written to file chronologically, this is possibly due to the order in which traces were pulled from a buffer and written to file.

The output of this stage is a binary file with the suffix "d2e". The main header information from the ndd file is retained in that of the d2e file, along with the total number of traces in the file

and total number of grouped events. Each event is then written iteratively to the file. Each event has a header, the beginning of which, is signified by the characters "EVENT". Next, the number assigned to that event in the file and number of traces which are present in the event are written. Following the event header, all traces for the event are iteratively written to file. Each trace has its own header which is similar to that of the ndd files. The boxID, channelID, wire type (anode or field), and timestamp information is stored in the header and is followed by the 1500 bins of ADC count data for the trace.

Once stored in d2e format, these files can be used in a couple of ways. The files can be loaded into the event browser, mentioned above, and used to simultaneously view all traces of an event. One can also use the browser to apply algorithms to analyze the event, some of which will be described in the sections that follow directly. By viewing the d2e files with the event browser, one gains visual feedback as to how the analysis algorithms work. The d2e files, after being automatically generated in the analysis chain, will also be passed into the next stage below.

Stage 2: Calculate Baseline and Noise Levels For Each Trace of all Events

The input to this stage is a d2e file generated in Stage 1. For each trace of each event the average pedestal (or baseline), and standard deviation about the pedestal are calculated. The latter tells one the size of the noise for each trace. The algorithm to do this is expounded upon in Stage 4. The ADCs used to digitize signals have a reported full range of 1800 mV, measurement by the developer of the readout electronics Jean-Luc Gauvreau resulted in 1807 mV [141]. This value will be used for any conversions of ADC counts to voltage in this work. The pedestal for each trace floats about midrange at $\sim$900 mV. For each trace the pedestal must be identified and then removed from the trace so that actual signal amplitudes, if present, and integrals can be measured. Pedestal and noise information for each trace of an event is then output in a ROOT file format that will be used by Stage 3. In the interest of disk space, these files may be deleted after Stage 3 has been completed.

Stage 3: Tabulate Health Statistics for Each Data File

The input to this stage is a ROOT file generated in Stage 2. This stage was developed primarily due to the fact that the detector was in an R&D phase over the time period that data was collected. Not all wires that were instrumented to be read out were active for each run, further, the wires which were active changed from one run to the next, see Section 2.1.6. Due to this, one needs a way to tabulate which wires were active for every file of every run. The aforementioned is one of the main tasks of this stage along with tabulation of other file statistics described below.

Spark events, see Section 2.2.1, are common within gaseous MWPC detectors such as DRIFT-IIe. Looking at Table 2.1, one can estimate the rate of sparks on individual wires to be 0.763 minute^{-1}. This value of was found by taking the number of spark-like signals regions in Table 2.1 for each file and dividing by the run time for that file. Each value was then further divided by the number of active anode wires for that run, which are reported in Table 3.5. These eight values were then averaged to estimate the number of spark-like signal regions per unit of time per wire[40]. For the untriggered and triggered runs analyzed in this work, see Tables 3.1, 3.2, and 3.5, the overall shortest run duration was $\sim$24 minutes. Assuming that the number of sparks observed per wire per minute follows a Poisson distribution where the mean value is 0.763 sparks per wire per minute, the probability of observing zero sparks over one minute is $P(0) = \frac{0.763^0 e^{-0.763}}{0!} \approx 0.466$. It follows that the probability of observing zero sparks over 24 consecutive minutes is $\approx 0.466^{24}$. Assuming that the state of all wires are $\sim$equal throughout each run, there is no reason to expect one wire to spark significantly more or less than the others[41]. With the preceding discussion, one can say with

[40] As a reminder, only those sparks that were the shortest in duration and consistent with the electronics shaping time were picked out for the analysis in Section 2.2.1. In addition, any traces that had more than one signal region identified were not analyzed. This implies that this estimated rate is lower than the true rate, making the estimate conservative. For instance, two sparks that occur in quick succession can appear on the same trace and were not counted.

[41] By equality, an assumption is made that all wires of the same type (anode or field) are all equal physically and in the conditions in which they are held. To be specific, all wires of the same type are of the same materials, dimensions, and the MWPC has been constructed carefully so that the wires are all secured and spaced isotropically. As to the conditions of each wire, it is assumed that the gas is distributed equally about each wire and that all wires of the same type are held at the same voltage.

confidence that if no traces are observed for a given wire for the file of a specific run, that wire was dead for that duration of time.

Based on the logic of the preceding paragraph, all alive wires are first found for a given file which was input into this stage. For each trace of each alive wire that is present in the file, the size of the noise (standard deviation about pedestal) was input to this stage from Stage 2. Knowing the size of the noise for each trace of each wire, the average noise across all traces observed for that wire over the course of the file is calculated, along with the uncertainty about this average.

Of the four electronics boxes that were available and enumerated 0 to 3, not all were active for each run. In Stage 1 it was shown that the wireID and MWPCID of a trace can be uniquely determined if one knows its channelID and boxID. It then follows that one can remap inversely to retrieve the channelID and boxID of a trace if the wireID and MWPCID are known. That is done here for all traces of a file to determine which electronics boxes were active. This statistic is useful in that it gives one an idea as to the shape of the active detector volume for the run.

For the purpose of calculating rates, the run duration in time for each file is calculated. One iterates through all traces of a file and finds the earliest and latest timestamps, the difference of which provides the run time for that file. After this, the next task is to tabulate which wires were dead and which wires are to be flagged as veto wires for the file. Dead wires, as explained above, are those for which no traces are observed. Since the alive wires have already been tabulated and since it is known which wires were instrumented, a comparison nets those wires which were dead. Both veto wires and active wires are subsets of wires which were alive. A veto wire is defined to be any wire, that if present in a track, that should raise a flag and prevent that track from further analysis. Active wires are those wires for which analysis should proceed. There are several ways in which a wire may be determined to be a veto wire, these are outlined below.

In prior phases of testing it was found that incorrect timestamps were being assigned to traces belonging to specific wires. A 24-bit timestamp TS was discussed in Section 2.1.5. It was found that for these wires TS was always being set to 0 or $2^{24} - 1$, that is it was always the maximum or minimum value allowed. This problem was fixed, however, since the problem had been observed

a guard was kept in place such that any wires which were observed to have traces with $TS = 0$ or $TS = 2^{24} - 1$ were deemed to be veto wires for that file. One does not expect to erroneously label a veto wire in this way often, assuming any TS for a trace is equally probable out of 2^{24} possibilities, the probability of a trace actually being assigned one of these two values is $\frac{2}{2^{24}}$, so for each wire one may expect this to occur once per every $\frac{2^{24}}{2}$ traces.

While browsing through events, it was noticed that some wires would have traces that were either completely flat or have a step-like feature. For both cases no noise was apparent on the wires. To veto wires for which these sort of features were observed, one can compare the RMS noise calculated for a trace against what one expects at minimum. From specifciations of the electronics, the minimum acheivable noise level is 3.0 mV [142]. A wire was therefore labeled as a veto wire if the noise observed for any traces of the wire were less than this value. After testing, this cut was not observed to veto wires other than those that were targeted. Comparison with Tables 3.1, 3.2, and 3.5 indicates that 3.0 mV is $\sim$3 times smaller than the smallest noise value observed on average.

For a given run, some of the four electronics boxes were active. An edge wire of any box which is adjacent to a nonactive electronics box or nonactive detector region is set as a veto wire. Two examples follow for clarification. As a reminder each box handles 60 anode wires and 60 field wires. Box 0 handles anode/field wires [0-59], box 1 wires [60-119], box 2 wires [120-179], and box 3 wires [180-239]. If all four boxes are active for a run then two wires are adjacent to regions of the detector which are not active at the bottom and top of the instrumented region, namely wires 0 and 239 are set as veto wires. Now suppose only boxes 0 and 2 are active for a run. Wire 0 of box 0 is adjacent to a region of the detector which is not instrumented, so wire 0 is labeled as a veto wire. Wire 59 of box zero also becomes a veto wire since it is adjacent to box 1 which is not active. Wires 120 and 179 of box 2 also become veto wires since they are adjacent to nonactive boxes 1 and 3, respectively.

A wire can be labeled as a veto wire in one other way. This actually doesn't get implemented in the analysis until later in Stage 4, see Track Analysis 06 below, once cuts to tracks are applied,

however, it is pertinent for the reader to be aware of these types of veto wires now. Any alive wire which is directly adjacent to a dead wire is labeled as veto wire. If a signal is deposited on a wire which is adjacent to a dead wire, one cannot discern as to whether the track may have also hit the dead wire, it is for this reason that wires of this type are labeled as veto wires. Suppose wire 33 is a dead wire, then wires 32 and 34 both become veto wires.

After the process above, the output for this stage is five different files. For all traces which belong to a given wire, the total number of traces observed for that wire as well as the size of the noise averaged over all traces for that wire have been calculated. Two plots are output to a ROOT file, the first histograms the number of traces observed for each wire, this is useful as one can identify wires which may be triggering more often than others and potentially cause issues during further analysis. The second is a plot of the average size of the noise which was observed for a wire plotted against its wire number. Next a text file is written that list all the statistics which have been calculated for the input file of this stage. This text file includes the timestamps for the earliest and latest traces of the input file, the electronics boxes which were active, the average amount of noise which was observed per wire, the number of traces per wire, a list of the dead wires, and lists of the veto wires specified separately for each of the classifications given above. This text file provides a useful reference to understand the state of the detector for that particular part of a run. Additionally, a set of three text files are output, two are references for the user and can be used if one needs to perform specific stages of the analysis on single files manually. These files are lists (one for the anode wires and one for the field wires) that specify the dead and veto wires in a format that is easily parseable. The third is a concatenation of the previous two files and is automatically fed into the next stage of analysis. This file will be called the dead-and-veto-wire file.

Stage 4: Nuclear Recoil Analysis

Three inputs are required for the this stage. The first is the d2e file, generated in stage 1, that corresponds to a given raw ndd file. Secondly, a log was generated that specifies the field wire voltage for each run, this file will be named the field-wire-voltage file. The cathode voltage was approximately the same for each run. These voltages are required for calculation of the electric

field strength for each run, and in part sets the drift speeds of the charge carriers. The third input is the concatenated dead-and-veto-wire file which was generated as output in stage 3. If automated batch analysis of files is being done, the correct dead-and-veto-wire file is grabbed via a Bash script, for manual analysis of files one needs to set this file. For this section, some terminology is used in reference to object-oriented programming, and specifically C++, for which it is assumed the reader has knowledge of.

As a reminder, each d2e file is a binary file of custom format. The file iteratively lists events, where each event is a set of traces grouped by their relative timing. Before describing how the analysis works, it will be described how the analysis code is structured. When the code was initially envisioned, it was a goal to write it in a manner in which the code could be extended to function for a detector which has an arbitrary number of MWPCs. The DRIFT-IIe detector has two MWPCs, but funding had been pursued by the DRIFT collaboration to scale up the experiment. With this knowledge in mind, the code was written as a set of custom classes that could be implemented in an object-oriented style, such that the classes would be readily available for future iterations of the experiment.

In Section 2.1.4, terms were defined to describe data collected with the detector. An event is a collection of traces, each of which may contain signal regions, that can be grouped into tracks. The classes of the analysis possess the same modularity. A simplified tree diagram, Figure 3.19, depicts the interplay of the different objects of the analysis. A plethora of function members and data members exist for the classes, the diagram shown is far from exhaustive, it is only to give one an idea of how the classes are structured.

Pointers were used extensively in order to increase the efficiency of the analysis in terms of utilization of disk space and computation speed. To this end, the custom classes use one of the powerful features of ROOT. That is the ability to write object pointers to file. To clarify, suppose two classes exist, class1 and class2, such that class2 contains a data member which points to an object of type class1. ROOT has the ability, to write an object of type class2 to file, and when the file is accessed at a later time it can reconstruct the pointer relationship to the object of type class1.

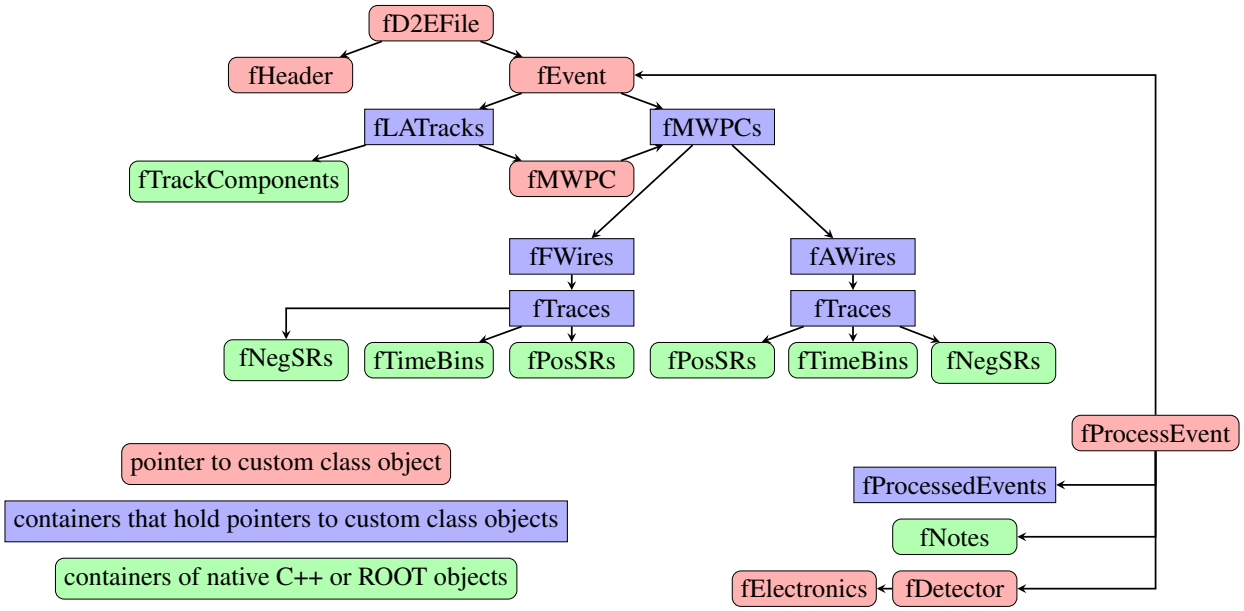

Figure 3.19: A tree diagram the represents how the different pieces of the analysis code interact.

Creating an object once, and then passing its address between objects can save both time and disk space, as opposed to copying and/or passing objects to other objects.

The tree diagram, Figure 3.19, has been composed of three different types of objects which have been defined within the diagram itself. Starting from the top of the tree and working downward, fD2EFile is a pointer to an instantiation of a custom class that can be used to access the different events contained within the file. One can iterate through the events or choose an event by its location within the file. The header information for the file is stored within fHeader. A pointer to fEvent is set within fD2EFile, fEvent is the current event which is being worked on. Within fEvent two containers of pointers exist[42], fLATracks and fMWPCs. The latter is a container of pointers, where each points to an instantiation of a class for each MWPC of the detector. The former is a container of pointers, where each points to a specific instantiation of a track, as stated previously a single event may be composed of more than a single track. Each track within the container has access to a data member fTrackComponents and each track has access to the MWPC on which the track appeared fMWPC. The fTrackComponents container lists the wire number, trace number, and

[42]In actuality there are more than two, fLFTracks, which is not shown, contains left-MWPC-field-wire tracks. Another two containers would be needed if the right MWPC were active.

signal region number within the trace for all signal regions which were determined to be part of the track. Using these components, the traces and signal regions can be accessed for each fLATrack through its fMWPC instead of having to copy this information into fLATrack. Each fMWPC can access two containers fFWires and fAWires, which contain pointers to class objects for each of the field wires and anode wires which were contained in the event. Each wire has access to a container fTraces for that wire. Each fTrace has access to the positive going signal regions fPosSRS, negative going signal regions fNegSRs, and fTimeBins which stores the 1500 bins of data for each trace.

The specifics of different analysis algorithms applied to each event are forthcoming. In general, algorithms are applied to each fEvent as follows. A class fProcessEvent is instantiated to handle this procedure. It has access to fEvent, on which it will be operating. Each time an algorithm is applied an element is added to the container fProcessedEvents. The first element of fProcessedEvents is a copy of fEvent in its original state. The second element will first be a copy of fEvent, and then after any analysis algorithm is applied, it is this second element which is modified. If another algorithm is applied a third element is created, and so on. Each time an algorithm is applied, a note is added to fNotes to indicate what was done. Implementing analysis in this way affords one an undo feature. If a person is using the event browser, they can apply an analysis algorithm to the event, inspect what has been visually done to the event, and if necessary undo the action by clicking a button which will pop the last element off of fProcessedEvents and reload the event in its previous state. This type of feature is valuable in debugging code. A second feature is afforded through this implementation, one can choose which elements of fProcessedEvents to output at the end of this stage. Outputting the final element only allows one access only to the fully-processed event. Outputting all elements would allow one access to the event at each step of the analysis. An algorithm, once applied to fEvent, will typically iterate over each fMWPC, for each fMWPC it will iterate over each wire type (anode or field), for each wire type it will iterate over each trace, and for each trace an algorithm will be applied. Once analysis has been applied at the trace level, analysis is also applied at the event and track levels. This is done by accessing the last element of fProcessedEvents, let this last element be named fEventOut. For each fEvenOut, one then iterates

through all tracks for that event and for each fill in other remaining data members which give information about the track. After analysis is applied at each level, one can then output the processed event to file for the next stage.

In the tree diagram, fDetector and fElectronics are pointers to instantiations of classes that can be used to more precisely describe the detector. For instance, for this dissertation, the shaping electronics associated with the wires were assumed to all have the same peaking time and gain. If one were to carefully measure these values for each electronic component, one could specify and access these values on a wire-by-wire basis.

Above the flow of the analysis was given in broad strokes. The remainder of this section will focus on detailing the analysis algorithms, which are applied in order of presentation. For some, as they are listed, suggestions for further possible improvements are provided. For each event within the d2e file, the following are performed for each trace of the event. From the discussion above, this implies that each of these algorithms adds an element to fProcessedEvents. Beyond this section, reference to the different class types, shown in the tree diagram of Figure 3.19 will be used sparsely. It is to be understood that, for instance, use of the term "event" implies one is working with an object of class "fEvent".

Trace Analysis 01: Each ADC has 12-bit resolution. The ADC range was measured to be 1807 mV. To convert the signals from ADC counts to mV, one multiplies the observed ADC counts by $\frac{1807 \text{ mV}}{2^{12}-1 \text{ ADC counts}}$. If either the maximum or minimum allowed voltage values are observed for a trace, a boolean flag *tracePassClipADCCut* is set to false for the trace indicating it does not pass this cut.

Trace Analysis 02: The pedestal, otherwise known as baseline, is calculated. First, the pedestal is estimated. This is done by taking the first 50 bins of the trace and calculating the average and standard deviation of these bins, let these values be associated with *pedestalFront*. This choice has been observed to usually be sufficient in avoiding any signal regions of the trace. One can now take $\textit{pedestalFront} \pm 5\sigma_{\textit{pedestalFront}}$ as a reasonable range over which one expects the pedestal to exist. Every signal bin of the trace was then histogrammed over the previously given range into 50

bins. This distribution was fit with a Gaussian, and the mean and standard deviation of this fit are then used as the final pedestal value and the size of the noise for the trace σ_{noise}. For anode wires, signals are positive by convention, so any signal bins that appear in the histogram will be on the right side of the histogram or out of the fit range.

As an example let us consider the single-wire track shown in Figure 3.20. All traces of this figure have been offset such that they do not lie on top of each other. A signal region is apparent for the middle anode wire, that is wire 157, wire 156(158) is below(above) 157. For each anode trace, the bin values were histogrammed as described above and fit with a Gaussian. For the distribution of anode wire 157, a tail is present on the right side. This tail is due to the signal region bins. In comparing with the traces of the adjacent wires, it is possible that this method tends to slightly inflate the pedestal and size of the noise for those traces that have signal regions. Values are reported for each pedestal within the figure captions.

This algorithm could be improved. For instance, one could just histogram all bins of a trace and pick out the mode value, which itself is an estimate of the pedestal. After this, one could fit only the half-max region about the mode value and use the mean and standard deviation as values for the pedestal and size of the noise, respectively. In doing this, the pedestal value and size of the noise may not undergo the slight inflation of size that may exist with the method above due to signal bins which are present in the right side of the distribution.

Trace Analysis 03: The pedestal value, as calculated for each trace, is subtracted to remove the baseline. This is shown in Figure 3.21. In this figure all traces for both anode and field wires lie on top of each other, that is the offset has been removed. Visibly it appears that the baseline of each trace is approximately zero. A check is forthcoming, that will be used to confirm this.

Trace Analysis 04: Here a similar routine is performed as was done two steps prior. The pedestal, *pedestalFront*, is calculated and stored with each trace by finding the average and standard deviation of the first 50 bins of the trace. The difference is that the pedestal has been subtracted, so, if all signal regions of the trace are well-contained *pedestalFront* should be consistent with

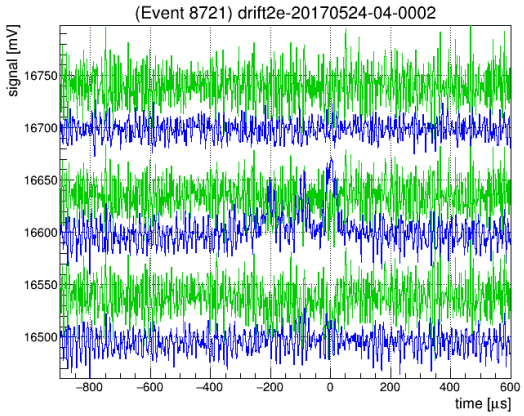

(a) An example-raw-single-wire track.

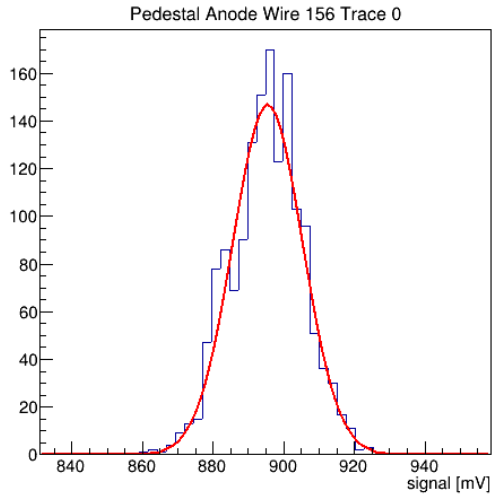

(b) Anode wire 156, bottom blue trace of (a). $pedestal = 898.89 \pm 8.52$ mV

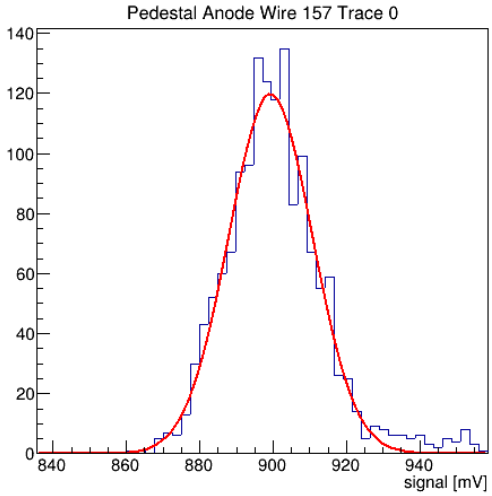

(c) Anode wire 157, middle blue trace of (a). $pedestal = 899.29 \pm 11.52$ mV

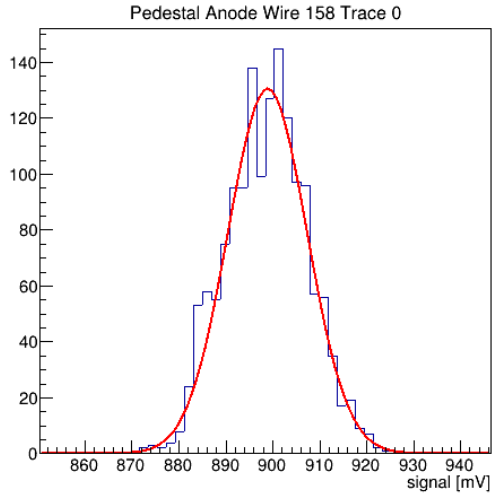

(d) Anode wire 158, top blue trace of (a). $pedestal = 895.45 \pm 9.99$ mV

Figure 3.20: An example-raw-single-wire track along with histograms depicting the pedestal calculation for each anode trace. The red curve of each histogram indicates the Gaussian fit for the histogram performed with ROOT [113].

zero. By well-contained, it is meant that each side of the trace contains baseline only and does not contain signal region bins.

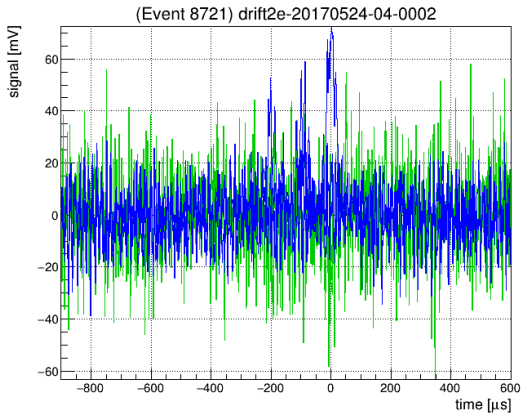

Figure 3.21: An example track after pedestal has been subtracted from each trace. No offset is present between traces to visually exemplify that the new baseline of each is near zero.

Trace Analysis 05: Complementary to the calculation of *pedestalFront*, *pedestalBack* is calculated and stored with each trace. This is done by calculating the average and standard deviation of the last 50 bins of each trace.

Trace Analysis 06: A check is executed to ensure that the pedestal has been sufficiently removed. Both *pedestalFront* and *pedestalBack* can be either positive or negative. When the pedestal was removed from the trace, it is possible that the new baseline now floats slightly below or slightly above zero. If either, $|\textit{pedestalFront}| - \sigma_{\textit{pedestalFront}} > 0$ or $|\textit{pedestalBack}| - \sigma_{\textit{pedestalBack}} > 0$, this indicates that the start and end of the trace are not consistent with zero with respect to the size of the noise. In this case, a boolean flag *tracePassPedestalCut* is set to false indicating the cut has not been passed.

Trace Analysis 07: In Stage 3, a wire was labeled as a veto wire if the noise observed for any traces of the wire were less than 3.0 mV. The cut here is a redundancy and should be removed to improve efficiency. This method was developed to check the size of the noise for traces prior to the method of Stage 3. In this step, if $\sigma_{noise} < 3.0$ mV, the boolean flag *tracePassNoiseCut* is set to false indicating the cut has not been passed.

Trace Analysis 08: Each trace is smoothed with a Gaussian kernel. In order to conserve the integrals of the traces, it is important that the weights of the kernel bins sum to unity. The smooth

is convolution of the kernel with the trace. In brief, this means that each bin is replaced with a value that is a Gaussian-weighted average of its surrounding bins.

For the algorithm at hand, the user inputs two values, the desired FWHM of the kernel, and how many standard deviations σ the kernel should extend about the peak. Here, a $\sigma = 4.0$ μs was used corresponding to $FWHM = 4.0\sqrt{8.0ln(2.0)}$, the kernel was allowed to span a region of 2.5σ on each side of the peak, here the value 2.5 is referred to as $lenKernel$. Each of the data bins has a time length of $\Delta_{tbin} = 1$ μs.

The number of kernel bins $nKernel = \frac{2 \cdot lenKernel \cdot \sigma}{\Delta_{tbin}}$, rounded down to the nearest integer. In order to keep the kernel symmetric, if the previous number is even, one is added. Here $nKernel = 21$.

Let the bins of the trace be indexed by i and the bins of the kernel be indexed by j. For a given i, one must iterate j from $i - (nKerenl - 1)/2$ to $i + (nKernel - 1)/2$ to perform the average. The j^{th} kernel weight relative to trace bin i is given by w_{ij}.

$$w_{ij} = \frac{\frac{1}{\sqrt{2\pi}\sigma} e^{\frac{-((j-i)\Delta_{tbin})^2}{2\sigma^2}}}{\sum_{j=(i-nKernel/2)}^{i+nKernel/2} \frac{1}{\sqrt{2\pi}\sigma} e^{\frac{-((j-i)\Delta_{tbin})^2}{2\sigma^2}}}$$

The kernel weights for $-10 \leq j - i \leq 0$ are 0.0044, 0.0080, 0.0136, 0.0218, 0.0327, 0.0461, 0.0610, 0.0759, 0.0888, 0.0975, 0.1006, respectively. The kernel weights for $1 \leq j - i \leq 10$ are not listed since the kernel is symmetric. Also, let s_i indicate the value associated with trace bin i, and let s'_i indicate the new value of bin i after the convolution is performed.

$$s'_i = \sum_{j=(i-nKernel/2)}^{i+nKernel/2} w_{ij} s_j$$

The above cannot be applied to the first or last $(nKerenl - 1)/2$ bins of the trace since some of the data that would be required for the calculation occurred either before the trace begins or after it ends. Here, this affects the first 10 bins and last 10 bins of the trace out of 1500 bins total. The front(back) 10 bins are all assigned the same average value which is calculated from the

first(last) several bins of the smoothed data directly adjacent to these regions. No complications were observed in treating these few bins differently, generally, signals are contained more centrally in the trace due to the triggering scheme. Further, if a signal were present in these front(back) regions, this should cause *pedestalFront*(*pedestalBack*) to be above the average baseline causing *tracePassPedestalCut* to be flagged to false. A smoothed example track is shown in Figure 3.22.

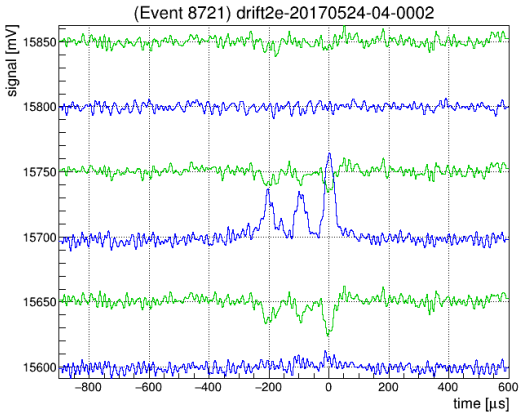

Figure 3.22: An example track after the Gaussian smooth is applied.

The width at hand was chosen mainly for consistency. Jean-Luc Gauvreau, of Occidental College, had previously performed some preliminary-and-independent analyses using this kernel width. In choosing a kernel width, one needs to choose a width that is long enough to reduce the noise yet not choose something too long as to smooth out structure in signal regions, such as from the minority peaks. The width used here was a choice, it is likely that this parameter could be further optimized, but that is not investigated in this work. The signal-to-noise ratio for each of the minority peaks, and the spacing between the minority peaks will affect the optimum choice of this value, and neither of these parameters is constant across all recoils.

FFT analysis was performed, using FFTW [143] algorithms, to discern if there were any discrete frequency bands that could be filtered. Example FFT power spectra appear in Figure 3.23. These power spectra are representative of the general shape that has been observed for these curves. In the figure, the largest spike in each spectrum occurs near 68 kHz. Overall, the appearance of the

noise is that of a $1/f$ nature as opposed to discrete-and-clearly-defined bands which could be notch filtered. Filtering, for instance, around 68 kHz was not observed to greatly impact the ability of the subsequent analysis routines to pick out signal regions. Some follow-up investigations were done in which the content of the power spectrum was observed as a function of time for some traces that appeared to contain baseline only. Preliminarily, it was seen that the shape of the spectrum itself can vary as a function of time although it was not carefully quantified, that is, the shape of the noise was not stable. One implication being that if one were to try and quantify the spectral content of the noise for a given wire from a snapshot in time, a trace, for the purpose of removing that spectrum from further traces on the same wire, the effect to the noise and signals present on these further traces may be dissimilar. Based on these initial findings, it was decided to forego any FFT filtering.

In reference to the FFT spectra shown, there is an interesting feature which one may be able to exploit in picking out a small signal from a noisy channel. First, in Figure 3.20(a), it is clear that a signal region is present for anode wire 157. In looking at the corresponding FFT spectrum for the wire, the peak at low frequency is indicative of this signal. One can also see structure at low frequency for wire 156 although by eye it is not apparent that there is a signal on the corresponding trace of Figure 3.20(a), however there are perhaps some hints of a signal visible in the smoothed trace of Figure 3.22. For anode wire 158, no structure is present at low frequency and no structure is visible in the corresponding smoothed trace. One can imagine an algorithm where the shape of the FFT spectrum can be used to pick out traces which have signals. By then dividing the trace into smaller chunks in time, one could perform FFT analysis on each and perhaps even identify where it is along the trace that the signal region begins and ends. To be clear, this is not done for this work, it is an observation only.

Trace Analysis 09: Peaks in the traces are identified via signal-to-noise. If all wires of the detector have similar noise, this effectively implies a similar peak-finding threshold for each wire. This peak-finding threshold is a software/analysis threshold as opposed to a hardware-trigger threshold. However, the detector noise at the time data was collected had not been optimized.

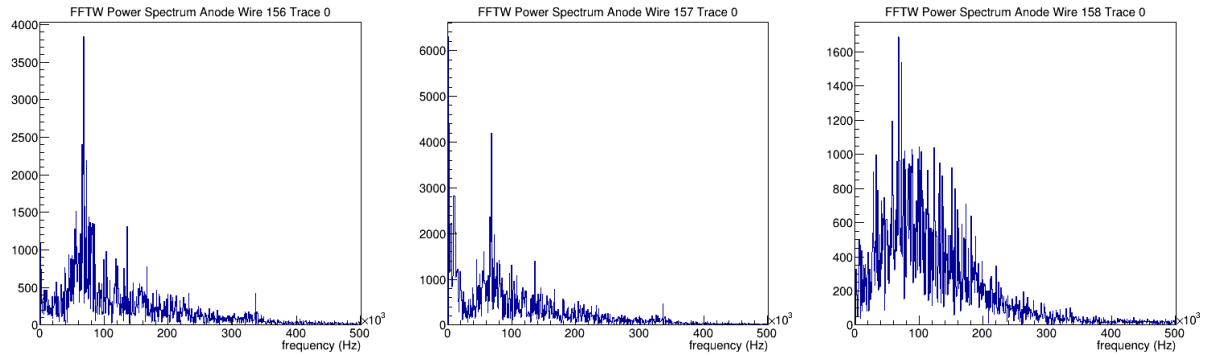

(a) FFT Anode wire 156 **(b)** FFT Anode wire 157 **(c)** FFT Anode wire 158

Figure 3.23: FFT power spectra for the anode wires traces shown in Figure 3.20(a). The anode wires are the blue traces of the referenced figure and are numbered 156, 157, 158 from bottom to top.

It was previously shown in Figure 3.2, that noise is not homogeneous across all wires. Instead, a fixed peak-finding threshold could be advantageous in identifying signal peaks on relatively noisy wires. In using a signal-to-noise threshold, the user is effectively fixing the level of confidence required for peak identification by requiring it to be a minimum number of standard deviations out of the noise n_{peak}. After a peak is identified, the signal region about this peak is defined by iterating to each side, about the peak, until a value is found that is a predefined number of noise standard deviations, n_{SR}, out of the pedestal. These two values are the inputs required for this algorithm, which is detailed below.

Each instance of a trace class includes four containers, one holds the bin numbers at which positive, or upward going, peaks are found and one holds the start and end bins about the peak bin, which defines the signal region for that peak. The other two containers are the same except for negative, or downward going, peaks and signal regions. Anode wire signals that are the result of a track of ionization being deposited in the detector are expected to be upward going by convention, and field wire signals are expected to be negative going. Each trace is searched for both positive and negative going peaks. Positive peak finding will be described below, the algorithm for negative peak finding only requires inversion of logic in some places.

First the maximum value within the trace is found. If the max value is $\geq n_{peak}\sigma_{noise}$, the bin at which this occurs is added to the container for positive peaks. Next, iterate bin-by-bin left of

the peak bin until the value for a bin is $\leq n_{SR}\sigma_{noise}$, one is then added to this value to define the start of the signal region. That is, the start of the signal region is the first bin, while moving left from the peak, that is $> n_{SR}\sigma_{noise}$. If the beginning of the trace is reached before this value is found, then the first bin of the trace would be the start of the signal region. Next, iterate bin-by-bin right of the peak and perform a similar process to find the end of the signal region. This pair of bin values is added to the container for positive going signal regions. Once the first peak and first signal region has been identified, the entire process is repeated until no more bin values are above $n_{peak}\sigma_{noise}$. For each consecutive peak search, the bins where signal regions have already been found are excluded from the search. For this dissertation, the search is performed with $n_{peak} = 2.5$ and $n_{SR} = 0$. An example track with three located peaks and signal regions is shown in Figure 3.24.

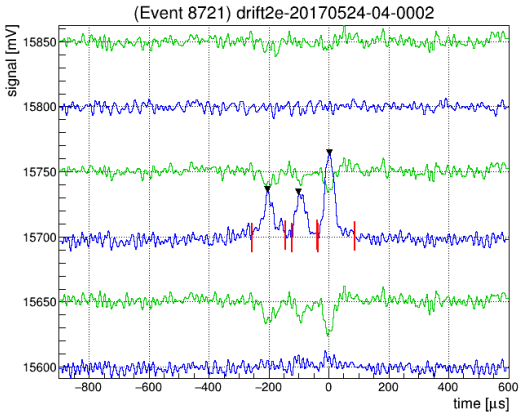

Figure 3.24: An example track after searching for peaks (labeled with black triangles) and signal regions (labeled with red vertical lines). For this search $n_{peak} = 2.5$ and $n_{SR} = 0$.

Trace Analysis 10: For the anode wire traces, if any negative going peaks were found in the previous step, this results in a flag *tracePassInversePeakCut* to be set to false. Anode wire signals that result from recoils are expected to be positive going. Downward going pulses on anode wires can be caused, for example, by spark events, see Figure 2.12(b). If a downward going signal were to overlap an actual recoil signal, this could distort the recoil signal. It is for this reason that this cut exists.

Trace Analysis 11: The algorithm for peak-finding which was performed two steps previous is performed again. In doing so, the previous peaks and signal regions which were found are cleared and then repopulated with new values. The peak-finding threshold, n_{peak}, is increased to 3.5, and n_{SR} is kept at zero. A lower n_{peak} was used previously such that one is extra sensitive to any parts of the trace that may cause *tracePassInversePeakCut* to be flagged to false, while requiring a larger level of confidence in picking out a signal region in this step, which may result from a recoil. The example track of Figure 3.24 is shown again in Figure 3.25 , with the increased peak-finding threshold. Only one peak has now been identified. The other peaks will be regained in forthcoming routines.

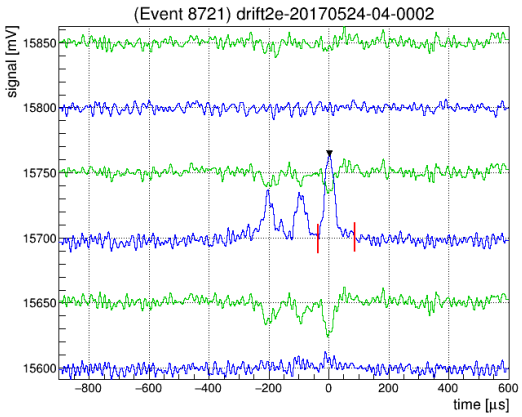

Figure 3.25: An example track after searching for peaks (labeled with black triangles) and signal regions (labeled with red vertical lines). For this search $n_{peak} = 3.5$ and $n_{SR} = 0$.

Trace Analysis 12: Once signal regions have been identified, it is reasonable to expect that not all peaks that may compose a track were identified due to the high software threshold. The signals of interest are known to contain minority peaks, it is therefore now also reasonable to search for peaks of smaller amplitude near ones that have already been identified. For instance, if a signal peak were to be found on anode wire n, wire n will now be searched for additional peaks at a reduced threshold, in part, as an attempt to identify any missed minority peaks. Additionally, wires $n - 1$ and $n + 1$, termed the neighbor wires, will also be searched at this reduced threshold

if anode traces are available for these wires for this specific event. For this step, $n_{peak} = 2.0$ and $n_{SR} = 0$, see Figure 3.26.

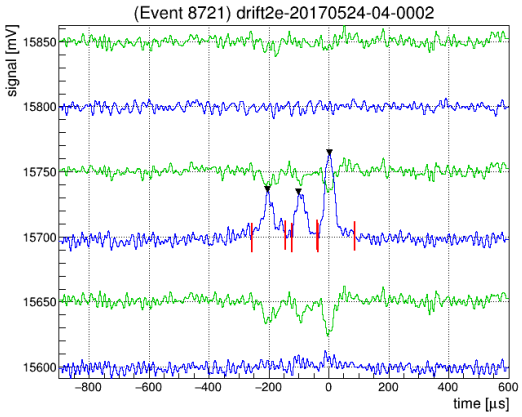

Figure 3.26: An example track after searching for peaks (labeled with black triangles) and signal regions (labeled with red vertical lines) at a lower threshold. For this search $n_{peak} = 2.0$ and $n_{SR} = 0$.

For multiple-wire tracks, individual signal regions that appear on on adjacent traces have not yet been grouped into tracks, that will be done in subsequent steps, see Track Analysis 01 and 04 below. However, the following discussion is relevant at present. This search at reduced threshold is performed in an attempt to better reconstruct a track. The integrals of any additional signal regions picked out in this step will improve energy reconstruction. Measurement of Δ_x is also improved since one can get a more accurate accounting of the number of wires that the track hit.

Trace Analysis 13: For a given trace, any signal regions which were identified in previous steps are combined into one new signal region. The earliest bin of this new signal region is the earliest signal region bin identified for that trace in the previous steps, and the latest bin of this new signal region is the latest signal region bin that had been identified in previous steps. Visually, the following can be seen in comparing the signal regions of Figure 3.26 to that of Figure 3.27. The location, bin index, of the largest amplitude peak is stored for this new combined signal region.

Up until this point, the goal has been to locate a region of interest that may contain a recoil signal. As seen in Figure 3.28(a) the S peak may sometimes be missed in the previous step, Track

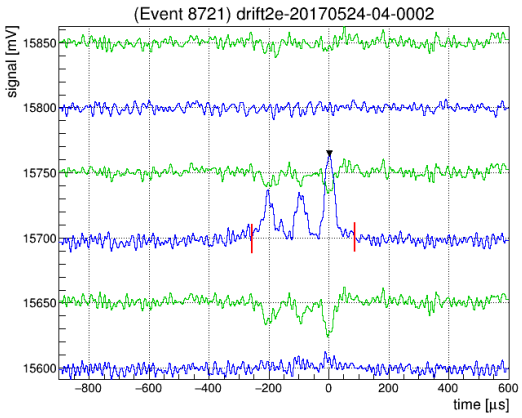

Figure 3.27: An example track after signal regions (labeled with red vertical lines) have been combined for each trace.

Analysis 12. Once a region of interest has been located, a more sensitive search will be used to identify where peaks are located within that region.

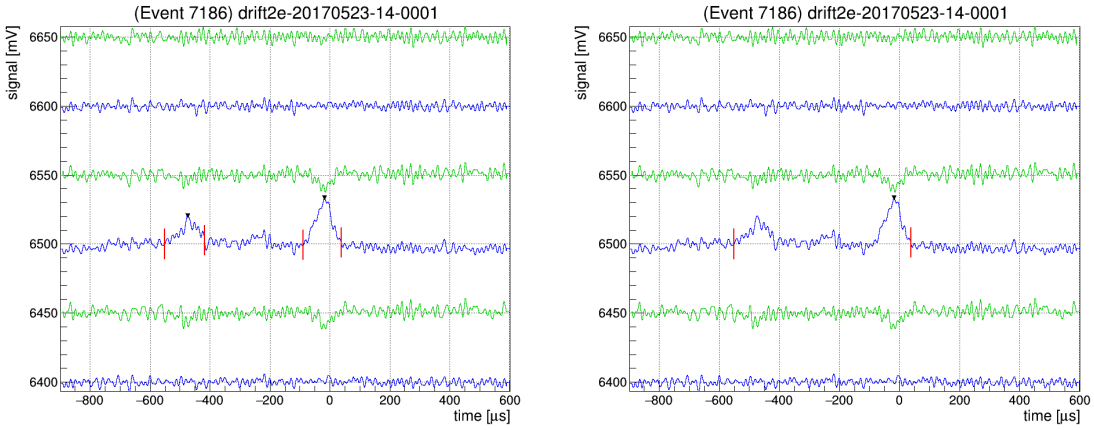

(a) Trace Analysis 12

(b) Trace Analysis 13

Figure 3.28: An example 1-wire track at two different steps during processing. (a) Trace Analysis 12, for which a search is performed on the signal wire as well as the neighboring wires at a reduced threshold. The S peak was not identified for this track. (b) Trace Analysis 13, for which the signal regions of a trace are combined. For both figures signal regions are labeled with red vertical lines.

Trace Analysis 14: The integral of the combined signal region of the trace is computed in units of mV·μs. Looking forward into the algorithm, application of the appropriate calibration constant

from Section 3.1.1 can be used to convert the integral to NIPs, a measure of energy. After signal regions are grouped into tracks, track energies are calculated and reported in Section 3.2.3.

Trace Analysis 15:

This step is analysis of the structure of each combined signal region, for example see Figure 3.28(b). The goal is to pick out signal regions that appear to be recoil-like. A recoil-like signal is apparent by-eye due to the presence of three or four anion peaks within the signal region. This analysis is not blind. In the following discussion some specific values have been chosen to pick out recoil-like signals. These were chosen empirically and based on information that had been accumulated within the collaboration about the structure of these signals, see Section 2.1.2. A right neutron run file 20170523-14-0001 was used to set these values. The event browser was used to page through the events of this file, and by-eye choose events that appeared to contain recoils. Data from the structure of these events were used to set the values used below. Approximately, a few tens of events were used. In total 2089 recoil-like tracks pass through the analysis.

One is interested in a combined signal region that has either three or four maxima. To locate extrema, an iterative approach is used. One smooths the signal, performs a search for extrema, and checks the number of maxima found. The process is repeated until the number of maxima converges on a value of less than or equal to four.

The first pass of the iterative process will be described by example. Let us work on the combined signal region identified in Figure 3.28(b). Let us name the start and end bins, identified by the red vertical lines, bin_0 and bin_f, respectively. Since the bin widths are 1 μs in duration these are equivalent to time. For this signal region $bin_0 = 349$ and $bin_f = 938$. First, the trace is smoothed. The length of a combined signal region is dependent on how far from the MWPC, along the z axis, the recoil occurred within the detector volume. Recall, the peaks of the signal spread further apart as this z distance increases. To account for this, the $FWHM$ of Gaussian smoothing kernel is set based on the signal region length. The choice was empirical. Two tracks that are deposited different z distances from the MWPC but are otherwise equal will have different peak spacing. Since one expects at most four peaks, one can use a wider smooth to more quickly home in on the

peak locations for the track that was deposited farther from the MWPC. The same smooth applied to the track that was deposited closer to the MWPC may wash out the structure.

$$FWHM = \frac{(bin_f - bin_0) * (1\ \mu\text{s})}{20} = 29.45\ \mu\text{s}$$

For this smooth the kernel length parameter, previous described in step Track Analysis 08, was set at $lenKernel = 2.5$ This smoothed trace appears in Figure 3.29(a).

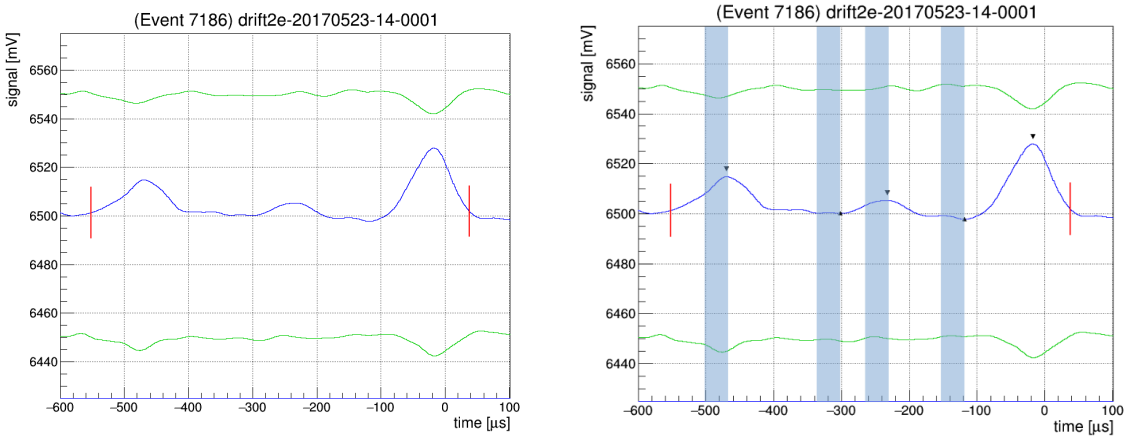

(a) Smoothing Before Extrema Search

(b) Extrema Search Performed

Figure 3.29: An example 1-wire track after a first pass of signal-region-length-based smoothing (a) and after the subsequent search for extrema (b). For both figures signal regions are labeled with red vertical lines. The small downward-pointing black triangles represent the maxima found during the search and the upward-pointing triangles represent the minima. Signal regions lines and the extrema markers are placed by the analysis algorithm. The highlighted region left of each extrema represents $nSwitch$ as described in the text. These regions were marked approximately by-hand.

Next the first pass at finding extrema is performed. It includes a parameter $nSwitch$ that is also based off of the signal region length. The calculation of $nSwitch$ returns the integer portion of the value. For the extrema search, $nSwitch$ was required to be odd, if the returned integer is even it is incremented positively by one.

$$nSwitch = \frac{bin_f - bin_0}{17} = 35$$

One starts the search at the bin of the combined signal region that contains the global maximum. This was previously identified and indicated by the small black triangle in Figure 3.27. Starting at this bin, one iterates bin-by-bin leftward. The first bin that is found that is smaller than the maximum and has $nSwitch$ bins left of it that are greater in value is identified to be the first local minima. Starting at the bin location of the first minima, one now searches for the next local maximum. Iterating leftward bin-by-bin, the first bin that is greater than the first local minima and has $nSwitch$ bins left of it that are less than its value is identified to be the second local maxima. The first local maxima is the global maximum. One keeps iterating leftward, picking out extrema in this way, until bin_0 is reached. In the same manner one iterates bin-by-bin rightward of the global maximum in search of extrema until bin_f is reached. The bin locations of the local minima and maxima are stored in two containers for the trace and sorted in ascending order. In Figure 3.29(b), three maxima were identified and two minima were identified. Looking back to Figure 3.28, it is now apparent that the S peak, which was not originally identified, has now been identified in searching for extrema.

Since less than or equal to four maxima were found, the iterative process of smoothing and searching for extrema was halted after the first pass. Other traces require further smoothing steps to converge. Remember, each time a process is performed on the traces, an element is added to fProcessEvent such that these changes can be tracked. This implies that each time a smooth or extrema search is performed, an element is added to fProcessEvent. For different traces, it will take differing numbers of iterations for this algorithm to converge. For uniformity, in all further steps of this analysis chain, operations will be performed on the trace belonging to the element of fProcessedEvents just prior to the extrema finding algorithm being applied. The maxima locations that were just identified are assumed to be the locations of the anion peaks. If four peaks were identified it is assumed the all of the D, P, S, and I peaks were found. If three peaks were found, it is assumed they are the P, S, and I peaks. The order listed, represents the order they should appear in the local maxima container for the trace since it was sorted in ascending order. The signal prior to searching for extrema and the anion peak locations are plotted in Figure 3.30. Further checks

must now be done to ensure the signal structure matches what one would expect from a nuclear recoil.

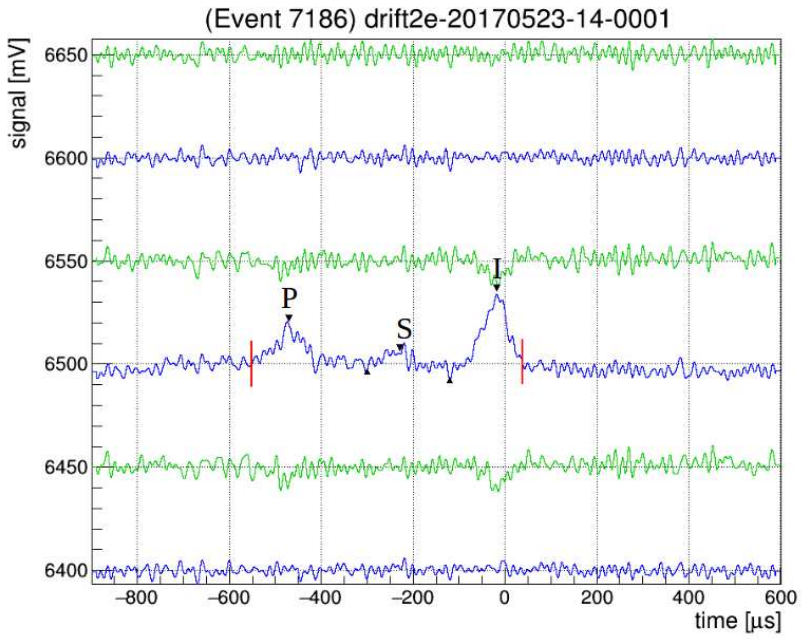

Figure 3.30: An example combined signal region after the location of the local maxima have been identified. It is assumed at this stage that these are the P, S, and I peaks, as labeled. The nearest minima left of the I peak is referred to as the I valley, and the nearest minima left of the S peak is referred to as the S valley. Further checks need to be performed to ensure that the maxima identified have the properties expected for a recoil signal with minority peaks.

If three or four maxima were found in the combined signal region, a boolean flag *tracePass-NumPeaksCut* is set to true. Next the minima are checked. In Figure 3.30 two minima are shown. For other signals regions it is possible that additional minima could be identified either before the earliest maximum or after the latest maximum. One iterates through the bin locations of all the minima. If the minima is located between the I peak and the S peak, it is labeled the I valley. If it is located between the S peak and the P peak it is labeled as the S valley, and if it is located between the P peak and the D peak it is labeled the P valley. Each time a minima meets one of the previous valley conditions, a counter is increased by one. If the number of peaks is four, then the number of valleys should be three. If the number of peaks is three, the number of valleys should be two. If

the previous condition is met a boolean flag *tracePassNumValleysCut* is set to true and all minima outside of the identified valleys are discarded.

If four peaks were identified, a check is done to make sure the latest maxima, currently identified as the I peak, is of a reasonable size. To check for this the signal region was integrated from the beginning of the signal region to the I valley bin, and the signal region was integrated from one bin past the I valley bin until the end of the signal region. The latter integral is then divided by the sum of the two integrals. If this ratio is ≤ 0.1, this indicates that the peak that is currently identified as the I peak should not be. This is because the I peak typically accounts for about half of the total signal region integral. The latest occurring minimum and maximum are removed from the containers that hold these bin indices. In this case, the maxima that was previously identified as the S peak now becomes the I peak, the previous P peak becomes the S peak, and the previous D peak becomes the P peak. The minima, or valleys, are also relabeled accordingly.

For each peak that has been identified as D, P, S, or I, it is determined if the half-maximum width is available. Tracks that are deposited close to the MWPC will not have sufficient time for the peaks to separate out and so the half-maximum width may not be available. For instance, for the I peak, one first iterates to the left of the I peak, bin-by-bin, up until the I valley at farthest. As soon as a bin value is encountered where its value is less than or equal to half of the peak value, this will be considered the start of the half-maximum width for the I peak. If the I valley bin is encountered before a half-maximum bin is found, this could be indicative of the peaks overlapping and a half-maximum width will not be determined for this peak. One then iterates right of the I peak, bin-by-bin, up until the end of the signal region is reached at farthest. As soon as a bin is encountered where its values is less than or equal to half of the peak value, this will be considered the end of the half-maximum width for the I peak. If both of the half-maximum bins are encountered for the I peak, these indices will be stored. Similar is done for all peaks. For each peak that has the half-maximum width available, the integral over this region is also stored.

With peak locations determined the distance from the MWPC, along the z axis of the detector, where the recoil was deposited can be computed. In this work this parameter is called z_{IP} and the

calculation of this value have previously been described in Section 2.1.2.

$$z_{IP} = \Delta t_{IP} \frac{E}{P} \sqrt{\frac{T}{T_0}} (\frac{1}{\mu_{0I}} - \frac{1}{\mu_{0P}})^{-1}$$

The reduced mobilities for the I and P carrier anions μ_{0I} and μ_{0P} were calculated in the section that was just referenced. The electric field strength $E = \frac{|V_{FW} - V_{cathode}|}{50 \text{ cm}}$, with $V_{cathode} = -30.0$ kV and V_{FW} is the field wire voltage. Since the field wire voltage differed slightly between runs, see Table 3.5, the correct field wire voltage is automatically populated on a run-by-run basis from the field-wire-voltage file. The gas temperature $T = 293$ K was used for this analysis, it was not tracked carefully for each run, and $T_0 = 273.15$ K. The gas pressure $P = 41.5$ Torr.

In section 2.1.2, it was stated that the S anions drift 2.5% faster than the I anions and the P anions drift 5.4% faster than the I anions. This implies that the relative spacing between the peaks can be used as a cut. The time difference between the I and S peak is calculated as well as the time difference between the I and P peak. The ratio of the former over the latter is used as a cut parameter. For this analysis if the ratio is ≥ 0.45 and ≤ 0.55, a boolean flag *tracePassTimeDiffCut* was set to true.

Integrals for each peak are computed. If the three P, S, and I peaks are present, for example Figure 3.30, an I peak integral is computed from the I valley (nearest minima left of the I peak) until the end of the signal region. A S peak integral is calculated from the S valley (nearest minima left of the S peak) until one bin prior to the I valley. A P peak integral is computed from the start of the signal region until one bin prior to the S valley. If a signal region also has a D peak, then the P peak integral is computed from the P valley (nearest minima left of the P peak) until one bin prior to the S valley and the D peak integral is computed from the beginning of the signal region until one bin prior to the P valley.

Using the integrals described in the preceding paragraph, a minority peak ratio $MPRatio$ is calculated. In this work, the $MPRatio$ is found by integrating from the start of the signal region until one bin prior to the I valley and then dividing this by the total signal region integral. That is, it is the fraction of charge contained in the minority peaks relative to that contained in the

sum of all peaks. Parameters similar to this one, have previously proven to provide a powerful cut in identifying nuclear recoils [77]. Nominally, the I peak contains half of the signal region charge, see Section 2.1.2. In this analysis, if $0.43 \leq MPRatio \leq 0.57$ then a boolean flag *tracePassMPRatioCut* was set to true.

The I anions are known to drift more slowly than the other anion species toward the MWPC, and the I anions have been observed to consistently produce the largest amplitude peak in the signal. Of the peaks that have been identified in the signal region, if the maximum amplitude peak is also the latest occurring peak, a boolean flag *tracePassMaxAmpPeakIsLatestCut* is set to true.

In aggregate, five boolean flags have been set for each trace during this step in the search for minority peaks. These are *tracePassNumPeaksCut*, *tracePassNumValleysCut*, *tracePassTimeDiffCut*, *tracePassMPRatioCut*, and *tracePassMaxAmpPeakIsLatestCut*. If all of these are true for the signal region of a trace, a single boolean flag to indicate this *tracePassMPAnaCuts* is set to true.

This concludes analysis at the trace level. Analysis is now required at the event level to group signal regions into tracks, and further calculation and scrutiny is required at the track level to pick out nuclear-recoil-like tracks.

Track Analysis 01: A search is performed at the event level, within fEventOut, to search for tracks. Remember, an event can contain multiple tracks. For each signal region that has been identified within the event a track component is generated and stored in a container, let it be named $trackComponents$. Each track component is composed of three values that uniquely specify the signal region within fEventOut. These three values are the wire number within the event, the trace number for that wire, and the signal region for that trace. Two other containers hold the start and end times of each signal region, let us call these times $\vec{t_0}$ and $\vec{t_f}$, respectively. The three containers share the same ordering such that the i^{th} element of each belongs to a unique signal region.

First the elements of the three containers are all reordered by sorting container $\vec{t_0}$ in chronological ascending order. Next, the elements are grouped into tracks. During this step, a track is comprised of all of the elements of $trackComponents$ that overlap, as specified below, in time. It is not necessary, during this step, for the signal regions to be on adjacent wires, this condition

will be enforced later. Starting with the first element of $trackComponents$, a new track, $track0$, is added to the event. One then iteratively steps through $trackComponents$. If $\vec{t_{0i}} \geq \vec{t_{0i-1}}$ and $\vec{t_{0i}} \leq \vec{t_{f_{i-1}}}$, then the i^{th} track component is added to $track0$. As soon as this condition is not satisfied a new track, $track1$, is added to the event with the i^{th} track component being the first signal region for $track1$. This process is repeated until all track components have been grouped into tracks.

Track Analysis 02:

With tracks identified within an event, track statistics are now filled. The filling of a track will be described by example with a two-wire track, Figure 3.31(a). One can generalize the logic to a track that appears over an arbitrary number of wires. This specific track has two track components as described in Track Analysis 01, there are two signal regions that compose this track.

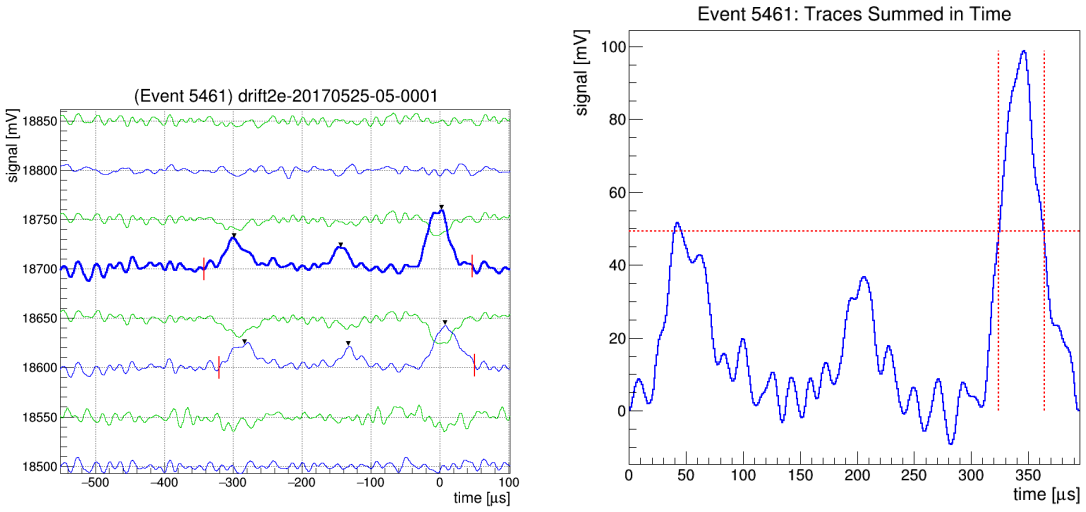

(a) **(b)**

Figure 3.31: (a) An example 2-wire recoil signal. The wire signals are offset for clarity. (b) The two individual signals have been summed together in time. The two vertical-dashed-red lines about the summed I peak indicate the width in time of the peak at half its maximum amplitude. This figure appears also in Section 3.2.4; it is additionally provided here for convenience.

First, the total track duration in time is determined. The start time of a track is the earliest signal region edge appearing on any of the traces. For the example track, this is marked by the left

signal region edge of the upper signal wire. The end time of the track is the latest signal region edge appearing on any of the traces, and for the example is marked by the right signal region edge of the lower signal wire. These two edges mark the total track duration and the signal regions are summed in time over this duration to get the track signal, Figure 3.31(b). The total track integral is computed over this region by summing together, in time, the signal regions that have been identified on each wire. In hindsight, I would recommend that one instead compute the total track integral by summing together, in time, all traces that have been identified to have signal, as well as the two anode traces that neighbor these directly, over the complete track duration. This may give a better value for the track energy.

A check is done to ensure that the traces that contain signal pass the five minority peak analysis trace cuts from above, this was indicated for each trace of a track by setting a boolean flag *tracePassMPAnaCuts* to true. For the example track, both traces that contain signal pass. This is not always the case. For instance, one could imagine that the track actually extended across three anode wires but the amount of charge deposited on the third wire was small and was not picked out when searching for peaks and signal regions. In step Trace Analysis 12, after signal regions have been found, neighboring anode wires are searched for peaks and signal regions at a reduced threshold. There are instances when only the signal region about the I peak is identified on a neighboring wire due to the small peak sizes relative to the noise. For example see the bottom anode trace of Figure 3.32. This signal region will not pass the minority peak analysis cuts and will have *tracePassMPAnaCuts* set to false. Of all of the signal regions that compose a track, at least 90% of the track integral was required to belong to traces that have passed the minority peak analysis cuts. This was done in order to not discard all tracks of this type. If the track meets this condition, a boolean *trackPassMPAnaTraceCuts* was set to true.

If *trackPassMPAnaTraceCuts* was set to true further statistics were calculated, such as the number of anode wires hit, the x extent of the track Δ_x, and the z extent of the track Δ_z. Δ_x is the extent of the track perpendicular to the anode wires which are spaced 2 mm apart, it is calculated essentially by counting the number of wires hit. The Δ_z extent is proportional to the width in time

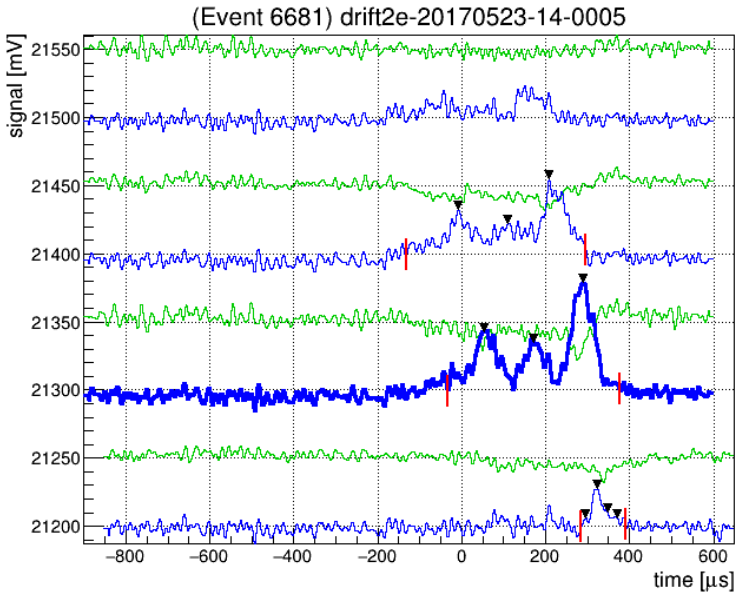

Figure 3.32: Shown is an example track that has a signal region (bottom anode trace) where only the actual I peak is enclosed in the signal region. The minority peaks were missed due to low signal to noise. This track was allowed to continue through the analysis chain due to this step, Track Analysis 02. This figure appears again as Figure 3.39; it is additionally placed here for convenience.

of one of the anion peaks. All signals regions of a track that pass the minority peak analysis cuts get their I peak signals summed together in time, see Figure 3.31. The half-maximum width in time of this summed I peak signal is used to determine Δ_z. The calculation of these range components have been described in Section 3.2.4.

Each track is composed of track components and each track component corresponds to a specific signal region. It is uniquely identified within an event by specifying three values within an event. These are the wire number, trace number for that wire, and signal region number for that trace. The signal region that possesses the largest amplitude I peak is referred to as the maximum amplitude component.

Track Analysis 03: Boolean flags *tracePassClipADCCut*, *tracePassPedestalCut*, *tracePassNoiseCut*, and *tracePassInversePeakCut* were set in Trace Analysis steps 01, 06, 07, and 10, respectively. If any of the traces that compose a track have any of these flags set to false, then a boolean flag *trackPassTraceCuts* is set to false for the track. This implies that at least one trace of

the track does not pass one of the trace cuts. All traces of a traces of a track must pass these cuts for that track to pass through the analysis in its entirety.

Track Analysis 04: When grouping tracks in Track Analysis 01, it was only required that signal regions on the traces be ordered logically in time. Here, one verifies that the signal regions are on consecutive wires. One-wire tracks automatically meet this condition. As an example, let us consider a track with three track components indexed by 0, 1, and 2. These signal regions occur on wires $wire_0$, $wire_1$, and $wire_2$, keep in mind that the numbers are indices and not absolute wire number. There are two ways in which this track can be verified to be on consecutive wires depending if the track components appear in ascending or descending order by wire number. If $wire_1 - wire_0 = 1$ and $wire_2 - wire_1 = 1$, then the wires are consecutive. If $wire_1 - wire_0 = -1$ and $wire_2 - wire_1 = -1$, the wires are also consecutive. If the track does not meet these conditions, a boolean flag *trackPassConsecutiveWiresCut* is set to false.

Track Analysis 05: The wires belonging to the track are compared to the veto wires listed in the concatenated dead-and-veto-wire file. The ways in that a wire could be determined to be a veto wire were discussed earlier in this section. If the track contains a veto wire, the boolean flag *trackPassVetoWiresCut* is set to false.

Track Analysis 06: The wires belonging to the track are compared to the dead wires listed in the concatenated dead-and-veto-wire file. It is not possible for a wire of a track to be a dead wire since no signals are observed for dead wires. If the track contains a wire that is adjacent to a dead wire, then the boolean flag *trackPassDeadWiresCut* is set to false.

Track Analysis 07: In this step a check is performed to ensure that the track is well-contained within the traces that are present in the event. A track can span multiple wires. For a track that spans multiple wires, let $wire_{min}$ represent the lower-most wire of the MWPC that the track contains and $wire_{max}$ represent the upper-most wire the track contains. If the processed event, fEventOut, does not have traces for $wire_{min-1}$ and $wire_{max+1}$, the track is not considered to be well-contained and a boolean flag *trackPassUpperAndLowerNeighborsCut* is set to false. A well-contained track is one for which traces are present in the event, over the time period that the signal regions of

the track are observed, with no signal regions being found on these traces. The one-wire tracks shown in Figure 3.27 and 3.28 are well-contained for the anode wire traces. The triggering scheme described in Section 2.1.5 allows for this check.

Track Analysis 08: For this dissertation, in part because several dead wires were present across the MWPC, it was chosen to only further analyze events for which a single track was present. If an event contained more than one track, a boolean flag *trackPassSingleTrackInEventCut* was set within each track to false.

Stage 5: Generation of Plots/Statistics

The output of Stage 4 is a file in ROOT format and is the input to this final stage. The custom event class structure, described at the start of this section, is written to file and further preserves the nested structure of the MWPC, wire, and trace classes that each event contains. Only those tracks that have passed all cuts described in the Track Analysis steps were written to file in order to conserve disk space. In this stage, one can plot and analyze any of the event, track, or trace statistics that have been collected throughout the analysis chain, for example the Δ_x and Δ_z extent of tracks. This is first done on a file-by-file basis and then the statistics of all files belonging to a specific triggered run type, background, left neutron, right neutron, top neutron, or front neutron, are collected into single ROOT files for those runs. In this stage, one further cut was applied for the nuclear recoil track data reported in this dissertation. It was required that the maximum amplitude component of a track have an identified half-maximum width. This essentially cuts tracks that have low z_{IP}, that is they occurred relatively close to the MWPC and did not have sufficient drift distance for peaks to separate.

3.3 Results

3.3.1 Range Components

The methods of Section 3.2.4 were applied to create the distributions of axial range components, Δx and Δz, for each of the Left (L), Right (R), Front (F), and Top (T) run types that were

described in Section 3.2.1. A depiction of the neutron source positions is provided in Figure 3.9. The distributions are shown in Table 3.8 and Figure 3.33.

Table 3.8: The number of tracks with Δx = 1 mm, 3 mm, 5 mm, and 7 mm for each of the neutron run types. The mean x length $\langle \Delta x \rangle$ is also calculated for each run type. The distributions are not Gaussian so the uncertainties, which are calculated as standard deviation over the square root of the number of events for each run type, are approximate.

	$N_{1\ mm}$	$N_{3\ mm}$	$N_{5\ mm}$	$N_{7\ mm}$	N	$\frac{N_{1\ mm}+N_{3\ mm}}{N}$	$\frac{N_{3\ mm}}{N_{1\ mm}}$	$\langle \Delta x \rangle$ [mm]
L	496	92	16	3	607	0.969	0.185	1.44 ± 0.04
R	256	45	7	0	308	0.977	0.176	1.38 ± 0.05
F	480	140	17	2	639	0.970	0.292	1.56 ± 0.04
T	408	107	19	1	535	0.963	0.262	1.55 ± 0.05

Further into this section the Δx and Δz information for each run type will be combined and a careful statistical analysis will be used to determine if the distributions from one run type to another are in fact different. For now, let us just compare the raw values obtained for the range component distributions. In Table 3.8 it is shown that for all run types 96.3% to 97.7% of tracks have x lengths of 1 or 3 mm. The ratio of these two bins $\frac{N_{3\ mm}}{N_{1\ mm}}$ yields values that are smaller for the L and R runs in comparison to the F and T runs. Further, comparison of the $\langle \Delta x \rangle$ values for each run type shows that those for the L and R runs are again smaller in comparison to the F and T runs. For the T run neutrons are most directed along the x axis on average, they are most directed along the y axis for the F run, and they are most along the z axis for the L and R runs. One would expect the recoils of each source position to, on average, have the largest range component corresponding to the axes just described. These statements are supported by Monte Carlo simulation work; the simulation set up is described in Appendix B. When the neutron source is placed in the T position, neutrons are more directed along the x axis than are neutrons from the L and R positions, one may therefore expect to observe larger $\frac{N_{3\ mm}}{N_{1\ mm}}$ and $\langle \Delta x \rangle$ values for the T run.

In Figure 3.33 the $\langle \Delta z \rangle$ of the L and R runs are larger than for the F and T runs. When then neutron source is placed in the L or R position, the neutrons are more directed along $\hat{z}$ in

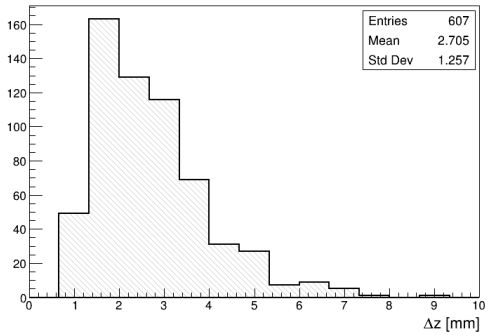

(a) Left $\langle \Delta z \rangle = 2.71 \pm 0.05$ mm

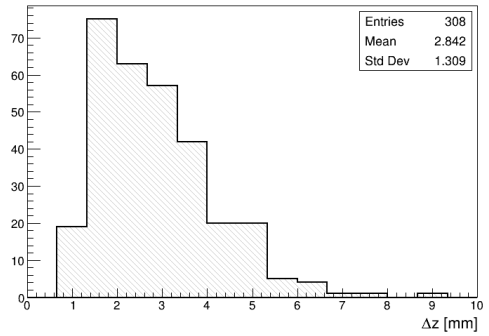

(b) Right $\langle \Delta z \rangle = 2.84 \pm 0.07$ mm

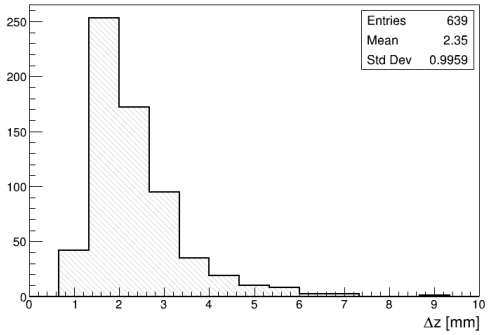

(c) Front $\langle \Delta z \rangle = 2.35 \pm 0.04$ mm

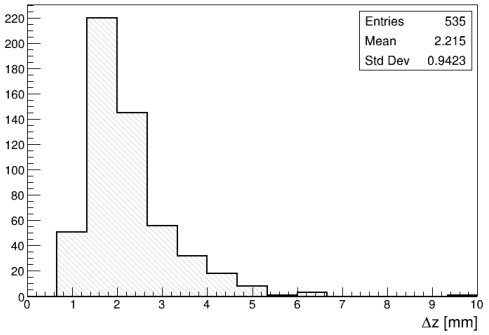

(d) Top $\langle \Delta z \rangle = 2.22 \pm 0.04$ mm

Figure 3.33: Δz distributions for each run type. Uncertainties on each $\langle \Delta z \rangle$ were calculated assuming the uncertainty on the mean scaled as one over the square root of the number of events for each run type. Since the distributions do not appear to be Gaussian, these should be taken as approximate only.

comparison to the F and T runs. In comparing the distributions by eye it appears that the that shape of the T and F runs are distinct from the L and R runs.

At first glance, the comparison of Δx and Δz values for a specific run, for instance the T run, may appear troublesome. For the T run, it has been assumed that neutron recoils are most directed, on average, along the x axis. However, $\langle \Delta x \rangle < \langle \Delta z \rangle$ for the T run. It should be recalled that Δx and Δz are measured in differing ways, see Section 3.2.4. Δx is arrived at essentially by counting the number of wires hit for a track, and Δz comes from the half-maximum width in time of the I peak signal.

For each track of each run type, the value $\frac{\Delta_x}{\Delta_z}$ was calculated and these were histogrammed in Figure 3.34. By eye it appears there are distinct differences in comparing the L and R to the F and

T runs. For the L and R run the second bin (from left) has the largest amplitude while the third bin (from left) has the largest amplitude for the F and T runs. Further the rightmost bin appears larger in the F and T runs in comparison to the L and R runs. The mean values of the L and R runs are 0.59 and 0.54, respectively, in comparison to the F and T runs which have mean values 0.71 and 0.74, respectively. Since the L and R runs are more directed along $\hat{z}$ and the T run more along $\hat{x}$ it seems reasonable that the average for the T run is larger. For the F run, recoils have a large y component on average which is not measured. The x and z components are expected to be similar in size for the F run; this was investigated with Monte Carlo simulation work. Assuming the previous to be true, it also seems reasonable that the mean $\frac{\Delta_x}{\Delta_z}$ for the F run is larger than that of the L and R runs. The expected x and z track components, being of similar length for the F run, result in a ratio that is larger than for the L and R runs, for which the z component is expected to be largest and appears in the denominator of the ratio. An unexpected result is the similarity in the mean $\frac{\Delta_x}{\Delta_z}$ values for the T and F runs. The simulation of Appendix B was not sufficient to understand this[43]. Nonetheless, the distributions can be statistically compared.

Two statistical tests were used to compare the $\frac{\Delta_x}{\Delta_z}$ distributions, one to another. A full description of the methods is provided in Section 3.3.2. The first first method is a χ^2 test for two histograms that have the same binning, which will be termed the χ^2-Two-Sample test. The second test is a permutation test that involves the pooling and Monte Carlo resampling of the $\frac{\Delta_x}{\Delta_z}$ distributions and will be named the MC-Permutation test. The results of the two tests are reported in Table 3.9. The significance of each test is expressed in units of the standard deviations σ from the mean of a normal distribution. A result with significance $\pm\, 5\sigma$ corresponds to a one-tailed p-value of 2.87×10^{-7}. This represents the probability of measuring a value equal to or more extreme than the test statistic that was calculated in comparing two of the histograms under the assumption that they were actually sampled from the same parent distribution. In other words a p-value of this size is strong evidence against the null hypothesis that the two histograms were sampled from the

[43] For this particular run of the simulation, any tracks that were found to drift and hit wires that had been, in general, labeled as dead and veto wires across the different experimental neutron exposures were discarded.

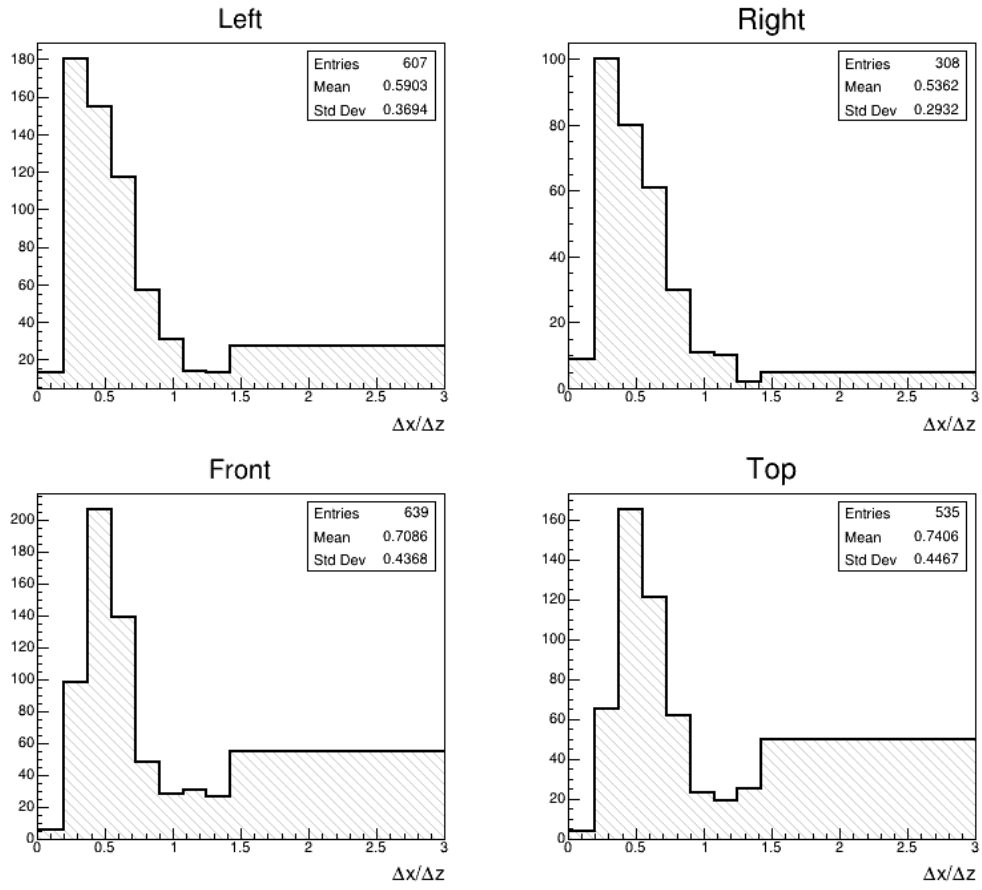

Figure 3.34: $\frac{\Delta_x}{\Delta_z}$ distributions for each run type. Variable bin widths were used to avoid having any zero entries in the histograms over the range shown. There is one bin of width 0.2 followed by 7 bins of width 0.175 followed by a final bin of width 1.575.

same parent distribution. For each pair of run types listed in the table, the ordering of the significance levels are in agreement for the two tests. Listing the pairs of run types in order of ascending significance goes as T-F, L-R, F-L, F-R, T-L, T-R for both statistical tests.

Concerning the L and R runs, during experimentation efforts were made to place the neutron source the same distance from the left detector volume and to have the source approximately centered on the detector volume for both cases. This was done so that the opening angle of neutrons incident on the detector would be approximately the same for the two cases. If the previous is approximately true, if the same distribution of materials existed between the source and the left detector volume for the two cases, and if the same wires were active in the detector for all runs,

Table 3.9: Statistical comparisons of the $\frac{\Delta_x}{\Delta_z}$ distributions between pairs of run types. For instance L-R indicates comparison of the L and R distributions. The significance levels $\mathbb{S}$ for two different tests are listed. The p-values are included as well for the χ^2-Two-Sample tests. $\tilde{\chi}^2_{\vec{M}}$ is a reduced chi square value and represents the goodness of the Gaussian fit on the test statistic distribution $\vec{M}$ which is described in Section 3.3.2. It is important that the fit is Gaussian in nature for the $\mathbb{S}$ of the MC-Permutation test to be accurate. For each of the six permutation tests performed the number of bins for $\vec{M}$ was held constant as opposed to letting this value float such as to select the binning for each of the six tests individually that would allow $\tilde{\chi}^2_{\vec{M}} \to 1$.

	$\tilde{\chi}^2_{\vec{M}}$	$\mathbb{S}$(MC-Permutation) [σ]	$\mathbb{S}$(χ^2-Two-Sample) [σ]
L-R	0.90	2.26	1.16 (p = 0.245)
T-L	0.99	6.24	6.75 (p = 1.513×10^{-11})
T-R	0.95	7.05	7.42 (p = 1.148×10^{-13})
F-L	1.16	5.26	6.01 (p = 1.856×10^{-9})
F-R	1.23	6.17	6.57 (p = 5.129×10^{-11})
T-F	0.94	1.21	0.98 (p = 0.328)

one may expect the $\frac{\Delta_x}{\Delta_z}$ distributions to be nearly identical for these two sets of runs[44]. For instance neutrons from a R run must pass through materials of the right detector as well as central cathode to reach the left detector volume which is not true for neutrons of a L run. Further, Table 3.7 indicates that the wires that were active for L runs are different from those active during the R, F, and T runs. Therefore, the shape of the active volume and distribution of possible recoil orientations may be slightly different for the two cases. A significance of 2.26(1.16)σ exists when comparing the L and R runs when applying the MC-Permutation(χ^2-Two-Sample) test. As such, the null hypothesis cannot be rejected, which is that the $\frac{\Delta_x}{\Delta_z}$ distributions of each are from a common distribution. Given that the two runs were not exact mirror images of each other, it is not unexpected that the two populations may be somewhat dissimilar.

The comparison of the $\frac{\Delta_x}{\Delta_z}$ between pairs of runs can be used to understand which populations can be differentiated. In comparing T-L, T-R, F-L, and F-R, $\mathbb{S}$ = 6.24(6.75), 7.05(7.42), 5.26(6.01), and 6.17(6.57) when applying the MC-Permutation(χ^2-Two-Sample) test, respectively. All four are comparisons of a pair of runs that are directed on average along axes perpendicular to each

[44]A further difference may be present for the L and R runs. The source is placed relatively close to the vessel in each case. As a result, as one steps in distance along the z axis of the detector volume, the angular distribution of recoils may change. This will be mirrored for the two runs. When this is combined with diffusion, which also depends on the z distance from the detector, the two recoil populations may possess an inherit difference.

other with one of the axes being the z axis. Differences in significance between T-L and T-R or F-L and F-R may exist due to the fact that the L and R runs were not exact mirror images of each other as described above. The T-F comparison yields $\mathbb{S}$ = 1.21(0.98) when applying the MC-Permutation(χ^2-Two-Sample) test, an indication that the detector is not effective at distinguishing the x-axis directed neutrons from the y-axis directed neutrons.

It can be concluded that for the single-wire-plane MWPCs of the DRIFT-IIe detector, measurement of directionality via the Δ_x and Δ_z axial range components is viable. The T-L, T-R, F-L, and F-R pairs all indicate significant differences during comparison. The data reported in this section will be used in the conclusion to this dissertation, Section 4, to understand how many WIMP-like recoils may need to be observed along the x and z axes of the detector in order to claim a significant result.

3.3.2 Statistical Analysis and Significance of Results

χ^2-Two-Sample Test

Suppose two one-dimensional arrays of values exist $\vec{v_1}$ and $\vec{v_2}$ that contain N_1 and N_2 entries, respectively. Let each of the arrays be histogrammed into distributions of k bins where the frequency of the i^{th} bins are nonzero and represented by n_{1i} and n_{2i} such that $\sum_{i=1}^{k} n_{1i} = N_1$ and $\sum_{i=1}^{k} n_{2i} = N_2$. The χ^2-Two-Sample test statistic, X^2, is given below and has been shown to approximately follow a chi square distribution with k-1 degrees of freedom χ^2_{k-1} [144][45].

$$X^2 = \frac{1}{N_1 N_2} \sum_{i=1}^{k} \frac{(N_2 n_{1i} - N_1 n_{2i})^2}{n_{1i} + n_{2i}} \tag{3.4}$$

The null hypothesis for this test is that the two distributions were sampled from the same parent distribution. One obtains strong evidence against the null hypothesis if the p-value is sufficiently small. The p-value is the probability of sampling a value from the test statistic distribution that

[45]The method described here is invoked in the TH1::Chi2Test() method of ROOT [113] which will be utilized for the comparison of histograms when using this method.

is equal to or more extreme than the test statistic that was observed, in this case X^2 above. For instance if the observed X^2 falls on the right tail of the χ^2_{k-1} distribution then the one-tailed p-value is $P(x \geq X^2) = \frac{\int_{X^2}^{\infty} dx \chi^2_{k-1}(x)}{\int_0^{\infty} dx \chi^2_{k-1}(x)}$, where here it has been assumed that χ^2_{k-1} is a function of x. P-values can readily be looked up or calculated via statistical software packages for χ^2 distributions.

Typically, a one-tailed p-value of 2.87×10^{-7} or two-tailed p-value of 5.73×10^{-7} is used to reject the null hypothesis. The significance of the test can be expressed in units of the standard deviation σ from the mean of a normal distribution. That is how many standard deviations from the mean does the measured p-value lie. The two previous p-values correspond to 5σ observations for one-tailed and two-tailed tests, respectively.

The measured $P(x \geq X^2)$ can now be converted to a normal distribution significance level. Since χ^2_{k-1} is not a symmetric function, a normal distribution significance level will be calculated by assuming the measured p-value lies in the right tail of the normal distribution and only considering the range $[0, \infty]$. This is equivalent to assuming the measured p-value lies in either tail and considering the range $[-\infty, \infty]$. For a normal distribution $f(x|\mu, \sigma) = \frac{1}{\sqrt{2\pi}\sigma} e^{\frac{-(x-\mu)^2}{2\sigma^2}}$ with $\mu = 0$ and $\sigma = 1$. In the following $\mathbb{S}$ represents the significance level.

$$P(x \geq X^2) = \frac{\frac{2}{\sqrt{2\pi}\sigma} \int_{\mathbb{S}\sigma}^{\infty} dx\, e^{\frac{-(x-\mu)^2}{2\sigma^2}}}{\frac{2}{\sqrt{2\pi}\sigma} \int_0^{\infty} dx\, e^{\frac{-(x-\mu)^2}{2\sigma^2}}}$$

$$P(x \geq X^2) = \frac{\sqrt{\frac{2}{\pi}} \int_{\mathbb{S}}^{\infty} dx\, e^{\frac{-x^2}{2}}}{\sqrt{\frac{2}{\pi}} \int_0^{\infty} dx\, e^{\frac{-x^2}{2}}}$$

$$P(x \geq X^2) = \frac{\sqrt{\frac{2}{\pi}} \int_0^{\infty} dx\, e^{\frac{-x^2}{2}} - \sqrt{\frac{2}{\pi}} \int_0^{\mathbb{S}} dx\, e^{\frac{-x^2}{2}}}{\sqrt{\frac{2}{\pi}} \int_0^{\infty} dx\, e^{\frac{-x^2}{2}}}$$

$$P(x \geq X^2) = 1 - erf(\frac{\mathbb{S}}{\sqrt{2}}) \tag{3.5}$$

For a given $P(x \geq X^2)$, Equation (3.5) can be solved numerically to get the normal distribution significance level $\mathbb{S}$.

MC-Permutation Test

This method is a Monte Carlo permutation test, which was developed into computer code for this work, and it can be used to statistically compare two histograms. Permutation tests, similar to the one presented here, are known statistical tools that have an origin dating back to the 1930s [145]. The null hypothesis of this test is that the two distributions are sampled from the same parent distribution, and this hypothesis may be rejected if the significance of the test $\mathbb{S}$ is sufficiently large as will be discussed later. Suppose two one-dimensional arrays of values exist $\vec{v_1}$ and $\vec{v_2}$ that contain N_1 and N_2 entries, respectively.

First one calculates the average of each of the arrays $\langle\vec{v_1}\rangle$ and $\langle\vec{v_2}\rangle$. The test statistic M will be defined as below. Let M_{obs} represent the test statistic observed when applying (3.6).

$$M = \langle\vec{v_1}\rangle - \langle\vec{v_2}\rangle \tag{3.6}$$

All $N = N_1 + N_2$ values are then pooled into one array $\vec{v}$ and the values are randomly shuffled within the array. One must then decide how many permutations m should be performed with the pooled data[46]. Let $\vec{v_1'}$ and $\vec{v_2'}$ be two temporary arrays which each can hold N_1 and N_2 values, respectively. Let $\vec{M}$ represent an array that can hold m values, how this array is filled is described in the algorithm below.

---

for *each permutation i such that* $0 \leq i < m$ **do**

1.) Randomly fill $\vec{v_1'}$ and $\vec{v_2'}$ by sampling $\vec{v}$. Checks are performed to ensure no values are resampled from $\vec{v}$.

2.) Calculate $\langle\vec{v_1'}\rangle$ and $\langle\vec{v_2'}\rangle$

3.) Calculate $M' = \langle\vec{v_1'}\rangle$ - $\langle\vec{v_2'}\rangle$

4.) Store M' in the i^{th} element of $\vec{M}$. $\vec{M}[i] = M'$

end

---

[46]A sufficiently large number should be chosen such that the desired precision in output is achieved, this is done by iteration. For instance, if one wants output values accurate to the hundredth, one would iteratively perform this method while increasing m until the output values converge at the hundredths place in the result. Here it was found $m = 10^4$ was sufficient to achieve this.

With $\vec{M}$ filled one can now histogram the m values of $\vec{M}$ and fit it with a Gaussian. Even if the two distributions of $\vec{v_1}$ and $\vec{v_2}$ are not themselves Gaussian the distribution of $\vec{M}$ is expected to be Gaussian due to the central limit theorem. Here the choice in number of bins needs to be manually adjusted such that the $\frac{\chi^2}{NDF}$ is reasonable for the fit. The standard deviation of the fit σ_{Mfit} can be extracted. The statistical significance of the method is then calculated (3.7). An $\mathbb{S}$ of $\geq |5|$ corresponds to a p-value $\leq \ 2.87\times10^{-7}$. Note that $\mathbb{S}$ can be positive or negative depending on the sign of M_{obs}.

$$\mathbb{S} = \frac{M_{obs}}{\sigma_{Mfit}} \tag{3.7}$$

3.3.3 Contamination in Recoil Track Populations

After applying the nuclear recoil analysis described in Section 3.2.5 all tracks which passed the analysis were inspected visually. In this section a variety of track types are described and will be enumerated alphabetically A to I, and examples of these events are shown. These tracks are cut from certain analyses such as of the z_{IP} distributions of Section 3.2.2 and energy distributions of Section 3.2.3. These types of tracks are termed *TracksCPA* since they are cut post-analysis. Since *TracksCPA* are identified by eye, to avoid self-induced biases these types of tracks are not cut when analyzing the range components for neutron recoil tracks; it was decided to remain rigorous in evaluating these two quantities as they are of main interest to this dissertation. This study of *TracksCPA* was done to understand how well the analysis performs at identifying nuclear recoil tracks.

TracksCPA$_A$ are characterized by a single observable peak which can be due to sparks or actual nuclear recoil tracks that occur very close to the MWPC and consequently do not have enough drift time for peak separation to occur. For these tracks, the analysis happens to find small peaks in the background noise which have spacings consistent with separation of minority peaks of an actual recoil signal. The tracks are not nuclear recoil-like and an analysis cut should be applied to remove these.

TracksCPA$_B$ are a class of track in which the identification of the minority peak positions is questionable. These tracks also have a relatively short falltime. These appear to be tracks which occur close to the MWPC and have an orientation favorable to overlap in the resulting minority carrier signals. The tracks are further questionable as the size of the minority peaks relative to the shoulder on the signal are not obviously larger than the size of the peaks in the noise. These tracks should be investigated further before implementing any software cuts.

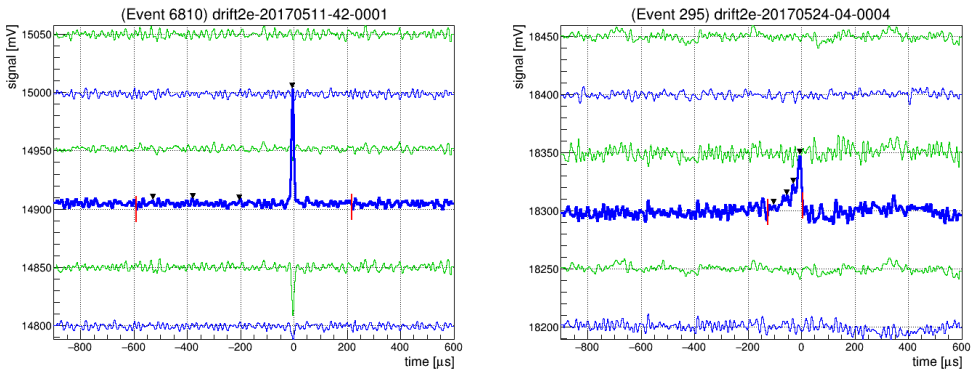

(a) *TracksCPA*$_A$ **(b)** *TracksCPA*$_B$

Figure 3.35

TracksCPA$_C$ are distinguished by two peaks in the signal. These types of signals may be observed for two overlapping spark events or a spark event that happens to overlap a low-z_{IP} recoil track. Type C tracks should be further investigated to ensure that these are not recoil tracks with a different than normal minority peak structure.

TracksCPA$_D$ appear to be good recoil tracks where the peaks are not clearly distinguishable, which may occur due to track orientation. They are only identified and removed by this cut since the identification of minority peaks in these tracks is questionable.

TracksCPA$_E$ are not well-contained. The top trace of this track has a signal which has been missed by the analysis. As a result, the energy of this recoil as well the components of its range will not be correctly reconstructed. Since the threshold for peak detection is based on the size of the background noise for a given wire, a signal was found for the middle trace but not the top trace.

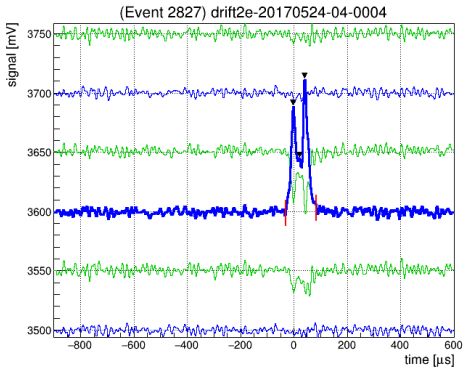

(a) *TracksCPA*$_C$

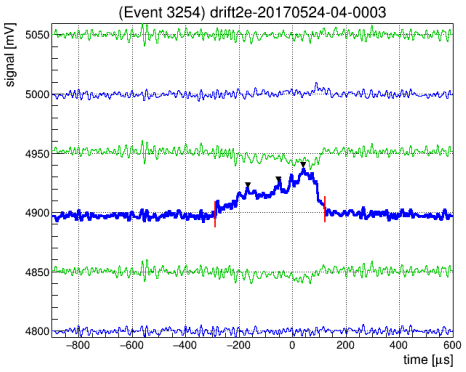

(b) *TracksCPA*$_D$

Figure 3.36

TracksCPA$_F$ occur when the I peak of the maximum amplitude trace has been misidentified. Further improvements should be made to the analysis to avoid these types of errors.

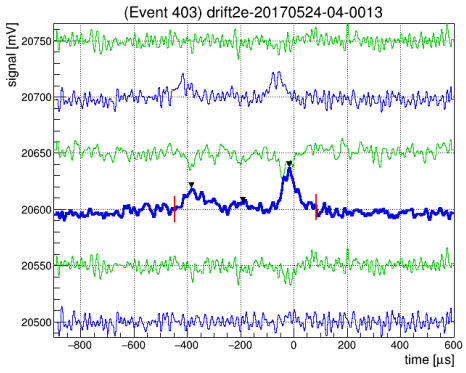

(a) *TracksCPA*$_E$

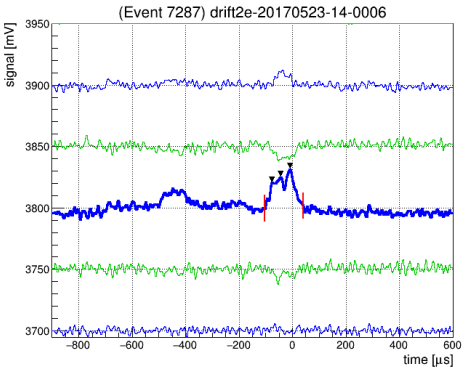

(b) *TracksCPA*$_F$

Figure 3.37

TracksCPA$_G$ are ones other than those above which do not appear to be recoil-like or may be actual recoils but have some defect apparent in the signal. The left type G track appears to be a good recoil but there is clearly a negative going signal affecting all wires for this event which is particularly problematic since it intersects the visible signal region. The negative going signals are likely not due to a real ionization event in the detector as the signals on both the anode and field

wires have the same polarity. The right G track may be a subset of *TracksCPA*$_C$, where here the two signals are not overlapping.

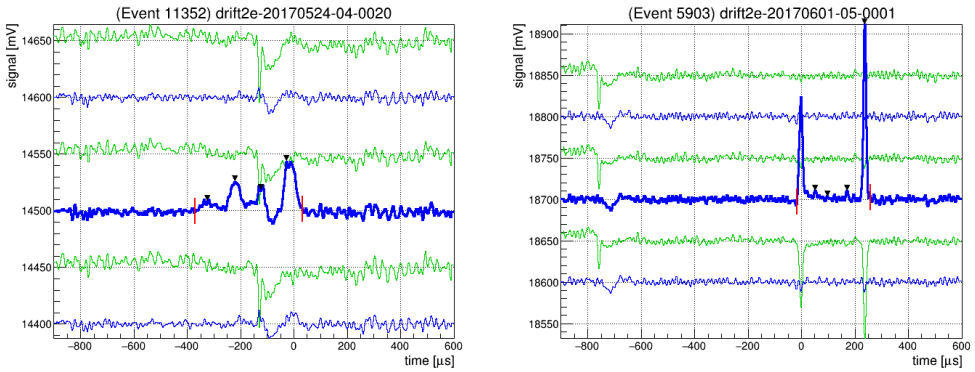

(a) *TracksCPA*$_G$ **(b)** *TracksCPA*$_G$

Figure 3.38

TracksCPA$_H$ have a misidentified I peak on one of the traces which does not possess the maximum amplitude signal. This has occurred for the bottom trace of this track. Upon careful inspection within the signal region for this trace, one can see that four peaks, due to noise, were identified across the time bins that visually appear to be for the I peak only. The actual minority peaks on the trace were missed due to the low signal to noise. This track was allowed to pass through the analysis due to the Track Analysis 02 stage of the analysis chain described in Section 3.2.5. In order to properly calculate the z extent of a track, Δz, the width in time at half maximum from the sum of all I peak signals of a track is used. Since the bottom trace does not have the expected minority peak structure it was not used for the z extent calculation. As such, tracks of this type may have an inaccurate calculated z extent.

TracksCPA$_I$ are ones in which the S and P peaks have been misidentified. Type I tracks only affect calculations of the MWPC to track vertex distance within the detector z_{IP}.

For each of the neutron run types L, R, F, and T, the number of each *TracksCPA* type observed for that data is reported in Table 3.10. *TracksCPA*$_I$ do not affect calculations of the range components of a track. The value $fraction_{AtoH}$ gives an estimate of how contaminated the populations

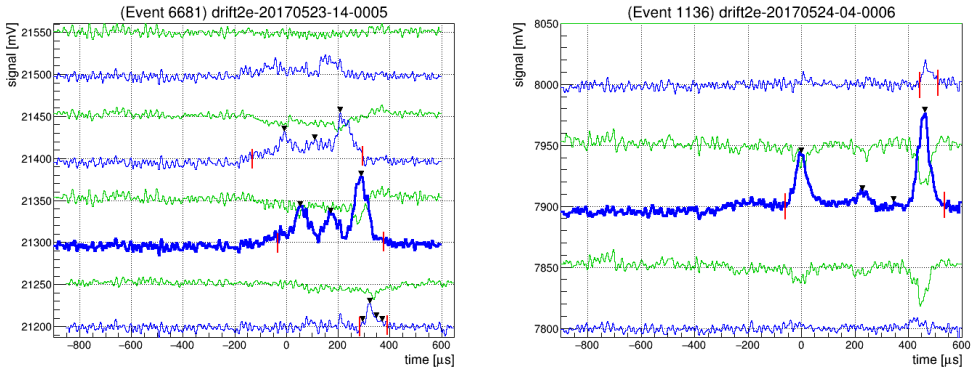

(a) *TracksCPA*$_H$ **(b)** *TracksCPA*$_I$

Figure 3.39

of these two parameters are with "bad" tracks. A maximum value 6.2% is observed across all neutron exposures. While some improvements need to be made to the analysis, the data used in this dissertation to measure the directional capabilities of the detector appears to be populated with recoil-like events at the ∼94% level[47]. It is of course possible that some of these events originate from radioactive contaminates within the components of the detector.

Table 3.10: The number of each *TracksCPA* type observed for the L, R, F, and T neutron exposures. The total number of tracks N_{tracks} observed for each exposure, the ratio of the number of tracks of types A to H over N_{tracks}, and the ratio of the number of type I tracks over N_{tracks} are also reported.

Run	A	B	C	D	E	F	G	H	I	N_{tracks}	$fraction_{AtoH}$	$fraction_I$
L	5	4	3	2	15	0	0	1	19	607	0.049	0.031
R	2	5	3	0	2	1	2	4	5	308	0.062	0.016
F	1	8	8	3	9	0	3	1	29	639	0.052	0.045
T	1	4	1	1	12	0	1	2	25	535	0.041	0.047

[47] An important clarification should be made. It is not the claim that the analysis algorithm picks out recoil-like tracks from the raw data files with 94% efficiency. It is the claim that of the tracks the analysis passed at least 94% of them appeared visually to match the intended definition of recoil-like. This check was meant to give confidence that track samples which were analyzed seem to be representative of recoil events. It further implies that the range component analysis may be conservative in reported significance.

Chapter 4

Conclusions and Summary

4.1 Number of WIMP Recoils Required for A Significant Detection

Based on the results of Section 3.3.1 it can be concluded that the range components of nuclear recoil tracks offer a viable signature within the DRIFT-IIe detector that could be used to search for WIMP dark matter. This conclusion will be developed in the discussion that follows. In the Introduction to this dissertation, specifically Section 1.6, it was proposed that a directional signature from the WIMP wind could possibly be observed by carefully orienting the DRIFT-IIe detector in a lab of the Boulby Underground Science Facility. This signature is known as sidereal modulation and is the result of the average direction of the WIMP wind sweeping across the detector over the course of a sidereal day. If one carefully orients the detector within the space, it could be set up such that in theory the wind passes $\sim$normal to one face of the detector and 12 sidereal hours later passes $\sim$normal to a face which is perpendicular to the first. In order to be sensitive to this signature requires that the detector be sensitive to the direction of the nuclear recoils resulting from the WIMP wind.

To verify that the range components of elastic nuclear recoils are dependent on the direction of the particles that cause them, a ^{252}Cf neutron source was placed at a few locations around the detector. The neutron run results, have been presented in Section 3.3.1. As a reminder, four runs have been considered Left (L), Right (R), Front (F), and Top (T). For each run type, the number of tracks which passed the analysis of Section 3.2.5 are 607, 308, 639, and 535 for the L, R, F, and T runs, respectively.

Using the populations of neutron tracks above, it can be estimated how many dark matter recoils, similar to those of the neutron recoils discussed in this work, would need to be observed in order to claim a significant detection. Based on the directed neutron data at hand, statistical

comparisons will be made between pairs of neutron exposures that were directed along the different axes of the detector. The endeavor of these comparisons is to approximate how many tracks would need to be accumulated for each each of two axes in order to claim significance at levels of 3σ and 5σ.

A 3σ observation is typically interpreted as evidence for a scientific phenomenon, while a 5σ observation is typically interpreted as discovery of a scientific phenomenon. If one were to analogize these two values in terms of coin flips, the probability of a 3σ observation occurring by chance alone, in the absence of any actual scientific phenomenon, would be equivalent to the chance of flipping 741 fair coins and only one landing head-side up. A 5σ observation corresponds to flipping 3.49×10^6 fair coins and only one landing head-side up[48].

In Section 3.2.3, the neutron recoil energy distributions were discussed. It was shown, by comparison of neutron results to the simulation of WIMPs, that the DRIFT-IIe detector is most sensitive to the energies of recoils resulting from WIMP masses $\gtrsim$ 1000 GeV. As of yet, energy cuts have not been applied to the neutron track populations in order to make the energy spectrum more WIMP-like. In the algorithm below, for each iteration within the algorithm, tracks are resampled from each population in a way that forces the energy distribution of each sample to match that expected from 1000 GeV WIMPs.

The 1000 GeV WIMP recoil energy distribution has been simulated via methods described in Appendix B. The WIMP recoil energies were histogrammed into six bins of width 1000 NIPs from 0 to 6000 NIPs. The WIMP recoil energy probability distribution P_E is reported in Table 4.1. In Section 3.2.3, it is seen that few neutron tracks are observed below 1000 NIPs, with the smallest overall energy of 917 NIPs being observed. For this reason, a detector threshold of 1000 NIPs is assumed here. This forces the probability of observing a WIMP recoil in the 0 to 1000 NIP energy bin to zero. The implication is that the detector is insensitive to $\sim$79% of 1000 GeV WIMP recoils since they belong to this lowest-energy bin. The above-threshold WIMP recoil energy probability

[48]The values reported here are associated with one-tailed statistical tests as that is what will be used in the subsequent discussion.

distribution $P_{Ethresh}$ is also shown in the table, probabilities have been renormalized to one after $P_{Ethresh}(0-1000\,NIPs)$ has been set to zero. The corresponding cumulative distribution $C_{Ethresh}$ has also been tabulated.

With the cumulative distribution at hand, one can sample neutron recoils from one of the four runs, and ensure the recoil energy distribution matches that of 1000 GeV WIMPs. To do this, one pseudorandomly samples a value p_{sample} from the uniform distribution ranging from [0.0,1.0], since probability spans this range. If $C_{Ethresh\ell} \leq p_{sample} < C_{Ethresh\ell+1}$, with ℓ enumerating the energy bins, one then pseudorandomly samples a neutron that has a recoil energy in the range E_ℓ to $E_{\ell+1}$. Additionally, sampling is performed such that an individual neutron track can only appear once in a given set of individual samples.

It is not the claim that $P_{Ethresh}$ is exactly the WIMP recoil energy distribution one should expect to observe with the detector. Further detector efficiencies have not been completely accounted for here. If a track is above threshold energy, this does not guarantee it will be observed. Tracks are identified by the amplitude of a signal relative to noise. If a track is deposited far from the MWPC, as a reminder the distance from the MWPC is z_{IP}, the ionization will have more time to diffuse as it travels to the MWPC. This may cause the track to be missed by the analysis. A second z_{IP}-dependent effect occurs for tracks of larger energy but small z_{IP}. For these tracks, all of the minority peaks may be piled on top of each other and hence inseparable in analysis causing the track to be missed. This can be seen in the two-dimensional efficiency map for the DRIFT-IId detector [77] [78]. For each energy bin ℓ a fraction of tracks will be lost due to z_{IP}-dependent efficiency. The fraction lost per bin however will not be a constant, this will change the overall shape of the observed energy spectrum. To account for this efficiency, further simulation work is needed but is not done in this dissertation. One needs to compare the observed number of ^{252}Cf neutron recoils per bin in energy and per bin in z_{IP} to those from simulation to understand this efficiency. Using this two-dimensional efficiency space, one could then simulate many WIMP recoils in the detector, keeping track of energy and the z position that they occur in the volume.

One could then sample the correct proportion of neutrons from each two-dimensional bin in order to mimic WIMP recoil events in an improved way.

Table 4.1: Tabulated is the WIMP recoil energy spectrum for 1000 GeV WIMPs, for which elastic scattering with sulfur has been considered. P_E values are the probability associated with each of the six energy bins. $P_{Ethresh}$ and $C_{Ethresh}$ are the probabilities and cumulative distribution values after the detector threshold of $\sim$1000 NIPs has been taken into account, which assigns a value of zero probability for the first energy bin, and the remaining probability distribution has been renormalized to one.

bin ℓ	Energy Range [NIPs]	P_E	$P_{Ethresh}$	$C_{Ethresh}$
0	[0,1000)	0.7898	0	0
1	[1000,2000)	0.1456	0.6926	0.6926
2	[2000,3000)	0.0433	0.2059	0.8985
3	[3000,4000)	0.0145	0.0692	0.9677
4	[4000,5000)	0.0049	0.0235	0.9912
5	[5000,6000)	0.0018	0.0088	1.0000

Having understood how one can sample neutron recoils from the L, R, F, or T run with a WIMP-like energy distribution, the statistical comparison of pairs of neutron runs will proceed. The comparison is a resampling technique that has evolved from the MC-Permutation Test presented in Section 3.3.2. A summary of this technique is provided, followed by a more detailed explanation on how the resampling algorithm was implemented in practice. Parts of the detailed explanation are outlined in a pseudocode format.

To summarize, for concreteness let us consider only two of the runs T and L. For each of these runs, for instance, if 30 T tracks are compared to 30 L tracks, one wants to understand how different these two samples are. Specifically what we are comparing are the $\frac{\Delta_x}{\Delta_z}$ values for these two samples. Since the T runs are more directed along $\hat{x}$ on average and the L runs are more directed along $\hat{z}$ on average, one would expect on average this ratio to be different for the two runs. However, as is, the recoil energy spectrum for each of the runs is a ^{252}Cf neutron recoil energy spectrum that is shaped by detector and analysis efficiencies. In order to make the comparison agree more closely with what one may expect from WIMPs, each of these samples of 30 are drawn such that on aggregate they possess a 1000 GeV WIMP energy spectrum. This specific WIMP mass was chosen, because it was previously shown that it is expected that this detector is most

sensitive to WIMPs at this mass or larger. For each of these two samples the MC-Permutation Test of Section 3.3.2 is applied. When this permutation test is performed, first the difference between the average of the two samples of 30 are calculated, let us call this the test statistic. The 60 total values are then combined into one pool. If the two samples of 30 were drawn from the same parent distribution, one would not expected to see large statistical differences in the average of two samples of 30 randomly drawn from the pooled distribution. Several permutations are drawn, two samples of 30, from the pooled distribution and this allows one to build a Gaussian distribution of the difference in the averages across all permutations. One can then quantify how many standard deviations away the test statistic is away from the average of this Gaussian. If the test statistic lies far way, this allows one to reject the null hypothesis that the two initial samples of 30 were drawn from the same parent distribution with large significance. The process has been described for two samples of 30, one drawn from the T data and one from the L data. A better estimate on significance is found by repeating the above process for many subsets of sample size 30 drawn from the T and L data to compute an average significance associated with this sample size. Finally, one can repeat the procedure and vary the sample size, to see how significance scales on average with sample size. A given sample size will be denoted by $N_{samples_i}$, the number of subsets drawn for each sample is a fixed number $N_{subsets}$, and the average significance across all subsets of a given sample size is denoted $\mathbb{S}_i$ with a standard deviation of $\sigma_{\mathbb{S}_i}$.

—Resampling Algorithm Begin————————————

The more detailed explanation, of the statistical technique used to compare runs, begins here. Suppose two sets of information exist about two of the neutron runs, set_1 and set_2. These sets contain information about each recoil track for each of the two runs, among which are energy E and the ratio of range components $\frac{\Delta_x}{\Delta_z}$. For set_1 Let $\vec{E_1}$ and $\vec{v_1}$ be arrays that each contain a number N_1 energy and $\frac{\Delta_x}{\Delta_z}$ values, respectively. Let similar arrays be assumed for set_2. In the algorithm, $N_{subsets}$ of samples will be drawn from each set. Each subset drawn will have a given number of samples $N_{samples}$, and for each sample the MC-Permutation Test will be applied for $N_{permutations}$ of the sample. $N_{subsets}$ and $N_{permutations}$ were fixed at 400 and 500, respectively. $N_{samples}$ was

varied from $N_{samples_{min}} = 30$ to $N_{samples_{max}}$, in steps of $\Delta N_{samples} = 10$. $N_{samples_{max}}$ is limited by the smaller of N_1 and N_2, more specifically, it is limited by the portion of these values which fall into the first energy bin for which the detector is sensitive. The number of samples that belong to the higher energy bins must have the correct proportions to match the probabilities $P_{Ethresh}$, for those bins. For instance, for a L run, 141 tracks belong to the energy bin $\ell = 1$, so, the approximate maximum number of tracks that can be drawn without repetition is $\frac{141}{P_{Ethresh1}} = 203$. However, since random sampling techniques are used, the true maximum number that can be sampled without repetition will be smaller. The number of neutron tracks belonging to each energy bin are listed in Table 4.2.

Table 4.2: Listed are the number of tracks which fall into each of the six energy bins for the Left, Right, Front, and Top neutron runs.

bin ℓ	Energy Range [NIPs]	L	R	F	T
0	[0,1000)	5	3	4	8
1	[1000,2000)	141	73	130	145
2	[2000,3000)	184	90	155	174
3	[3000,4000)	88	48	90	71
4	[4000,5000)	74	30	80	56
5	[5000,6000)	36	19	46	36

In the following, let each step in sample size be indexed by i, and each pair of subsets drawn be indexed by j. For each pair of subsets $\vec{v_{1ij}} \subseteq \vec{v_1}$ and $\vec{v_{2ij}} \subseteq \vec{v_1}$, a significance $\mathbb{S}_{ij}$ is output after application of the MC-Permutation Test on that pair of subsets. These $\mathbb{S}_{ij}$ are histogrammed for all j belonging to a given i, and the average $\mathbb{S}_i$ across all j subsets for a given sample size $N_{samples_i}$ and standard deviation $\sigma_{\mathbb{S}_i}$ are extracted.

I.) Arrays are defined to hold the average significance and standard deviation across all subsets of a given sample size. Let these arrays be named $\vec{\mathbb{S}_i}$ and $\vec{\sigma_{\mathbb{S}_i}}$. For instance, the first element of $\vec{\mathbb{S}_i}$ holds the average significance returned in comparing $N_{subsets} = 400$ pairs of $\vec{v_{1ij}}$ and $\vec{v_{2ij}}$ each of sample size $N_{samples_{min}} = 30$.

II.) Two arrays are defined $E_1\vec{indices}$ and $E_2\vec{indices}$. Each is six elements in length to match that

of the energy binning of $P_{Ethresh}$ above, and each element of each array is a list of indices. The first element of $E_1\vec{indices}$ is populated with the indices of each element of $\vec{E_1}$ that has an energy in NIPs in the range $[0, 1000)$, similarly the second element of $E_1\vec{indices}$ is populated with the indices of each element of $\vec{E_1}$ that has an energy in NIPs in the range $[1000, 2000)$, and so forth for the remaining bins up to 6000 NIPs. The same is done to populate $E_2\vec{indices}$.

III.) Iterate over each sample size, $N_{samples_i}$.

For ($N_{samples_{min}} \leq N_{samples_i} \leq N_{samples_{max}}$ **, step size =** $\Delta N_{samples}$**):**

A.) Two arrays are defined $\vec{ECounts_1}$ and $\vec{ECounts_2}$, that are $N_{subsets}$ in length. Each element is a list that stores the number of tracks to draw for each energy bin. Above the energy bins have been indexed by ℓ, which implies that $ECounts_{1jl}$ and $ECounts_{2jl}$ hold the number of tracks of energy E_ℓ to $E_{\ell+1}$ that should be drawn from $\vec{v_1}$ and $\vec{v_2}$ for the j^{th} subset of each.

B.) $\vec{ECounts_1}$ and $\vec{ECounts_2}$ are populated. For each subset j, $N_{samples_i}$ values, named $p_{sample_{ij}}$, are pseudorandomly drawn from the uniform distribution $[0.0, 1.0]$. If $C_{Ethresh\ell} \leq p_{sample_{ij}} < C_{Ethresh\ell+1}$, $ECounts_{1jl}$ and $ECounts_{2jl}$ are both incremented by one. This process ensures that the sampling for each subset has an energy distribution which matches that of 1000 GeV WIMPs.

For ($0 \leq j < N_{subsets}$**):**

1.) The indices belonging to each element of $E_1\vec{indices}$ and $E_2\vec{indices}$ are randomly shuffled, this will allow for a random sampling of $\vec{v_1}$ and $\vec{v_2}$.

2.) $\vec{v_{1ij}}$ and $\vec{v_{2ij}}$ are populated. The first $ECounts_{1jl}$ indices in $E_1\vec{indices}_\ell$ for all ℓ define the elements of $\vec{v_1}$ which compose subset $\vec{v_{1ij}}$. Similar is done to populate $\vec{v_{2ij}}$.

3.) The MC-Permutation Test, as described in Section Section 3.3.2, is applied to arrays $\vec{v_{1ij}}$ and $\vec{v_{2ij}}$. For each subset, $N_{permutations}$ was fixed at 500. The significance of the test is returned and stored in $\mathbb{S}_{ij}$.

C.) For each sample size $N_{samples_i}$, the $\mathbb{S}_{ij}$ are histrogrammed. Checks are performed to ensure that the distribution is well contained over the region it was defined to span and that the underflow and overflow bins have not been populated by more than a few entries out of the $N_{subsets}$ entries in total. The average and standard deviation are calculated across all entries and stored in $\mathbb{S}_i$ and $\sigma_{\mathbb{S}_i}$, respectively. Since the distributions appear approximately symmetric and Gaussian, $\frac{\sigma_{\mathbb{S}_i}}{\sqrt{N_{subsets}}}$ will be used at the uncertainty on the mean.

—Resampling Algorithm End————————————

In proceeding, one must take into account the assumption about the detector placement in the Boulby lab. It has been assumed that the detector has been placed in the lab such that at a specific time in a sidereal day the WIMP wind is blowing through the top of the detector (along the x axis) and 12 sidereal hours later through a side which is normal to the z axis. These two axes are those for which recoil range components can be measured. Neutrons from a top (T) run were directed along the x axis of the detector and L and R neutron runs were along the z axis of the detector. The algorithm above was used to compare runs T to L and T to R. The results of these two comparisons are in Tables 4.3 and 4.4.

Table 4.3: (T-L Comparison) The algorithm above has been applied to compare Top and Left runs. For each sample size $N_{samples_i}$, $\mathbb{S}_i$ gives the average significance output from the MC-Permutation test for $N_{subsets} = 500$ pairs of subsets drawn. The standard deviation about each average and uncertainty on the mean are also reported. An extra digit of precision has been kept for each value.

$N_{samples_i}$	30	40	50	60	70	80	90
$\mathbb{S}_i$	0.891	1.087	1.170	1.339	1.509	1.479	1.620
$\sigma_{\mathbb{S}_i}$	0.902	0.874	0.930	0.898	0.825	0.837	0.784
$\frac{\sigma_{\mathbb{S}_i}}{\sqrt{N_{subsets}}}$	0.045	0.044	0.047	0.045	0.041	0.042	0.039
$N_{samples_i}$	100	110	120	130	140	150	160
$\mathbb{S}_i$	1.697	1.796	1.917	1.978	2.024	2.186	2.153
$\sigma_{\mathbb{S}_i}$	0.792	0.728	0.739	0.804	0.759	0.677	0.727
$\frac{\sigma_{\mathbb{S}_i}}{\sqrt{N_{subsets}}}$	0.040	0.036	0.037	0.040	0.038	0.034	0.036

For each of these two tables, there appears to be a trend of decreasing standard deviation $\sigma_{\mathbb{S}_i}$ with increasing sample size $N_{samples_i}$. This is not expected provided that the size of a data set is large in comparison to the number of samples being drawn. This trend is likely due to the finite sizes of the data sets. As the sample size approaches the size of a data set, there is less variance between different draws of that sample size.

Table 4.4: (T-R Comparison) The algorithm above has been applied to compare Top and Right runs. For further discussion, see Table 4.3.

$N_{samples_i}$	30	40	50	60	70	80
$\mathbb{S}_i$	1.194	1.393	1.542	1.655	1.911	1.967
$\sigma_{\mathbb{S}_i}$	0.813	0.812	0.766	0.745	0.710	0.723
$\frac{\sigma_{\mathbb{S}_i}}{\sqrt{N_{subsets}}}$	0.041	0.041	0.038	0.037	0.035	0.036

For each of the two comparisons Top-to-Left (T-L) and Top-to-Right (T-R), $\mathbb{S}_i$ was plotted against $N_{samples_i}$, with error bars on $\mathbb{S}_i$ given by $\delta_{\mathbb{S}_i} \equiv \frac{\sigma_{\mathbb{S}_i}}{\sqrt{N_{subsets}}}$. These plots appear in Figure 4.1. Each of plots was fit with a function of the form $\mathbb{S}_i = c\sqrt{N_{samples_i}}$. Where c is a constant that was allowed to float during the fit. The fit was performed with ROOT using χ^2 minimization to determine c. Using the c value measured in each case, one can estimate the $N_{samples_i}$ required for significance levels of 3σ and 5σ.

$$N_{samples_i} = \frac{\mathbb{S}_i^2}{c^2}$$

Let $\delta_{N_{samples_i}}$ and δ_c represent the uncertainties on the respective quantities. For fixed significance, standard propagation of uncertainty nets the expression for $\delta_{N_{samples_i}}$.

$$\frac{\delta_{N_{samples_i}}}{N_{samples_i}} = 2\frac{\delta_c}{c}$$

Let $N_{3\sigma}$ be the number of samples needed from each pair of runs for a significance of 3σ, and $N_{5\sigma}$ the number of samples needed for 5σ. The T-L comparison yields $N_{3\sigma} = 302 \pm 4$ and $N_{5\sigma} = 840 \pm 11$. The T-R comparison yields $N_{3\sigma} = 185 \pm 4$ and $N_{5\sigma} = 515 \pm 10$. If the L

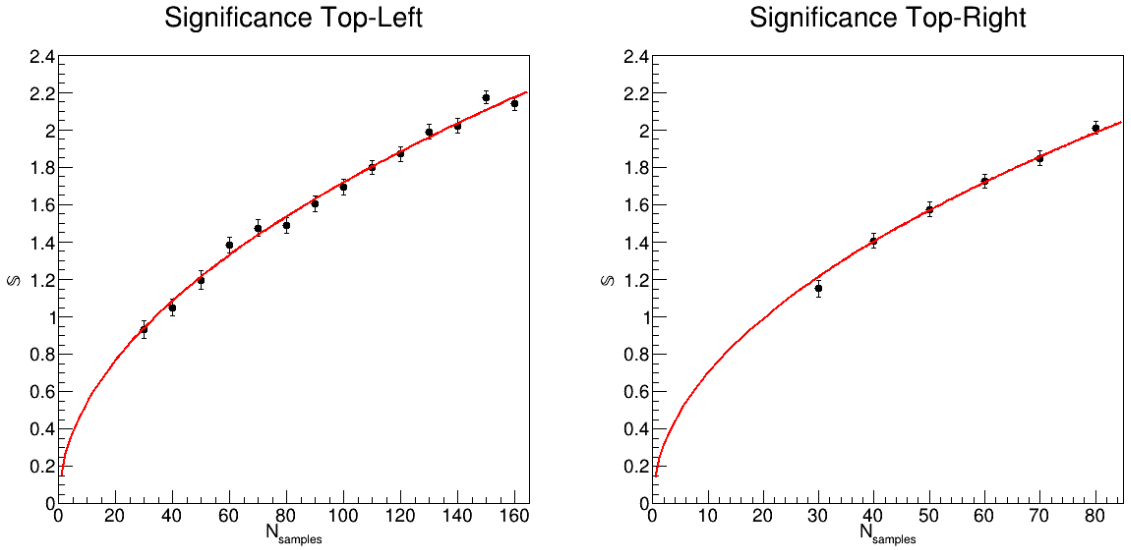

(a) $c = 0.1725 \pm 0.0011$, $\chi^2 = 14.5$, $NDF = 13$, $\frac{\chi^2}{NDF} = 1.11$, p-value $= 0.34$ **(b)** $c = 0.2204 \pm 0.0021$, $\chi^2 = 5.87$, $NDF = 5$, $\frac{\chi^2}{NDF} = 1.17$, p-value $= 0.32$

Figure 4.1: Plots (a) comparison of Top and Left runs, and (b) comparison of Top and Right runs show average significance $\mathbb{S}_i$ plotted versus $N_{samples_i}$, which represents how many tracks have been sampled from each pair of runs. Each average is over $N_{subsets} = 400$ pairs of subsets. Each plot has been fit with a function of the form $\mathbb{S}_i = c\sqrt{N_{samples_i}}$, and the best fit line is plotted. Information about each fit appears below the figures.

and R neutron runs had been perfect mirror images of each other about the active detector volume, one would expect these values reported for T-L and T-R to be consistent with each other. In Table 3.9, the significance values from the MC-Permutation Test, are reported when comparing the full data sets for the T, L, and R runs. The significance values were 2.26, 6.24, and 7.05 in comparing L-R, T-L, and T-R, respectively. Since the L-R significance of 2.26 may indicate the L and R runs were not mirror images of each other, it is expected that differing numbers of samples are needed to achieve a particular significance when comparing each to the T run. In addition, for the full data sets the significance of the T-R comparison is larger than that of T-L, despite the fact the fact that R run had about half the number of tracks that had been accumulated for the L run. Therefore, it is expected that more samples will be required to achieve a particular significance when comparing Top-to-Left versus Top-to-Right runs. One could consider, for instance, the spread in the two $N_{3\sigma}$ values for the T-L and T-R comparisons to be a systematic uncertainty. A second approach, and the one that is chosen here, is to use the larger values in order to be conservative. Therefore, it

is estimated that an upper limit of $N_{3\sigma} = 302 \pm 4$ and $N_{5\sigma} = 840 \pm 11$ are required to reach significance levels of 3σ and 5σ on average. Two checks are offered in Appendix C. One check is to confirm that the c and δ_c values output from the fit routine are consistent with expectations, and a second to check that adequate sampling has been performed in the algorithm above to output consistent results.

In Section 3.1.1, it was reported that the average observed signal integrals deposited by ^{55}Fe may be systematically low by up to 24%. Since the energy calibration constant scales inversely with the average signal integral, this implies that the energy calibration constants used in this work may be up to 24% high, which also implies that the calculated neutron recoil energies, Section 3.2.3, may be too high. Systematically shifting the measured energy distributions by 24% to lower energies may imply that the detector threshold is approximately 760 NIPs versus 1000 NIPs. Another implication is that some of the recoil tracks that previously had energies above 6000 NIPs will now be shifted to lower energies and fall below this value of 6000 NIPs, which is needed to be consistent in energy to WIMP-induced recoils. These higher energy tracks, which on average would be expected to be more directional, would now be sampled via the methods presented in this conclusion to determine how many WIMP-like tracks one needs to collect to achieve a specific significance. The methods presented in this conclusion were reapplied taking this systematic shift in recoil energy into account. For simplicity the measured neutron recoil energies were all shifted to lower values by 25%. The simulated WIMP recoil and neutron recoil energies were then binned into eight bins that were 750 NIPs in width up to 6000 NIPs. The new detector energy threshold was considered to be 750 NIPs. It was determined that in comparing Top-to-Left $N_{3\sigma} = 207 \pm 2$ when systematically shifting energies. This implies that up to 31% fewer tracks may need to be collected.

4.2 Neutron Exposure and WIMP Wind Recoil Directionality

Above, the number of tracks, assuming a 1000 GeV WIMP energy spectrum above the detector threshold, were sampled from each of the T and L runs in order to understand how many tracks

need to be accumulated in order to reach a particular significance. A final study is presented in this section. It is intended to give one a visual comparison of recoil directions when comparing neutron and WIMP detector exposures and show that recoil directionality of neutron exposures does reasonably approximate that of WIMP exposures.

In the introduction to this dissertation a sidereal modulation, see Section 1.6, DM detection signature was discussed. In order to observe this signature, a DM detector needs to have sensitivity to the change in direction of the theoretical WIMP wind over the course of a sidereal day. It has been shown in this conclusion that the DRIFT-IIe detector does have directional sensitivity, where directionality was accessed via range components (orientation) of nuclear recoil tracks. In this work the WIMP wind was mimicked by placing a neutron source at various locations around the detector. Specifically, the T and L neutron runs are of interest, which were intended to mimic the wind blowing down (along the x axis) and through the side (along the z axis) of the detector. In Section 1.6 it was determined that the WIMP wind should be blowing most south (z axis) through the detector $\sim$538.2 minutes into the local sidereal day at Boulby. It was also determined that the wind should be blowing most downward (x axis) through the detector $\sim$1255 minutes into the local sidereal day.

A visual comparison is provided via simulation of nuclear recoil directions within the detector when comparing L (z axis) neutron recoils to a sample of WIMP recoils that were collected with timestamps near 538.2 minutes into the local sidereal day. A comparison of T (x axis) neutron recoils to a sample of WIMP recoils collected with timestamps near 1255 minutes into the local sidereal day is also provided. The methods used for WIMP and neutron run simulations are described in Appendix B. Details specific to these runs of the simulations are provided followed by the results.

The x axis of the detector is perpendicular to the wires of the MWPCs, the y axis is parallel to the wires of the MWPCs, and the z axis is along the drift direction. Let us define two angles in spherical coordinates that one can use to describe the direction of recoils in the detector. Let θ be the polar angle as measured from the z axis with $0 \leq \theta \leq \pi$. Let ϕ be the azimuthal angle

in the x-y plane, with $0 \leq \phi \leq 2\pi$. Let $\phi = 0$ correspond to a vector oriented along positive $\hat{x}$, and let ϕ increase from zero as that vector is rotated in the x-y plane about the z-axis towards the positive $\hat{y}$ direction. WIMP interactions were allowed to occur over the course of a full year. For the study of WIMPs blowing most south (z axis) through the detector, only those WIMPs that had local sidereal minute timestamps in the range [538.2-45,538.2+45] were kept, representative of a 90-minute window of time centered on the time of interest. A 90-minute window was also used for WIMPs that blow down through the detector. For each study $\sim$500,000 WIMPs, which fell into the appropriate time window, and neutrons were simulated above the 1000 NIP detector energy threshold. A WIMP mass of 1000 GeV was assumed. For the L and T neutron runs, the ^{252}Cf source was placed at the same positions used for the real experimental runs of this work, which are described in Section 3.2.1. It was assumed that the full instrumented volume of the detector, described in Section 2.1.6, was active. Dead and veto wires were not taken into consideration. The θ and ϕ recoil angles were accumulated for each WIMP and neutron run type. For each run type the angles were used to populate a two-dimensional histogram that had 36 θ bins and 72 ϕ bins. These histograms are shown in Figure 4.2.

In the discussion that follows, the reader is reminded of Figures 3.9 and 1.7(b) that show the neutron source positions relative to the detector and a sketch of the principle of sidereal modulation, respectively. For the L neutron run, $\theta > \frac{\pi}{2}$ for all recoils. This is expected since the source was placed left of the detector and neutrons had to move along the positive $\hat{z}$ direction to interact in the detector and θ is the polar angle as measured from $\hat{z}$. The distribution across ϕ appears uniform for the L neutron run since the source was placed left of the detector such that it was on an axis along the normal of the center of the x-y plane of the detector volume. The angular distribution of recoils from the generally south WIMP wind has similar characteristics, although an increase in scattering density is found near $\phi = \pi$. When $\phi = \pi$, this corresponds to a vector pointing along the $-\hat{x}$ direction which is downward through the detector and perpendicular to the wires. Since the latitude of the detector Boulby is not at the optimal $\sim 45^{\circ}$ latitude but is instead at $\sim 55^{\circ}$ the recoils on average pick up a $-\hat{x}$ directional component. To visualize this, it is suggested that the

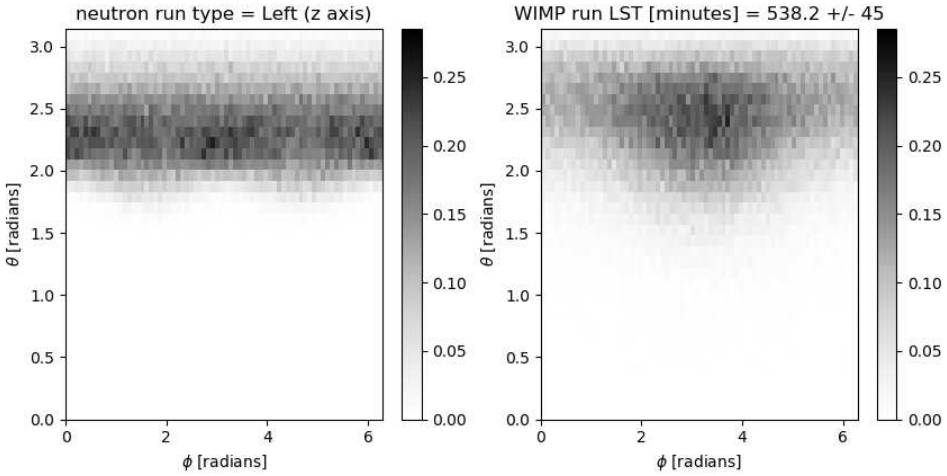

(a) Left Neutron and South WIMP Wind

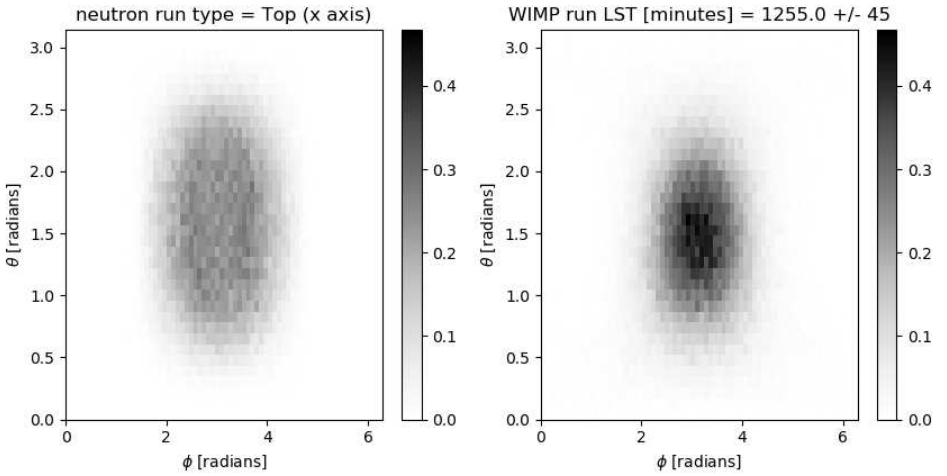

(b) Top Neutron and Down WIMP wind

Figure 4.2: (a) Simulated recoil angles are histogrammed for a L neutron exposure and for WIMPs blowing generally south through the detector. (b) Histograms are shown for a Top neutron exposure and WIMPs blowing generally down through the detector.

reader refer to Figure 1.7(b) and imagine shifting the detector by 10° of latitude. One will also notice upon careful inspection that some WIMP recoils have $\theta < \frac{\pi}{2}$. Since the WIMP velocity distribution is expected to be Maxwell-Boltzmann in the galactic frame and is then boosted into the lab frame, this implies that some of the WIMP velocities actually have a component that is directed opposite that from which the WIMP wind should appear to be coming on average.

For the T neutron run, the source was placed above the detector such that it was on an axis along the normal of the center of the y-z plane of the detector volume. Again $\phi = \pi$ corresponds to a vector along $-\hat{x}$ and so it is expected that the distribution be centered there. Recoils are allowed to occur in both the positive and negative $\hat{z}$ directions allowing θ to span the full range. Since the source was approximately centered on the detector volume from above, equal numbers of recoils are expected along the positive and negative $\hat{z}$ directions and the distribution is centered about $\theta = \frac{\pi}{2}$. The recoil angle distribution of the generally downward WIMP wind appears similar although with a tighter grouping.

One should not expect agreement within each pair of cases that would be indicative of a good fit from typical statistical tests. After all, the neutron source was essentially a stationary point source in the lab while the WIMP velocity distribution was assumed to be Maxwell-Boltzmann and then transformed into the lab frame.

4.3 Summary of Work Done

In this dissertation the directional detection capability of the DRIFT-IIe detector was investigated through its sensitivity to the range of nuclear recoil tracks in two dimensions. Here I will summarize the work that I performed towards this goal and towards understanding the DRIFT-IIe detector in general. The contributions that I made were through analysis, simulation, and experiment.

I developed the full analysis software chain (Sections 3.2.5 and 3.1.3) that was used to process the data collected for this work. The chain processed the data from a raw state through picking out calibration and nuclear recoil signals. An event browser was also built that could be used to view and apply the processes of the analysis chain in a manual mode, so one can visually inspect the events as different parts of the analysis are applied. These were written in the C++ language in a modular manner that could be reused and scaled. The code heavily implemented ROOT, and was built using CMake.

Sparks were analyzed (Section 2.2.1) to understand properties of the shaping electronics used for signal readout. The structure of the shaping response kernel as well as the shaper gain were measured. The latter is necessary to understand the gas gain achievable by the detector which I investigated (3.1.2).

I performed Garfield++ simulations (Section 2.1.3) to study carrier anion drift, avalanche, production of avalanche ions, and signal production at the wires. I wrote a simulation in the Python language (Appendix B.0.3) to understand the energies and directionality of nuclear recoils, which were due to neutron source exposures. I also applied the WIMP wind simulation (Appendix B.0.4) to understand those properties of recoils induced by WIMPs. Further simulation of neutron exposures was done with GEANT4 [119] although some of that work was not utilized for this dissertation. The starting pieces exist to develop a full end-to-end simulation of the detector, which is to be understood as from the time a source particle is fired to signal production at the wires.

I used the analysis software that I developed to extract energy calibration signals from 55Fe source exposures (Section 3.1.1). I additionally applied the software to extract nuclear recoils that contained minority peak structure, and to understand the range of nuclear recoils in two dimensions due to neutron exposures (Section 3.3.1). Post analysis, I visually inspected all of the tracks that passed through the recoil analysis to study the ability of the algorithms to process these signals (Section 3.3.3). In total four neutron exposure positions (Section 3.2.1) were analyzed for this work. The distributions of the nuclear range components in two dimensions were compared against each other for each of the four populations using a Monte Carlo resampling technique (Section 3.3.2) that I developed into code. Additionally, I studied the energy distributions (Section 3.2.3) for these runs, and extracted distributions of the distance away from the MWPC these recoils occurred (Section 3.2.2). Ultimately, I used a combination of WIMP simulation, the neutron recoil range component data, and the Monte Carlo resampling technique to understand how many WIMP events[49] would need to be observed to claim a significant detection (Section 4.1).

[49]Prior to finishing this work, I also presented some preliminary results at the 2020 American Physical Society Four Corners Meeting.

I visited Occidental College on a few occasions to work with the detector. I was present and assisted in getting the detector prepared to take the data that was used in this dissertation. I helped to mark out the different neutron source positions, and I helped to perform some repair work, such as after a wire of the left MWPC broke during operation. Finally, I assisted in collecting initial 55Fe, untriggered background, neutron source exposure, and untriggered background run data.

Bibliography

[1] F. Zwicky. Republication of: The redshift of extragalactic nebulae. *General Relativity and Gravitation*, 41:207–224, 2009 (Original Paper: F. Zwicky, Die Rotverschiebung von extragalaktischen Nebeln, Helvetica Physica. Acta 6, 110-127 (1933).).

[2] F. Zwicky. On the Masses of Nebulae and of Clusters of Nebulae. *The Astrophysical Journal*, 86:217–246, 1937.

[3] G. Bertone, D. Hooper. History of Dark Matter. *Reviews of Modern Physics*, 90, 2018.

[4] S.M. Faber, J.S. Gallagher. Masses and Mass-to-Light Ratios of Galaxies. *Annual Review of Astronomy and Astrophysics*, 17:135–187, 1979.

[5] B. Fuchs, C. Mollenhoff, J. Heidt. Decomposition of the rotation curves of distant field galaxies. *Astronomy and Astrophysics*, 336:878–882, 1998.

[6] B. Fuchs. The Amount of Dark Matter in Spiral Galaxies. Dark Matter in Astro and Particle Physics Proceedings of the International Conference DARK 2000 Heidelberg, Germany, 10-14 July 2000.

[7] T.S. Van Albada, J.N. Bahcall, K. Begeman, R. Sanscisi. Distribution of Dark Matter in the Spiral Galaxy NGC 3198. *The Astrophysical Journal*, 295:305–313, 1985.

[8] K.C. Freeman. On the Disks of Spiral and SO Galaxies. *The Astrophysical Journal*, 160:811–830, 1970.

[9] V.C. Rubin, W.K. Ford Jr., N. Thonnard. Rotational Properties of 21 Sc Galaxies with a Large Range of Luminosities and Radii, From NGC 4605 (R = 4 kpc) to UGC 2885 (R = 122 kpc). *The Astrophysical Journal*, 238:471–487, 1980.

[10] M. Persic, P. Salucci, F. Stel. The universal rotation curve of spiral galaxies - I. The dark matter connection. *Monthly Notices of the Royal Astronomical Society*, 281:27–47, 1996.

[11] M. Milgrom. A Modification of the Newtonian Dynamics as a Possible Alternative to the Hidden Mass Hypothesis. *The Astrophysical Journal*, 270:365–370, 1983.

[12] R.H. Sanders, S.S. McGaugh. Modified Newtonian Dynamics as an Alternative to Dark Matter. *Annual Review of Astronomy and Astrophysics*, 40:263–317, 2002.

[13] P. Schneider, J. Ehlers, E.E. Falco. *Gravitational Lenses*. Springer, 1999.

[14] D. Clowe et al. A Direct Empirical Proof of the Existence of Dark Matter. *The Astrophysical Journal*, 648:L109–L113, 2006.

[15] A. Liddle. *An Introduction to Modern Cosmology (Second Edition)*. John Wiley and Sons, 2003.

[16] M. Bradac et al. Revealing the Properties of Dark Matter in the Merging Cluster MACS J0025.4-1222. *The Astrophysical Journal*, 687:959–967, 2008.

[17] S. Weinberg. *Cosmology*. Oxford University Press, 2008.

[18] M. Boylan-Kolchin et al. Resolving cosmic structure formation with the Millennium-II Simulation. *Monthly Notices of the Royal Astronomical Society*, 398:1150–1164, 2009.

[19] M. Tanabashi et al. (Particle Data Group). Review of Particle Physics. *Physical Review D 98, 030001*, 2018.

[20] R.H. Cyburt et al. Big bang nucleosynthesis: Present status. *Reviews of Modern Physics*, 88, 2016.

[21] K. Garrett, G. Duda. Dark Matter: A Primer. *Advances in Astronomy*, 2011 Article ID 968283, 2010.

[22] Planck Collaboration: N. Aghanim et al. Planck 2018 results. VI. Cosmological parameters. *arXiv:1807.06209v2*.

[23] D.J. Fixsen. The Temperature of the Cosmic Microwave Background. *The Astrophysical Journal*, 707:916–920, 2009.

[24] G. Hinshaw et al. Nine-Year Wilkinson Microwave Anisotropy Probe (WMAP) Observations: Cosmological Parameter Results. *The Astrophysical Journal Supplement Series*, 208:19, 2013.

[25] M. Taoso, G. Bertone, A. Masiero. Dark matter candidates: a ten-point test. *Journal of Cosmology and Astroparticle Physics*, 03, 2008 022.

[26] J.L. Feng. Dark Matter Candidates from Particle Physics and Methods of Detection. *Annual Review of Astronomy and Astrophysics*, 48:495–545, 2010.

[27] M. Battaglieri et al. US Cosmic Visions: New Ideas in Dark Matter 2017 : Community Report. *arXiv:1707.04591*.

[28] R.J. Scherrer, M.S. Turner. On the relic, cosmic abundance of stable, weakly interacting massive particless. *Physical Review D 33, 6*, 1986.

[29] P. Gondolo, G. Gelmini. Cosmic Abundances of Stable Particles: Improved Analysis. *Nuclear Physics B*, 360:145–179, 1991.

[30] K. Griest, D. Seckel. Three exceptions in the calculation of relic abundances. *Physical Review D 43, 10*, 1991.

[31] J. Edsjo, P. Gondolo. Neutralino relic density including coannihilations. *Physical Review D 56, 4*, 1997.

[32] G. Jungman, M. Kamionkowski, K. Griest. Supersymmetric Dark Matter. *Physics Reports*, 267:195–373, 1996.

[33] J.L. Feng. Dark Matter Phenomenology. *AIP Conference Proceedings 1182, 224 (2009)*.

[34] J.L. Feng, J. Kumar. Dark-Matter Particles without Weak-Scale Masses or Weak Interactions. *Physical Review Letters 101, 231301*, 2008.

[35] M. E. Peskin. Supersymmetric dark matter in the harsh light of the Large Hadron Collider. *Proceedings of the Natural Academy of Sciences of the United States of America*, 112, 40:12256–12263, 2015.

[36] J.D. Lewin, P.F. Smith. Review of mathematics, numerical factors, and corrections for dark matter experiments based on elastic nuclear recoil. *Astroparticle Physics*, 6:87–112, 1996.

[37] F. Mayet et al. A review of the discovery reach of directional Dark Matter detection. *Physics Reports*, 627:1–49, 2016.

[38] R.K. Pathria, P.D. Beale. *Statistical Mechanics*. Elsevier, Third edition, 2011.

[39] A.K. Drukier, K. Freese, D.N. Spergel. Detecting cold dark-matter candidates. *Physical Review D 33, 12*, 1986.

[40] P.J. McMillan, J.J. Binney. The uncertainty in Galactic parameters. *Monthly Notices of the Royal Astronomical Society*, 402:934–940, 2010.

[41] A-C. Eilers et al. The Circular Velocity Curve of the Milky Way from 5 to 25 kpc. *The Astrophysical Journal*, 871:120, 2019.

[42] S.S. McGaugh. A Precise Milky Way Rotation Curve Model for an Accurate Galactocentric Distance. *arXiv:1808.09435v1*.

[43] R. Drimmel, E. Poggio. On the Solar Velocity. *Research Notes of the American Astronomical Society*, 2:4, 2018.

[44] P.J.T. Leonard, S. Tremaine. The Local Galactic Escape Speed. *The Astrophysical Journal*, 353:486–493, 1990.

[45] T. Piffl et al. The RAVE survey: the Galactic escape speed and the mass of the Milky Way. *Astronomy and Astrophysics*, 562, 2014.

[46] A. J. Deason et al. The local high velocity tail and the Galactic escape speed. *Monthly Notices of the Royal Astronomical Society*, 485:3514–3526, 2019.

[47] J.I. Read. The local dark matter density. *Journal of Physics G: Nuclear and Particle Physics*, 41, 063101, 2014.

[48] Gaia Collaboration, D. Katz et al. Gaia Data Release 2 Mapping the Milky Way disc kinematics. *Astronomy and Astrophysics*, 616, 2018.

[49] J.F. Navarro, C.S. Frenk, S.D.M. White. The Structure of Cold Dark Matter Halos. *The Astrophysical Journal*, 462:563–575, 1996.

[50] A.D. Ludlow et al. The mass profile and accretion history of cold dark matter haloes. *Monthly Notices of the Royal Astronomical Society*, 432:1103–1113, 2013.

[51] J.M. Gaskins. A review of indirect searches for particle dark matter. *Contemporary Physics*, 57:4:496–525, 2016.

[52] A.U. Abeysekara et al. Sensitivity of HAWC to high-mass dark matter annihilations. *Physical Review D 90, 122002*, 2014.

[53] A. Albert et al. Dark Matter Limits from Dwarf Spheroidal Galaxies with the HAWC Gamma-Ray Observatory. *The Astrophysical Journal*, 853:154, 2018.

[54] F. Kahlhoefer. Review of LHC dark matter searches. *International Journal of Modern Physics A*, 32:13, 2017.

[55] P.J. Fox et al. Missing energy signatures of dark matter at the LHC. *Physical Review D 85, 056011*, 2012.

[56] M. Schumann. Direct detection of WIMP dark matter: concepts and status. *Journal of Physics G: Nuclear and Particle Physics*, 46 103003, 2019.

[57] R. Essig, J. Mardon, T. Volansky. Direct detection of sub-GeV dark matter. *Physical Review D 85, 076007*, 2012.

[58] O. Abramoff et al. SENSEI: Direct-Detection Constraints on Sub-GeV Dark Matter from a Shallow Underground Run Using a Prototype Skipper CCD. *Physical Review Letters 122, 161801*, 2019.

[59] J. Engel, S. Pittel, P. Vogel. Nuclear Physics of Dark Matter Detection. *International Journal of Modern Physics E*, 1:1:1–37, 1992.

[60] E. Aprile et al. Search for WIMP inelastic scattering off xenon nuclei with XENON100. *Physical Review D 96, 022008*, 2017.

[61] Sven Vahsen. Status of the CYGNUS Directional Recoil Observatory Project. Presented at APS April Meeting 2020. https://absuploads.aps.org/presentation.cfm?pid=17801.

[62] M. Battaglieri et al. Dark matter search in a Beam-Dump eXperiment (BDX) at Jefferson Lab. *arXiv:1607.01390*.

[63] M. Battaglieri et al. Dark matter search in a Beam-Dump eXperiment (BDX) at Jefferson Lab: an update on PR12-16-001. *arXiv:1712.01518*.

[64] D.P. Snowden-Ifft et al. Directional light-WIMP time-projection-chamber detector for electron beam-dump experiments. *Physical Review D 99, 061301(R)*, 2019.

[65] B. Morgan, A.M. Green, N.J.C Spooner. Directional statistics for realistic weakly interacting massive particle direct detection experiments. *Physical Review D 71, 103507*, 2005.

[66] A.M. Green, B. Morgan. Optimizing WIMP directional detectors. *Astroparticle Physics*, 27:142–149, 2007.

[67] J. Billard. Comparing readout strategies to directly detect dark matter. *Physical Review D 91, 023513*, 2015.

[68] N.J.C. Spooner et al. Simulations of the nuclear recoil head-tail signature in gases relevant to directional dark matter searches. *Astroparticle Physics*, 34:284–292, 2010.

[69] M. Schumann. Dark Matter Search With Liquid Noble Gases. *47th Rencontres de Moriond on Cosmology*, pages 247–254, 2012.

[70] E. Aprile, T. Doke. Liquid xenon detectors for particle physics and astrophysics. *Reviews of Modern Physics*, 82, 2010.

[71] E. Aprile et al. Dark Matter Search Results from a One Ton-Year Exposure of XENON1T. *Physical Review Letters 121, 111302*, 2018.

[72] D.S. Akerib et al. Results from a Search for Dark Matter in the Complete LUX Exposure. *Physical Review Letters 118, 021303*, 2017.

[73] X. Cui et al. Dark Matter Results from 54-Ton-Day Exposure of PandaX-II Experiment. *Physical Review Letters 119, 181302*, 2017.

[74] G. Adhikari et al. An experiment to search for dark-matter interactions using sodium iodide detectors. *Nature*, 564, 2018.

[75] C. Savage et al. Compatibility of DAMA/LIBRA dark matter detection with other searches. *Journal of Cosmology and Particle Astrophysics*, 04, 2009.

[76] F. Ruppin et al. Complementarity of dark matter detectors in light of the neutrino background. *Physical Review D 90, 083510*, 2014.

[77] J.B.R. Battat et al. First background-free limit from a directional dark matter experiment: Results from a fully fiducialised DRIFT detector. *Physics of the Dark Universe*, 9-10:1–7, 2015.

[78] J.B.R. Battat et al. Low threshold results and limits from the DRIFT directional dark matter detector. *Astroparticle Physics*, 91:65–74, 2017.

[79] K. Freese, J. Frieman, A. Gould. Signal modulation in cold-dark-matter detection. *Physical Review D 37, 12*, 1988.

[80] D.N. Spergel. Motion of the Earth and the detection of weakly interacting massive particles. *Physical Review D 37, 6*, 1988.

[81] J.B.R. Battat et al. Measurement of directional range components of nuclear recoil tracks in a fiducialised dark matter detector. *Journal of Instrumentation 12 P10009*, 2017.

[82] R. Bernabei et al. First Model Independent Results From DAMA/LIBRA-Phase2. *Nuclear Physics and Atomic Energy*, 19:4:307–325, 2018.

[83] J. Amare et al. ANAIS-112 status: two years results on annual modulation. *Journal of Physics: Conference Series*, 1468 012014, 2020.

[84] P. Montini et al. Dark matter search with the SABRE experiment. *arXiv:1807.08073v1*.

[85] M. Antonello et al. The SABRE project and the SABRE Proof-of-Principle. *arXiv:1806.09340v2*.

[86] G. Adhikari et al. Search for a Dark Matter-Induced Annual Modulation Signal in NaI(Tl) with the COSINE-100 Experiment. *Physical Review Letters 123, 031302*, 2019.

[87] A. Murphy, S. Paling. The Boulby Mine Underground Science Facility: The Search for Dark Matter, and Beyond. *Nuclear Physics News*, 22:1:19–24, 2012.

[88] S. Burgos et al. Measurement of the range component directional signature in a DRIFT-II detector using 252 Cf neutrons. *Nuclear Instruments and Methods in Physics Research A*, 600:417–423, 2009.

[89] P. Virtanen et al. SciPy 1.0: Fundamental Algorithms for Scientific Computing in Python. *Nature Methods*, 17:261–272, 2020.

[90] G.J. Alner et al. The DRIFT-II dark matter detector: Design and commissioning. *Nuclear Instruments and Methods in Physics Research A*, 555:173–183, 2005.

[91] D.P. Snowden-Ifft, C.J. Martoff, J.M. Burwell. Low pressure negative ion time projection chamber for dark matter search. *Physical Review D 61, 101301(R)*, 2000.

[92] C.J. Martoff et al. Suppressing drift chamber diffusion without magnetic field. *Nuclear Instruments and Methods in Physics Research A*, 440:355–359, 2000.

[93] J.B.R. Battat et al. Reducing DRIFT backgrounds with a submicron aluminized-mylar cathode. *Nuclear Instruments and Methods in Physics Research A*, 794:33–46, 2015.

[94] Brookhaven National Laboratory Instrumentation Division. LARASIC5 (IC127). *This datasheet was provided by Jean-Luc Gauvreau who designed the electronic readout for DRIFT-IIe.*

[95] Linear Technology Corporation. Linear Technology LTC2365/LTC2366 1Msps/3Msps, 12-Bit Serial Sampling ADCs in TSOT. Datasheet: https://www.analog.com/en/products/ltc2365.html.

[96] H.M. Araujo et al. Measurements of neutrons produced by high-energy muons at the Boulby Underground Laboratory. *Astroparticle Physics*, 29:471–481, 2008.

[97] M. Robinson et al. Measurements of muon flux at 1070 m vertical depth in the Boulby underground laboratory. *Nuclear Instruments and Methods in Physics Research A*, 511:347–353, 2003.

[98] E.Tziaferi et al. First measurement of low intensity fast neutron background from rock at the Boulby Underground Laboratory. *Astroparticle Physics*, 27:326–338, 2007.

[99] S. Burgos et al. Studies of neutron detection and backgrounds with the DRIFT-IIa dark matter detector. *Astroparticle Physics*, 28:409–421, 2007.

[100] Daniel P. Snowden-Ifft. Discovery of multiple, ionization-created CS2 anions and a new mode of operation for drift chambers. *Review of Scientific Instruments*, 85, 2014.

[101] D.P. Snowden-Ifft. Second Pass at Fall 2013 No-Flow O2 Analysis Memo. *Internal Drift Collaboration Document (2014 February 17)*.

[102] D.P. Snowden-Ifft. First Pass at an Oxy Automated Analysis of Minority Peaks Memo. *Internal Drift Collaboration Document (2014 June 16)*.

[103] D.R. Tovey et al. A new model-independent method for extracting spin-dependent cross section limits from dark matter searches. *Physics Letters B*, 488:17–26, 2000.

[104] J. Ellis, R.A. Flores. Elastic supersymmetric relic-nucleus scattering revisited. *Physics Letters B*, 263:259–266, 1991.

[105] J. Engel, S. Pittel, P. Vogel. Nuclear Physics of Dark Matter Detection. *International Journal of Modern Physics E*, 1:1–37, 1992.

[106] J.D. Vergados. Searching for cold dark matter. *Journal of Physics G: Nuclear and Particle Physics*, 22:253–272, 1996.

[107] James F. Ziegler, M.D. Ziegler, J.P. Biersack. SRIM - The stopping and range of ions in matter (2010). *Nuclear Instruments and Methods in Physics Research B*, 268:1818–1823, 2010.

[108] W. Blum, W. Riegler, and L. Rolandi. *Particle Detection with Drift Chambers*. Springer, 2008.

[109] The Document Foundation. LibreOffice. https://www.libreoffice.org/.

[110] Tohru Ohnuki, Daniel P. Snowden-Ifft, and C. Jeff Martoff. Measurement of carbon disulfide anion diffusion in a TPC. *Nuclear Instruments and Methods in Physics Research A*, 463:142–148, 2001.

[111] D. P. Snowden-Ifft and J.-L. Gauvreau. High precision measurements of carbon disulfide negative ion mobility and diffusion. *Review of Scientific Instruments*, 84, 2013.

[112] R. Veenhof et al. Garfield++ - simulation of gaseous detectors. https://garfieldpp.web.cern.ch/garfieldpp/.

[113] Rene Brun and Fons Rademakers. ROOT - An Object Oriented Data Analysis Framework. Proceedings AIHENP'96 Workshop, Lausanne, Sep. 1996, Nucl. Inst. and Meth. in Phys. Res. A 389 (1997) 81-86. See also http://root.cern.ch/.

[114] A. Kalamarides et al. Negative ion formation K(nd)-CS_2 collisions: Detection of electric-field-induced detachment of CS_2^-. *The Journal of Chemical Physics*, 89:7226–7228, 1988.

[115] L. Suess, R. Parthasarathy, F.B. Dunning. Rydberg electron transfer to CS_2: properties of the product CS_2^- ions. *Chemical Physics Letters*, 372:692–697, 2003.

[116] M.P. Dion, C.J. Martoff, M. Hosack. On the mechanism of Townsend avalanche for negative molecular ions. *Astroparticle Physics*, 33:216–220, 2010.

[117] K. Pushkin, D. Snowden-Ifft. Measurements of W-value, mobility, and gas gain in electronegative gaseous CS_2 and CS_2 gas mixtures. *Nuclear Instruments and Methods in Physics Research A*, 606:569–577, 2009.

[118] N. Gee, G. Ramanan, G.R. Freeman. Density effects on ion mobilities in electron attaching fluids: CS_2, SF_6, and C_6F_6. *Canadian Journal of Chemistry*, 68:1527–1531, 1990.

[119] S. Agostinelli et al. GEANT4–a simulation toolkit. *Nuclear Instruments and Methods in Physics Research A*, 506:250–303, 2003.

[120] J. Brack et al. Background Assay and Rejection in DRIFT. *Physics Procedia*, 61:130–137, 2015.

[121] D.P. Snowden-Ifft et al. Low energy alphas in the drift detector. *Nuclear Instruments and Methods in Physics Research A*, 516:406–413, 2004.

[122] J.B.R. Battat et al. Radon in the DRIFT-II directional dark matter TPC: emanation, detection and mitigation. *Journal of Instrumentation 9 P11004*, 2014.

[123] J. Brack et al. Long-term study of backgrounds in the DRIFT-II directional dark matter experiment. *Journal of Instrumentation 9 P07021*, 2014.

[124] V. Chiste M.M. Be. Decay Data Evaluation Project, Laboratoire National Henri Becquerel. [Online] http://www.lnhb.fr/nuclides/Fe-55_tables.pdf.

[125] M. Pipe. *Limits on spin-dependent WIMP-proton cross-sections using the DRIFT-IId directional dark matter detector*. PhD thesis, Department of Physics and Astronomy, University of Sheffield, 2011.

[126] S. Burgos et al. Low energy electron and nuclear recoil thresholds in the DRIFT-II negative ion TPC for dark matter searches. *Journal of Instrumentation 4 P04014*, 2009.

[127] A. Thompson et al. *X-Ray Data Booklet*. Center for X-Ray Optics and Advanced Light Source, Lawrence Berkeley National Laboratory, Berkeley, CA, October 2009.

[128] M.J. Berger , J.H. Hubbell, S.M. Seltzer, J. Chang, J.S. Coursey, R. Sukumar, D.S. Zucker, and K. Olsen. XCOM: Photon Cross Section Database (version 1.5). [Online] http://physics.nist.gov/xcom [2018, July 18]. National Institute of Standards and Technology, Gaithersburg, MD.

[129] J. H. Scofield. Theoretical Photoionization Cross Sections From 1 to 1500 keV. Technical report, Lawrence Livermore Laboratory, January 1973.

[130] J.H. Hubbell et al. A Review, Bibliography, and Tabulation of K, L, and Higher Atomic Shell X-Ray Fluorescence Yields. *Journal of Physical and Chemical Reference Data 23*, pages 339–364, 1994.

[131] L.E. Davis et al. *Handbook of Auger Electron Spectroscopy, Second Edition*. Physical Electronics Division, Perkin-Elmer Corporation, Eden Prairie, MN, 1976.

[132] NIST X-ray Photoelectron Spectroscopy Database, NIST Standard Reference Database Number 20, National Institute of Standards and Technology, Gaithersburg MD, 20899 (2000), doi:10.18434/T4T88K, (retrieved [2018 July 18]).

[133] M.O. Krause. Atomic radiative and radiationless yields for K and L shells. *Journal of Physical and Chemical Reference Data 8*, pages 307–327, 1979.

[134] I.K. Bronic, B. Grosswendt. Ionization yield formation in argon-isobutane mixtures as measured by a proportional-counter method. *Nuclear Instruments and Methods in Physics Research B*, 117:5–17, 1996.

[135] D. Srdoc. Dependence of the Energy Per Ion Pair on the Photon Energy Below 6 keV in Various Gases. *Nuclear Instruments and Methods*, 108:327–332, 1973.

[136] P.J. Linstrom and W.G. Mallard, Eds. NIST Chemistry WebBook, NIST Standard Reference Database Number 69. *National Institute of Standards and Technology, Gaithersburg MD, 20899, https://doi.org/10.18434/T4D303, (retrieved [2019 July 30]).* .

[137] D.P. Snowden-Ifft et al. Neutron recoils in the DRIFT detector. *Nuclear Instruments and Methods in Physics Research A*, 498:155–164, 2003.

[138] A. Hitachi. Bragg-like curve for dark matter searches: Binary gases. *Radiation Physics and Chemistry*, 77:1311–1317, 2008.

[139] Free Software Foundation, Inc. GNU Bash. https://www.gnu.org/software/bash/.

[140] Kitware, Inc. and Contributors. CMake - Cross Platform Makefile Generator. https://cmake.org/.

[141] Jean-Luc Gauvreau. Occidental College. Personal email communication (2015 July 17).

[142] Jean-Luc Gauvreau. Occidental College. Personal communication while working in the Occidental College lab (2016 June 20).

[143] Matteo Frigo and Steven G. Johnson. The design and implementation of FFTW3. *Proceedings of the IEEE*, 93(2):216–231, 2005. Special issue on "Program Generation, Optimization, and Platform Adaptation".

[144] N.D. Gagunashvili. Comparison of weighted and unweighted histograms. *arXiv:physics/0605123*.

[145] R.R. Wilcox. *Applying Contemporary Statistical Techniques*. Elsevier, 2003.

[146] B. deB. Darwent. Bond Dissociation Energies in Simple Molecules. *U.S. Department of Commerce National Bureau of Standards*, 1970.

[147] Jae Won Shin et al. GEANT4 and PHITS simulations of the shielding of neutrons from the 252Cf source. *Journal of the Korean Physical Society*, 65:591–598, September 2014.

[148] X-5 Monte Carlo Team Los Alamos National Laboratory. MCNP - A General Monte Carlo N-Particle Transport Code, Version 5 Volume I: Overview and Theory. *LA-UR-03-1987*, revised 2008.

[149] M.B. Chadwick, M. Herman, P. Obložinský, et al. ENDF/B-VII.1 Nuclear Data for Science and Technology: Cross Sections, Covariances, Fission Product Yields and Decay Data . *Nuclear Data Sheets*, 112(12):2887–2996, 2011. Special Issue on ENDF/B-VII.1 Library [accessed online] https://www.nndc.bnl.gov/sigma/.

[150] M. Berglund, M.E. Wieser. Isotopic compositions of the elements 2009 (IUPAC Technical Report). *Pure and Applied Chemistry*, 83(2):397–410, 2011.

[151] Fernando Pérez and Brian E. Granger. IPython: a system for interactive scientific computing. *Computing in Science and Engineering*, 9(3):21–29, May 2007.

[152] C.R. Harris et al. Array programming with NumPy. *Nature*, 585:357–362, 2020.

[153] J. D. Hunter. Matplotlib: A 2d graphics environment. *Computing in Science & Engineering*, 9(3):90–95, 2007.

[154] J. Lindhard et al. Integral Equations Governing Radiation Effects. *Mat. Fys. Medd. Dan. Vid. Selsk. 33, no. 10 (1963).*

[155] B.W. Carroll, D.A. Ostlie. *An Introduction to Modern Astrophysics (Second Edition).* Pearson Education, Inc., 2007.

[156] G.B. Arfken and H.J. Weber. *Mathematical Methods for Physicists*. Elsevier, Sixth edition, 2005.

Appendix A

Mean Free Path of ^{252}Cf neutrons

Let us assume a beam of neutrons impinging on a target of particles of type j that are uniformly distributed and are assumed to be at rest relative to the neutrons. The mean free path is typically given by $\ell_i = 1/(\eta_j \sigma_{ij})$, where η_j gives the number density of particles j in the volume and σ_{ij} is the interaction cross section of a neutron of energy E_i with particle j. If the target is composed of multiple species of individual particles then $\ell_i = 1/(\sum_j \eta_j \sigma_{ij})$.

For 40 Torr CS_2 or 40:1.5 Torr CS_2:O_2, one does not have individual C, S, and O atoms but rather CS_2 and O_2 molecules. The energies of dissociation for $\mathrm{CS} \rightarrow \mathrm{C} + \mathrm{S}$, $\mathrm{CS_2} \rightarrow \mathrm{CS} + \mathrm{S}$, and $\mathrm{O_2} \rightarrow \mathrm{O} + \mathrm{O}$ are $757\ \frac{\mathrm{kJ}}{\mathrm{mol}}$, $397\ \frac{\mathrm{kJ}}{\mathrm{mol}}$, and $498\ \frac{\mathrm{kJ}}{\mathrm{mol}}$, respecitively [146]. These correspond to $7.85\ \frac{\mathrm{eV}}{\mathrm{bond}}$, $4.11\ \frac{\mathrm{eV}}{\mathrm{bond}}$, and $5.17\ \frac{\mathrm{eV}}{\mathrm{bond}}$, respectively. The neutrons that will be considered have an average energy of 2.3 MeV, which is much greater than the bond energies of the molecules in the target gas. Therefore, the assumption of individual particles in the previous paragraph is reasonable. Assuming a target gas temperature of 293 K, the CS_2 and O_2 molecules have kinetic energies of $\frac{3}{2}k_B T = 0.03788$ eV which corresponds to speeds of 310 m/s and 478 m/s, respectively. By comparison a neutron of energy 2.3 MeV has a speed of 2.10×10^7 m/s. Therefore, the assumption that the target particles are at rest with respect to the incoming neutrons is also reasonable[50].

If the neutrons are emitted from a ^{252}Cf source, The probability density p_i of a neutron being emitted from the source with energy E_i will be approximated by the Watt Fission Spectrum [147] [148]. Where $a = 1.025$ MeV, $b = 2.926$ MeV^{-1}, and $c \approx 0.300$ is a normalization constant found by integrating the density function from 0 to ∞ and setting this value equal to 1.

$$p_i = c \cdot \sinh(\sqrt{bE_i}) \cdot e^{-E_i/a}$$

[50] To be more careful, momentum should be considered. Sulfur is approximately 32 times as massive as a neutron. Using the quoted speeds, S carries 0.05% of the momentum that the neutron carries.

The mean neutron energy $\langle E_i \rangle = \frac{\int_0^\infty dE_i E_i p_i}{\int_0^\infty dE_i p_i} = 2.31$ MeV. The mode neutron energy is found by taking $\frac{dp_i}{dE_i} = 0$ and solving for E_i which results in $mode(E_i) = 0.90$ MeV. For the purpose of calculation, $0 \leq E_i \leq 20$ MeV will be sampled and accounts for greater than 0.999999 of the spectrum.

The cross sections σ_{ij} for neutrons of energies E_i interacting with particle $j = \mathrm{C}, \mathrm{S}, \text{ or } \mathrm{O}$ were retrieved from the ENDF/B-VII.1 library on the National Nuclear Data Center website [149]. All interactions were assumed to occur with ^{12}C, ^{32}S, and ^{16}O since the natural abundance of each of these isotopes are approximately 98.9%, 95.0%, and 99.8%, respectively [150]. Cross section data were then saved to lists for neutrons with energies of 0 to 20 MeV. With a model of the neutron energy spectrum and cross sections given, the energy-averaged mean free path $\langle \ell \rangle$ for a given target gas can be calculated. For 40 Torr CS_2 gas with $T = 293$ K the number densities $\eta_C = 1.318 \times 10^{24}$ m^{-3} and $\eta_S = 2.636 \times 10^{24}$ m^{-3} are given by the ideal gas law. An addition of 1.5 Torr of O_2 corresponds to a number density of $\eta_O = 9.886 \times 10^{22}$ m^{-3}.

$$\langle \ell \rangle = \sum_i p_i \frac{1}{\sum_j \eta_j \sigma_{ij}}$$

The mean free paths in 40 Torr CS_2 and 40:1.5 Torr CS_2:O_2 are reported in the table below. For each of the target gases, the mean free path was calculated for two cases: one in which the total cross sections of neutrons in the gas were considered; and one in which only the elastic scattering cross sections were considered. Each calculation of $\langle \ell \rangle$ was done numerically, where the probability density for neutron energy p_i was discretized into bins of width 0.01 MeV from 0 to 20 MeV. For each sampled energy E_i, σ_{ij} was found by iterating through a list of cross section data and choosing the value which corresponded most closely to a neutron having the chosen E_i.

From the table it can be seen that neutrons, of the energies considered, mainly interact with the gas via elastic scattering since for both target gases the ratio of $\langle \ell \rangle_{total} / \langle \ell \rangle_{elastic} = 0.89$.

It is informative to calculate the mean free path in 40:1.5 Torr CS_2:O_2 due to the C, S, and O components of the gas independently. Using the previously given number densities, numeri-

Table A.1: The mean free path of ^{252}Cf neutrons in 40 Torr CS_2 and 40:1.5 Torr CS_2:O_2 target gases.

Cross Section	gas	$\langle \ell \rangle$ [m]
total	CS_2	1031
elastic	CS_2	1155
total	CS_2:O_2	1004
elastic	CS_2:O_2	1124

cal calculations similar to those above were performed considering three cases in which only C, S, or O scatters were allowed. When the total cross sections of neutrons with each gas component were considered mean free paths of 1895, 3783, and 62583 m were calculated for S, C, and O, respectively. If elastic scattering cross sections of neutrons with each gas component were considered mean free paths of 2210, 3924, and 64296 m were calculated for S, C, and O. Assuming that the probability of a neutron making it some distance d in the detector volume without interacting with the gas goes as $e^{-d/\ell}$, then the probability that it interacts with the gas before making it a distance d is $1 - e^{-d/\ell}$. Let $d = 1$ m be used to estimate the size of the detection volume. The relative probability of a C elastic recoil in comparison to one with S is $(1-e^{-1/3924})/(1-e^{-1/2210}) = 0.563$. The relative probability of an O elastic recoil in comparison to one with S is $(1 - e^{-1/64296})/(1 - e^{-1/2210}) = 0.034$. These relative probabilities indicate that most recoils occurs with S, followed by C, with very few occurring with O. It should be made explicit that this does not mean that one may expect to observe 56 C recoils for every 100 S recoils. S and C recoils of equal energy will deposit different densities of ionization in the gas and their overall ranges will be different. Therefore the detector and analysis may not be equally efficient in observing each recoil type.

Appendix B

Simulation of WIMP and Neutron Runs

Simulations were written in the Python language to understand nuclear recoils generated by the WIMP wind and by neutron exposures. The simulations were run using the IPython [151] interactive shell. Packages such as NumPy [152] and SciPy [89] were utilized, and Matplotlib [153] was used for visualization. Below, the models that were used in the simulations will be described without including full details of how the models were written into code.

B.0.1 Nuclear Recoils

The nuclear recoils for both WIMPs and neutrons were treated as elastic hard-sphere scatters. Let the incident particle, whether WIMP or neutron, be labeled m_s and let the recoiling nucleus be labeled m_r, which is assumed to be initially at rest. The situation is sketched in the lab frame in Figure B.1. The impact parameter is labeled b, R is the summed radii of the two particles, α_r is the polar angle of the recoil, and α_s that of the incident particle. The polar angles are measured relative to the incoming direction of the incident particle m_s. The azimuthal angle β_r of the recoil, not shown, lies in the $x' - y'$ plane and is defined to be zero for a vector aligned along $\hat{x'}$. The azimuthal angle is chosen by pseudorandomly sampling a value from the uniform distribution $0 \leq \beta_r \leq 2\pi$. It should be emphasized that one is not working in fixed detector coordinates in the section, for each incident/recoil pair of particles, the orientation of this coordinate system is unique within the detector. To remind one of this, directions have been labeled with a "′" symbol.

Let the speed of the incident particle be v_s and the speeds of the two particles directly after the collision be u_s and u_r. The expressions for energy and momentum conservation follow.

$$energy: \quad \frac{1}{2}m_s v_s^2 = \frac{1}{2}m_s u_s^2 + \frac{1}{2}m_r u_r^2$$

$$\hat{z'}: \quad m_s v_s = m_s u_s cos\alpha_s + m_r u_r cos\alpha_r$$

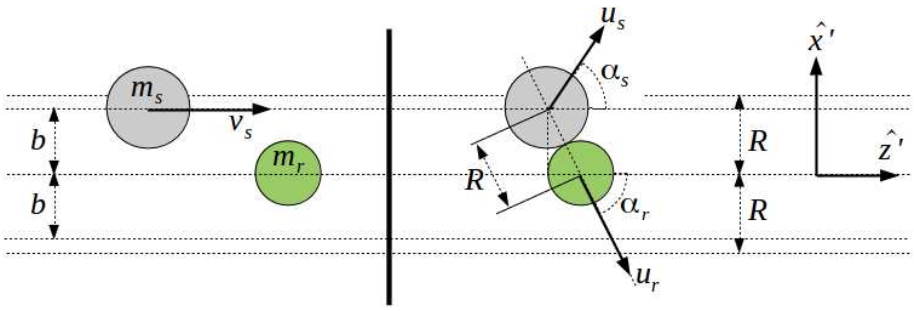

Figure B.1: A sketch of hard-sphere scattering in the lab frame for a mass m_s incident upon mass m_r that was initially at rest.

$$\hat{x}': \quad 0 = m_s u_s sin\alpha_s - m_r u_r sin\alpha_r$$

The three above equations can be used to find an expression for the recoil speed u_s in terms of the masses of the two particles, the speed of the incident particle v_s, and the polar angle of the recoil α_r.

$$u_r = \frac{2m_s v_s}{m_s + m_r} cos\alpha_r$$

An expression for the recoil energy follows directly.

$$E_r = \frac{1}{2} m_r u_r^2 = E_s \frac{4m_s m_r}{(m_s + m_r)^2} cos^2\alpha_r \quad w/ \quad E_s = \frac{1}{2} m_s v_s^2$$

Based on the geometry of the figure, $b = Rsin\alpha_r$. Equivalently, the recoil energy can be written to include the impact parameter.

$$cos^2\alpha_r = 1 - sin^2\alpha_r = 1 - \frac{b^2}{R^2}$$

$$E_r = E_s \frac{4m_s m_r}{(m_s + m_r)^2} (1 - \frac{b^2}{R^2})$$

If one now imagines standing at the left side of the figure and peering down $\hat{z}'$, both masses will appear to be circles in two dimensions and will collide if $b \leq R$, or equivalently if they are contained within the circular cross section πR^2. If the two spheres collide the probability that the impact parameter was contained within the annulus of infinitesimal thickness b and $b + db$ is found

by the ratio of the annulus area and total cross section.

$$p(b)db = \frac{2\pi b}{\pi R^2}db = \frac{2b}{R^2}db$$

Notice that for a given incident particle energy, the recoil energy is set by the impact parameter b. This implies that probability of a recoil having an energy between E_r and $E_r + dE_r$ is equal to the probability of the impact parameter being between b and $b + bd$.

$$E_r = E_s\frac{4m_sm_r}{(m_s+m_r)^2}(1-\frac{b^2}{R^2}) \quad \rightarrow \quad \left|\frac{dE_r}{db}\right| = \frac{2b}{R^2}\frac{4E_sm_sm_r}{(m_s+m_r)^2} \quad \rightarrow \quad db = \frac{R^2}{2b}\frac{(m_s+m_r)^2}{4E_sm_sm_r}dE_r$$

The absolute value was taken since the two infinitesimals are essentially bin widths, when considering the discrete distributions, each of which are positive. The absolute value sign was then dropped for steps that follow.

$$p(b)db = \frac{2b}{R^2}db = (\frac{2b}{R^2})(\frac{R^2}{2b}\frac{(m_s+m_r)^2}{4E_sm_sm_r}dE_r) = \frac{(m_s+m_r)^2}{4E_sm_sm_r}dE_r \quad \rightarrow \quad p(E_r) = \frac{(m_s+m_r)^2}{4E_sm_sm_r}$$

The result is a constant for a given incident particle energy E_s, meaning that the probability density function is flat across all allowed energies. The polar angle of the recoil $\frac{\pi}{2} \geq \alpha_r \geq 0$ corresponds to an energy range of $0 \leq E_r \leq \frac{4m_sm_r}{(m_s+m_r)^2}E_s$. In simulation recoil energies can be chosen by sampling a uniform distribution over this range.

The probability density function for α_r can be constructed in a similar fashion.

$$b = Rsin\alpha_r \quad \rightarrow \quad \left|\frac{db}{d\alpha_r}\right| = R|cos\alpha_r| \quad \rightarrow \quad db = Rcos\alpha_r d\alpha_r$$

The absolute value signs were dropped in the rightmost expression since $cos\alpha_r$ is positive over the range of allowed angles.

$$p(b)db = \frac{2b}{R^2}db = (\frac{2(Rsin\alpha_r)}{R^2})(Rcos\alpha_r d\alpha_r) = sin(2\alpha_r)d\alpha_r \quad \rightarrow \quad p(\alpha_r) = sin(2\alpha_r)$$

In simulation α_r can be chosen by sampling a probability density function of the shape $sin(2\alpha_r)$. One does not want to both randomly sample E_r and α_r for each recoil. Once one has been sampled the other follows from the equation for recoil energy E_r that is a function of α_r.

B.0.2 Energy Conversion to NIPs

After simulation of nuclear recoil energies, the conversion of energy values to NIPs is accomplished by scaling with the Lindhard or quenching factor [154], which was discussed in Section 2.3. The asymptotic form for the independent element approach [138] was used to calculate quenching factors in this work. This assumes that for a binary gas such as CS_2, that quenching occurs via C ions with C or S ions with S independently in the gas. For S recoils, over an energy range of 50 to 250 keV_r, which is relevant to this work, it is estimated that this approach agrees within $\sim$5% of the quenching factor curve for S recoils in 40 Torr CS_2 that appears in reference [138]. The asymptotic form of the quenching factor q_r is given below, and it is was reproduced from [36] [154]. The variables Z and A are atomic number and mass, respectively. When calculating ϵ energies E_r must be given in units of keV_r.

$$\epsilon = 11.5 E_r Z^{-7/3}$$

$$g(\epsilon) = 3\epsilon^{0.15} + 0.7\epsilon^{0.6} + \epsilon$$

$$k = 0.133 Z^{2/3} A^{-1/2}$$

$$q_r = \frac{k g(\epsilon)}{1 + k g(\epsilon)}$$

For S, $Z = 16$ and $A = 32$ yields a value of $k = 0.149$. Once the recoil energy of a S or C ion has been simulated in units of keV_r, the NIPs energy of the recoil can be calculated since the amount of energy needed to produce an ion pair in the gas $W_{55_{Fe}}$ has previously been measured, see Section 2.3. Similar can be done for C recoils for which $Z = 6$ and $A = 12$ results in a value of $k = 0.127$. Carbon recoils were not considered in this work.

$$NIPs_r = \frac{q_r E_r}{W_{55_{Fe}}}$$

B.0.3 Neutron Run Simulation

For neutron runs, it was assumed that neutrons were emitted from a ^{252}Cf source. The neutron energy distribution was described by the Watt Fission Spectrum that has previously been provided in Appendix A. It was assumed that all neutron recoils were of the isotope ^{32}S, which comprises 95.0% of the natural sulfur abundance. Recall, the gas mixture used for the experimental work for this dissertation was 40:1.5 Torr CS_2:O_2. Only S recoils are considered in the simulation at present due to the combination of facts that O comprises only 1.6% of the target by mass, and the observation of C recoils has been determined to be suppressed by a factor of $\sim$100 relative to S recoils with a previous DRIFT detector [88].

The elastic scattering cross section versus energy distribution for neutron-^{32}S interactions was retrieved from the ENDF/B-VII.1 library on the National Nuclear Data Center website [149]. This distribution extended up to a neutron energy of 20 MeV. This was used to construct a probability density histogram, which represents the probability of a neutron interacting per bin in neutron energy. The energy binning of the ENDF/B-VII.1 data was preserved.

For each energy bin of the cross-section-probability-density histogram, the Watt Fission Spectrum function was evaluated for that energy. This resulted in a histogram that has the same binning as the cross-section-probability-density histogram. This second histogram was area normalized to one such that it is also a probability density histogram. This second histogram describes the probability of a neutron being emitted with a certain energy from the ^{252}Cf source.

At this point, one has two probability density histograms with the same binning across neutron energy. One distribution describes the probability of sampling a neutron from the source with a specific energy. The second describes The probability of a neutron of a specific energy elastically scattering with S. To get the correct proportion of neutrons of a specific energy bin being emitted from the source and then interacting with S, the two probability density histograms were multiplied

bin-by-bin and the resulting histogram was area normalized to one. It is this resultant probability density histogram that is sampled to choose neutron energies in simulation.

The neutron source was assumed to be a point source. In the simulation, the source could be placed anywhere relative to the detector. The source positions that are described in Section 3.2.1 for the Left, Right, Front, and Top neutron runs were coded into the simulation. That is, one could easily choose one of the source positions that was actually used for experimentation.

Interactions other than with the gas were ignored for this simulation, including interactions as neutron pass through the wall of the vessel. A GEANT4 [119] study was done in which a ^{252}Cf source was placed 1 m away from a square sheet of 304-grade stainless steel sheet that was 1 cm thick and had side lengths of 1 m. The source was placed such that the 1 m distance is that along an axis that is normal to the center of the sheet. Approximately 11,000 neutrons passed through the sheet. The initial and final momentum vectors of each neutron were saved which correspond, respectively, to before and after the neutron passed through the sheet. It was found that the neutron energy changes were $\sim$15% at most and greater than 85% of the neutrons passed through with their direction unchanged. Of the neutrons that did have their direction changed, the most probable angles, measured as a polar angle from their initial momentum direction, were between $\sim$15-45°.

Only recoils that occurred in the active volume of the detector were simulated. Recall, the detector was not fully instrumented to read out all wires of the detector. Only the portion for which readout was available, see Section 2.1.6, was simulated. The mean free path for elastic scatters of ^{252}Cf neutrons in 40:1.5 Torr CS_2:O_2 is $\sim$1124 m, see Appendix A. Since this is much larger than the dimensions of the detector it was assumed that any interaction location within the active volume of the detector was equally probable. To choose a neutron interaction site within the active volume, uniform random positions were sampled along the three dimensions of the active volume. The S recoil energy and direction, relative to the incoming neutron, are sampled as described in Appendix B.0.1. The velocity of the recoil is then projected to detector coordinates. The three Cartesian detector coordinate axes are x (perpendicular to the wires of the MWPC), y (parallel to

the wires of the MWPC), and z (along the axis of anion drift). Recoil energy can be converted to NIPs via the method of Appendix B.0.2.

In some applications of the simulation, one needs to approximate the length of sulfur recoil tracks. For this simulation, tracks of ionization were assumed to be straight lines. The length of these tracks scaled linearly with recoil energy, see references [137] and [68]. Length of a sulfur recoil track was found by multiplying the recoil energy by the factor 0.0182 mm/keV. Any tracks that were found to exit the active volume of the detector were culled. Since the anode wire positions can be individually specified within the simulation, any tracks that were found to drift and hit wires that had been, in general, labeled as dead or veto wires, see Section 3.2.5, for actual experimental runs could be also be culled. This latter discarding of tracks was only applied in some runs of the simulation, and explicit references to this are given as needed in the main body of this work.

This was an initial simulation, it is deficient of some features that would provide a more realistic simulation. It would be more complete to consider recoils from all components of the gas C, S, and O. Neutron induced recoils were assumed to follow a distribution of orientations, relative to the incoming neutron direction, as described by hard-sphere elastic scattering. It would be better to perform the previous step with GEANT4 [119]. Neutrons were assumed to only interact with the gas and no affects were attributed to neutrons scattering off any other material prior to interaction in the gas. Tracks were assumed to be straight, and track straggling was not included. Details of the tracks that are due to it being formed of individual anions were neglected; for instance, diffusion, as the anions drift towards the MWPC was neglected. Ionization density along a track was not taken into account, which is important since the size of a signal for a given wire is proportional to how much ionization is present per sampling bin in time of the readout electronics. That fact that real signals for the gas mixture contain minority peak structure was not considered. For a better simulation one should include the previous considerations as well as simulating signals for the wires as described in Section 2.1.3, and further folding in the shaping electronics response, noise, and any processing that was performed during the analysis chain of Section 3.2.5.

B.0.4 WIMP Run Simulation

The WIMP wind simulation was initially developed by a previous Colorado State University graduate student Matt Williams. This simulation was utilized and further developed for this dissertation. One starts by specifying how many WIMP recoils to simulate along with a specific WIMP mass. For this work, a mass of 1000 GeV was typically used. One must also define the detector location, latitude and longitude, on Earth. For this work, the detector was sited at the Boulby Underground Laboratory at a (latitude,longitude) of (54.550450°, -0.821137°). These coordinates are listed in Decimal Degree notation, meaning that latitude is bounded within the range [-90,90] degrees from the equator and longitude is bounded within the [-180,180] degrees from the Prime Meridian. These coordinates were retrieved from Google Maps on 23 June 2020. One must also specify the dates/times over which the WIMPs should be sampled. Recall, the velocities of WIMPs relative to an Earth-based detector theoretically change over time and this enables one to search for annual and sidereal modulation signatures.

In reference frame of the galaxy WIMPs were assumed to have a truncated Maxwell-Boltzmann velocity distribution; the Standard Halo Model is described in Section 1.4. The motion of the Sun as it moves in a circle about the center of the galaxy, corrections to the previous motion (known as the peculiar motion), the motion of the Earth about the Sun for the dates that were sampled, and the detector location combined with the rotation of Earth about its axis must all be considered to transform WIMP velocities in a galactic frame to a lab frame on Earth. These transformations will not be discussed here. Some information can be found in references [155] and [36]. After the transformations, one obtains the three WIMP velocity components in lab/detector coordinates for each WIMP.

Once in the lab frame, nuclear recoils are generated via the methods of Appendix B.0.1. One must choose the correct proportions of each nuclear recoil species based on the specific gas mixture being used. For this work 40:1.5 Torr CS_2:O_2 was used. Three nuclear recoil species may be present S, C, and O. For these nuclei, spin-independent iteraction cross sections were assumed, which theoretically scale as A^2 [36] with A being nuclear mass. The fraction of atoms in the gas

that are S is given by $f_S = \frac{40}{41.5}\frac{2}{3}$. Similarly, $f_C = \frac{40}{41.5}\frac{1}{3}$ and $f_O = \frac{1.5}{41.5}$. The proportion of nuclear recoils of type S, C, or O is given by w_i below.

$$w_i = \frac{f_i A_i^2}{\sum_i f_i A_i^2} \quad i = \{S, C, O\}$$

Based on this model 92.22% of the recoils should be S, 6.48% C, and 1.30% O. However the observation of C recoils has previously been found to be suppressed for DRIFT detectors due to a relatively low ionization density along these tracks. Additionally, O recoils are not expected to contribute substantially, therefore it was decided to consider S recoils only for the simulation runs discussed in this work.

The outputs of the simulation are the WIMP velocities in lab coordinates, the identities of the corresponding nuclear recoils (for example C, S, or O), and the velocities of the corresponding nuclear recoils in lab coordinates. One is able to generate objects such as recoil energy distributions as well as understand the directionality of the recoils within the detector.

Appendix C

Checks to Accompany Conclusion Results

Two checks are presented here to accompany results presented in the conclusion to this dissertation, Section 4. One check is to confirm that the c and δ_c values output from the fit routine are consistent with expectations, and the other is to check that adequate sampling has been performed in the algorithm above to output consistent results. The former will be addressed first. The fit to each plot of Figure 4.1 was of the form $\mathbb{S}_i = c\sqrt{N_{samples_i}}$, and χ^2 minimization was used to extract the fit parameter c.

$$\chi^2 = \sum_i \frac{(\mathbb{S}_i - c\sqrt{N_{samples_i}})^2}{\delta^2_{\mathbb{S}_i}}$$

Minimization can be achieved by taking the derivative with respect to c and setting the resultant expression equal to zero.

$$0 = \frac{\partial \chi^2}{\partial c} = 2\sum_i \frac{(\mathbb{S}_i - c\sqrt{N_{samples_i}})(-\sqrt{N_{samples_i}})}{\delta^2_{\mathbb{S}_i}} = 2c\sum_i \frac{N_{samples_i}}{\delta^2_{\mathbb{S}_i}} - 2\sum_i \frac{\sqrt{N_{samples_i}}\mathbb{S}_i}{\delta^2_{\mathbb{S}_i}}$$

One finds an expression for c, the dummy index has been changed in the denominator to emphasize the sums can be performed independent of each other. Using the formula below and the values from Tables 4.3 and 4.4 for T-L and T-R, respectively, $c = 0.1725$ for T-L and $c = 0.2204$ for T-R. The two previous values match those returned by the fit routine, which are reported in Figure 4.1.

$$c = \frac{\sum_i \frac{\sqrt{N_{samples_i}}\mathbb{S}_i}{\delta^2_{\mathbb{S}_i}}}{\sum_m \frac{N_{samples_m}}{\delta^2_{\mathbb{S}_m}}}$$

An expression for the derivative of c with respect to a given $\mathbb{S}_i$ is now found, and it has only one nonzero value for the summands of the previous numerator. The previous denominator is a constant.

$$\frac{\partial c}{\partial \mathbb{S}_i} = \frac{\frac{\sqrt{N_{samples_i}}}{\delta^2_{\mathbb{S}_i}}}{\sum_m \frac{N_{samples_m}}{\delta^2_{\mathbb{S}_m}}}$$

With the above formula, one is now prepared to formulate an expression for δ_c using standard uncertainty propagation.

$$\delta_c^2 = \sum_i (\frac{\partial c}{\partial \mathbb{S}_i} \delta^2_{\mathbb{S}_i})^2 = \sum_i \frac{\frac{N_{samples_i} \delta^2_{\mathbb{S}_i}}{\delta^4_{\mathbb{S}_i}}}{(\sum_m \frac{N_{samples_m}}{\delta^2_{\mathbb{S}_m}})^2} = \frac{\sum_i \frac{N_{samples_i}}{\delta^2_{\mathbb{S}_i}}}{(\sum_m \frac{N_{samples_m}}{\delta^2_{\mathbb{S}_m}})^2}$$

Observing that the denominator is the numerator squared nets a simplified expression. A switch back to the original dummy index has been implemented.

$$\delta_c^2 = \frac{1}{\sum_i \frac{N_{samples_i}}{\delta^2_{\mathbb{S}_i}}}$$

The steps above were performed after reviewing reference [156], and the expression directly above was applied to each set of values in Tables 4.3 and 4.4 for T-L and T-R, respectively. A value of $\delta_c = 0.0011$ was calculated for T-L and $\delta_c = 0.0021$ for T-R. Both match the uncertainties returned by the fit routine above, which are reported in Figure 4.1. This check confirms that the uncertainties output from the fit routine match what is expected from a χ^2 minimization.

Above, $N_{subsets} = 400$ and $N_{permutations} = 500$. In order to check that adequate samples were drawn with the algorithm a consistency check was performed to ensure that the T-L and T-R results agree across multiple runs of the algorithm. For each of T-L and T-R, the algorithm was run five times. Table C.1, summarizes the outputs for all T-L and T-R comparisons. The outputs from the

algorithm are listed in the same sequence in that they were generated in time. So, the first set of outputs are those which have already been presented above.

Table C.1: The analysis algorithm has been run five times each when comparing the Top-Left and Top-Right Pairs of Runs. A comparison of the run statistics for each set of five provide a check on output consistency.

algorithm run	c	δ_c	χ^2	NDF	$\tilde{\chi}^2$	p-value
T-L 1	0.17247	0.00105	14.5	13	1.11	0.341
T-L 2	0.17382	0.00108	15.9	13	1.22	0.257
T-L 3	0.17370	0.00107	3.76	13	0.290	0.993
T-L 4	0.17397	0.00109	20.1	13	1.55	0.0923
T-L 5	0.17459	0.00110	8.47	13	0.65	0.812
average	0.1737		12.5	13	0.964	0.50 ± 0.17
σ	0.0008					
T-R 1	0.22039	0.00205	5.87	5	1.17	0.319
T-R 2	0.21990	0.00204	4.46	5	0.893	0.485
T-R 3	0.22295	0.00206	1.51	5	0.302	0.912
T-R 4	0.22570	0.00203	6.32	5	1.26	0.276
T-R 5	0.22015	0.00207	11.1	5	2.22	0.0491
average	0.222		5.86	5	1.17	0.41 ± 0.14
σ	0.002					

It can be seen that the c fit parameter is consistent across runs of the algorithm for both T-L and T-R. The standard deviations about the average c values also are consistent with the size of the individual uncertainties for each run of the algorithm. The values show convergence on the c value across runs with uncertainty in the third digit of precision. Further, the χ^2 and NDF values for the T-L and T-R runs result on average in p-values that are indicative of reasonable fits, for which a p-value of ~ 0.5 is sought.

Appendix D

Acronyms

BBN: Big Bang Nucleosynthesis

CMB: Cosmic Microwave Background

DM: Dark Matter

DRIFT: Directional Recoil Identification From Tracks

FFT: Fast Fourier Transform

GMT: Greenwich Mean Time

LST: Local Sidereal Time

MOND: Modified Newtonian Dynamics

MWPC: Multi-Wire Proportional Counter, LMWPC indicates Left-MWPC and RMWPC indicates Right-MWPC

NIPs: Number of Ions Pairs

NITPC: Negative-Ion Time Projection Chamber

RPR: Radon Progeny Recoil

TPC: Time Projection Chamber

UTC: Coordinated Universal Time

WIMP: Weakly Interacting Massive Particle